# 1D Nanomaterials 2012

Guest Editors: Yanqiu Zhu, Renzhi Ma, Raymond Whitby, and Steve Acquah

# 1D Nanomaterials 2012

# 1D Nanomaterials 2012

Guest Editors: Yanqiu Zhu, Renzhi Ma, Raymond Whitby, and Steve Acquah

# Editorial Board

# Contents

## *Editorial*

# 1D Nanomaterials 2012

## Yanqiu Zhu,[1] Renzhi Ma,[2] Raymond Whitby,[3] and Steve Acquah[4]

[1] *International Center for Materials Nanoarchitectonics (MANA), National Institute for Materials Science, Tsukuba, Ibaraki 305-0044, Japan*

[2] *College of Engineering, Mathematics and Physical Sciences, University of Exeter, Exeter EX4 4Qf, UK*

[3] *Nanoscience and Nanotechnology Group, Faculty of Science and Engineering, University of Brighton, Huxley Building, Brighton BN2 4GJ, UK*

[4] *Department of Chemistry and Biochemistry, Florida State University, Tallahassee, FL 32306-4390, USA*

Correspondence should be addressed to Renzhi Ma; ma.renzhi@nims.go.jp

We witnessed an initial hyped period and enthusiasm on carbon nanotubes in the 1990s later went through a significant expansion into nanotubes of other materials (metal dichalcogenides, boron nitride, etc.) as well as various nanowires and nanorods. While much of the hype might have gone, the research on one-dimensional (1D) nanomaterials has matured as one of the most active research areas within the nanoscience and nanotechnology community, flourishing with ample, exciting, and new research opportunities. Just like any other research frontier, researchers working in the 1D nanomaterials field are constantly striving to develop new fundamental science as well as potential applications. It remains a common belief that versatility and tunability of 1D nanomaterials would challenge many new rising tasks coming from our resource and energy demanding modern society. The traditional semiconductor industry has produced so many devices and systems from transistors, sensors, lasers, and LEDs to more sophisticated solar panels, which are now part of our daily lives. By downsizing the core components or parts to 1D form, one might wonder how fundamentally the dimensionality and morphology would impact the device performance, this is, as always, requiring us to fully understand the structure-property relationship in 1D nanomaterials. It may be equally crucial in connecting discovery-driven fundamental science to market-driven technology industry concerning potentially relevant findings derived from these novel materials. The importance of a platform that allows active researchers in this field to present their new development in a timely and efficient manner is therefore self-evident. Following the success of two early special issues devoted to 1D nanomaterials, this is the third one in a row organized by the same group of guest editors, attesting that such a platform has been well received by the readers.

A total of 18 articles (out of 36 submissions) are presented in the current issue. Twelve of them were contributed from Asia region, 5 from North America, and 1 from Europe. Reasonably diversified object materials are covered, but carbon nanotubes (C. Mateo-Mateo et al.; B.-W. Jeong; S. Park et al.; K.-S. Lin et al.) and ZnO nanowires (H. Qi et al.; S. Wang et al.; D.-H. Kuo and J.-Y. He; M. H. Mamat et al.) have attracted most research interest, maintaining their comfortable leading positions in nanotube and nanowire categories, respectively, as we have noticed in preceding special issues. Though CVD (S. Park et al.; H. Qi et al.; D.-H. Kuo and J.-Y. He; M. Cross and W. Varhue) and hydrothermal (M. H. Razali et al.) processes have been extensively applied in the synthesis, less common but promising methods such as diffusion-controlled solid state formation (S. G. Jeon et al.) and electrospinning (S. Q. Zhu et al.) are also introduced. It is also interesting to observe that, even in conventional CVD setup, a more sophisticated control on the growth of 1D nanomaterials was attempted by employing techniques such as catalytic bilayers (H. Qi et al.; D.-H. Kuo and J.-Y. He) and electrostatic forces (M. Cross and W. Varhue). A couple of articles reported specified spectroscopic studies on 1D nanomaterials/composites using Raman spectroscopy (E. E. Ibrahim et al.) and X-ray absorption spectroscopy (Md.

A. Mannan et al.), which may inspire the use of elegant characterization protocols and tools for some particular purposes.

Nanoelectronics, nanophotonics, nanomaterials for energy conversion and storage, and nano-bio interfacing materials, to name a few, have emerged as important subfields for 1D nanomaterials research, and each represents an exciting direction. By taking a glimpse at this special issue, one can also get a quick idea that these exciting research directions are well represented. The application prospects reported in these articles range from efficient light emitter (N. Ekthammathata et al.) to transparent conductive electrode (S. B. Sepulveda-Mora and S. G. Cloutier) and ultraviolet photoconductive sensor (M. H. Mamat et al.), from diluted magnetic semiconductor (S. Wang, et al.) to surface enhanced Raman scattering on a single nanowire (H. Qi et al.) and DNA molecules (C. Deng et al.), as well as hydrogen storage for fuel cells (K.-S. Lin et al.), and so forth. We are pleased to have included these contributions representing future research directions and technology trends.

On the other hand, as stated in the 2011 Editorial, we feel that the toxicity and recycling issues concerning 1D nanomaterials have been generally overlooked. The future of nanoscience and nanotechnology, most likely not limited to 1D regime, will be largely dependent on how well we can balance the cost and performance in order to construct any real and practical device and system. As guest editors, we would like to signalize this message again and invite future studies to address the health, safety, and economic concerns related with 1D nanomaterials, which, if not well tackled, may become a bottle neck to achieve real and practical engineering applications.

## Acknowledgments

*Yanqiu Zhu*
*Renzhi Ma*
*Raymond Whitby*
*Steve Acquah*

*Research Article*

# Study on the Morphologies and Formational Mechanism of Poly(hydroxybutyrate-co-hydroxyvalerate) Ultrafine Fibers by Dry-Jet-Wet-Electrospinning

**Shuqi Zhu,[1] Hao Yu,[2] Yanmo Chen,[1] and Meifang Zhu[2]**

[1] *College of Material Science & Engineering, Donghua University, Songjiang, Shanghai 201620, China*
[2] *State Key Lab for Modification of Chemical Fibers and Polymer Materials, 2999 North Renmin Road, Songjiang, Shanghai 201620, China*

Correspondence should be addressed to Hao Yu, yuhao@dhu.edu.cn and Meifang Zhu, zhumf@dhu.edu.cn

Dry-jet-wet-electrospinning (DJWE) was carried out to study the formational mechanism of poly(hydroxybutyrate-co-hydroxyvalerate) electrospun fibers. Morphological comparison between normal electrospinning (NE) and DJWE was investigated. The results showed that jet could solidify quickly in DJWE to avoid bead collapse or fiber coherence. Jet structures could be maintained at very low collection distance. Beanpod-like beads, which were named as primary beads, could be seen at the boundary of stability and instability section and divided into spindle-like beads with longer collection distance. Bead-free electrospun fibers from DJWE had few bonding points among each other, and fast solidification and double-diffusion led to rough and shriveled fiber surface. DJWE mats were higher hydrophobic than that from NE due to more loose structure and higher surface porosity. Higher bead ratio on the surface and rounder bead structure resulted in higher hydrophobicity.

## 1. Introduction

Electrospinning was regarded as a very convenient and effective method for preparing nanofibers and ultrafine fibers, which could be used for filtration [1, 2], tissue engineering scaffolds [3–5], protective clothes [6, 7], carriers for enzymes [8, 9], sensors [10–12], and so forth. Many researchers focused on the theories and the phenomena of the electrospinning process [13–16]. However, there were some difficulties in studying the morphology at very low collection distance. For example, the transformation process of instability section, especially the deformation of beads, which was of great importance for understanding the formation of ultrafine fibers, could not be observed clearly by high-speed photography. Besides, as the solidification mechanism of the normal electrospun fibers was solvent volatilization, the jet near the needle contained a large amount of solvent and could not maintain the structures when collected on glass slides or aluminum foils. So the fiber collected at low distance always deformed or even collapsed

on solid substrates and the exact morphology could not be observed.

Dry-jet-wet-electrospinning (DJWE) was one electrospinning method for producing fibers from nonvolatile solvent, such as room temperature ionic liquids [17, 18]. It was also used for preparing aligned nanofiber yarns [19]. This method, though usually called wet electrospinning, actually had the similar fiber solidification mechanism with dry-jet-wet-spinning, only differed in driving force. Fibers were electrospun into the coagulation bath, with precipitant for polymers in it. In another word, the polymer could not be dissolved in the bath, whereas the solvent could. The fiber solidified by double-diffusion of the solvent and the bath liquid, which was much faster than volatilization mechanism in normal electrospinning (NE). So the morphology of the fiber could be kept even at a low collection distance.

Moreover, electrospun mat usually had higher hydrophobicity than solution cast film, due to higher surface roughness. And some works found that mats with beaded structures were higher hydrophobic, even superhydrophobic

[20–23], though beaded structures were usually considered as defects in electrospinning. However, it was difficult to prepare mats with high bead density, for beads collapsed as a result of residue solvent.

In this work, poly(hydroxybutyrate-co-hydroxyvalerate) (PHBV)/chloroform electrospinning solution was used as a model [23, 24]. PHBV was biosynthesized aliphatic co-polyester, which varied with different morphologies. Its electrospun products were also used to study the morphologies and surface wettability [25, 26]. Chloroform is volatile solvent but could not be removed completely at low collection distance. Ethanol was used as coagulation bath, because chloroform was soluble and PHBV was precipitated in it. The morphologies of beaded and bead-free electrospun mats produced by NE and DJWE were compared. Some new structures and phenomena could be seen in DJWE method, and theories on bead deformation process at very low collection distance were introduced. Finally, the wettability of all the electrospun mats prepared by NE and DJWE was compared using water contact angle.

## 2. Experimental

*2.1. Materials.* PHBV was kindly supplied by Ningbo Tianan Biomaterial Co. Ltd., Mw = $3.0 \times 10^5$ g/mol (measured by GPC), HV mol% = 2% (measured by $^1$H NMR). Chloroform was purchased from Boer Chemical Reagent Co. Ltd. Anhydrous ethanol and ethyl acetate were purchased from Shanghai Chemical Reagent Co. Ltd. PHBV was Soxhlet extracted by chloroform at 80°C and then deposited with ethyl acetate. The deposition was filtrated and vacuum dried at 40°C for 12 h, and pure PHBV was acquired.

*2.2. Electrospinning Apparatus.* The apparatus used in this research was shown in Figure 1. A PHD 22/2000 syringe pump (Harvard Apparatus, Inc.) was used to feed the solution. The PTFE tube connected the syringe with the stainless needle. The inner diameter of needle was about 0.8 mm. The positive pole of the high voltage supply was connected to the needle, and the negative pole was connected to the iron plate under the coagulation bath and grounded. The liquid in the coagulation bath was anhydrous ethanol. And aluminum foil was used to collect fibers in NE.

*2.3. Electrospinning.* The PHBV/chloroform electrospinning solution was prepared as in Table 1. The solution viscosity, conductivity, and surface tension were measured by R/S Plus Rheometer (Brookfield, Inc.), EL30 conductivity meter (Mettler Toledo), and OCA40 video based contact angle measurement device (Dataphysics), respectively.

Electrospinng was carried out at room temperature (20°C) and humidity of 60–70%. The applied voltage between the needle and ground was 10 kV, and the feeding rate was 3 mL/h. The mats were collected on aluminum foil or in ethanol bath at various distances. All the mats were dried in the air at room temperature for 24 h, and then vacuum dried for 12 h. The morphology was observed by scanning electronic microscopy (SEM, JSM-5600LV, JEOL

Ltd.). The water contact angles were measured by OCA40 video based contact angle measurement instrument (Dataphysics).

## 3. Results and Discussion

*3.1. Morphological Comparison of Beaded Electrospun Fibers by DJWE and NE.* Fibers electrospun from 6 wt% PHBV solution by NE and DJWE at various distances varied considerably in morphology (Figure 2). The solution of that concentration had a jet of 3–5 cm stability section. If the jet was collected by NE, it could be observed that the jets did not solidify when they were collected on Al foil. And lower collection distance was used, more collapsed jets could be observed. So the detailed structure of the jet could be obtained if the jet was collected by NE. If the jet was collected by DJWE, it could be seen that all the fibers, no matter how long in distance the jet was collected, had original shape and clear boundary with each other. No collapsed or adhered fibers could be seen. When collected at 3 cm, the jet was in the stability section, and thinned slowly and continuously. So the fiber diameter was large, and no beads or thin fibers could be seen. If the collection distance was 6 cm, the jet had just entered the instability section, so the jet started to swing. Fibers having much lower diameters than the jet and beaded structures between two adjacent fibers appeared at this collection distance. It was interesting that the beads were beanpod-like, which had not reported yet. And compared to the spindle-like beads at longer distance, the beanpod-like beads were 2 times in volume, and had tendency to split into two spindle-like beads. It could be inferred that the spindle-like beads came from the splitting of beanpod-like beads. To distinguish the two different beads, the beanpod-like beads were named as primary beads, and spindle-like beans were named as secondary beans. Because of large residual solvent, the primary beads were easily collapsed in NE. Normally they could not be observed. When increasing the collection distance, the shape of the beads did not change again, and the fibers became longer but the diameter changed little, which was consistent with our previous work [27].

*3.2. Bead Formation Mechanism at the Boundary of Stability and Instability Section.* The beanpod-like beads were seldom reported in previous works, but they were a key to understand the deformation process of the jet during electrospinning at the boundary of stability and instability sections. When at the stability section, the jet diameter decreased slowly and continuously, containing a large amount of solvent. After entering the instability section, the jet whipped and swung. The defects of the jet were firstly stretched by the electrical field into thinner fibers, whereas the unstretched parts remained cylindrical because of viscosity. These cylindrical parts, with the central region shrinking slightly due to surface tension, became the primary beads. The fibers had faster solvent evaporation and solidified quickly as the result of large specific surface area than the beaded structures. Fast solidification and tensile strengthening made the fiber stronger. So when the

TABLE 1: The components and parameters of electrospinning solutions.

| No. | PHBV (g) | Concentration (wt%) | Chloroform (g) | Ethanol (g) | Viscosity* (Pa·s) | Conductivity (µS/cm) | Surface tension (mN/m) |
|---|---|---|---|---|---|---|---|
| 1 | 0.8 | 4 | 19.2 | 0 | 0.151 | Not detected** | 27.29 |
| 2 | 1.2 | 6 | 18.8 | 0 | 0.546 | Not detected** | 27.51 |
| 3 | 1.6 | 8 | 16.4 | 2 | 1.097 | 0.89 | 29.17 |

* The viscosity was measured at shearing rate of 100/s.
** The conductivity was lower than 0.001 µS/cm and could not be detected.
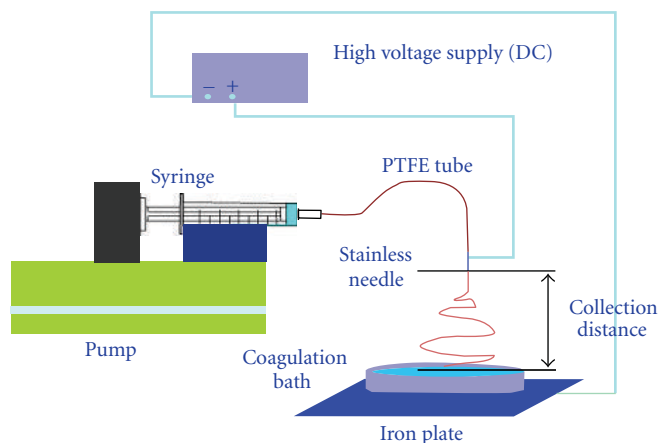


FIGURE 1: Illustration of the apparatus for dry-jet-wet-electrospinning.

thinner fibers had better strength than the primary beads, the beads would be deformed by the electric field force instead of fibers. Due to the effect of the electrical force and surface tension, the primary beads were stretched into two or more spindle-like beads. All the deformation process was illustrated in Figure 3. When further increasing the collection distance, the length of fibers between adjacent beads increased and beaded structures changed little except for the decreasing volume, which transformed into new fibers. But if the fiber strength was weaker than the primary beads strength, the fiber might be broken down, or secondary beads would not turn up. Then the primary beads contracted into spindle-like or spherical beads as a result of surface tension.

In further proof of this theory, the 4 wt% PHBV solution was electrospun into ethanol bath and collected at 4 cm and 6 cm. The jet collected at 4 cm obtained primary beads and very short fibers between adjacent beads (Figure 4(a)). Other than cylinder-like beads, the primary beads were spherical with diameter of 20 µm. The viscosity of 4 wt% solution was much lower than that of 6 wt %. So the primary beads could not keep their structures when the surface tension acted on them. When collected at 6 cm, the beads were slightly stretched but had similar diameters as that obtained at 4 cm (Figure 4(b)). Broken ends of fibers could be seen in the mat. The most likely reason was that the jet had such low polymer concentration. So the obtained fibers had poor mechanical properties. When the jet was stretched, the fiber was easily broken down, and the primary beads could not be stretched into secondary beads.

*3.3. Morphological Comparison of Bead-Free Electrospun Fibers.* 8 wt% PHBV solution with 10 wt% of ethanol could be electrospun into ultrafine PHBV fibers without beads, due to higher conductivity and viscosity than 6 wt% PHBV solution (Table 1). The PHBV fiber prepared by NE did not solidify when collected and heavily cohered with each other because chloroform evaporated incompletely (Figure 5(a)). If the collection distance was increased to 12 cm, chloroform further evaporated and the coherence alleviated, but there were still many bonds among fibers (Figure 5(b)). Due to slow evaporation of solvent, the fiber surface was smooth without pores. However, if the PHBV fiber was prepared by DJWE, the surface of fiber was rough and shriveled (Figure 5(c)). But the fibers were cylindrical with slightly rough surface if they were collected in the bath at 12 cm (Figure 5(d)). Both of the samples from DJWE showed few bond points and clear boundary for each fiber. The roughness and shrinkage of the fiber surface collected at 6 cm was a result of the fast solidification and double-diffusion of solvent and nonsolvent. When the jet was immersed into the bath, the surface was firstly solidified into shell structure to restrict the fiber external diameter. Then the solvent transferred towards the bath, while the nonsolvent had the opposite transference direction during the double-diffusion process. The core part of the fiber solidified at a relatively low rate and formed a compact structure, which led to the shrinkage of the surface during the process. If the collection distance increased, a large part of the solvent was removed by evaporation before fibers were immersed into bath. It was a relatively tempered solidification process, so

(a1)



(b1)



(a2)



(b2)



(a3)



(b3)



(a4)



(b4)

(a)

(b)
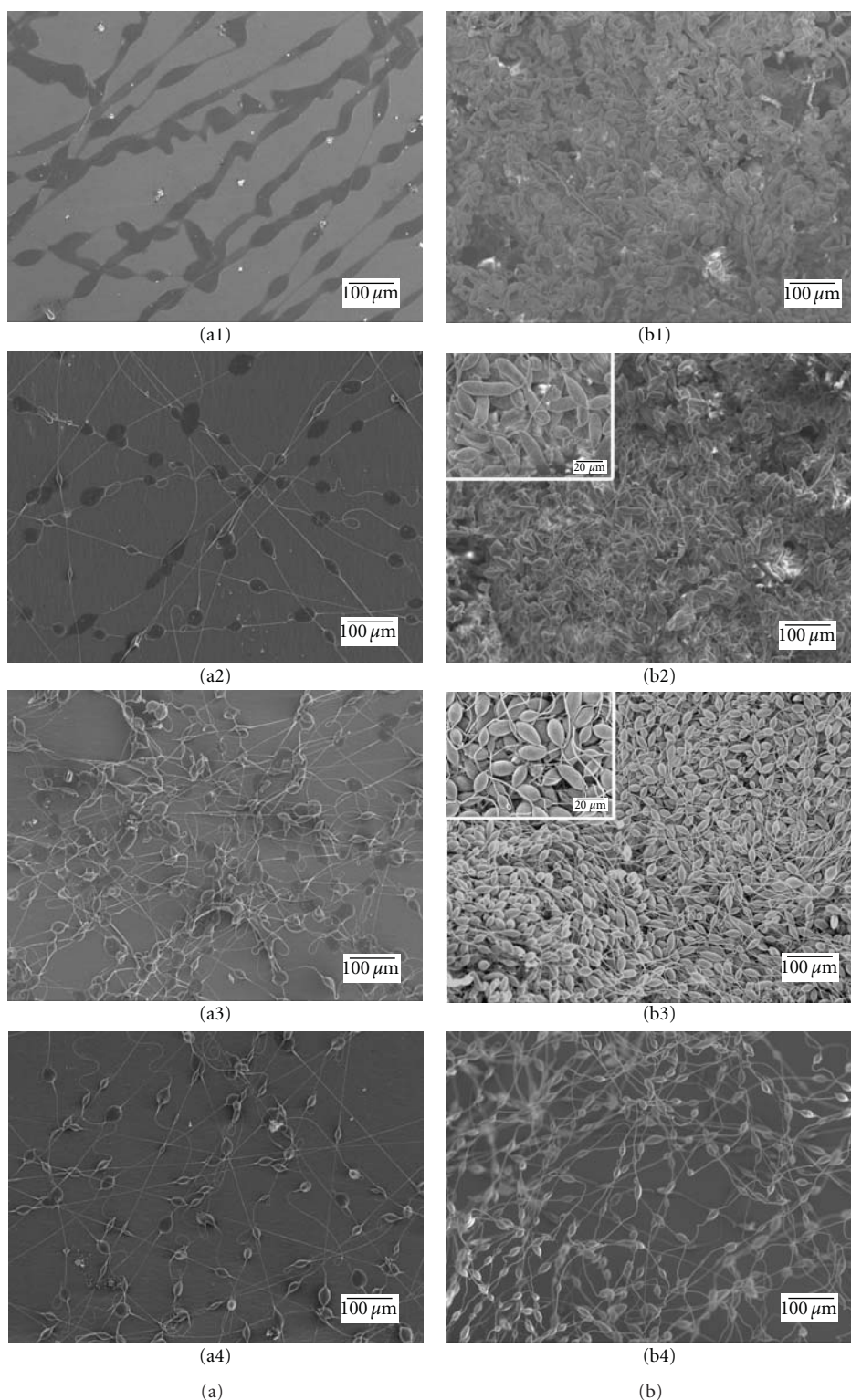
FIGURE 2: Electrospun PHBV fiber prepared by NE (a) and DJWE (b). 1: 3 cm; 2: 6 cm; 3: 9 cm; 4: 12 cm.

the fiber kept cylindrical and the diameter decreased with the evaporation of chloroform. After immersed into the bath, though undergoing the similar process as collected at 6 cm, the fiber's core part shrank little because of less residual solvent.

3.4. Wettability. The water contact angles of electrospun mats collected at different distances and substrates varied a lot due to the morphology (Figure 6). It could be concluded that beaded fiber mats prepared by DJWE from 6 wt% PHBV solution had higher water contact angle than that prepared
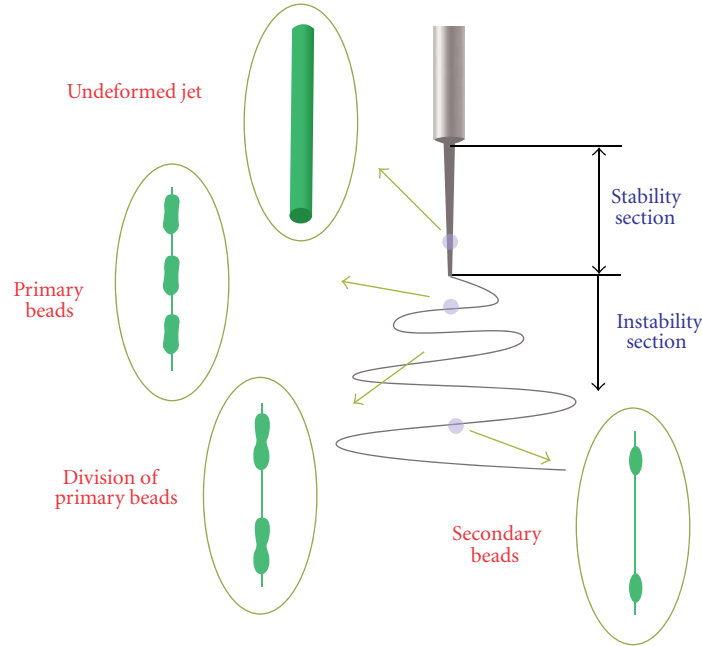
FIGURE 3: Mechanism of the PHBV beaded fiber formation at the boundary of stability and instability sections.



(a)         (b)
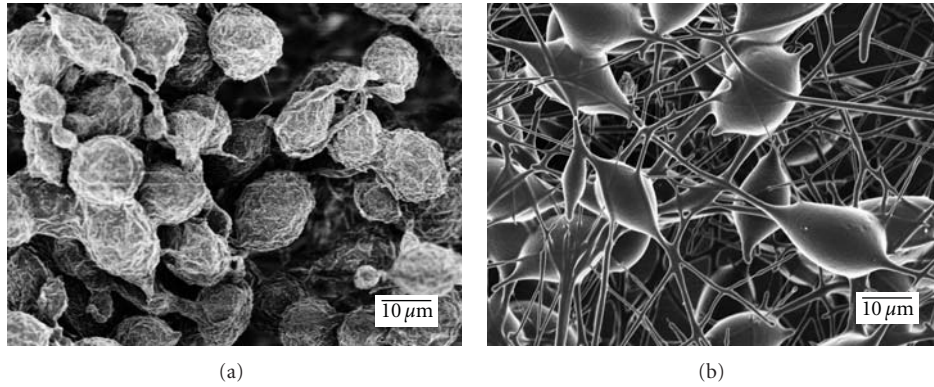
FIGURE 4: Beaded fibers prepared by DJWE of 4 wt% PHBV solution with collection distance of 4 cm (a) and 6 cm (b).

by normal electrospinning. Besides, mats with rounder beads and higher bead ratio had higher contact angle. According to the Cassie and Baxter's work [28], the apparent contact angle ($\theta'$) associated with the surface composition has the following relationship:

$$\cos \theta' = f_1 \cos \theta_1 + f_2 \cos \theta_2, \qquad (1)$$

where $f_1$ and $f_2$ are the fractions of the surface with contact angle of $\theta_1$ and $\theta_2$. If one component is air, whose contact angle was $180°$, the equation can be written as follows:

$$\cos \theta' = f_1 \cos \theta_1 - f_2. \qquad (2)$$

It could be inferred from this equation that the composite surface containing larger air fraction ($f_2$) had higher apparent contact angle ($\theta'$). Beaded fiber mats could create rougher surface which held more air and therefore, higher contact angle.

The wettability differed even widely for the 4 wt% PHBV solution prepared by DJWE and normal electrospinning with a collection distance of 4 cm. During normal electrospinning, all the beads collapsed into flat sheets (Figure 7). Though with rather rough surface, the mat had even lower contact angle than solution cast film ($77°$). This might be due to the shallow surface pores which helped the water spreading. On the other hand, the mats prepared by DJWE had the highest contact angle ($142°$) (Figure 3(a)), as a result of high beads density and round beads with rough surface, which was $67°$ higher than that of the solution cast film, and $72°$ higher than that prepared by normal electrospinning. However, the mat was rather weak and brittle, because the beads, which were considered as defects of electrospun fibers, had bad mechanical properties.

For the beaded nanofiber mats from 6 wt% PHBV solution, there were similar trends (Figure 2). Because the beads and fibers did not cohere heavily, the mats could

(a)

(b)

(c)

(d)
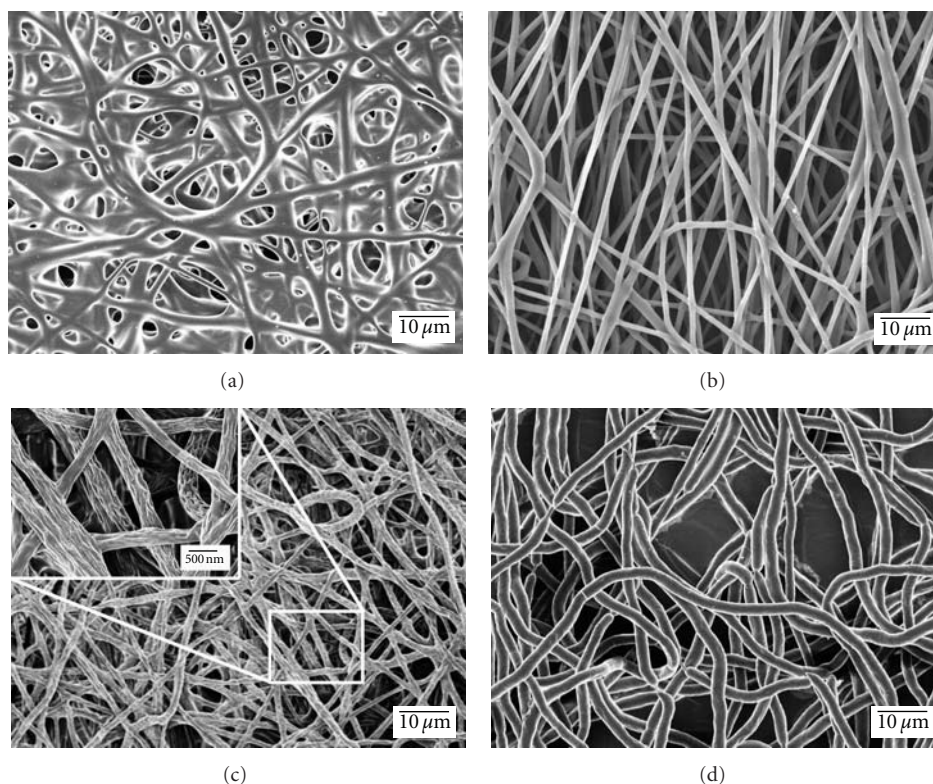
FIGURE 5: Morphologies of PHBV ultrafine fibers prepared by normal electrospinning (NE) (a, b) and dry-jet-wet-electrospinning (DJWE) (c, d). Collection distances were 6 cm for (a) and (c), 12 cm for (b) and (d).
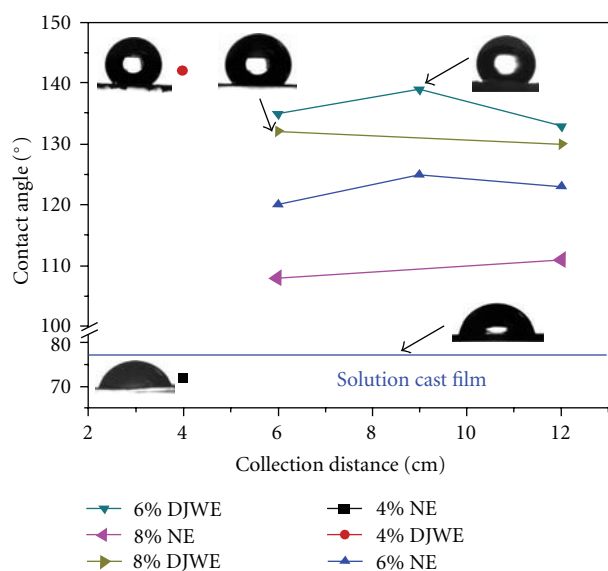


FIGURE 6: Water contact angle for electrospun mats prepared by normal electrospinning (NE) and dry-jet-wet-electrospinning (DJWE) at various distances.

held more air, and therefore were more hydrophobic than that from 4 wt% solution. And the beads from DJWE mats were beanpod-like or spindle-like, so the hydrophobicity was lower than that from 4 wt% solution. Both mats from NE
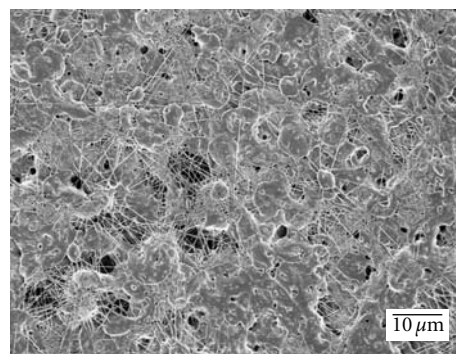


FIGURE 7: Electrospun mats from 4 wt% solution by normal electrospinning with collection distance of 4 cm.

and DJWE had the highest hydrophobicity at the collection distance of 9 cm. At this collection distance, the shape of beads was the nearest to sphere, and the bead ratio was the highest. The results implied that electrospun mats with higher bead density and rounder beads had higher porosity, which meant higher hydrophobicity.

The bead-free fibers prepared by the two methods also had similar tendency in wettability. The water contact angles of fiber mat prepared by DJWE were 130°, about 20° higher than that prepared by normal electrospinning (both collected at 12 cm). The increasing of contact angle might be the result of less coherence among fibers and consequently loose

deposited structure. DJWE fiber mats collected at 6 cm were a little more hydrophobic than that collected at 12 cm, which was because of the rough fiber surface.

## 4. Conclusions

Dry-jet-wet-electrospinning was carried out in this work to collect the electrospun jet at low distance to study the bead deformation mechanism of the PHBV fiber and the relationship between morphology and wettability. A beanpod-like bead which we named as primary bead was discovered and the formation of beaded PHBV fiber could be explained as follows: the jet was firstly stretched at the defects and formed the primary beads and fibers between adjacent beads. Then, if the fibers solidified and were stronger than the beads, the primary beads were further stretched and secondary beads which were common in electrospun fiber appeared. Otherwise, the fiber might be broken down by the electric field force. The bead-free fibers from DJWE had larger diameter but rougher surface than that from NE, due to the quick double-diffusion process.

The mats prepared by DJWE had obviously higher water contact angle than those by normal electrospinning, due to less adhesion and higher porosity. PHBV bead fiber mats with rounder beads and higher bead density were more hydrophobic. Therefore, the mat wettability was closely related to its surface morphology, and the hydrophobicity could be adjusted by the electrospun fiber morphology and the accumulation structures.

## Acknowledgments

## References

[1] X. H. Qin and S. Y. Wang, "Filtration properties of electrospinning nanofibers," *Journal of Applied Polymer Science*, vol. 102, no. 2, pp. 1285–1290, 2006.

[2] C. H. Hung and W. W. F. Leung, "Filtration of nano-aerosol using nanofiber filter under low Peclet number and transitional flow regime," *Separation and Purification Technology*, vol. 79, no. 1, pp. 34–42, 2011.

[3] J. A. Matthews, G. E. Wnek, D. G. Simpson, and G. L. Bowlin, "Electrospinning of collagen nanofibers," *Biomacromolecules*, vol. 3, no. 2, pp. 232–238, 2002.

[4] F. Yang, R. Murugan, S. Wang, and S. Ramakrishna, "Electrospinning of nano/micro scale poly(l-lactic acid) aligned fibers and their potential in neural tissue engineering," *Biomaterials*, vol. 26, no. 15, pp. 2603–2610, 2005.

[5] W. J. Li, C. T. Laurencin, E. J. Caterson, R. S. Tuan, and F. K. Ko, "Electrospun nanofibrous structure: a novel scaffold for tissue engineering," *Journal of Biomedical Materials Research*, vol. 60, no. 4, pp. 613–621, 2002.

[6] L. Chen, L. Bromberg, H. Schreuder-Gibson, J. Walker, T. A. Hatton, and G. C. Rutledge, "Chemical protection fabrics via surface oximation of electrospun polyacrylonitrile fiber mats,"
*Journal of Materials Chemistry*, vol. 19, no. 16, pp. 2432–2438, 2009.

[7] L. Chen, L. Bromberg, J. A. Lee et al., "Multifunctional electrospun fabrics via layer-by-layer electrostatic assembly for chemical and biological protection," *Chemistry of Materials*, vol. 22, no. 4, pp. 1429–1436, 2010.

[8] X. J. Huang, A. G. Yu, J. Jiang, C. Pan, J. W. Qian, and Z. K. Xu, "Surface modification of nanofibrous poly(acrylonitrile-co-acrylic acid) membrane with biomacromolecules for lipase immobilization," *Journal of Molecular Catalysis B*, vol. 57, no. 1–4, pp. 250–256, 2009.

[9] J. Kim, J. W. Grate, and P. Wang, "Nanobiocatalysis and its potential applications," *Trends in Biotechnology*, vol. 26, no. 11, pp. 639–646, 2008.

[10] X. Wang, B. Ding, J. Yu, M. Wang, and F. Pan, "A highly sensitive humidity sensor based on a nanofibrous membrane coated quartz crystal microbalance," *Nanotechnology*, vol. 21, no. 5, Article ID 055502, 2010.

[11] C. Zhang, X. Wang, J. Lin, B. Ding, J. Yu, and N. Pan, "Nanoporous polystyrene fibers functionalized by polyethyleneimine for enhanced formaldehyde sensing," *Sensors and Actuators B*, vol. 152, no. 2, pp. 316–323, 2011.

[12] X. Wang, B. Ding, J. Yu, Y. Si, S. Yang, and G. Sun, "Electro-netting: fabrication of two-dimensional nano-nets for highly sensitive trimethylamine sensing," *Nanoscale*, vol. 3, no. 3, pp. 911–915, 2011.

[13] H. Fong, I. Chun, and D. H. Reneker, "Beaded nanofibers formed during electrospinning," *Polymer*, vol. 40, no. 16, pp. 4585–4592, 1999.

[14] D. H. Reneker and A. L. Yarin, "Electrospinning jets and polymer nanofibers," *Polymer*, vol. 49, no. 10, pp. 2387–2425, 2008.

[15] M. M. Hohman, M. Shin, G. Rutledge, and M. P. Brenner, "Electrospinning and electrically forced jets. I. Stability theory," *Physics of Fluids*, vol. 13, no. 8, pp. 2201–2220, 2001.

[16] Y. M. Shin, M. M. Hohman, M. P. Brenner, and G. C. Rutledge, "Experimental characterization of electrospinning: the electrically forced jet and instabilities," *Polymer*, vol. 42, no. 25, pp. 9955–9967, 2001.

[17] G. Viswanathan, S. Murugesan, V. Pushparaj, O. Nalamasu, P. M. Ajayan, and R. J. Linhardt, "Preparation of biopolymer fibers by electrospinning from room temperature ionic liquids," *Biomacromolecules*, vol. 7, no. 2, pp. 415–418, 2006.

[18] S. Xu, J. Zhang, A. He, J. Li, H. Zhang, and C. C. Han, "Electrospinning of native cellulose from nonvolatile solvent system," *Polymer*, vol. 49, no. 12, pp. 2911–2917, 2008.

[19] E. Smit, U. Buttner, and R. D. Sanderson, "Continuous yarns from electrospun fibers," *Polymer*, vol. 46, no. 8, pp. 2419–2423, 2005.

[20] K. Acatay, E. Simsek, C. Ow-Yang, and Y. Z. Menceloglu, "Tunable, superhydrophobically stable polymeric surfaces by electrospinning," *Angewandte Chemie—International Edition*, vol. 43, no. 39, pp. 5210–5213, 2004.

[21] M. Ma, Y. Mao, M. Gupta, K. K. Gleason, and G. C. Rutledge, "Superhydrophobic fabrics produced by electrospinning and chemical vapor deposition," *Macromolecules*, vol. 38, no. 23, pp. 9742–9748, 2005.

[22] N. Q. Zhan, Y. X. Li, C. Q. Zhang et al., "A novel multinozzle electrospinning process for preparing superhydrophobic PS films with controllable bead-on-string/microfiber morphology," *Journal of Colloid and Interface Science*, vol. 345, no. 2, pp. 491–495, 2010.

[23] M. F. Zhu, W. W. Zuo, H. Yu, W. Yang, and Y. Chen, "Superhydrophobic surface directly created by electrospinning

based on hydrophilic material," *Journal of Materials Science*, vol. 41, no. 12, pp. 3793–3797, 2006.

[24] Y. Il. Yoon, H. S. Moon, W. S. Lyoo, T. S. Lee, and W. H. Park, "Superhydrophobicity of PHBV fibrous surface with bead-on-string structure," *Journal of Colloid and Interface Science*, vol. 320, no. 1, pp. 91–95, 2008.

[25] K. Sombatmankhong, O. Suwantong, S. Waleetorncheepsa-wat, and P. Supaphol, "Electrospun fiber mats of poly(3-hydroxybutyrate), poly(3-hydroxybutyrate-co-3-hydroxyval-erate), and their blends," *Journal of Polymer Science B*, vol. 44, no. 19, pp. 2923–2933, 2006.

[26] Y. I. Yoon, H. S. Moon, W. S. Lyoo, T. S. Lee, and W. H. Park, "Superhydrophobicity of PHBV fibrous surface with bead-on-string structure," *Journal of Colloid and Interface Science*, vol. 320, no. 1, pp. 91–95, 2008.

[27] W. Zuo, M. Zhu, W. Yang, H. Yu, Y. Chen, and Y. Zhang, "Experimental study on relationship between jet instability and formation of beaded fibers during electrospinning," *Polymer Engineering and Science*, vol. 45, no. 5, pp. 704–709, 2005.

[28] A. B. D. Cassie and S. Baxter, "Wettability of porous surfaces," *Transactions of the Faraday Society*, vol. 40, pp. 546–551, 1944.

*Research Article*

# Polarization Dependence of Surface Enhanced Raman Scattering on a Single Dielectric Nanowire

## Hua Qi, R. W. Rendell, O. J. Glembocki, and S. M. Prokes

*Electronics Science and Technology Division, Naval Research Laboratory, Washington, DC 20375, USA*

Correspondence should be addressed to Hua Qi, qhqihua@yahoo.com

Our measurements of surface enhanced Raman scattering (SERS) on $Ga_2O_3$ dielectric nanowires (NWs) core/silver composites indicate that the SERS enhancement is highly dependent on the polarization direction of the incident laser light. The polarization dependence of the SERS signal with respect to the direction of a single NW was studied by changing the incident light angle. Further investigations demonstrate that the SERS intensity is not only dependent on the direction and wavelength of the incident light, but also on the species of the SERS active molecule. The largest signals were observed on an NW when the incident 514.5 nm light was polarized perpendicular to the length of the NW, while the opposite phenomenon was observed at the wavelength of 785 nm. Our theoretical simulations of the polarization dependence at 514.5 nm and 785 nm are in good agreement with the experimental results.

## 1. Introduction

Surface enhanced Raman scattering (SERS) has been regarded as a unique technique to detect trace levels of chemical compounds, since the vibrational information is very specific to the bonds in the molecules. In recent years, there has been significant interest in exploring various nanostructures as SERS substrates to optimize the electromagnetic field enhancement and significantly improve sensitivity. In the case of nonspherical nanoparticles it has been shown that the SERS enhancement is strongly dependent on the direction of polarization of the exciting incident light [1–12]. Of particular interest are cylindrical geometries because the enhancement is a function of the aspect ratio. In addition, in the case of very long Ag nanowires it has been shown that surface plasmons can be launched at one end of the nanowires and travel to the other end. Recently there has been interest in metal coated dielectric core nanowires because they form plasmonic shells [13, 14]. These geometries can form the basis of plasmonically modulated photonic devices. It is well known that the local electric field in plasmonic coupling of closely spaced particles, usually called "hot spots," can be orders of magnitude stronger than those on individual particles. The importance of "hot spots" in SERS process has been widely discussed [15–21].

In this work, a highly effective SERS composite of dielectric $Ga_2O_3$ NWs core/silver was employed to investigate the SERS intensity dependence on the laser polarization. Experimental results show that both variable wavelength and angle of the incident light play very important roles on the resulting SERS intensity. Our theoretical simulations indicated that the maximum SERS enhancement could be obtained when the polarization is perpendicular to the NW length at 514.5 nm excitation, while the opposite phenomena should be expected at a laser wavelength of 785 nm. All of these expectations are in good agreement with our experimental observations. In addition, further experiment shows that the orientation of self-assembled monolayer of active SERS molecules on the NWs may affect the SERS enhancement as well.

## 2. Experimental Details

Random $Ga_2O_3$ NWs were grown via the vapor-liquid-solid (VLS) growth mechanism [22]. The gallium metal (99.995% pure) used as a source was placed 6 inches upstream from

the Si (100) substrate, which had a 20 nm gold film. The furnace was heated to 900°C while flowing simultaneously a mixture of argon and oxygen gases in a ratio of 6 : 1 through the tube. To study the SERS behavior of a single NW, the $Ga_2O_3$ NWs as grown on a Si substrate were sonicated off in methanol, dropped and dried on a bare silicon surface for further SERS study.

The discrete single NWs were covered with a layer of silver produced by an electroless (EL) plating approach for the SERS behavior study, which has been described in our previous report [13, 14]. Briefly, the silver ion in Tollen reagent was reduced to neutral Ag and then homogenously deposited on the NWs surface. The morphology of the silver on the NW surface is directly related to the chemical concentration and reaction time. Usually, short reaction time of the silver electroless plating process results in closely spaced but separate nanoparticles, while longer times lead to linking up of the islands into a rough layer.

The SERS line maps were carried out using a confocal $\mu$-Raman system which consisted of a Mitutoyo Microscope and an Ocean Optics QE65000 spectrometer equipped with a thermoelectrically cooled CCD. The 514.5 nm line of an $Ar^+$ ion laser was used as the excitation source. The microscope utilized a 100x 0.7 NA objective for focusing the laser light and was coupled to the spectrometer through a fiber optic cable. The maps were collected with low laser power of 0.75 mW at the sample. This was done to prevent desorption and damage to the benzenethiol and to prevent alterations to the Ag layer. The SERS intensity dependence on variable polarization angles was performed using a Delta Nu system which consists of an Olympus Microscope and a Raman spectrometer equipped with a thermoelectrically cooled CCD. The 785 nm line of Ti: Sapphire laser was used as the excitation source to detect the SERS strength dependence on a single NW/silver composite. The microscope utilized a 50x 0.75 NA objective for focusing the laser light. The spectra were collected with a laser power of 3 mW at the sample.

The full Maxwell's equations are solved numerically using the finite elements method (FEM) through the RF module of the COMSOL Multiphysics finite-elements package [23]. We used FEM simulations because they are more appropriate for the complex geometries of nanowires placed on a substrate [24]. FEM approaches have been shown to agree well with finite difference time domain simulations [24, 25]. In addition, the FEM technique implemented via COMSOL has been shown to be capable of accurate simulation for nanoshell structures on substrates if sufficiently accurate meshing is used and appropriate absorbing perfectly matched layers PML are used on the boundaries [26–28]. This approach allows us to treat the scattering problem by bringing in planes waves of a specific polarization and then calculating the scattered fields. As another test of the numerical simulations, we find excellent agreement between the COMSOL results with the analytical Mie solutions for scattering from an Ag sphere [24, 27]. The modeling of the nanowires in air above an Si substrate requires the construction of separate PML boundaries for both the Si and air regions. The dielectric constants of each PML match its adjoining region, either Si or air. To avoid artifacts due to

scattering at the boundaries between the Si and air regions of the PML's, the scattering at the air-Si interface is incorporated into the incident-polarized plane wave by means of analytical functions for the Fresnel coefficients. The resulting incident field is thus an exact solution in the absence of the nanowire. The numerical finite element solution for the scattered field is then calculated in the presence of the nanowire. This requires sufficient meshing to adequately resolve both the nanowires with shells and the PML boundaries [27, 28].

## 3. Results and Discussion

To demonstrate the surface enhanced Raman scattering (SERS) polarization dependence on the direction of the nanowires (NWs), we carried out the mapping investigations on NW/Ag composite on the same NW using a 514.5 nm excitation with parallel and perpendicular laser polarization, respectively. The $Ga_2O_3$ NWs, used in all experiments, were grown via the vapor-liquid-solid (VLS) growth mechanism. Empirically, the length and diameter of $Ga_2O_3$ NWs depended on the growth time and gas flow rate, as well as the catalyst size. In our growth, the diameters varied from 50 nm to 300 nm, and the length was usually greater than 10 microns. Energy dispersive X-ray (EDX) analysis showed that the chemical composition of the NWs was stoichiometric $Ga_2O_3$. Benzenethiol (BT) was used as the SERS active molecules.

The intensity dependence maps of the 1576 $cm^{-1}$ BT SERS band on incident laser polarization are shown in Figures 1(a) and 1(b), by which the polarization dependence can be easily visualized. Both of the images were mapped at the same region of the sample by rotating the sample. Figure 1(c) shows the corresponding microscope image of the SERS mapping area. From the maps, it is obvious that the signal strength is maximized when the laser is perpendicular to the NW.

To verify our experimental observation, we performed the simulations using the RF module of COMSOL Multiphysics, which provides a finite-element solution of Maxwell's equations. Figures 2(a) and 2(b) show the simulated SERS maps of the NW with length of 500 nm at a laser wavelength of 514.5 nm, indicating that the strongest SERS signal occurs when the polarization is perpendicular to the NW longitude, which clearly confirmed the incident laser polarization effects on the SERS strength, as we obtained in experiments shown in Figure 1. It is noted in the maps that the plasmon oscillations are clearly observed along the NW when the polarization is parallel to the NW, while the transverse modes have excitations along the radial direction and hence much shorter period and uniform in NW's longitudinal direction.

Furthermore, more comprehensive simulations were carried out in the range of wavelength from 400 nm to 900 nm, as shown in Figure 3, which includes the wavelength of 514.5 nm used in the mapping experiments and simulations above. By comparison of Figures 3(a) and 3(b), it is obvious that, in the case of parallel, the SERS enhancement factor is $10^6 \sim 10^7$, while the perpendicular case shows

(a)



(b)



(c)
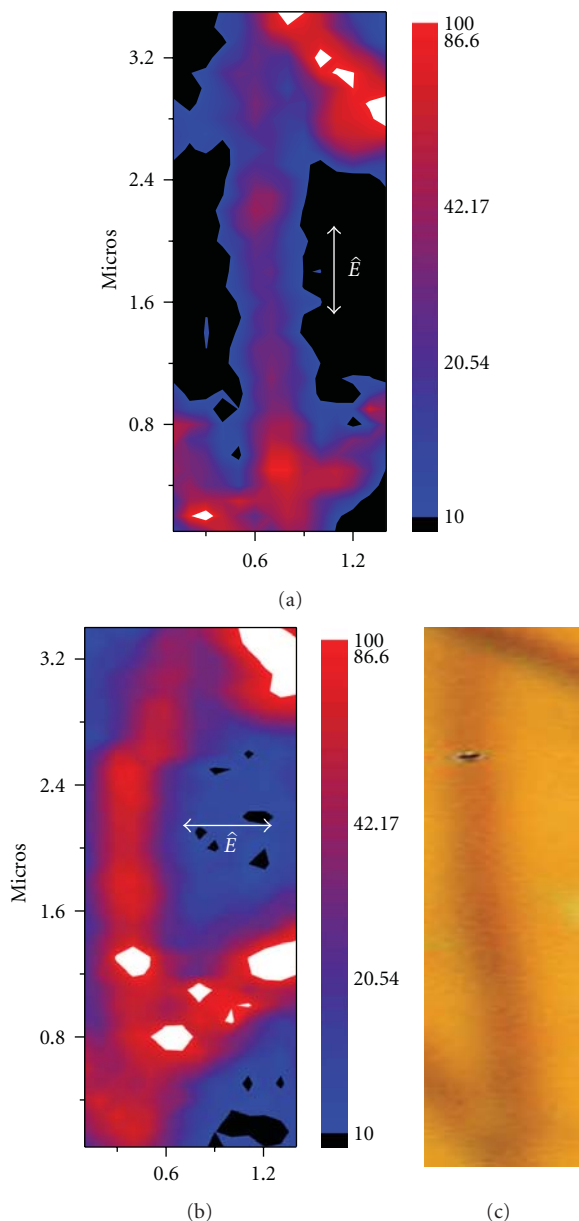
FIGURE 1: Experimental maps of the 1576 cm$^{-1}$ BT SERS band of NW/Ag composite using a laser with 514.5 nm wavelength at the same NW, and the sample was rotated for parallel/perpendicular polarization mapping; the polarization is parallel (a) and perpendicular (b) to the NW. (c) Corresponding microscope image of the SERS mapping region of (a) and (b).



(a)



(b)

FIGURE 2: Log plots of SERS enhancement simulated at a wavelength of 514.5 nm when the NW direction is parallel (a) and perpendicular (b) to the polarization.

an enhancement factor of $10^8 \sim 10^9$, clearly indicating that the NW/Ag composites show stronger SERS enhancement when the laser polarization is perpendicular to the NW direction at 514.5 nm, which is in good agreement with the experimental mapping images of Figure 1 and the theoretical simulation mapping results of Figure 2.

From Figures 3(a) and 3(b), it is expected, at the wavelength of 785 nm (red laser), that the strongest SERS signals should be observed when the laser polarization parallelized to the NW longitude direction, which is completely opposite

to the observations at the excitation of 514.5 nm. Hence, we performed further investigations of SERS enhancements dependence on the incident angles using incident laser of 785 nm and 514.5 nm. In the process of measurements, data were collected at three different angles, including 0°, 45°, and 90°, respectively. The representative BT SERS line of 1576 cm$^{-1}$ at different angles and laser wavelengths are shown in Figure 4. The red and green lines are roughly linear fitting of the experimental data obtained at three angles, which clearly indicates the trends of SERS enhancement dependence on the incident laser angles and the different wavelengths. It is noted that the data were normalized to the maximum intensity.

More detailed simulations of the SERS polarization dependence of the NW core/Ag composites for the incident wavelength of 785 nm and 514.5 nm are shown in Figures 5(a) and 5(b), respectively, which provide a continuous SERS enhancement trend from 0° to 90°. As can be seen in the calculation, the largest SERS enhancement is completely flipped
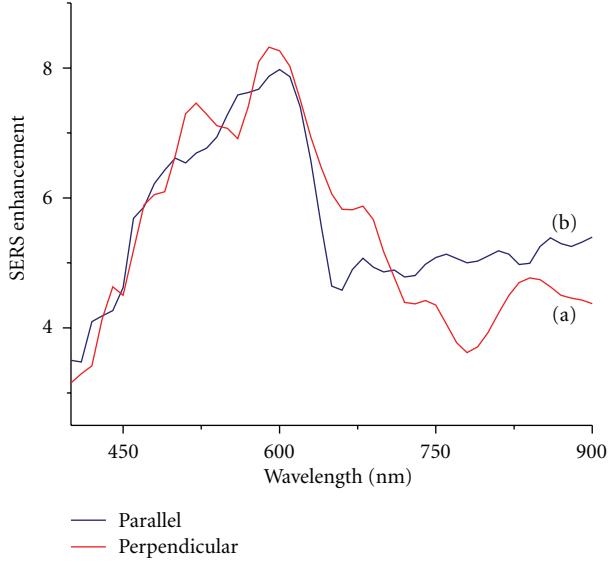
FIGURE 3: Simulations of SERS enhancements in the range of wavelength from 400 nm to 900 nm. The NW direction is parallel (red) and perpendicular (blue) to the polarization.
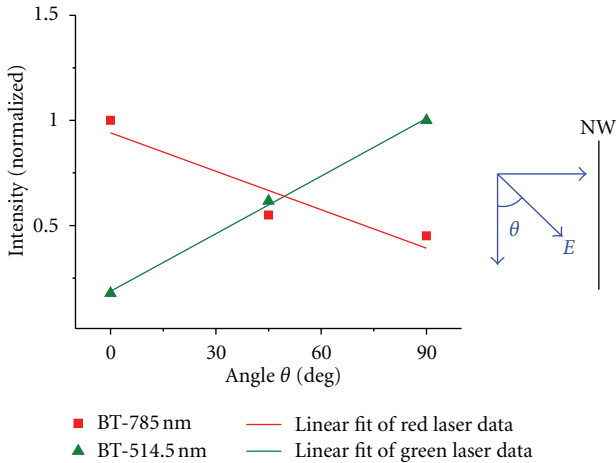


FIGURE 4: Experimental polarization angle dependence of surface enhanced Raman scattering (SERS) on nanowire at the wavelength of $\lambda = 785$ nm (red squares and its linear fitting line) and $\lambda = 514.5$ nm (green triangles and its linear fitting line) the data were normalized to the maximum intensity.

at the excitation wavelength of 785 nm and 514.5 nm, which matches very well with our experimental observations as shown in Figure 4. For SERS, the Raman intensity generally increases by a factor of $E^4$, where the first two powers of the enhancement are due to the local electromagnetic field which in the present case is predominantly due to the contact between the nanowire and the Si substrate. The second two powers of the enhancement factor are the Raman emission enhancement. As a result of these two contributions to the SERS enhancement, it has been argued [9] that this should lead to a simple $\sin^2(\theta)$ polarization dependence for a nanowire. If $\theta$ is the polarization angle of the incident

light with respect to the direction along the length of the nanowire, then the local electric field is $|E_{\mathrm{loc}}(\omega,\theta)| = |E_{\max}(\omega)|\sin(\theta)$ where $E_{\max}$ is the maximum of the local electric field. However, the direction of the induced electric field between the nanowire and the substrate is always in the direction across the nanowire-substrate contact ($\theta = \pi/2$) and independent of the incident polarization. Thus the total SERS enhancement is expected to be proportional to

$$
\begin{aligned}
G &= \left|\frac{E_{\max}(\omega_L)}{E_0(\omega_L)}\right|^2 \left|\frac{E_{\max}(\omega_R)}{E_0(\omega_R)}\right|^2 \sin^2\left(\theta + \varphi_{\mathrm{phase}}\right) \\
&= \left|\frac{E_{\max}}{E_0}\right|^4 \sin^2\left(\theta + \varphi_{\mathrm{phase}}\right),
\end{aligned}
\tag{1}
$$

where generally a phase shift phase is also expected due to the fact that metallic nanowires on substrates which are tens of microns in length can function as Fabry-Perot cavities resulting in geometry specific standing plasmon waves [26, 29, 30]. Polarization dependences as in (1) have been previously observed [9, 30]. This is also consistent with the simulation results in Figure 5 where the difference between (a) and (b) can be described in terms of a different phase shift occurring at each excitation wavelength. This can be expected due to the observations that in the Fabry-Perot behavior of nanowires on substrates [26, 29], the surface plasmon wavelength has been found to differ from the excitation wavelength (e.g., between 400–600 nm for excitation at 785 nm [26, 29]) and is geometry dependent. As a result, the plasmon standing waves will generally occur with different relative phase shifts and the maximum enhancement may occur at a different polarization angle depending on the excitation wavelength. This has been observed for the first time in the present work and the result is consistent with previous observations of metallic nanowires on substrates [26, 29, 30].

From the comprehensive simulation results of Figure 3, we can see that the polarization angle dependence of the wire at 633 nm would exhibit similar behavior to that shown for the 514 nm in Figure 5(b), but the SERS enhancement in the 90° case shows stronger enhancements and more extended fields compared to the 514 nm case shown in Figure 2(a). For the 0° case, the SERS enhancement would be predicted to be weaker at 633 nm compared to the 514 nm case. This is shown in Figure 6.

In addition, the NW/Ag composites SERS dependence on the polarization was experimentally investigated using a laser excitation of 785 nm to investigate the incident angle effects on the SERS enhancement in detail. Figures 7(a) and 7(b) show the high resolution SEM image of an isolated bare NW and NW/Ag composites. As shown in Figure 7(b), a rough layer of silver was clearly plated on the NW surface, which is produced by an electroless (EL) approach [13, 14]. From the SEM image, the silver nanoparticles display 3D islands with a diameter range of 20 nm. The space between the particles is less than 10–20 nm, which leads to the strong plasmonic oscillation due to coupling of individual nanoparticles/island formed on NWs, as we reported previously [13]. The SERS spectra were carried out by changing the angle $\theta$ in 15° increments between the electric field of the incident light and the axis parallel to the NW length, as shown in

(a)



(b)
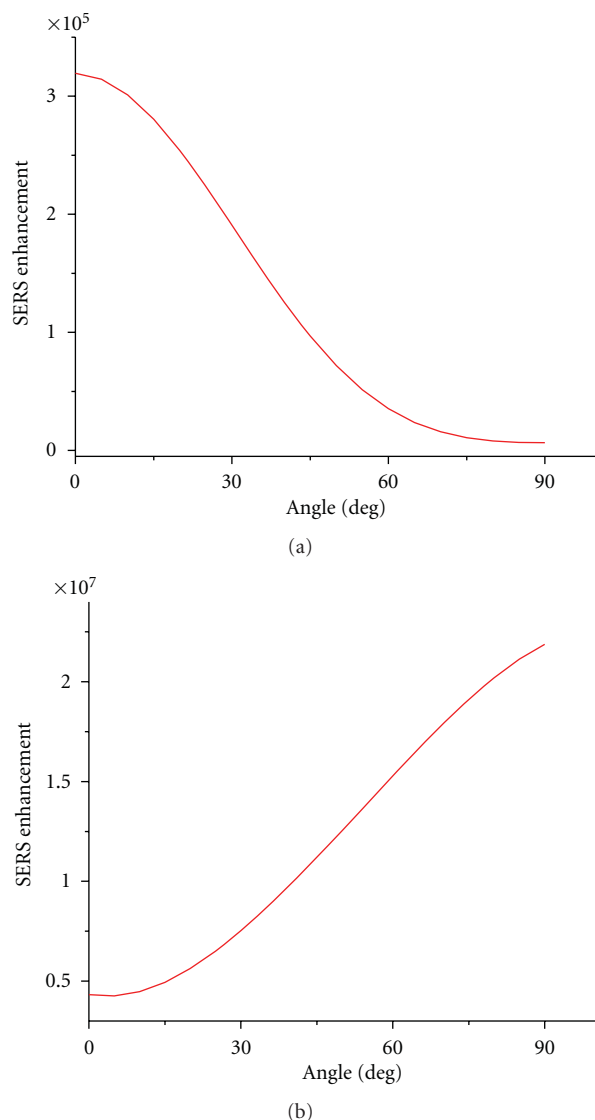
FIGURE 5: Simulation of polarization angle dependence of surface enhanced Raman scattering (SERS) averaged over nanowire surface excluding the wire ends for (a) $\lambda = 785$ nm and (b) $\lambda = 514.5$ nm.
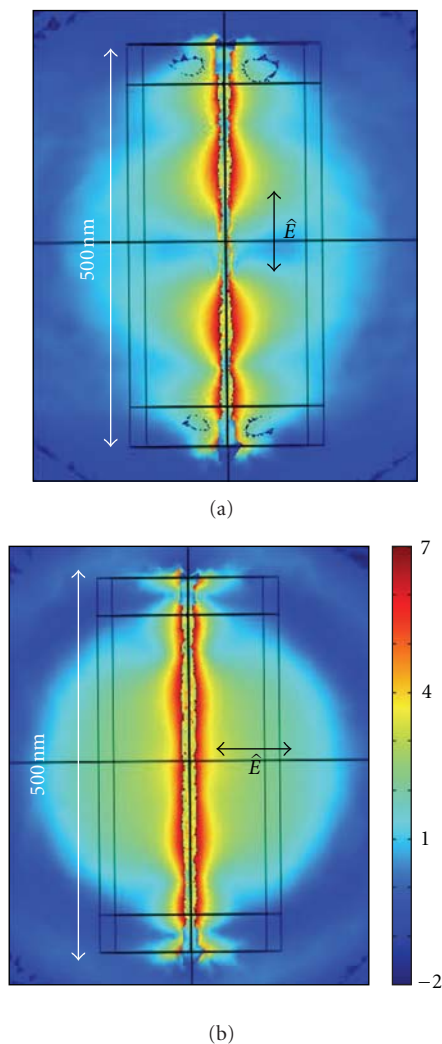


(a)



(b)

FIGURE 6: Log plots of SERS enhancement simulated at a wavelength of 633 nm when the NW direction is parallel (a) and perpendicular (b) to the polarization.

the sketch of **Figure 7(b)**. To minimize the time-dependence degradation influence of the SERS signal intensity during the measurements, two cycles of SERS measurements, from 0° to 90°, then back to 0°, were performed on a single NW. The data obtained from those two cycles were averaged for the spectra plots of each angle.

**Figure 7(c)** shows a series of SERS spectra as a function of the incident light polarization angles from 0° to 90°. Here benzenethiol (BT) molecules were used as SERS active molecules. The major Raman peaks at 1001, 1023, 1073, and 1574 cm$^{-1}$ can be assigned to symmetric ring breathing, in-plane phenyl ring bending, in plane C–H bending, and in plane C–C stretching of the phenyl ring from BT, respectively, which is in good agreement with those reported previously [31–36]. It is clear that the SERS signal displayed strong dependence on the polarization direction of the incident laser on a single NW, and the strongest SERS intensity was observed when the polarization is parallel to the NW length at an angle of 0°.

A plot of the normalized intensity data of the representative BT SERS band as a function of polarization angle is shown in **Figure 7(d)** (red curve), by which the polarization dependence can be easily visualized. It is obvious that the strength of SERS signals is maximized at 0°, which is different from the SERS strength dependence on laser polarization reported previously on pure silver or gold NWs with sparse noble metal particles [8, 9]. The latter reported that the maximum of the SERS enhancement was observed when the polarization was perpendicular to the metal NWs. The difference may be attributed to the fact that the dielectric Ga$_2$O$_3$ NWs SERS substrate and the uniform coverage of silver particles layer play important roles in this polarization dependence process. That is to say the NWs SERS behavior is also related to the structure and composites of the SERS substrate.
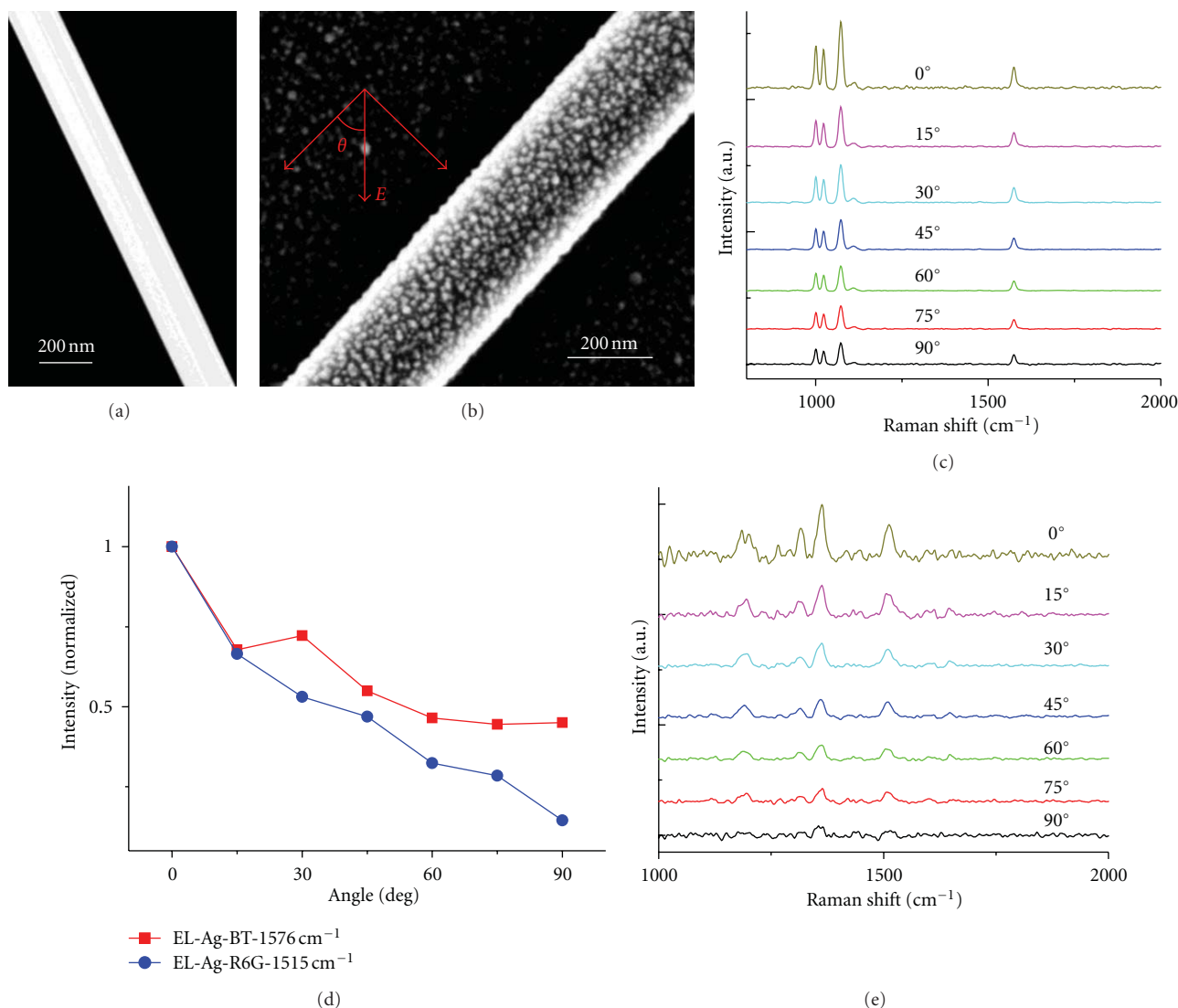
FIGURE 7: SEM image of a bare (a) and an electroless silver plated (b) NW. Inset of (b): the sketch indicates the laser polarization direction. (c) SERS dependence of a single NW/Ag composite on the laser polarization angles for Benzenethiol (BT) molecules at a wavelength of 785 nm. (d) Plot of intensity of SERS representative lines of BT (red) and rhodamine 6G (R6G) (blue) versus angles and the data were normalized to the maximum intensity. (e) SERS dependence of a single NW/Ag composite on the laser polarization angles for R6G molecules at a wavelength of 785 nm.

Additionally, a bump was observed at the angle of around 30° for BT molecules as shown in Figure 7(d) (red curve). A possible explanation to this observed bump around 30° is that the orientation of the attached active molecules may have effect on this polarization dependence behavior. It is well known that the benzene rings of BT could easily form a self-assembled monolayer on a silver surface. In our study, the dielectric core was wrapped with a layer of silver, which provides a favorable condition for the formation of the ordered self-assembled monolayer (SAM). However, numerous reports in the literatures indicate that the orientation of the phenyl ring plane vary from perpendicular to flat from the substrate surface [37–45]. The SAM orientation of BT may affect the SERS enhancement factor when the incident light angle is variable. Here, as shown in the Figure 8(a),

we assumed that the BT SAM was deduced to be tilted about 60° from the substrate surface, which is similar to the research results obtained by Szafranski et al. [37]. Hence the abrupt increase of SERS signals at the angle of around 30° could be attributed to the perpendicularity between laser polarization direction and the phenyl ring plane. This is consistent with the electrostatic model interpretation of Gunnarsson et al. [46] for the relative SERS intensities of rhodamine 6G and thiophenol in terms of the orientation of the phenol ring out from the surface. This observation implies that the SERS signal strength highly depends on the molecules packing structure on the active substrate, which may provide a useful way to investigate the orientation of self-assembly molecular monolayer on surface via SERS technique.

(a)



(b)
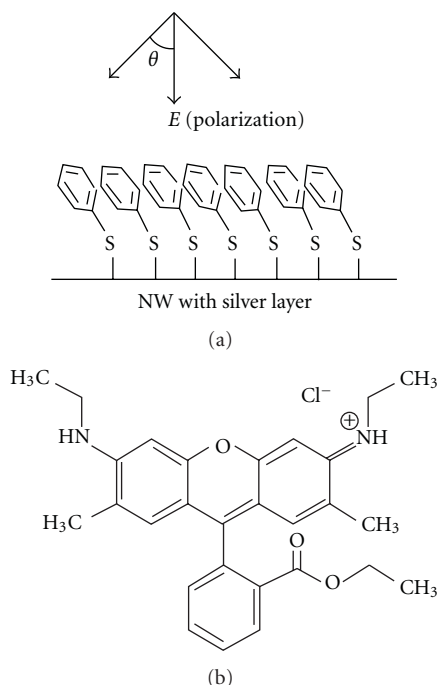
Figure 8: (a) A scheme of BT molecules orientation on the substrate and their interaction with polarized laser. (b) The structure of R6G.

To eliminate the effect of the SAM on the polarization behavior, and to investigate the pure polarization dependence on the NW direction, a random physically adsorbed layer of rhodamine 6G (R6G) was employed to study the SERS dependence on a single $Ga_2O_3$ NW. Figure 7(e) shows a series of SERS spectra of R6G with variable angles. Since R6G was attached randomly on an NW surface, this could effectively remove the polarization effect caused by the ordered molecular orientation. Hence the SERS polarization dependence behavior would completely come from the NW/Ag composite. Representative SERS line of R6G versus angle was plotted in Figure 7(d), which clearly show that the signal intensity of R6G increases with a decrease of the incident light angle. The signal is maximized when the polarization direction of the light is parallel to the NW direction ($\theta = 0°$), which is in good agreement with the observation of BT molecule at the same incident wavelength of 785 nm.

It is observed that R6G random molecules layer shows a stronger polarization effect than BT ordered layer, which is opposite to what one would expect. However if the size of the molecules and the roughness of the silver particles on NWs are taken into account, the fact should be easier to understand. As shown in Figure 8, it is clear to see that the area of R6G is much larger than BT. This means that, per unit, the number of R6G molecules is much smaller than BT, which results in the ordered fact of benzene rings in the case of R6G, somehow. Additionally the silver particles on NWs are separated island, not perfectly smooth surface, which may cause the disorder pack of the BT molecules, and reduce the enhancement dependence on the polarization. Based on these facts, it is possible and reasonable that R6G layer shows a stronger polarization effect.

It has been reported that the bare single-crystalline silver NW showed SERS enhancement only when the laser polarization direction was perpendicular to the long axis of the NW [47]. In the case of the dielectric $Ga_2O_3$ NW core/silver layer composites, we observed SERS enhancements for both perpendicular and parallel polarization directions. This can also be attributed to the structure difference of the SERS active substrate. Some calculations indicated that the maximum enhancement of the plasmon resonances in noble metal spheroids arises from the region of the highest curvature [48–50]. Recently Hill et al. reported the high efficacy of gold-nanoparticle- (NP-) gold film system in generating large field enhancements due to the extremely close distance between the NP and the film, clearly demonstrating the importance of the substrate gap for SERS enhancement [51]. We have also demonstrated that there is a significant interaction between the spherical silver NPs on the ZnO NW due the closely spaced NPs, and the islands also interact with the dielectric NW substrate, further increasing the enhancement [13]. In addition, the SERS enhancement dependence on the polarization direction was observed for all bands at the excitation source of 785 nm and 514.5 nm. In recent years, a significant amount of work has been published on SERS, some of which has been on nanostructures, such as 1D nanowires [52, 53]. However, there are no reports of results such as those that we are presenting in this work. Thus all of these studies deepen the understanding of the strong SERS enhancement using dielectric NW core/silver layer composites and the underlying plasmonic behavior, which is critical to the development of sensor technology that can eventually be used for trace chemical, biological, and explosive sensing.

## 4. Conclusions

We have demonstrated the strong SERS dependence on the polarization direction of the incident light by investigating dielectric $Ga_2O_3$ NW core/silver composites, which showed that the SERS enhancement not only relies on the polarization direction of light with respect to the NW, but also on the wavelength of the incident laser and the orientation of SERS active molecules. Specifically, the strongest intensity of the SERS enhancement is obtained when the polarization of the incident light is parallel to the NW length at the incident wavelength of 785 nm, while the signal is maximized when the polarization is perpendicular to the NW length at 514.5 nm, which were confirmed by both experimental and theoretical simulation results. Therefore the SERS enhancement can be maximized by optimizing the direction of the NW, the incident angle of the laser polarization, the orientation of the molecules, and the wavelength of the laser.

## Acknowledgments

# References

[1] H. Xux and M. Käll, "Polarization-dependent surface-enhanced raman spectroscopy of isolated silver nanoaggregates," *ChemPhysChem*, vol. 4, no. 9, pp. 1001–1005, 2003.

[2] J. P. Kottmann and O. J. F. Martin, "Plasmon resonant coupling in metallic nanowires," *Optics Express*, vol. 8, no. 12, pp. 655–663, 2001.

[3] S. A. Maier, P. G. Kik, H. A. Atwater et al., "Local detection of electromagnetic energy transport below the diffraction limit in metal nanoparticle plasmon waveguides," *Nature Materials*, vol. 2, no. 4, pp. 229–232, 2003.

[4] T. Dadosh, J. Sperling, G. W. Bryant et al., "Plasmonic control of the shape of the raman spectrum of a single molecule in a silver nanoparticle dimer," *ACS Nano*, vol. 3, no. 7, pp. 1988–1994, 2009.

[5] I. K. J. Kretzers, R. J. Parker, R. V. Olkhov, and A. M. Shaw, "Aggregation kinetics of gold nanoparticles at the silica-water interface," *Journal of Physical Chemistry C*, vol. 113, no. 14, pp. 5514–5519, 2009.

[6] Y. Sun, G. Wei, Y. Song et al., "Type I collagen-templated assembly of silver nanoparticles and their application in surface-enhanced Raman scattering," *Nanotechnology*, vol. 19, no. 11, Article ID 115604, 2008.

[7] R. Gunawidjaja, S. Peleshanko, H. Ko, and V. V. Tsukruk, "Bimetallic nanocobs: decorating silver nanowires with gold nanoparticles," *Advanced Materials*, vol. 20, no. 8, pp. 1544–1549, 2008.

[8] J. L. Seung, M. B. Jeong, and M. Moskovits, "Polarization-dependent surface-enhanced raman scattering from a silver-nanoparticle-decorated single silver nanowire," *Nano Letters*, vol. 8, no. 10, pp. 3244–3247, 2008.

[9] H. Wei, F. Hao, Y. Huang, W. Wang, P. Nordlander, and H. Xu, "Polarization dependence of surface-enhanced Raman scattering in gold nanoparticle-nanowire systems," *Nano Letters*, vol. 8, no. 8, pp. 2497–2502, 2008.

[10] B. J. Wiley, Y. Chen, J. M. McLellan et al., "Synthesis and optical properties of silver nanobars and nanorice," *Nano Letters*, vol. 7, no. 4, pp. 1032–1036, 2007.

[11] J. M. McLellan, Z. Y. Li, A. R. Siekkinen, and Y. Xia, "The SERS activity of a supported ag nanocube strongly depends on its orientation relative to laser polarization," *Nano Letters*, vol. 7, no. 4, pp. 1013–1017, 2007.

[12] H. Wang, D. W. Brandl, F. Le, P. Nordlander, and N. J. Halas, "Nanorice: a hybrid plasmonic nanostructure," *Nano Letters*, vol. 6, no. 4, pp. 827–832, 2006.

[13] H. Qi, D. Alexson, O. Glembocki, and S. M. Prokes, "Plasmonic coupling on dielectric nanowire core-metal sheath composites," *Nanotechnology*, vol. 21, no. 8, Article ID 085705, 2010.

[14] H. Qi, D. Alexson, O. Glembocki, and S. M. Prokes, "The effect of size and size distribution on the oxidation kinetics and plasmonics of nanoscale Ag particles," *Nanotechnology*, vol. 21, no. 21, Article ID 215706, 2010.

[15] K. Kneipp, H. Kneipp, R. Manoharan et al., "Extremely large enhancement factors in surface-enhanced Raman scattering for molecules on colloidal gold clusters," *Applied Spectroscopy*, vol. 52, no. 12, pp. 1493–1497, 1998.

[16] H. Xu, J. Aizpurua, M. Käll, and P. Apell, "Electromagnetic contributions to single-molecule sensitivity in surface-enhanced Raman scattering," *Physical Review E*, vol. 62, no. 3, pp. 4318–4324, 2000.

[17] Z. Wang, S. Pan, T. D. Krauss, H. Du, and L. J. Rothberg, "The structural basis for giant enhancement enabling single-molecule Raman scattering," *Proceedings of the National Academy of Sciences of the United States of America*, vol. 100, no. 15, pp. 8638–8643, 2003.

[18] K. Kneipp, Y. Wang, R. R. Dasari, and M. S. Feld, "Approach to single molecule detection using surface-enhanced resonance Raman scattering SERRS: a study using rhodamine 6G on colloidal silver," *Applied Spectroscopy*, vol. 49, no. 6, pp. 780–784, 1995.

[19] D. M. Kuncicky, S. D. Christesen, and O. D. Velev, "Role of the micro- and nanostructure in the performance of surface-enhanced Raman scattering substrates assembled from gold nanoparticles," *Applied Spectroscopy*, vol. 59, no. 4, pp. 401–409, 2005.

[20] P. M. Tessier, O. D. Velev, A. T. Kalambur, J. F. Rabolt, A. M. Lenhoff, and E. W. Kaler, "Assembly of gold nanostructured films templated by colloidal crystals and use in surface-enhanced Raman spectroscopy," *Journal of the American Chemical Society*, vol. 122, no. 39, pp. 9554–9555, 2000.

[21] A. Tao, F. Kim, C. Hess et al., "Langmuir-Blodgett silver nanowire monolayers for molecular sensing using surface-enhanced Raman spectroscopy," *Nano Letters*, vol. 3, no. 9, pp. 1229–1233, 2003.

[22] S. M. Prokes, O. J. Glembocki, R. W. Rendell, and M. G. Ancona, "Enhanced plasmon coupling in crossed dielectric/metal nanowire composite geometries and applications to surface-enhanced Raman spectroscopy," *Applied Physics Letters*, vol. 90, no. 9, Article ID 093105, 3 pages, 2007.

[23] COMSOL Multiphysics, COMSOL Inc., http://www.comsol.com/.

[24] J. Zhao, A. O. Pinchuk, J. M. McMahon et al., "Methods for describing the electromagnetic properties of silver and gold nanoparticles," *Accounts of Chemical Research*, vol. 41, no. 12, pp. 1710–1720, 2008.

[25] M. Micic, N. Klymyshyn, Y. D. Suh, and H. P. Lu, "Finite element method simulation of the field distribution for AFM tip-enhanced surface-enhanced Raman scanning microscopy," *Journal of Physical Chemistry B*, vol. 107, no. 7, pp. 1574–1584, 2003.

[26] H. Ditlbacher, A. Hohenau, D. Wagner et al., "Silver nanowires as surface plasmon resonators," *Physical Review Letters*, vol. 95, no. 25, Article ID 257403, 4 pages, 2005.

[27] M. W. Knight and N. J. Halas, "Nanoshells to nanoeggs to nanocups: optical properties of reduced symmetry core-shell nanoparticles beyond the quasistatic limit," *New Journal of Physics*, vol. 10, Article ID 105006, 2008.

[28] M. W. Knight, Y. Wu, J. B. Lassiter, P. Nordlander, and N. J. Halas, "Substrates matter: influence of an adjacent dielectric on an individual plasmonic nanoparticle," *Nano Letters*, vol. 9, no. 5, pp. 2188–2192, 2009.

[29] T. Laroche and C. Girard, "Near-field optical properties of single plasmonic nanowires," *Applied Physics Letters*, vol. 89, no. 23, Article ID 233119, 3 pages, 2006.

[30] M. W. Knight, N. K. Grady, R. Bardhan, F. Hao, P. Nordlander, and N. J. Halas, "Nanoparticle-mediated coupling of light into a nanowire," *Nano Letters*, vol. 7, no. 8, pp. 2346–2350, 2007.

[31] C. Jiang, W. Y. Lio, and V. V. Tsukruk, "Surface enhanced raman scattering monitoring of chain alignment in freely suspended nanomembranes," *Physical Review Letters*, vol. 95, no. 11, Article ID 115503, 4 pages, 2005.

[32] J. Ding, V. I. Birss, and G. Liu, "Formation and properties of polystyrene-block-poly(2-cinnamoylethyl methacrylate) brushes studied by surface-enhanced raman scattering

and transmission electron microscopy," *Macromolecules*, vol. 30, no. 5, pp. 1442–1448, 1997.

[33] W. M. Sears, J. L. Hunt, and J. R. Stevens, "Raman scattering from polymerizing styrene. I. Vibrational mode analysis," *Journal of Chemical Physics*, vol. 75, no. 4, pp. 1589–1598, 1981.

[34] V. Zucolotto, M. Ferreira, C. Cordeiro et al., "Unusual interactions binding iron tetrasulfonated phthalocyanine and poly(allylamine hydrochloride) in layer-by-layer films," *Journal of Physical Chemistry B*, vol. 107, no. 16, pp. 3733–3737, 2003.

[35] R. Aroca and A. Thedchanamoorthy, "Vibrational studies of molecular organization in evaporated phthalocyanine thin solid films," *Chemistry of Materials*, vol. 7, no. 1, pp. 69–74, 1995.

[36] J. H. Kim, T. Kang, S. M. Yoo, S. Y. Lee, B. Kim, and Y. K. Choi, "A well-ordered flower-like gold nanostructure for integrated sensors via surface-enhanced Raman scattering," *Nanotechnology*, vol. 20, no. 23, Article ID 235302, 2009.

[37] C. A. Szafranski, W. Tanner, P. E. Laibinis, and R. L. Garrell, "Surface-enhanced Raman spectroscopy of aromatic thiols and disulfides on gold electrodes," *Langmuir*, vol. 14, no. 13, pp. 3570–3579, 1998.

[38] M. Takahashi, M. Fujita, and M. Ito, "SERS application to some electroorganic reactions," *Surface Science*, vol. 158, no. 1–3, pp. 307–313, 1985.

[39] A. A. Mani, Z. D. Schultz, B. Champagne et al., "Molecule orientation in self-assembled monolayers determined by infrared-visible sum-frequency generation spectroscopy," *Applied Surface Science*, vol. 237, no. 1–4, pp. 444–449, 2004.

[40] K. T. Carron and L. G. Hurley, "Axial and azimuthal angle determination with surface-enhanced Raman spectroscopy: thiophenol on copper, silver, and gold metal surfaces," *Journal of Physical Chemistry*, vol. 95, no. 24, pp. 9979–9984, 1991.

[41] S. Frey, V. Stadler, K. Heister et al., "Structure of thioaromatic self-assembled monolayers on gold and silver," *Langmuir*, vol. 17, no. 8, pp. 2408–2415, 2001.

[42] L. J. Wan, M. Terashima, H. Noda, and M. Osawa, "Molecular orientation and ordered structure of benzenethiol adsorbed on gold(111)," *Journal of Physical Chemistry B*, vol. 104, no. 15, pp. 3563–3569, 2000.

[43] S. W. Han, S. J. Lee, and K. Kim, "Self-assembled monolayers of aromatic thiol and selenol on silver: comparative study of adsorptivity and stability," *Langmuir*, vol. 17, no. 22, pp. 6981–6987, 2001.

[44] A. Bilić, J. R. Reimers, and N. S. Hush, "The structure, energetics, and nature of the chemical bonding of phenylthiol adsorbed on the Au(111) surface: implications for density-functional calculations of molecular-electronic conduction," *Journal of Chemical Physics*, vol. 122, no. 9, Article ID 094708, 15 pages, 2005.

[45] C. J. Sandroff and D. R. Herschbach, "Surface-enhanced Raman study of organic sulfides adsorbed on silver: facile cleavage of S-S and C-S bonds," *Journal of Physical Chemistry*, vol. 86, no. 17, pp. 3277–3279, 1982.

[46] L. Gunnarsson, E. J. Bjerneld, H. Xu, S. Petronis, B. Kasemo, and M. Käll, "Interparticle coupling effects in nanofabricated substrates for surface-enhanced Raman scattering," *Applied Physics Letters*, vol. 78, no. 6, 3 pages, 2001.

[47] P. Mohanty, I. Yoon, T. Kang et al., "Simple vapor-phase synthesis of single-crystalline Ag nanowires and single-nanowire surface-enhanced raman scattering," *Journal of the American Chemical Society*, vol. 129, no. 31, pp. 9576–9577, 2007.

[48] M. Moskovits, "Surface-enhanced spectroscopy," *Reviews of Modern Physics*, vol. 57, no. 3, pp. 783–826, 1985.

[49] D. S. Wang and M. Kerker, "Enhanced Raman scattering by molecules adsorbed at the surface of colloidal spheroids," *Physical Review B*, vol. 24, no. 4, pp. 1777–1790, 1981.

[50] P. J. Kottman, O. J. F. Martin, D. R. Smith, and S. Schultz, "Plasmon resonances of silver nanowires with a nonregular cross section," *Physical Review B*, vol. 64, no. 23, Article ID 235402, 10 pages, 2001.

[51] R. T. Hill, J. J. Mock, Y. Urzhumov et al., "Leveraging nanoscale plasmonic modes to achieve reproducible enhancement of light," *Nano Letters*, vol. 10, no. 10, pp. 4150–4154, 2010.

[52] J. Chen, T. Mårtensson, K. A. Dick et al., "Surface-enhanced Raman scattering of rhodamine 6G on nanowire arrays decorated with gold nanoparticles," *Nanotechnology*, vol. 19, no. 27, Article ID 275712, 2008.

[53] R. Kattumenu, C. H. Lee, L. Tian, M. E. McConney, and S. Singamaneni, "Nanorod decorated nanowires as highly efficient SERS-active hybrids," *Journal of Materials Chemistry*, vol. 21, no. 39, pp. 15218–15223, 2011.

*Research Article*

# Morphological and Structural Studies of Titanate and Titania Nanostructured Materials Obtained after Heat Treatments of Hydrothermally Produced Layered Titanate

**Mohd Hasmizam Razali,[1, 2] Ahmad-Fauzi Mohd Noor,[1] Abdul Rahman Mohamed,[3] and Srimala Sreekantan[1]**

[1] *School of Material and Mineral Resources Engineering, Engineering Campus, University of Science, Malaysia, Seri Ampangan, Nibong Tebal, 14300 Pulau Pinang, Malaysia*

[2] *Department of Chemical Sciences, Faculty of Science and Technology, Universiti Malaysia Terengganu, 21030 Kuala Terengganu, Malaysia*

[3] *School of Chemical Engineering, Engineering Campus, University of Science, Malaysia, Seri Ampangan, Nibong Tebal, 14300 Pulau Pinang, Malaysia*

Correspondence should be addressed to Ahmad-Fauzi Mohd Noor, afauzi@eng.usm.my

Different types of titanate and titania nanostructured materials have been successfully synthesised and characterized using field emission scanning electron microscopy (FESEM), transmission electron microscopy (TEM), X-ray diffraction (XRD) and raman spectroscopy. Elemental analysis was determined by energy dispersive X-ray spectroscopy (EDX) analyzer while thermogravimetric-differential scanning calorimetry (TG-DSC) was used to determine thermal stability. In this study, we found that nanotubes were formed during the washing treatment stage with HCl and distilled water. When the pH of the washing solution was 12, sodium titanate nanotubes were obtained, while when the pH of the washing solution was 7, hydrogen titanate nanotubes were obtained. Sodium titanate nanotubes were thermally stable up to 500°C; however, at 700°C, the nanotubes structure transform to solid nanorods. Meanwhile, hydrogen titanate nanotubes decomposed to produce titania nanotubes after heat treatment at 300°C for 2 hours. At 500°C, the tubular structure broke to small segments due to destruction of the nanotube. Further heat treatment at 700°C, led to the destruction and collapse of the nanotubes structure produce titania nanoparticles.

## 1. Introduction

After years of evolutionary research on titanate and titania nanostructured material production, many technologies based on "bottom up" processes such as the sol-gel method [1–3], chemical vapour deposition [4], template method [5], anodic anodization method [6], and hydrothermal method [7] have been developed. However, from the viewpoint of their environmental impact and cost operation for large-scale production, the hydrothermal method offers the best option since this method is simple, inexpensive, and efficient for obtaining products with high purity in both phases and morphology.

The hydrothermal method, based on wet chemistry method, is a versatile heterogeneous chemical reaction in the presence of a solvent, aqueous or nonaqueous, conducted in steel pressure vessels called autoclaves with or without Teflon liners under controlled temperature and pressure [8]. The temperature and the amount of solution added to the autoclave largely determine the internal pressure produced. Under the hydrothermal condition, it is possible to grow nanostructured metal oxides by dissolution and crystallization, thereby creating a distinctive difference in their characteristics at the nanoscale level [8].

Even though the hydrothermal method has caught the interest of researchers to synthesize nanostructured titanate

and titania materials, particularly the nanotubes, somehow the formation mechanism of the nanotubes hydrothermally is still debatable. Furthermore, different crystal structures and compositions have been presented to describe the nanotubes structure. Therefore, it is very important to study the actual mechanism of nanotube formation and to determine at which stage the nanotubes structure was formed. This in turn will determine the composition and phase structure.

Based on previous studies, researchers claimed that the nanotubes are form either during the hydrothermal process or during washing treatment with HCl and distilled water. In 2005, Lim et al. [9] reported that the nanotubes of $TiO_2$ are formed during the hydrothermal process. During the hydrothermal process at high temperature, the sodium cations ($Na^+$) residing between the edge-shared ($TiO_6$) octahedral layers can be replaced gradually by $H_2O$ molecules. The size of intercalated $H_2O$ molecules is larger than that of $Na^+$ ions, hence the interlayer distance becomes enlarged, and the static interaction between neighboring ($TiO_6$) octahedral sheets is weakened. Subsequently, the layered titanate particles exfoliate to form nanosheets. To release strain energy, the nanosheets curl up from the edges to form $TiO_2$ nanotubes.

Later, Peng et al. [10] proposed in their study that during alkaline treatment, anatase titania nanoparticles undergo delamination in the alkali solution to produce single-layer $TiO_2$ sheets. The $TiO_2$ sheet is an unstable structure due to its high surface-to-volume ratio or high system energy. At low treatment temperature (lower than 170°C), $TiO_2$ sheets might fold up by epitaxial growth to form titania nanotubes. During further treatment at higher temperature (higher than 190°C), titania nanotubes can self-assemble into a bundle-like superstructure of titania nanotubes.

Other researchers like Wang et al. [11] also found that tubes structure was formed during the hydrothermal process. They reported that during the reaction process, titanium dioxide reacts with NaOH forming layered alkali titanate. These layered crystals are very thin and easily exfoliate into individual nanosheets that are highly anisotropic in two dimensions. At a high pressure of 2 bars and a high temperature of about 150°C, the layered structure would roll up into nanotubes due to surface tension.

Nakahira et al. [12] reported that in the primary stages of hydrothermal treatment, the nanosheet-like products (layered sodium titanate) were preferentially formed and, subsequently, their nanosheets were exfoliated from layered sodium titanate, curled, and scrolled to nanotubes. Thus, the sodium titanate nanotubes were formed during these hydrothermal treatments.

Kasuga et al. [13] found out that titania nanotubes were formed after washing with distilled water and HCl aqueous solution. Kasuga proposed that the NaOH treatment broke some surface Ti–O–Ti bonds of the raw material, forming Ti–O–Na and Ti–OH bonds in their place. The subsequent acid washing destroyed the surface activation leading to dehydration of the Ti-OH bonds allowing the formation of Ti-O–Ti bond and (Ti–O···H–O–Ti). The Ti–OH bonds formed through this procedure were believed to form from the decreasing Ti bond distance on the sheet's surface during the dehydration process. A residual electrostatic repulsion from the Ti–O–Na bonds was believed to induce the ends of the formed sheet to connect, hence forming the tube structure of $TiO_2$.

Besides $TiO_2$ nanotubes, researchers also reported that the obtained nanotubes materials were in different crystal structures and compositions such as hydrogen trititanate ($H_2Ti_3O_7$) [14], tetratitanate ($H_2Ti_4O_9 \cdot H_2O$) [15], lepidocrocite titanate $Na_xH_{2-x}Ti_3O_7$ [16], and $H_2Ti_2O_4(OH)_2$ [17]. Therefore, this study was embarked to evaluate the crystal structure and morphology of the products obtained after heat treatment of the as-synthesized samples at different pH values of washing solution. It can provide strong evidence about its original crystal structure and allow us to know when the nanotube structures were formed.

## 2. Methodology

*2.1. Preparation.* 2 grams of $TiO_2$ precursor powder (Merck) was dispersed in 10 M NaOH (100 mL) and was subjected to hydrothermal treatment at 150°C for 24 hours in autoclave. When the reaction was completed, the white solid was collected and divided to two parts. The first portion was washed with 0.1 M HCl (200 mL) followed by distilled water until a pH 12 of washing solution was obtained. Meanwhile, a second portion was washed with 0.1 M HCl (200 ml) followed by distilled water until a pH 7 of washing solution was obtained. Then, the white solid was separated and collected from both solutions and subsequently dried at 80°C for 24 hours. After drying, the obtained powder from pH 12 and pH 7 washing solution was named as-synthesized samples A and B, respectively. Subsequently, both samples were heated at 300°C, 500°C, and 700°C for 2 hours in the air.

*2.2. Characterization.* Energy-dispersive X-ray spectroscopy (EDX) analyzer was used for elemental analysis in the sample, while the morphology was studied using scanning electron microscope with GEMINI field emission (FESEM) and JOEL transmission electron microscope (TEM). X-ray powder diffraction (XRD) analysis was performed using a diffractometer D5000 Siemens kristalloflex with Cu $K_\alpha$ radiation ($\lambda = 1.54060$ Å). Scans were performed in the step of 0.2°/second over the range of $2\theta$ from 20 up to 80°. Raman spectra were analysed using RENISHAW Invia Raman microscope and recorded in the range 100–1000 $cm^{-1}$. Thermal stability study of the sample was done using thermogravimetry and differential scanning calorimetry (TG-DSC) SDT Q600.

## 3. Results and Discussion

Figure S1 of the supplementary matrial avalible online at doi: 10.1155/2012/962073 shows the FESEM micrograph of the $TiO_2$ precursor, revealing agglomerated irregularly shaped particles containing Ti and O as indicated by EDX (Figure S3). On the other hand, spherical particles of the $TiO_2$
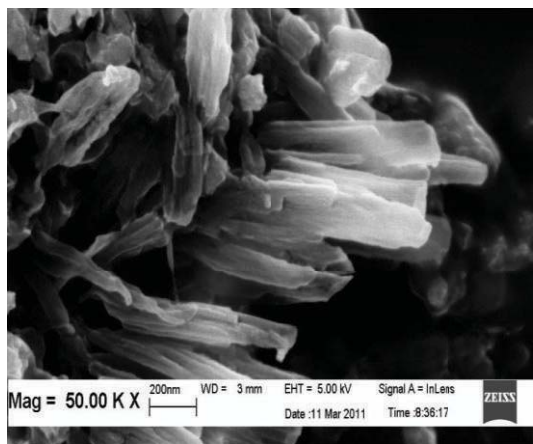
FIGURE 1: FESEM micrograph of $Na_2Ti_3O_7$.

TABLE 1: Sodium content in the sample.

| Samples | Na (wt%) |
|---|---|
| Without washing | 45.93 |
| As-synthesised sample A | 10.46 |
| As-synthesised sample B | 0.00 |



FIGURE 2: TG-DSC spectrum for the as-synthesised sample A.



FIGURE 3: TG-DSC spectrum for the as-synthesised sample B.

precursor can be seen clearly in the TEM micrograph with the particle size being about 160 nm (Figure S2). During the hydrothermal treatment, the titanium dioxide precursor ($TiO_2$) reacts with NaOH forming a highly disordered phase of $Na_2Ti_3O_7$ which is present in the layered structure form [18]. $TiO_2$ is an amphoteric oxide it can react as an acid or base depending on the pH of the solution. Since the reaction was carried out in 10 M NaOH (high pH~14 and high basicity), $TiO_2$ acted as an acid to react with NaOH (alkaline) to produce layered titanate of $Na_2Ti_3O_7$ salt and water, $H_2O$, according to the following equation [18]:

$$3TiO_2 + 2NaOH \longrightarrow Na_2Ti_3O_7 + H_2O \qquad (1)$$
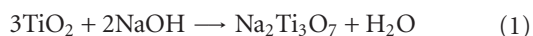
The layered-like structure of $Na_2Ti_3O_7$ was shown in the FESEM micrograph (Figure 1) containing Na, Ti, and O as indicated by EDX (Figure S5).

After the hydrothermal treatment, the obtained product (layered titanate, $Na_2Ti_3O_7$) was washed with HCl (0.1 M) and distilled water. Washing plays an important role in controlling the amount of $Na^+$ ions remaining in the sample solution, thus influencing the bending of the layered titanate. Zhang et al. [19] stated that due to the imbalance of $H^+$ and $Na^+$ ion concentrations on the two different sides of the layered-like structure, excess surface energy and the layered-like structure bends to form nanotubes.

In this study, washing was carried out until the pHs of the washing solutions was 7 and 12, respectively, and this will influence the amount of sodium remaining in the samples. Hence, EDX analysis was carried out to investigate the presence of sodium in the samples because it is vital in determining the thermal stability, phase structure, and morphology of the synthesized nanostructured materials. For comparison, elemental analysis for the sample obtained after
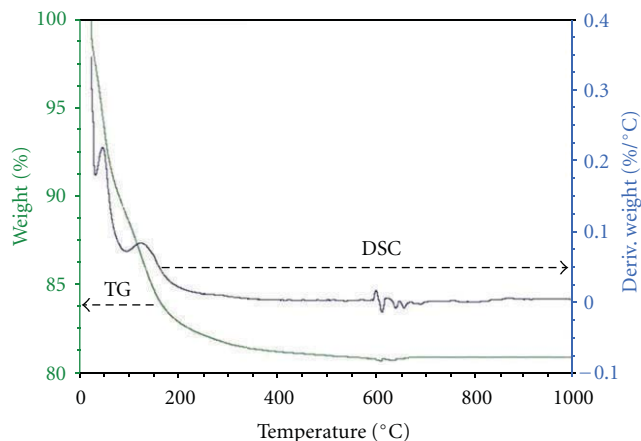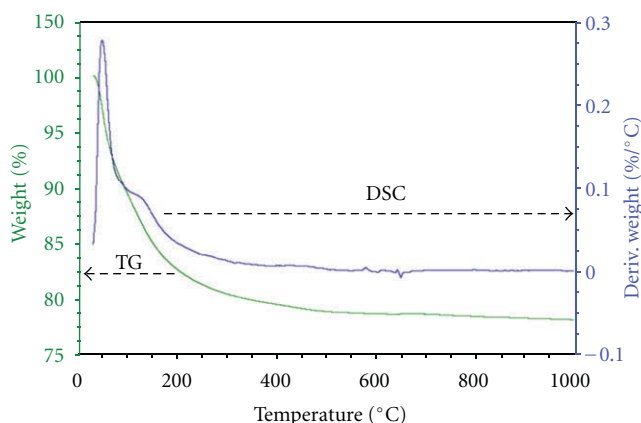
hydrothermal process (without washing) was performed and that sample was found to consist of 45.93 wt% of sodium (Table 1) (Figure S4). After washing till the pH 12, sodium content was found to be reduced to 10.46 wt% (as-synthesised sample A) (Table 1) (Figure S5). It was shown that about 35 wt% of sodium ions has been exchanged with hydrogen ions. Meanwhile, when the sample was completely washed, with the pH of washing solution equal to 7 (as-synthesised sample B), no more sodium was detected, which indicated that sodium ions were completely removed and exchanged with hydrogen ions during washing with HCl and distilled water (Table 1) (Figure S6).

Hydrogen cannot be detected by EDX, but nevertheless, theoretically, $H^+$ is extremely reactive chemically due to its very small size of only about 1/64,000th of the radius of a hydrogen atom and the fact that it exists as a free proton which makes it react immediately by exchange with $Na^+$. Based on the density functional theory, the sodium ion can be replaced by hydrogen ion although the $Na_2Ti_3O_7$ structure is very stable [19]. This is possible since the sodium ions are only weakly bonded to the negatively charged $Ti_3O_7^{2-}$ layers. While the Na–O bond length in $Na_2Ti_3O_7$ is above 2Å, the bond length of H–O in $H_2Ti_3O_7$ is about 1Å. Therefore, the
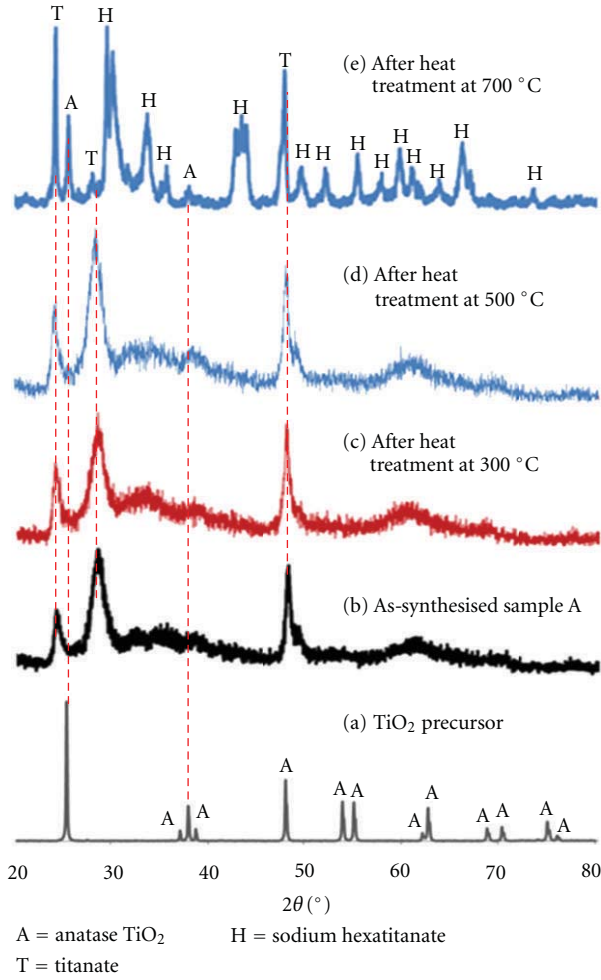
FIGURE 4: XRD patterns of (a) TiO$_2$ precursors, (b) as-synthesised sample A and after heat treatments at (c) 300°C, (d) 500°C, and (e) 700°C for 2 hours.



FIGURE 5: XRD patterns of (a) TiO$_2$ precursor, (b) as-synthesised sample B and after heat treatments at (c) 300°C, (d) 500°C, and (e) 700°C for 2 hours.

hydrogen ion exchange process is irreversible. Furthermore elution strength of H$^+$ is larger than Na$^+$; therefore, the ion exchange between H$^+$ and Na$^+$ is possible to occur according to the following equation.

Dissolution-crystallisation layered structure:

$$Na_2Ti_3O_7 \longrightarrow 2Na^+ + Ti_3O_7^{2-} \quad (2)$$

Ion exchanged during washing occurs as follows:

$$2Na^+ + Ti_3O_7^{2-} + H^+ + Cl^-$$
$$\longrightarrow H^+ + Ti_3O_7^{2-} + 2Na^+ + Cl^- \quad (3)$$

Crystallisation for salt formation is as follows:

$$Na^+ + Cl^- \longrightarrow NaCl \,(\text{dissolved in an aqueous solution}) \quad (4)$$

Crystallisation for titanate formation is as follows:

$$2H^+ + Ti_3O_7^{2-} \longrightarrow H_2Ti_3O_7 \quad (5)$$
(white precipitate in an aqueous solution)

The ion exchange reaction occurred very fast as no electron pair was needed to be broken and the rate of the process is limited only by the rate at which ions can be diffused in and out of the exchanger structure. Thus, it was expected that the titanate product obtained in this study can be used as an ion exchanger due to the rapidity and efficiency of their actions. Furthermore, the ion exchange and structural properties of titanate allows for efficient ion mobility in the interstices and an open mesoporous structure for electrolyte diffusion. These features give rise to a high discharge/charge capability, high rate capability, and excellent stability, and this is one key requirement for lithium batteries.

In order to study the thermal stability of the titanate products, thermogravimetric and differential scanning calorimetry (TG-DSC) was performed in nitrogen atmosphere from room temperature to 1000°C, with heating rate of 5°C/min.

Both samples show almost similar TG curves (Figures 2 and 3), showing decrease in mass starting at room temperature until 700°C, with total mass loss of about 22%. In general, the weight loss between room temperature till 100°C is due to the removal of adsorbed water from the surface. When the temperature is further increased up to 200°C, the intercalated water molecules such as dissociated molecular H$_2$O, physisorbed molecular H$_2$O and chemisorbed molecular H$_2$O are removed. This also includes Ti–OH bonds within tubular structure [20]. Subsequently, a small weight
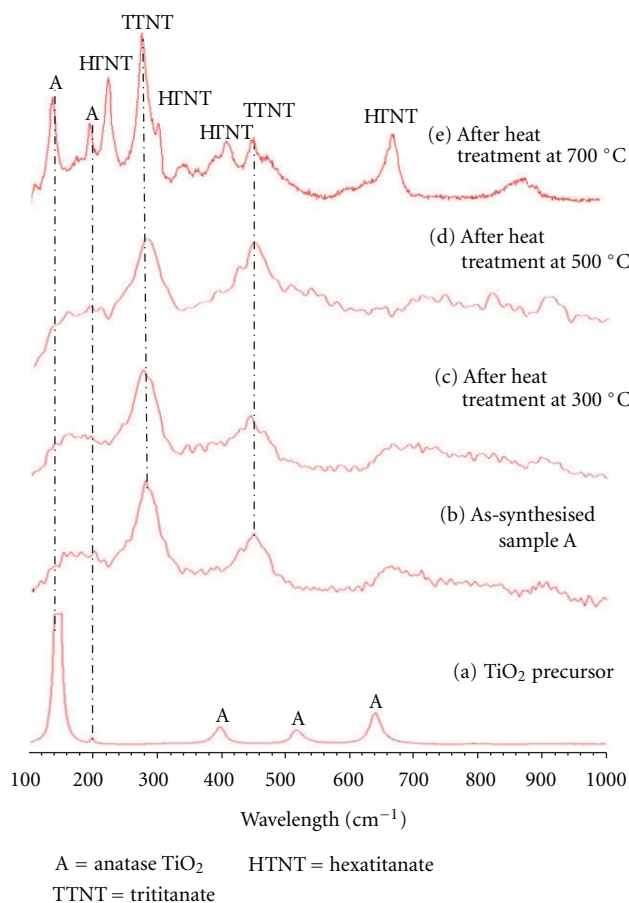
FIGURE 6: Raman spectra of (a) TiO$_2$ precursor (b) as-synthesised sample A and after heat treatments at (c) 300°C, (d) 500°C, and (e) 700°C for 2 hours.
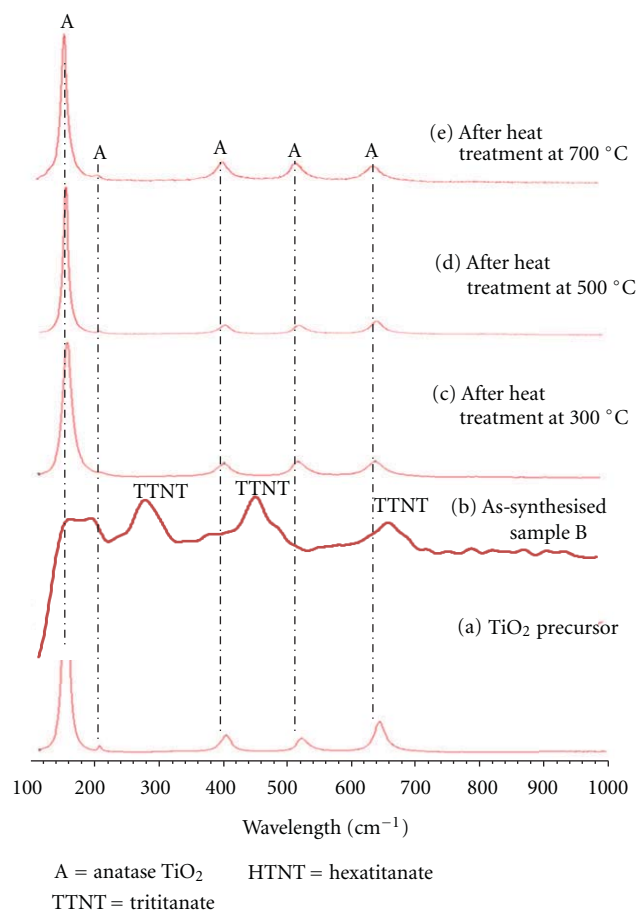


FIGURE 7: Raman spectra of (a) TiO$_2$ precursors, (b) as-synthesised sample B and after heat treatments at (c) 300°C, (d) 500°C, and (e) 700°C for 2 hours.

loss in the region of 200–700°C was due to the dehydration of titanate nanotubes and transformation of phase structure.

On the other hand, the DSC graphs in Figures 2 and 3 show larger two endothermic peaks at 70°C and 150°C which are characteristics for the evaporation of different states of adsorbed water molecules. Few smaller endothermic and exothermic peaks at 600–700°C are attributed to the transformation of morphology and phase crystal structures.

X-ray diffraction was carried out to study the crystal structure of the samples and effect of heat treatment on the crystal structure. The X-ray diffractogram patterns of the as-synthesized sample A is shown in Figure 4. The TiO$_2$ precursor shows a series of sharp and narrow peaks, the highest being 101 at 25.27°, which is characteristic of the anatase TiO$_2$ phase structure (Figure 4(a)). Meanwhile, XRD pattern of as-synthesised sample A and after heat treatment at 300°C and 500°C shows the presence of similar peaks which are identical to sodium titanate [21] (Figures 4(b), 4(c), and 4(d)). Similar diffraction peaks suggesting the maintenance of the crystallographic and morphological structure up to 500°C and this could be ascribed to the interlayer spacing typical for one-dimensional titanate structure [22].

After 700°C heat treatment, emergence of new sharp and narrow peaks took place indicating that the crystallinity of the sample is increased. These new peaks can be assigned to sodium hexatitanate and titania anatase (Figure 4(e)). The presence of sodium hexatitanate phase in the thermal products is a crucial phenomenon in understanding the structural properties of titanate nanostructures. It seems that at higher temperatures sodium titanates undergo a dimerization-like process leading to the formation of sodium hexatitanates. The basic difference in the structures of sodium trititanates and sodium hexatitanates is that the former presents a lamellar structure with Ti$_3$O$_7$$^{2-}$ corrugated layers and two interlamellar Na$^+$ ions [23]. Previously, Sauvet et al. [24] proposed that at higher temperatures sodium trititanates tend to fuse and the formation of Na$_2$Ti$_6$O$_{13}$ is the result of the "dimerization-like" process of Na$_2$Ti$_3$O$_7$. The presence of Na$_2$Ti$_6$O$_{13}$ in the thermal products can be considered as strong evidence that the structure and composition of as-synthesised sample A are very similar to Na$_2$Ti$_3$O$_7$ and a general formula may be assigned as Na$_{2-x}$H$_x$Ti$_3$O$_7$ due to some of the Na$^+$ being exchanged with H$^+$ during washing treatment.

(a)

(b)

(c)

(d)

Figure 8: FESEM micrographs of (a) as-synthesized sample A and after heat treatments at (b) 300°C, (c) 500°C, and (d) 700°C for 2 hours.

Figure 5 presents the XRD patterns of as-synthesized sample B and its derivatives obtained at different temperatures as well-$TiO_2$ precursor for comparison. The $TiO_2$ precursor shows the existence of a series of sharp and narrow peaks which is characteristic of the anatase $TiO_2$ phase structure (Figure 5(a)). Meanwhile, XRD pattern of as-synthesized sample B (Figure 5(b)) is identical to hydrogen titanate, ($H_2Ti_3O_7$) [25]. For the samples after heat treatment at 300°C, 500°C, and 700°C (Figures 5(c), 5(d), and 5(e)), they show similar peaks which are assigned to $TiO_2$ anatase, but an increase in degree of crystallinity.

From the XRD analysis, it may be inferred that the composition and structure of the as-synthesised sample B is very similar to layered protonic titanate with a general formula that may be assigned as $H_2Ti_3O_7$. After heat treatment at 300°C or at higher temperature ($\leq$700°C) for 2 hours, $H_2Ti_3O_7$ decomposes to produce $TiO_2$ with anatase phase according to the following equation [25]:

$$H_2Ti_3O_7 \longrightarrow 3TiO_2 + H_2O \qquad (6)$$
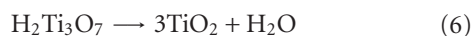
It has been recognized that anatase $TiO_2$ is preferred because of its high photocatalytic activity, since it has a more negative conduction band edge potential (higher potential energy of photogenerated electrons). Anatase $TiO_2$ also has strong photoinduced redox power, thus it could be a superior photocatalytic material for purification and disinfection of water and air, as well as remediation of hazardous waste [26]. Furthermore, the with high surface area of nanostructured $TiO_2$ anatase increases the rate of a photocatalytic reaction, due to the presence of more active sites. The hollow structure of nanotubes can also potentially enhance electron percolation and light conversion, as well as the improved ion diffusion at the semiconductor photocatalyst-electrolyte interface [27, 28]. Therefore, synthesized nanostructured $TiO_2$ nanotubes in this study could potentially contribute to a high performance photocatalyst.

Further characterization was employed using raman spectroscopy. According to the factor group analysis, anatase $TiO_2$ has six raman active modes (A1g + 2B1g + 3Eg) [29]. Previously, Ohsaka et al. [30] studied the raman spectrum of an anatase $TiO_2$ single crystal and they identified six peaks which appeared at 144 cm$^{-1}$ (Eg), 197 cm$^{-1}$ (Eg), 399 cm$^{-1}$ (B1g), 513 cm$^{-1}$ (A1g), 519 cm$^{-1}$ (B1g), and 639 cm$^{-1}$ (Eg). In this study, fives peaks at 143 cm$^{-1}$ (Eg), 197 cm$^{-1}$ (Eg),

(a)

(b)

(c)

(d)

FIGURE 9: TEM micrographs of (a) as-synthesized sample A and after heat treatments at (b) 300°C, (c) 500°C, and (d) 700°C for 2 hours.

396 cm$^{-1}$ (B1g), 516 cm$^{-1}$ (A1g/B1g), and 639 cm$^{-1}$ (Eg) were traced for the TiO$_2$ precursor (Figure 6(a)). According to Bergeret al. [31], the strongest peak at 143 cm$^{-1}$ was attributed to the external vibration of the anatase structure, therefore it could be concluded that TiO$_2$ precursor is an anatase phase. This finding is in agreement with the XRD result, which showed that TiO$_2$ precursor is in anatase phase. In contrast, for as-synthesized sample A (Figure 6(b)) and after heat treatment at 300°C and 500°C for 2 hours (Figures 6(c) and 6(d)) peaks at only about 280 cm$^{-1}$ and 446 cm$^{-1}$ were observed. The broad peak at 280 cm$^{-1}$ is assigned to the characteristic phonon mode of titanate structure [32], while the peak at 446 cm$^{-1}$ is assigned to the Ti–O bending vibration involving six coordinated titanium atoms and three coordinated oxygen atoms in the layered titanate structure [29]. After heat treatment at 700°C, peaks at 280 cm$^{-1}$ and 446 cm$^{-1}$ can still be observed and a few new peaks appeared at about 135 cm$^{-1}$, 222 cm$^{-1}$, 405 cm$^{-1}$, 449 cm$^{-1}$, 630 cm$^{-1}$ and 673 cm$^{-1}$ (Figure 6(e)) suggesting that the presence of anatase of TiO$_2$ and hexatitanate structures.

On the other hand, the as-synthesized sample B showed the presence of three peaks at about 280 cm$^{-1}$, 446 cm$^{-1}$, and 664 cm$^{-1}$ (Figure 7(b)). As reported previously, the broad peak at 280 cm$^{-1}$ is assigned to the characteristic phonon mode of titanate nanotube structures [29] and the peak at 446 cm$^{-1}$ is belongs to the Ti–O bending vibration involving six coordinated titanium atoms and three coordinated oxygen atom in layered titanate [31]. Meanwhile, the peak at 664 cm$^{-1}$ is due to the Ti–O–H vibration [32]. Therefore, it could be concluded that as-synthesized sample B is H$_2$Ti$_3$O$_7$, which confirms the XRD result. After heat treatment at 300°C, 500°C, and 700°C for 2 hours, similar raman spectra (Figures 7(c), 7(d), and 7(e)) with TiO$_2$ precursor (Figure 7(a)) were observed, indicating that they are also TiO$_2$ in anatase phase.

The results obtained in this study clearly indicate that the structure of as-synthesised samples A (solid powder obtained after drying at 80°C for 24 h of white solid collected from pH 12 of washing solution) and as-synthesised sample B (solid powder obtained after drying at 80°C for 24 h of white solid collected from pH 7 of washing solution) are Na$_{2-x}$H$_x$Ti$_3$O$_7$ and H$_2$Ti$_3$O$_7$, respectively.

Surface morphology of the samples was observed using FESEM and TEM. The FESEM micrographs of as-synthesized sample A revealed the formation of a hair-like structure with ±10 nm in diameter (Figure 8(a)).
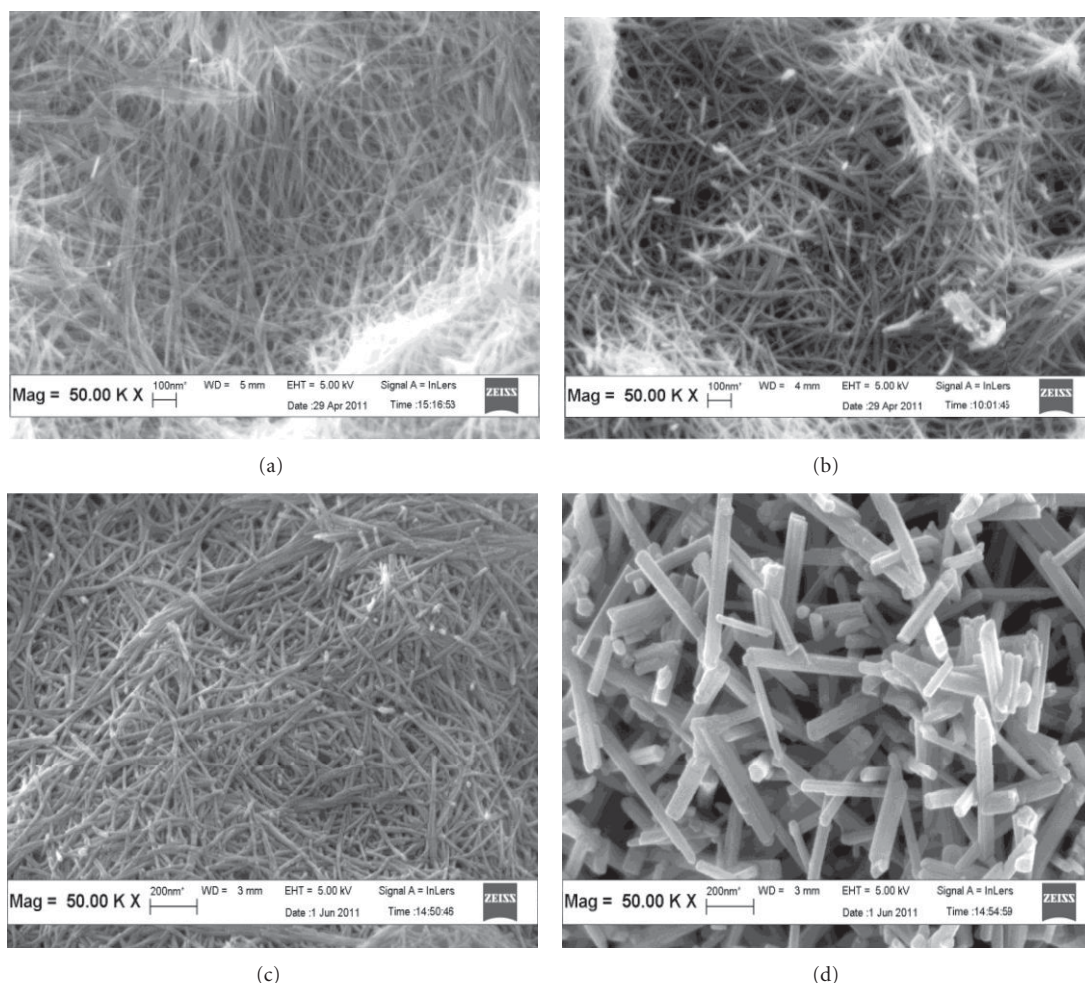
(a)



(b)



(c)



(d)
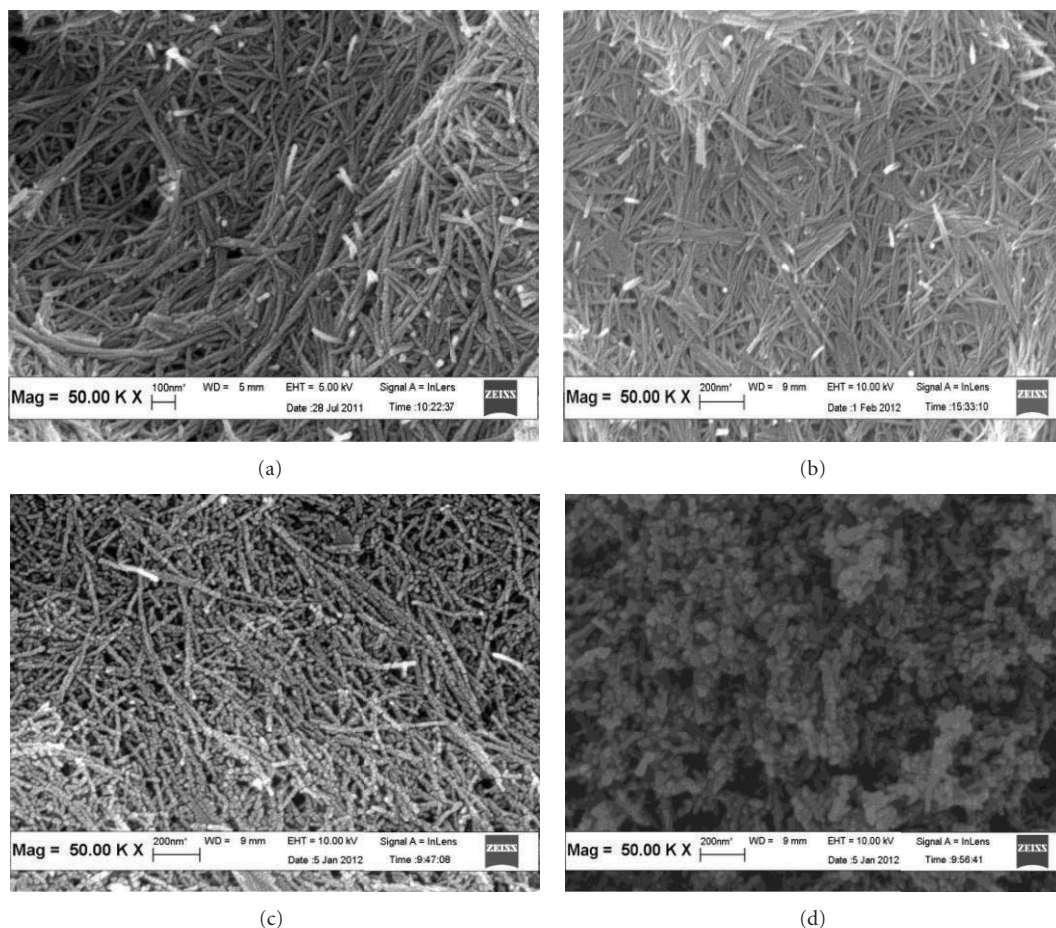
FIGURE 10: FESEM micrographs of (a) as-synthesised sample B and after heat treatments at (b) 300°C, (c) 500°C, and (d) 700°C for 2 hours.

Further observation with TEM showed the existence of a hollow structure inside the $TiO_2$ tubule indicating that nanotubes structures were obtained (Figure 9(a)). The inner and outer diameters of nanotubes are about 4 nm and 10 nm, respectively. After heat treatment at 300 and 500°C for 2 hours (Figures 8(b), 9(b), 8(c), and 9(c)), the samples still showed similar surface morphology with the as-synthesized sample, and thus revealing that there were no great influences on surface morphology of the nanotube structure at low annealing temperature (≤500°C). This indicated that the nanotube structure of as-synthesised sample A was thermally stable up to 500°C. However, when the annealing temperature was increased to 700°C, the nanotube structure had completely transformed to nanorods. The nanorod (nonhollow structure) with ±65 nm diameter were formed due to the mobilizations of dissolved $Na^+$ into the nanotubes inner channel (as well as the boundary pores among nanotubes) and then recrystallized to form nanorods (Figures 8(d) and 9(d)). The existence of sodium in the as-synthesised sample A was shown previously by EDX analysis.

As-synthesised sample B also shows the presence of a hair-like tubular structure (±10 nm in diameter) (Figure 10(a)) with the existence of a hollow space inside the tubular structure (±4 nm in diameter) (Figure 11(a)).

Thus, the nanotubes with about ±4 nm inner and ±10 nm outer diameters were obtained. After heat treatment at 300°C for 2 hours, there was no significant influence on morphology of the material (Figure 10(b)). The nanotubes preserve their shape with their inner diameter being almost similar; however, their outer diameter increases up to 12 nm (Figure 11(b)), due to the dehydration of intralayered OH groups [33]. Surprisingly, at 500°C heat treatment, the morphology of the material was affected significantly. The tubular structures were broken to small segments due to destruction of the nanotubes. However, frames of the tubular structures were still visible (Figures 10(c) and 11(c)). When the heating temperature was increased to 700°C, the nanotube structure was completely destroyed and the individual tubes had formed into nanoparticle structures with particle size around 20 nm (Figures 10(d) and 11(d)). This was probably a result of dehydration of interlayered OH groups which induced the change of the crystalline structure and destroyed the nanotubes structure to produce nanoparticles, when the temperature of heat treatment was higher [33, 34].

The absence of the $Na^+$ in the as-synthesised sample B would cause the tube structure to be easily destroyed even after heat treatment at 500°C. Sodium ion was reported to play an important role in pinning adjacent layers, thus

(a)

(b)

(c)

(d)

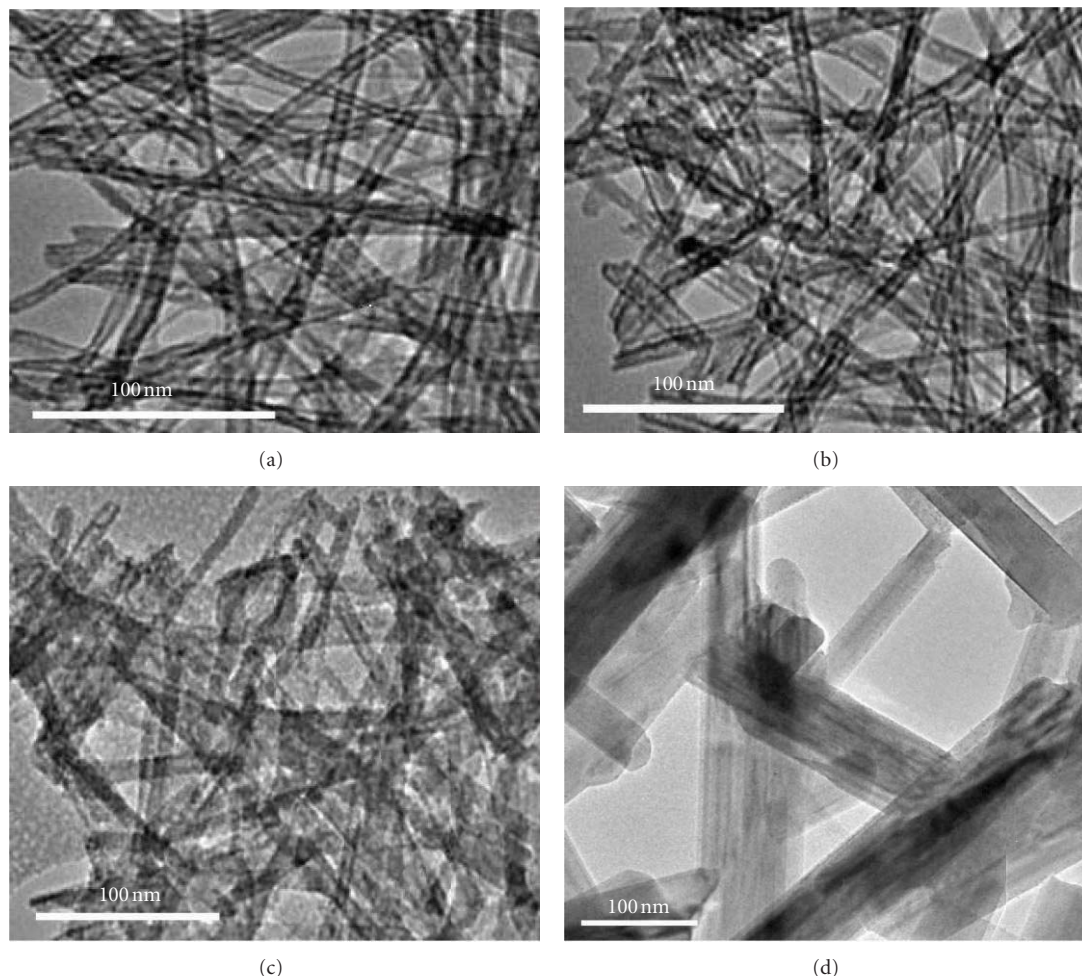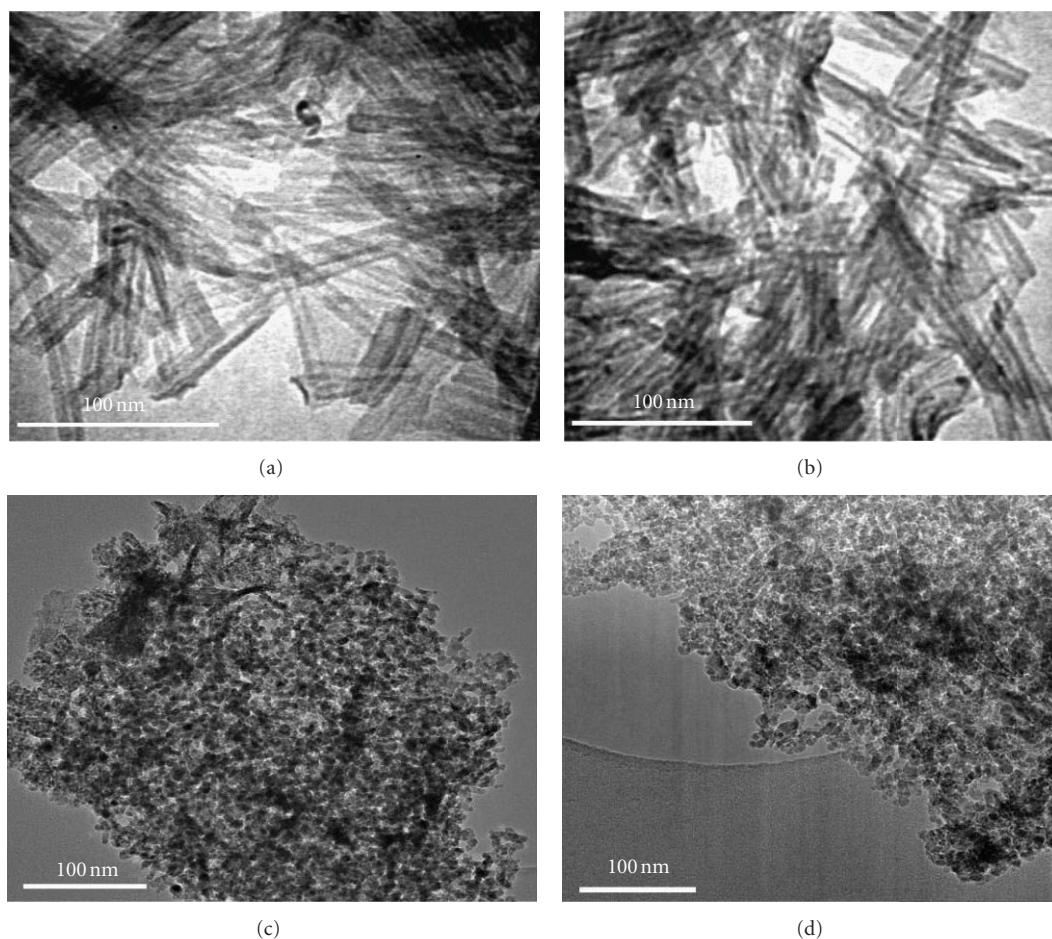FIGURE 11: TEM micrographs of (a) as-synthesised sample B and after heat treatments at (b) 300°C, (c) 500°C, and (d) 700°C for 2 hours.

stabilizing the layered structure and tubular morphology [35].

## 4. Conclusion

Upon hydrothermal treatment of $TiO_2$ in NaOH, a disordered phase with a layered structure was formed. This disordered layered structured phase transformed into titanate nanotubes after being washed with HCl and distilled. When the pH of washing solution was 12, sodium titanate nanotube was obtained. The obtained nanotubes were thermally stable up to 500°C; however, at 700°C heating treatment nanotubes transformed to the titanate nanorods; while when the pH of washing solution was 7, hydrogen titanate nanotubes were obtained. After heat treatment at 300°C for 2 hours, hydrogen titanate nanotubes decomposed to produce titania nanotubes. After further heat treatment at 500°C, the tubular structure broke to small segments due to destruction of nanotube and, at 700°C, nanotube structure was totally destroyed and subsequently transformed to nanoparticle. Nanoparticles and nanotubes of titania obtained in this study have an anatase phase which is expected to be a high performance photocatalyst.

## References

[1] T. Sugimoto, X. Zhou, and A. Muramatsu, "Synthesis of uniform anatase $TiO_2$ nanoparticles by gel-sol method: 4. Shape control," *Journal of Colloid and Interface Science*, vol. 259, no. 1, pp. 53–61, 2003.

[2] C. Su, B. Y. Hong, and C. M. Tseng, "Sol-gel preparation and photocatalysis of titanium dioxide," *Catalysis Today*, vol. 96, no. 3, pp. 119–126, 2004.

[3] T. Sugimoto, X. Zhou, and A. Muramatsu, "Synthesis of uniform anatase $TiO_2$ nanoparticles by gel-sol method: 1. Solution chemistry of $Ti(OH)_n(4 - n)+$ complexes," *Journal of Colloid and Interface Science*, vol. 252, no. 2, pp. 339–346, 2002.

[4] T. Maekawa, K. Kurosaki, T. Tanaka, and S. Yamanaka, "Thermal conductivity of titanium dioxide films grown by metal-organic chemical vapor deposition," *Surface and Coatings Technology*, vol. 202, no. 13, pp. 3067–3071, 2008.

 [5] J. H. Lee, I. C. Leu, M. C. Hsu, Y. W. Chung, and M. H. Hon, "Fabrication of aligned $TiO_2$ one-dimensional nanostructured arrays using a one-step templating solution approach," *Journal of Physical Chemistry B*, vol. 109, no. 27, pp. 13056–13059, 2005.

 [6] N. R. De Tacconi, C. R. Chenthamarakshan, G. Yogeeswaran et al., "Nanoporous $TiO_2$ and WO3 films by anodization of titanium and tungsten substrates: influence of process variables on morphology and photoelectrochemical response," *Journal of Physical Chemistry B*, vol. 110, no. 50, pp. 25347–25355, 2006.

 [7] D. S. Kim and S.Y. Kwak, "The hydrothermal synthesis of mesoporous $TiO_2$ with high crystallinity, thermal stability, large surface area, and enhanced photocatalytic activity," *Applied Catalysis A*, vol. 323, pp. 110–118, 2007.

 [8] K. Byrappa and M. Yoshimura, *Handbook of Hydrothermal Technology—A Technology for Crystal Growth and Materials Processing*, Noyes, Park Ridge, NJ, USA, 2001.

 [9] S. H. Lim, J. Luo, Z. Zhong, W. Ji, and J. Lin, "Room-temperature hydrogen uptake by $TiO_2$ nanotubes," *Inorganic Chemistry*, vol. 44, no. 12, pp. 4124–4126, 2005.

[10] H. Peng, G. Li, and Z. Zhang, "Synthesis of bundle-like structure of titania nanotubes," *Materials Letters*, vol. 59, no. 10, pp. 1142–1145, 2005.

[11] D. Wang, F. Zhou, Y. Liu, and W. Liu, "Synthesis and characterization of anatase $TiO_2$ nanotubes with uniform diameter from titanium powder," *Materials Letters*, vol. 62, no. 12-13, pp. 1819–1822, 2008.

[12] A. Nakahira, T. Kubo, and C. Numako, "Formation mechanism of $TiO_2$-derived titanate nanotubes prepared by the hydrothermal process," *Inorganic Chemistry*, vol. 49, no. 13, pp. 5845–5852, 2010.

[13] T. Kasuga, M. Hiramatsu, A. Hoson, T. Sekino, and K. Niihara, "Formation of titanium oxide nanotube," *Langmuir*, vol. 14, no. 12, pp. 3160–3163, 1998.

[14] Q. Chen, G. H. Du, S. Zhang, and L. M. Peng, "The structure of trititanate nanotubes," *Acta Crystallographica Section B*, vol. 58, no. 4, pp. 587–593, 2002.

[15] A. Nakahira, W. Kato, M. Tamai, T. Isshiki, K. Nishio, and H. Aritani, "Synthesis of nanotube from a layered $H_2Ti_4O_9 \cdot _7H_2O$ in a hydrothermal treatment using various titania sources," *Journal of Materials Science*, vol. 39, no. 13, pp. 4239–4245, 2004.

[16] M. Qamar, C. R. Yoon, H. J. Oh et al., "Effect of post treatments on the structure and thermal stability of titanate nanotubes," *Nanotechnology*, vol. 17, no. 24, pp. 5922–5929, 2006.

[17] M. Zhang, Z. S. Jin, J. J. Yung, and Z. Zhang, "Effect of annealing temperature on morphology, structure and photocatalytic behavior of nanotubed $H_2Ti_2O_4(OH)_2$," *Journal of Molecular Catalysis A*, vol. 217, pp. 203–210, 2004.

[18] Q. Chen, W. Z. Zhou, G. H. Du, and L. M. Peng, "Tritanate nanotubes made via a single alkali treatment," *Advanced Materials*, vol. 14, pp. 1208–1211, 2002.

[19] S. Zhang, L. M. Peng, Q. Chen, G. H. Du, G. Dawson, and W. Z. Zhou, "Formation Mechanism of $H_2Ti_3O_7$ Nanotubes," *Physical Review Letters*, vol. 91, Article ID 256103, 2003.

[20] L. Qian, Z. L. Du, S. Y. Yang, and Z. S. Yin, "Raman-study of titania nanotube by soft chemical-process," *Journal of Molecular Structure*, vol. 749, pp. 103–107, 2005.

[21] Y. Lan, X. P. Gao, H. Y. Zhu et al., "Titanate nanotubes and nanorods prepared from rutile powder," *Advanced Functional Materials*, vol. 15, no. 8, pp. 1310–1318, 2005.

[22] S. Ribbens, V. Meynen, G. V. Tendeloo et al., "Development of photocatalytic efficient Ti-based nanotubes and nanoribbons by conventional and microwave assisted synthesis strategies," *Microporous and Mesoporous Materials*, vol. 114, no. 1–3, pp. 401–409, 2008.

[23] O. V. Yakubovich and V. V. Kirrev, "Refinement of the crystal structure of $Na_2Ti_3O_7$," *Crystallography Reports*, vol. 48, pp. 24–28, 2003.

[24] A. L. Sauvet, S. Baliteau, C. Lopez, and P. Fabry, "Synthesis and characterization of sodium titanates $Na_2Ti_3O_7$ and $Na_2Ti_6O_{13}$," *Journal of Solid State Chemistry*, vol. 177, no. 12, pp. 4508–4515, 2004.

[25] M. Qamar, C. R. Yoon, H. J. Oh et al., "Preparation and photocatalytic activity of nanotubes obtained from titanium dioxide," *Catalysis Today*, vol. 131, no. 1–4, pp. 3–14, 2008.

[26] H. F. Yu, Z. W. Zhang, and F.C. Hu, "Phase stabilities and photocatalytic activities of P/ZN-$TiO_2$ nanoparticles able to operate under uv-vis light irradiation," *Journal of Alloys and Compounds*, vol. 465, pp. 484–490, 2008.

[27] Y. Chen, J. C. Crittenden, S. Hackney, L. Sutter, and D. W. Hand, "Preparation of a novel $TiO_2$-based p-n junction nanotube photocatalyst," *Environmental Science and Technology*, vol. 39, no. 5, pp. 1201–1208, 2005.

[28] G. K. Mor, O. K. Varghese, M. Paulose, K. Shankar, and C. A. Grimes, "A review on highly ordered, vertically oriented $TiO_2$ nanotube arrays: fabrication, material properties, and solar energy applications," *Solar Energy Materials and Solar Cells*, vol. 90, no. 14, pp. 2011–2075, 2006.

[29] H. C. Choi, Y. M. Jung, and S. B. Kim, "Size effects in the Raman spectra of $TiO_2$ nanoparticles," *Vibrational Spectroscopy*, vol. 37, no. 1, pp. 33–38, 2005.

[30] T. Ohsaka, F. Izumi, and Y. Fujiki, "Raman spectrum of anatase, $TiO_2$," *Journal of Raman Spectroscopy*, vol. 7, pp. 321–324, 1978.

[31] H. Berger, H. Tang, and F. Levy, "Growth and Raman spectroscopic characterization of $TiO_2$ anatase single crystals," *Journal of Crystal Growth*, vol. 130, pp. 108–112, 1993.

[32] Z. Tang, L. Zhou, L. Yang, and F. Wang, "A study on the structure transformation and luminescence of Eu(III) titanate nanotubes synthesized at various hydrothermal temperatures," *Journal of Alloys and Compounds*, vol. 481, no. 1-2, pp. 704–709, 2009.

[33] R. Ma, K. Fukuda, T. Sasaki, M. Osada, and Y. Bando, "Structural features of titanate nanotubes/nanobelts revealed by raman, X-ray absorption fine structure and electron diffraction characterizations," *Journal of Physical Chemistry B*, vol. 109, no. 13, pp. 6210–6214, 2005.

[34] C. K. Lee, C. C. Wang, M. D. Lyu, L. C. Juang, S. S. Liu, and S. H. Hung, "Effects of sodium content and calcination temperature on the morphology, structure and photocatalytic activity of nanotubular titanates," *Journal of Colloid and Interface Science*, vol. 316, no. 2, pp. 562–569, 2007.

[35] G. S. Kim, Y. S. Kim, H. K. Seo, and H. S. Shin, "Hydrothermal synthesis of titanate nanotubes followed by electrodeposition process," *Korean Journal of Chemical Engineering*, vol. 23, no. 6, pp. 1037–1045, 2006.

*Research Article*

# Ostwald Ripening of Platinum Nanoparticles Confined in a Carbon Nanotube/Silica-Templated Cylindrical Space

**Cintia Mateo-Mateo,[1] Carmen Vázquez-Vázquez,[1] Moisés Pérez-Lorenzo,[1] Verónica Salgueiriño,[2] and Miguel A. Correa-Duarte[1]**

[1] *Departamento de Química Física, Universidade de Vigo, 36310 Vigo, Spain*
[2] *Departamento de Física Aplicada, Universidade de Vigo, 36310 Vigo, Spain*

Correspondence should be addressed to
Verónica Salgueiriño, vsalgue@uvigo.es and Miguel A. Correa-Duarte, macorrea@uvigo.es

Sintering of nanoparticles mediated by an Ostwald ripening mechanism is generally assessed examining the final particle size distributions. Based on this methodology, a general approach for depositing platinum nanoparticles onto carbon nanotubes in solution has been employed in order to evaluate the sintering process of these metallic nanoparticles at increasing temperatures in a carbon nanotube/silica-templated confined space.

## 1. Introduction

Nanoparticles (NPs) are inherently unstable due to their high surface area and therefore tend to grow and increase their average size [1, 2]. Sintering refers to the increase in mean particle size that occurs as a system of NPs evolves to attain a lower-energy state [3]. The driving force in a process of sintering of NPs corresponds to their increased surface free energy, if compared with bulk, by which NPs present a metastable solid state and inevitably tend to aggregate into larger nanostructures [2].

Sintering is an acute drawback in catalysis, especially if working at elevated temperatures. In the case of supported catalysts, sintering is typically attributed to mass-transport mechanisms involving atomic migration to subsequent coalescence with neighboring NPs. The kinetic models proposed have been established considering an Ostwald ripening, by which the migration mechanism refers to diffusion of atoms between immobile NPs either on the surface of the support or through the gas phase [4]. In these conditions, the concentration of atomic species is higher in the vicinity of small particles than of large particles. There is, consequently, a concentration gradient that leads to a net flux of atomic species from the smaller particles toward the larger ones, so the larger particles eventually grow at the expense of the smaller ones. Accordingly, Yang et al. studied the sintering of Au NPs on $TiO_2$ and were able to explain the observed evolution of particle sizes using a ripening model [5], and Simonsen et al. confirmed that Ostwald ripening is responsible for the sintering of Pt under oxidative atmospheres [6]. Since Pt is known to form a volatile oxide, they claimed as plausible that this Pt oxide constitutes the mobile phase responsible for Pt sintering.

In the Ostwald ripening process, the atomic species are exchanged among immobile NPs driven by a difference in their chemical potential, as described by the Gibbs-Thomson equation. In addition to NP size, parameters such as morphology of the NPs and NP-support interactions will also play a role in the sintering process [2]. Additionally, given the increasing importance of reactions in restricted dimensions such as Pt catalyst-bearing nanoreactors (e.g., nanocapsules) [7], the influence of confined spaces on the Ostwald ripening should be carefully assessed given its critical influence on the catalytic efficiency of metallic nanoparticles.

Herein, we engineer the deposition of small Pt nanoparticles on one-dimensional CNT templates and their later encapsulation with an inorganic silica shell. Such a system was developed to study the sintering of Pt NPs in specific conditions given by elevated temperatures and the confined cylindrical nanospace given to the Pt NPs to grow. The direct observation of sintering in these extreme conditions is demonstrated in terms of an evolution of the average size distribution from Gaussian to log-normal.

## 2. Experimental Section

*2.1. Polymer-Wrapping Functionalization of CNTs [8].* CNTs (MWNTs from Nanolab, 5–15 $\mu$m length and 10–15 nm diameter, 95% purity) were redispersed in ultrapure water (18 M$\Omega$-cm) according to the following procedure. Briefly, CNTs were dispersed in a 1 wt.% aqueous solution of pollyallylamine hydrochloride (PAH, 0.5 M NaCl, pH = 10) up to a concentration of 150 mg/L. A combination of rapid stirring and sonication was used to ensure the presence of individually well-dispersed CNTs (this is demonstrated by the fact that CNTs appear individually coated with Pt NPs and subsequently with the outer silica shell (vide infra)). Excess of PAH was removed by three centrifugation cycles at 9000 rpm, at 25°C during 12 h to be later redispersed in aqueous solution.

*2.2. Synthesis of Platinum NPs [7].* Pt NPs were synthesized as follows: to a solution containing 43 mL of ultrapure water, 2.5 mL of sodium citrate (0.1 M) and 2.5 mL of 0.05 M $H_2PtCl_6$, and 2.45 mL of sodium borohydride (0.015 M) were added as reducing agent (citrate/$H_2PtCl_6$/NaBH$_4$ in a molar ratio of 2 : 1 : 0.3). The solution was stirred for 10 min.

*2.3. NPs Deposition onto CNTs [7].* CNTs@PAH (12 mL, 0.016 mg/mL) were added to 50 mL of Pt NPs (0.5 mM). After 1 h, the solution was centrifuged three times (3500 rpm, RT, 20 min) and redispersed in 20 mL of ultrapure water removing the nonadsorbed Pt NPs after centrifuging.

*2.4. Silica Coating of CNTs@Pt.* Silicon oxide was deposited on the CNTs@Pt nanocomposites using two different steps [9]. In the first silica-deposition step, the hydrolysis and condensation of 3-aminopropyltrimethoxysilane (APS) and tetraethoxysilane (TEOS) were carried out under acidic conditions. Ethanol (20 mL) containing APS and TEOS (typically 2.88 $\mu$L APS and 33.8 $\mu$L TEOS) was added dropwise to 10 mL of an aqueous dispersion of CNTs@Pt (0.03 mg/mL) containing citric acid (10 mM, pH∼3) under magnetic stirring. In the second step and after stirring for 2 h 30 min, the pH value of the solution was rapidly increased so that the silane condensation was carried out under basic conditions. Therefore, a solution of NH$_4$OH (0.01 M) was added dropwise until a pH value of 8–10 was reached. Subsequently, the solution was aged for 3 h and a compact, uniform, 15 nm thick silica shell was obtained. Subsequently, the solution was centrifuged (950 rpm, 10 min, RT) and redispersed three times in EtOH.

*2.5. Sintering of CNTs@Pt@SiO$_2$.* Thermogravimetric Analysis (TGA) of CNTs coated with Pt NPs and silica shell was carried out heating up to 830°C. The sintering process was studied heating up the composite nanostructures at two temperatures (550 and 800°C) in order to tune the NP agglomeration.

## 3. Results and Discussion

CNTs are some of the most intensively explored nanostructured materials. Their unique properties render these structures as ideal templates for the design of nanosized architectures [10]. In this case, their uniform curvature allows the deposition of Pt NPs to be further coated with silica, in an effort to isolate them in a cylindrical and therefore curved confined space. Accordingly, a general approach for depositing NPs onto CNTs in solution has been employed [8]. This approach, with an initial step based on the polymer wrapping technique, allows the manipulation of CNTs in solution. The polymer wrapping method, developed by O'Connell et al. [11], stems from a functionalization of CNTs through noncovalent attachment. This technique is based on the thermodynamic preference of CNT-polymer interactions over CNT-water interactions, which favors the hiding of the hydrophobic surface of CNTs in aqueous solution, giving rise to a better dispersion [12, 13]. In this way, CNTs can be wrapped either with a negatively or positively charged polyelectrolyte (PE) depending on the surface charge of the metallic nanoparticles to be deposited. The polymer layer allows a homogenous high-density coverage of charges on the tips and walls of CNTs and, as result, an efficient deposition of the metallic nanoparticles through electrostatic interactions. A further synthetic approach consists of the use of this initial polymer layer as a primer for adsorption of successive oppositely charged PE layers. Thus, an ordered polymer multilayer around the carbon nanotube is obtained. Through this method, better known as layer-by-layer assembly technique (LbL) [14], an easy and exact modulation of the polymer shell thickness can be attained by controlling the number of deposition steps. This technique has indeed been demonstrated to be very efficient not only for the coating of CNTs with different types of NPs [12] but also for tuning the distance in between [15].

In our case, Pt NPs were driven to the surface of the CNTs taking advantage of the PE (PAH) previously deposited on the surface of these supports. Because of the positively charged surface provided by this polymer, these NPs were easily attached becoming fixed in the final composite nanostructure. It must be noted that the Pt NPs employed were previously synthesized in aqueous solution, reducing $H_2PtCl_6$ salt with sodium borohydride and stabilizing them with citrate ions, which confers them a negatively charged surface. Figure 1 shows TEM images at different magnification of the CNTs coated with the Pt NPs, very homogeneously distributed all over the surface of the carbon nanostructures. It is also worthy to mention the pretty narrow size distribution of such small metallic nanoparticles, centered at 2.62 ± 0.60 nm (95% of NPs). Without a doubt,
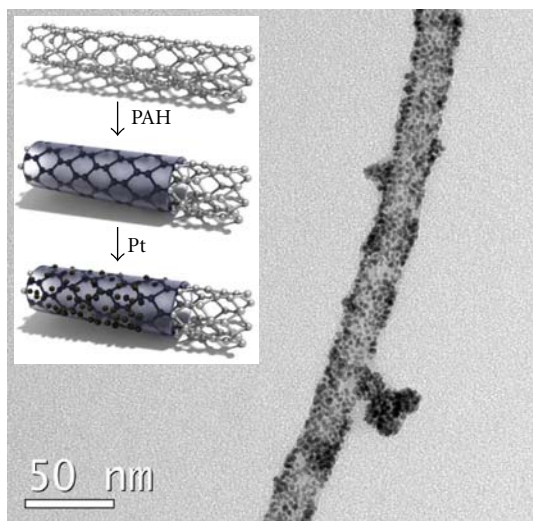
FIGURE 1: TEM image of a representative CNT coated with Pt nanoparticles homogeneously distributed on their surface (inset: scheme of the process employed to drive first the PAH and later the Pt NPs to the surface of CNTs).

it is also important to draw attention to the aggregates of Pt nanoparticles, assembled during the process and located or distributed all along every CNT. These aggregates of NPs were likely formed once the positively charged CNT solution was added, considering the fact that it may carry different ions necessary for the assembly of the PE layer and may consequently increase the ionic strength. These conditions can therefore explain some previous aggregation of the NPs, which, however, does not prevent their homogeneous deposition onto the CNTs.

As next step, these composite nanostructures were coated with silica. Figure 2 shows the TEM images at different magnification of the CNT@Pt@SiO$_2$ nanocomposites, offering a 15 nm thick silica shell. The high homogeneity of the coating allows the silica shell to maintain its thickness even around the aggregates of Pt NPs previously mentioned. The silica coating was carried out in two different deposition steps; considering first the hydrolysis and condensation of 3-aminopropyltrimethoxy-silane (APS) and tetraethoxysilane (TEOS), carried out under acidic conditions and consequently under basic conditions. Subsequently, the solution was aged for 10 h and a compact, uniform, 15 nm thick silica shell was obtained.

The as-prepared composite nanostructures based on CNTs and Pt NPs and coated with silica were heated up to 550 and 800°C in air atmosphere, in two independent experiments. In order to follow the carbonization processes of the composite nanostructures that take place under these conditions, a thermogravimetric analysis (TGA) was performed. Figure 3 includes the TGA as a function of temperature that indicates ~97.7 wt.% left in the sample tested, in this case after heating up to 830°C in air. The TGA analysis offers different steps in the carbonization that can be attributed to the citrate ions surrounding the Pt NPs, the PAH wrapping the CNTs, and the CNTs themselves, which
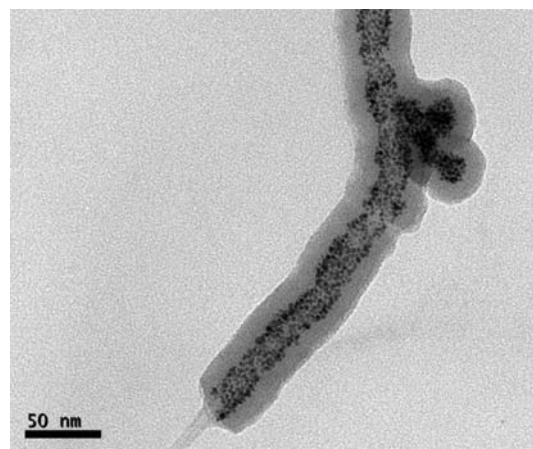


(a)
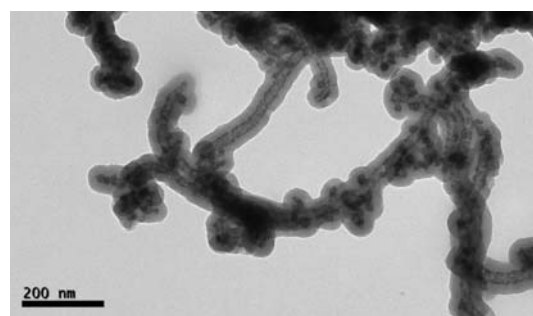


(b)

FIGURE 2: TEM images of CNTs coated with a 15 nm thick silica shell.
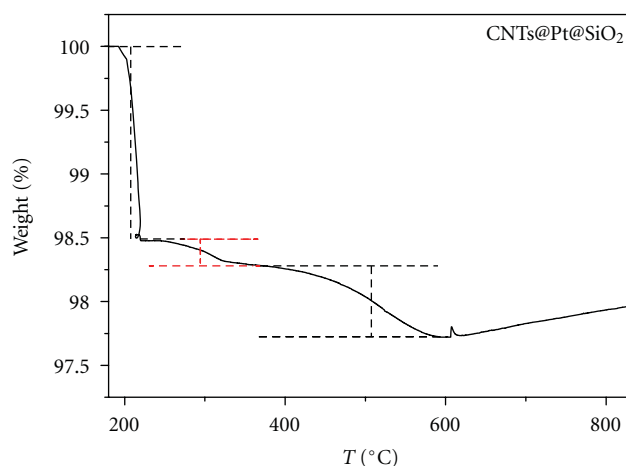


FIGURE 3: TGA analysis while heating the composite nanostructures up to 830°C.

in air, have been reported to completely decompose after the temperature reached 500°C [16], justifying therefore the wt.% losses. In order to understand this rather low weight-reduction, it should be taken into account the extraordinary lightness of CNTs and the branched nature of PAH (that renders possible the wrapping around the CNTs). Both the carbon support and the polyelectrolyte exhibit notably low

(a)



(b)



(c)



(d)
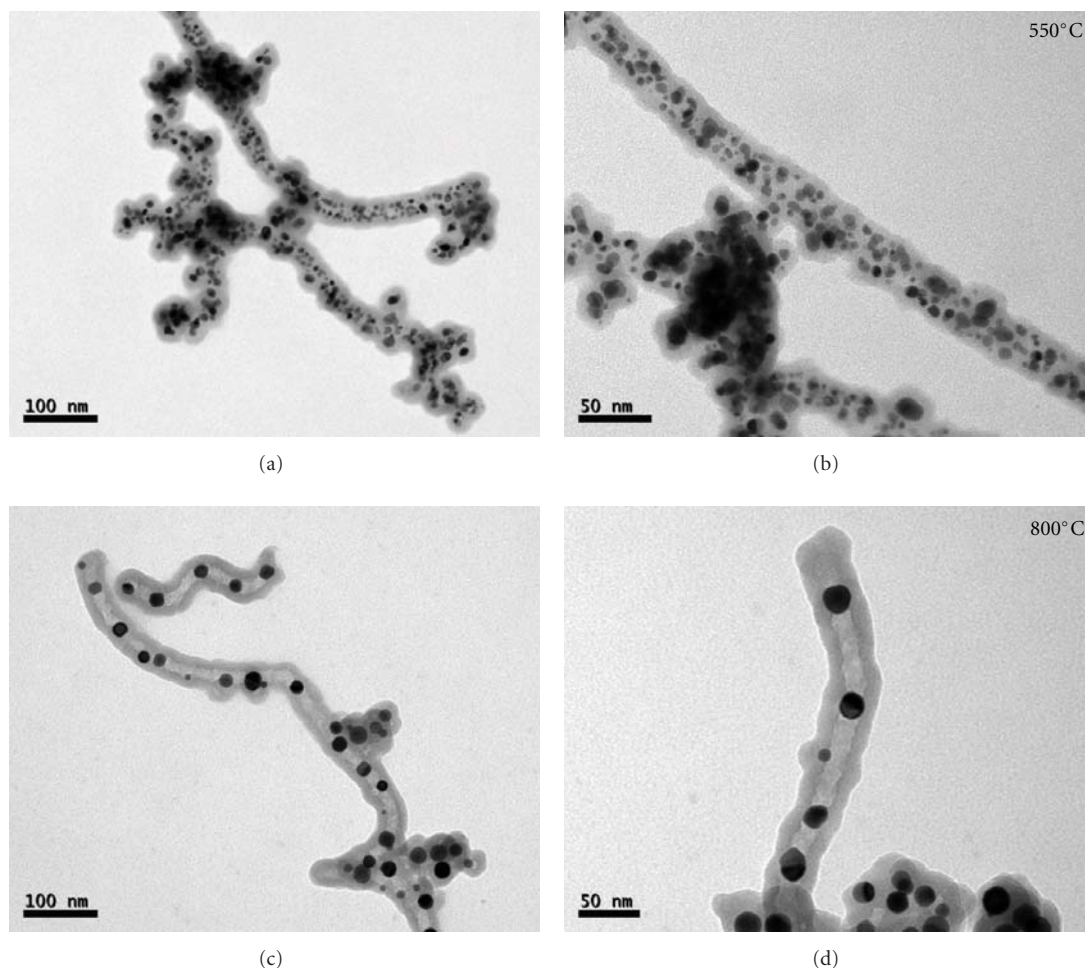
FIGURE 4: TEM images of the as-prepared composite nanostructures based on CNTs and Pt NPs and coated with silica, heated up to 550°C ((a) and (b)) and to 800°C ((c) and (d)).

densities, which results in the considerably low wt.% losses mentioned.

After heating up to 550 and 800°C in two independent experiments, TEM analysis of the two samples tested was also performed. Figures 4(a) and 4(b) include TEM images of the nanocomposites after heated up to 550°C, while Figures 4(c) and 4(d) show those heated up to 800°C, reflecting clear changes in the composite nanostructures morphology and in the size of the Pt NPs initially employed.

Clearly, the inner structure of the composites has changed, with a heterogeneous and broader distribution of bigger Pt NPs, not anymore supported onto the CNTs. At 550°C the carbonization processes of likely all the organic compounds has already taken place (according to the TGA included in Figure 3) and consequently, no organic frame maintains the NPs in the cylinder-like morphology as when surrounding the CNTs. In this regard, the temperature has started two processes: the carbonization of the organic material and the diffusion [17] of the Pt atoms that initially formed part of the 2.62 nm NPs. Considering the increased surface-to-volume ratio of such small Pt NPs, a nonequilibrium process is likely to start as temperature

increases, in such a way that the system tries to restore the equilibrium by forming bigger aggregates. Pt atoms initiate therefore a migration to meet again allowing the growth of the bigger NPs. In this sense, the previously formed aggregates of NPs may act as nuclei where to start a growth process. Nevertheless, at $T < 550°C$ the migration process may be slow enough (small migration distances), so that Pt atoms deposit shortly after starting their migration. This situation favors the formation of a broader size distribution ($8.58 \pm 2.45$ nm (95% of NPs)) of bigger particles, as shown in Figures 4(a) and 4(b). Hence, we can consider the simultaneous dissolution and reaggregation of the NPs, known as Ostwald ripening or coarsening [18]. Since the 2.62 nm particles are no more stabilized by the citrate ions, already carbonized due to the important increase in temperature and reflected by the TGA analysis (Figure 3), larger nanoparticles are formed at the expense of dissolving smaller ones [19]. These considerations agree with a slow growth rate, which also yields broad size distributions [20].

Figures 4(c) and 4(d) show TEM images of the composites after heated up to 800°C. The interior of the now formed silica cylinders appears completely clean (compared,

(a)



(b)



(c)
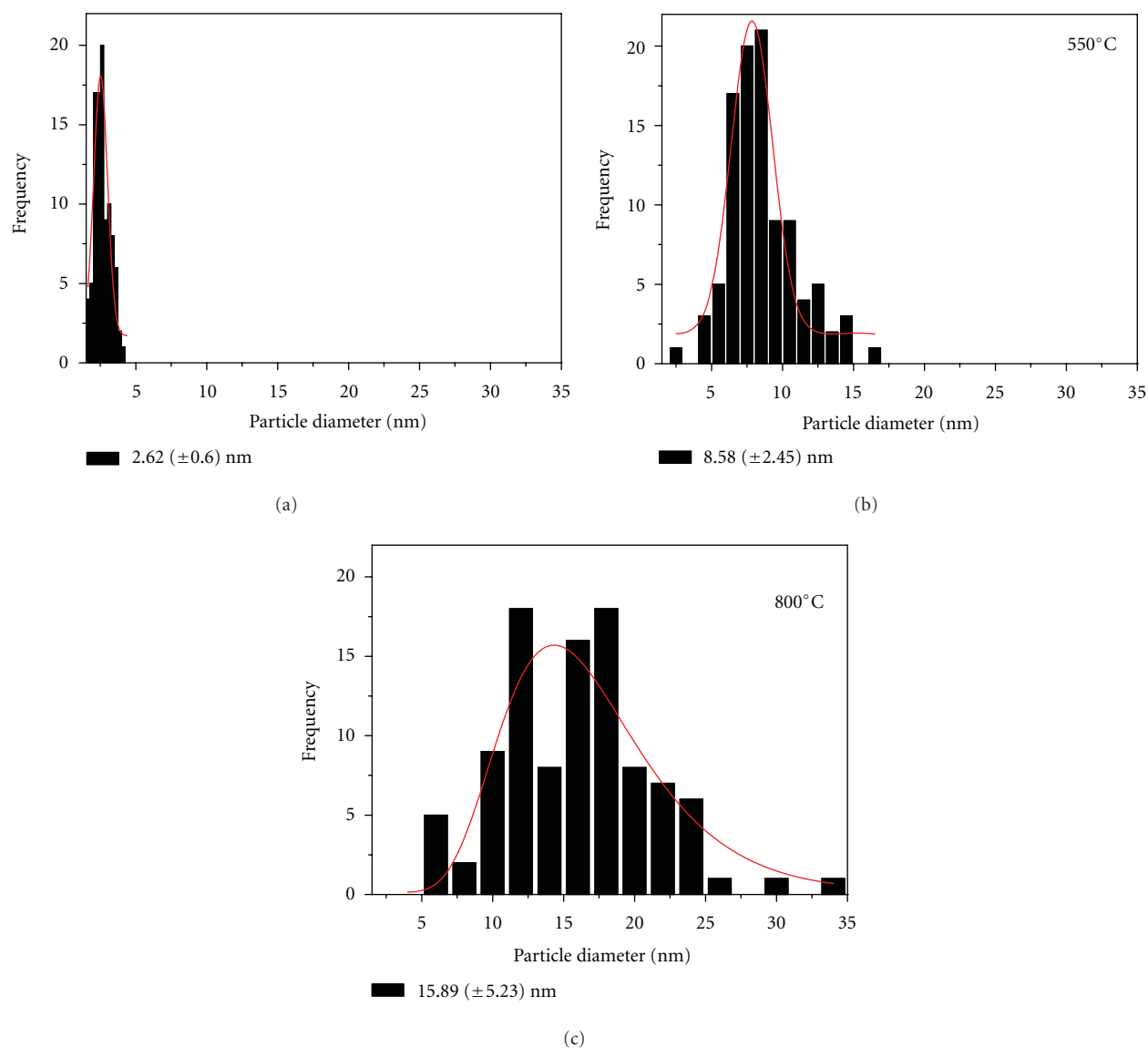
FIGURE 5: Average size distributions of the Pt NPs based on TEM images of the samples heated up to 550 and 800°C.

for example, with the turbid nature of the material appearing in Figures 4(a) and 4(b)), without any organic remains (from the CNTs, citrate ions and PEs) that likely have sublimed. Simultaneously, the silica has compacted leaving an empty inner space in the composite nanostructures. The Pt NPs have now grown until reaching an average size distribution of 15.89 ± 5.23 nm (95% of NPs).

According to the migration of atoms proposed with an outcome determined by the diffusion and the deposition flux, this process would then end when atoms have hit NPs of size larger than the critical, that is, stable, in order to condense on them. With increasing sizes, the NPs become more and more stable and impinging atoms condense solely at the bigger ones. In the present case, temperature triggers the migration of the atoms. At low temperatures, migration average distances are small, so that a high density of stable bigger NPs can grow. With increasing temperature, the migration distance also increases and larger and far

apart nanoparticles can grow, as shown in the TEM images of Figures 4(c) and 4(d). The TEM images also reveal the increase in the mean particle size due to disappearance of the smaller ones.

The evolution in the particle size distribution reflected by the TEM images is related to the sintering process, described statistically in the light of a simple kinetic model for ripening. Indeed, the heat treatment resulted in a general increase in size and an improvement in the spherical shape, consistent with surface energy minimization. Figure 5 includes the size distribution of the Pt NPs: initially (a), after heating the composites up to 550°C (b) and up to 800°C (c). The initial Gaussian shape of the average size distribution, that also works for the NPs after heating up to 550°C (though broader), varies in the third case (after heating up to 800°C) to a log-normal fit, as a tail of larger NPs emerges on the right side of the mean value, consequently broadening the average size distribution.

TEM images and resulting average size distributions, indicating that smaller NPs have eventually disappeared and larger ones have been obtained, are consistent with a sintering process of Pt NPs governed by an Ostwald ripening mechanism. The corresponding mass-transport can be justified if mediated by Pt atoms, or more likely by Pt-oxygen species (the sintering rate of Pt NPs in oxidative environments was reported to be accelerated due to the formation of volatile Pt-oxygen species)[21]. Besides the oxygen-rich environment, we have to take into account the increased temperatures reached and the fact that Pt NPs are neither free nor supported on planar substrates but confined in the cylindrical empty spaces given once the carbonization of CNTs and the compaction of silica are accomplished. Consequently, a local effect favoring the exchange rate of diffusing species between NPs is very much favored.

## 4. Conclusions

Transmission electron microscopy has been employed in order to monitor the evolution of Pt NPs deposited onto the surface of carbon nanotubes while heating independently up to 550 and 800°C. These experiments reveal unequivocally a favored Ostwald-ripening-operated sintering process taking place in the CNT/silica-templated confined space formed as temperature is raised.

## Acknowledgments

## References

[1] R. T. K. Baker, C. H. Bartholomew, and D. B. Dadyburjor, *Sintering and Redispersion: Mechanisms and Kinetics. Stability of Supported Catalysts: Sintering and Redispersion*, Edited by J. A. Horsley, Catalytica, Mountain View, Calif, USA, 1991.

[2] S. B. Simonsen, I. Chorkendorff, S. Dahl et al., "Effect of particle morphology on the ripening of supported Pt nanoparticles," *Journal of Physical Chemistry C*, vol. 116, no. 9, pp. 5646–5653, 2012.

[3] S. R. Challa, A. T. Delariva, T. W. Hansen et al., "Relating rates of catalyst sintering to the disappearance of individual nanoparticles during Ostwald ripening," *Journal of the American Chemical Society*, vol. 133, no. 51, pp. 20672–20675, 2011.

[4] P. Wynblatt and N. A. Gjostein, "Supported metal crystallites," *Progress in Solid State Chemistry*, vol. 9, pp. 21–58, 1975.

[5] F. Yang, M. S. Chen, and D. W. Goodman, "Sintering of Au particles supported on TiO₂(110) during CO oxidation," *Journal of Physical Chemistry C*, vol. 113, no. 1, pp. 254–260, 2009.

[6] S. B. Simonsen, I. Chorkendorff, S. Dahl, M. Skoglundh, J. Sehested, and S. Helveg, "Direct observations of oxygen-induced platinum nanoparticle ripening studied by in situ

TEM," *Journal of the American Chemical Society*, vol. 132, no. 23, pp. 7968–7975, 2010.

[7] M. Sanlés, M. Pérez-Lorenzo, B. Rodríguez-González, V. Salgueiriño, and M. A. Correa-Duarte, "Highly active nanoreactors: nanomaterial encapsulation based on confined catalysis," *Angewandte Chemie International Edition*, vol. 51, pp. 3877–3882, 2012.

[8] M. de Dios, V. Salgueirino, M. Pérez-Lorenzo, and M. A. Correa-Duarte, "Synthesis of carbon nanotube-inorganic hybrid nanocomposites: an instructional experiment in nanomaterials chemistry," "*Journal of Chemical Education*, vol. 89, pp. 280–283, 2012.

[9] M. Grzelczak, M. A. Correa-Duarte, and L. M. Liz-Marzán, "Carbon nanotubes encapsulated in wormlike hollow silica shells," *Small*, vol. 2, no. 10, pp. 1174–1177, 2006.

[10] A. A. Dameron, S. Pylypenko, J. B. Bult et al., "Aligned carbon nanotube array functionalization for enhanced atomic layer deposition of platinum electro-catalysts," *Applied Surface Science*, vol. 258, no. 13, pp. 5212–5221, 2012.

[11] M. J. O'Connell, P. Boul, L. M. Ericson et al., "Reversible water-solubilization of single-walled carbon nanotubes by polymer wrapping," *Chemical Physics Letters*, vol. 342, no. 3-4, pp. 265–271, 2001.

[12] M. A. Correa-Duarte and L. M. Liz-Marzán, "Carbon nanotubes as templates for one-dimensional nanoparticle assemblies," *Journal of Materials Chemistry*, vol. 16, no. 1, pp. 22–25, 2006.

[13] S. Kawasaki, G. Catalan, H. J. Fan et al., "Conformal oxide coating of carbon nanotubes," *Applied Physics Letters*, vol. 92, no. 5, Article ID 053109, 2008.

[14] M. A. Correa-Duarte, N. Sobal, L. M. Liz-Marzán, and M. Giersig, "Linear assemblies of silica-coated gold nanoparticles using carbon nanotubes as templates," *Advanced Materials*, vol. 16, no. 23-24, pp. 2179–2184, 2004.

[15] F. Rivadulla, C. Mateo-Mateo, and M. A. Correa-Duarte, "Layer-by-layer polymer coating of carbon nanotubes: tuning of electrical conductivity in random networks," *Journal of the American Chemical Society*, vol. 132, no. 11, pp. 3751–3755, 2010.

[16] R. B. Mathur, S. Seth, C. Lal et al., "Co-synthesis, purification and characterization of single- and multi-walled carbon nanotubes using the electric arc method," *Carbon*, vol. 45, no. 1, pp. 132–140, 2007.

[17] H. Rôder, E. Hahn, H. Brune, J. P. Bucher, and K. Kern, "Building one- and two-dimensional nanostructures by diffusion-controlled aggregation at surfaces," *Nature*, vol. 366, no. 6451, pp. 141–143, 1993.

[18] M. Bowker, "Surface science: the going rate for catalysts," *Nature Materials*, vol. 1, no. 4, pp. 205–206, 2002.

[19] F. Huang, H. Zhang, and J. F. Banfieldt, "Two-stage crystal-growth kinetics observed during hydrothermal coarsening of nanocrystalline ZnS," *Nano Letters*, vol. 3, no. 3, pp. 373–378, 2003.

[20] Y. Yin and A. P. Alivisatos, "Colloidal nanocrystal synthesis and the organic-inorganic interface," *Nature*, vol. 437, no. 7059, pp. 664–670, 2005.

[21] P. Loof, B. Stenbom, H. Norden, and B. Kasemo, "Rapid sintering in NO of nanometer-sized Pt particles on $\gamma$-Al₂O₃ observed by CO temperature-programmed desorption and transmission electron microscopy," *Journal of Catalysis*, vol. 144, no. 1, pp. 60–76, 1993.

*Research Article*

# Effect of Si and SiO$_2$ Substrates on the Geometries of As-Grown Carbon Coils

## Semi Park,[1] Sung-Hoon Kim,[1] and Tae-Gyu Kim[2]

[1] *Department of Engineering in Energy and Applied Chemistry, Silla University, Busan 617-736, Republic of Korea*
[2] *Department of Nanomechatronics Engineering, Pusan National University, Kyungnam 627-706, Republic of Korea*

Correspondence should be addressed to Sung-Hoon Kim, shkim@silla.ac.kr

Carbon coils could be synthesized using C$_2$H$_2$/H$_2$ as source gases and SF$_6$ as an incorporated additive gas under thermal chemical vapor deposition system. Si substrate, SiO$_2$ thin film deposited Si substrate (SiO$_2$ substrate), and quartz substrate were employed to elucidate the effect of substrate on the formation of carbon coils. The characteristics (formation densities, morphologies, and geometries) of the deposited carbon coils on the substrate were investigated. In case of Si substrate, the microsized carbon coils were dominant on the substrate surface. While, in case of SiO$_2$ substrate, the nanosized carbon coils were prevailing on the substrate surface. The surface morphologies of samples were investigated step by step during the reaction process. The cause for the different geometry formation of carbon coils according to the different substrates was discussed in association with the different thermal expansion coefficient values of Si and SiO$_2$ substrates and the different etched characteristics of Si and SiO$_2$ substrates by SF$_6$ + H$_2$ flow.

## 1. Introduction

Recently, carbon nano/microcoils were noticed for the promising materials to be used in electromagnetic absorbers, high sensitive nano/microsized detectors, effective reinforcing fillers for composites, essential building blocks for the fabrication of nanodevices, and so forth [1–5]. For the synthesis of carbon coils, chemical vapor deposition (CVD) method using metal catalyst is regarded as an effective technology due to its applicable feature. Up to the present, significant parameters in catalytic CVD system for the formation of carbon coils, such as the diverse combination of source gases and the various characteristics (shapes and compositions) for the used catalyst, have been deeply investigated [6–9].

Among the parameters, the characteristics of the used metal catalyst was known to be a decisive factor to determine the final growth geometry of as-grown carbon coils [10–16]. Supporting substrates seemed to be one of the significant parameters for the formation of carbon coils because the characteristics of the metal catalyst would be affected by the nature of supporting substrate. Consequently, the substrate-influenced metal catalyst could affect the geometry of the as-grown carbon coils.

In this respect, the research for the substrate effect on the characteristics of as-grown carbon coils is considered as a primary step for the carbon coils synthesis reaction. Bai obtained a more or less controlled morphology of carbon coils through the careful choice of alumina substrate pore size [17]. Huang et al. reported that the changed morphologies of Si substrate by corrosion would play an important role in the formation of carbon nanocoils [18]. Veziri et al. demonstrated that the morphology of carbon nanostructures grown by CVD on porous supports is strongly affected by the porosity and chemical composition of the supporting substrate [19]. They suggested that tuning of carbon morphology cannot only take place by changing the CVD conditions (carbon precursor, reaction temperature and time, gas flow rates, etc.) but also by appropriately modifying the supporting substrate, the catalyst, and the interaction between them. Despite these efforts, further investigation for the effect of the substrate on the formation of carbon coils is still required.
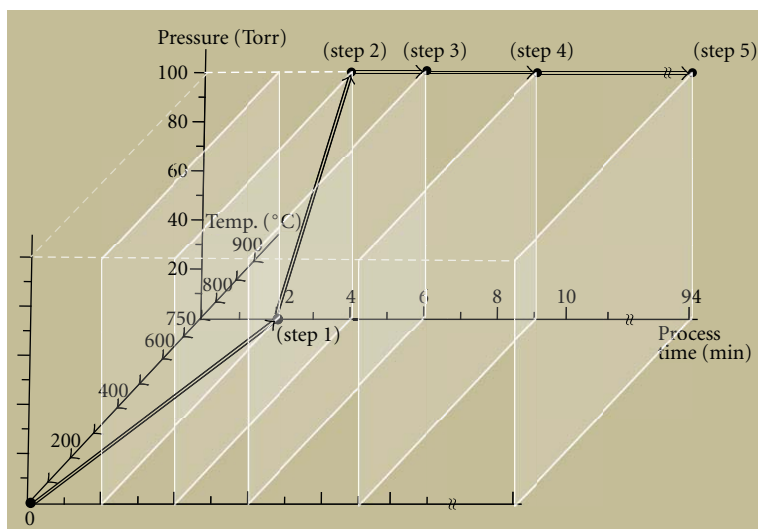
Figure 1: Step by step situations for the processes during the overall reaction.

In this work, different substrates, namely, Si substrate, SiO$_2$ thin film deposited Si substrate (SiO$_2$ substrate), and quartz substrate were employed to elucidate the effect of substrate on the formation of carbon coils. During the reaction process, the reaction was terminated step by step and the morphologies of as-grown sample surfaces were investigated according to the terminated step. Specifically silicon and its oxide substrates were chosen with keeping experimental conditions unchanged. Based on these results, the cause for this different geometry formation of carbon coils according to the different substrates was discussed.

## 2. Experimental Details

For silicon substrate, p-type Si (100) substrates were used. For its oxide substrate, SiO$_2$ layered Si substrates and quartz substrates were employed. SiO$_2$ layered Si substrates in this work were prepared by the thermal oxidation of $2.0 \times 2.0$ cm$^2$ p-type Si (100) substrates. The thickness of silicon oxide (SiO$_2$) layer on Si substrate was estimated about 300 nm.

A 0.1 mg Ni powder (99.7%) was evaporated for 1 min to form Ni catalyst layer on the substrate using thermal evaporator. The estimated Ni catalyst layer on the substrate was about 100 nm.

For carbon coils deposition, thermal CVD system was employed. C$_2$H$_2$ and H$_2$ were used as source gases. SF$_6$, as an incorporated additive gas, was injected into the reactor during the initial reaction stage. The flow rate for C$_2$H$_2$, H$_2$, and SF$_6$ was fixed at 15, 35, and 35 standard cm$^3$ per minute (sccm), respectively. According to the different reaction processes, the reaction processes were terminated by five steps. Figure 1 shows the step by step situations for the reaction processes during the overall reaction. The reaction conditions according to different processes were shown in Table 1. Detailed morphologies of carbon-coil-deposited substrates were investigated using field emission scanning electron microscopy (FESEM, Hitach 4500).

## 3. Results and Discussion

Ten samples (samples A–J) having the different substrates (Si and SiO$_2$ substrates) and the different reaction process steps (see Figure 1) were prepared. FESEM images showing the surface morphologies of the samples were measured after finishing the different reaction process steps. Indeed, the different substrates (Si and SiO$_2$ substrates) were simultaneously mounted into the reaction chamber. So, the carbon coils formation reaction on the different substrates could have a constant experimental condition.

After step (1), namely, finishing the substrate temperature set to 750°C, the Ni catalyst layer was converted to a lot of nanosized Ni grains and these grains were uniformly dispersed on the substrate as shown in Figure 2. The shapes and the densities of these grains for Si and SiO$_2$ substrates were almost similar (compare Figures 2(a) with 2(b)). Diameters of these grains were around a few hundred nanometers.

After step (2), namely, finishing the total pressure set to 100 Torr, both the nanosized (less than 100 nm in diameter) carbon nanofilaments (CNFs) and a few number of the microsized (more than 300 nm in diameter) CNFs were sparsely observed on Si substrate surface (sample C) as shown in Figures 3(a) and 3(b). The microsized CNFs were more frequently observed at the edge area of the substrate (see the inside of the oval in Figure 3(b)). The nanosized CNFs were usually gathered around the tip area of the microsized CNFs as shown in Figures 3(c) and 3(d). For SiO$_2$ substrate, the developed CNFs seemed to be more uniformly dispersed, compared with those of Si substrate (compare Figures 3(e) with 3(a)). Instead of the microsized CNFs, the nanosized CNFs were mostly observed as shown in Figure 3(f). In some position on the substrate the microsized CNFs could be observed as shown in Figure 3(g). Indeed, most of the microsized CNFs were observed as a form of linear-type sticking two similar-shaped carbon nanofilaments as shown in the inside of oval area in Figure 3(h).

TABLE 1: Experimental conditions of the deposition of carbon coils for the different samples.

| Process steps | Samples | C$_2$H$_2$ flow rate (sccm) | H$_2$ flow rate (sccm) | SF$_6$ flow rate (sccm) | Total pressure (Torr) | Total deposition time (min) | Source gases flow time (min) | | | Substrate kinds and temp. (°C) |
|---|---|---|---|---|---|---|---|---|---|---|
| | | | | | | | C$_2$H$_2$ | H$_2$ | SF$_6$ | |
| (1) | A | — | — | — | — | — | — | — | — | Si, 25 ~ 750 |
| (1) | B | — | — | — | 0 ~ 100 | — | — | — | — | SiO$_2$, 25 ~ 750 |
| (2) | C | 15 | 35 | 35 | 0 ~ 100 | — | — | — | — | Si, 750 |
| (2) | D | 15 | 35 | 35 | 0 ~ 100 | — | — | — | — | SiO$_2$, 750 |
| (3) | E | 15 | 35 | 35 | 100 | 2 | 2 | 2 | 2 | Si, 750 |
| (3) | F | 15 | 35 | 35 | 100 | 2 | 2 | 2 | 2 | SiO$_2$, 750 |
| (4) | G | 15 | 35 | 35 | 100 | 5 | 5 | 5 | 5 | Si, 750 |
| (4) | H | 15 | 35 | 35 | 100 | 5 | 5 | 5 | 5 | SiO$_2$, 750 |
| (5) | I | 15 | 35 | 35 | 100 | 90 | 90 | 90 | 5 | Si, 750 |
| (5) | J | 15 | 35 | 35 | 100 | 90 | 90 | 90 | 5 | SiO$_2$, 750 |

(a)

(b)
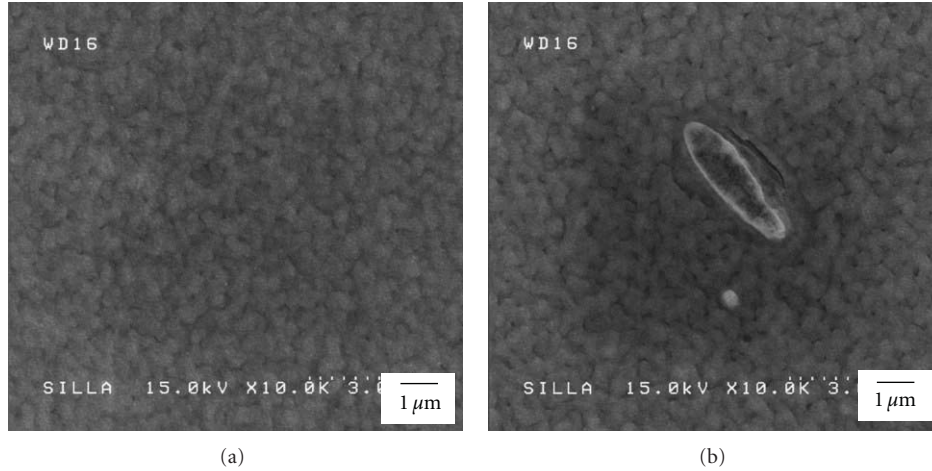
FIGURE 2: FESEM images for (a) sample A and (b) sample B after process step (1).



(a)

(b)

(c)

(d)

(e)

(f)

(g)

(h)
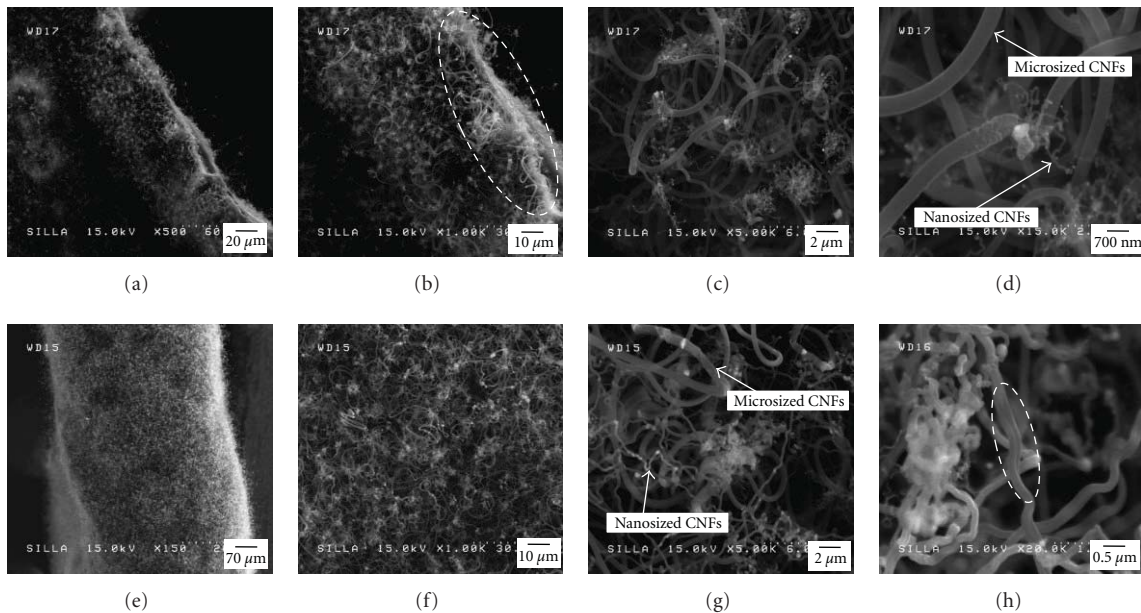
FIGURE 3: FESEM images for sample C under the magnification of (a) 500, (b) 1,000, (c) 5,000, and (d) 15,000 and for sample D under the magnification of (e) 150, (f) 1,000, (g) 5,000, and (h) 20,000.

Step (3): after 2.0 minutes reaction, the length of CNFs on the Si substrate seems to be much longer than those on $SiO_2$ substrate (compare Figures 4(b) with 4(f)). As shown in Figures 4(d) and 4(h), two individual CNFs seemed to independently come out from Ni grains (see white dots in the circle of Figures 4(d) and 4(h)) and then grow to the opposite direction with each other, irrespectively of the substrate.

After 5.0 minutes deposition reaction, in case of Si substrate, the initiation of carbon coils geometry formation could be observed on sample G as shown in Figures 5(a)–5(c). In this case not only the microsized carbon coils but also the nanosized carbon coils could be observed on the substrate. Around the tip area of the microsized carbon coils, the nanosized CNFs were mainly gathered (see Figure 5(c)). In $SiO_2$ substrate case, however, the nanosized carbon coils

were mostly formed on the surface of the substrate as shown in Figures 5(d)–5(f). The formation of the microsized carbon coils is rare, and they are usually buried among a lot of the nanosized carbon coils as shown in Figure 5(f). Indeed, the initial reaction stage with $SF_6$ would be responsible for the geometries of as-grown carbon coils. After initial reaction, the proceeded reaction times, such as 10, 30, and 60, did not seem to give any distinctive variation for the geometries of carbon coils [6]. So we investigated the morphologies of the samples after finishing the deposition reaction.

After finishing the deposition reaction (90 min), in case of Si substrate the well-developed microsized carbon coils were mostly observed on the surface of the substrate as shown in Figure 6(a). The length of the microsized carbon coils is more than ten micrometers (see Figure 6(b)). The
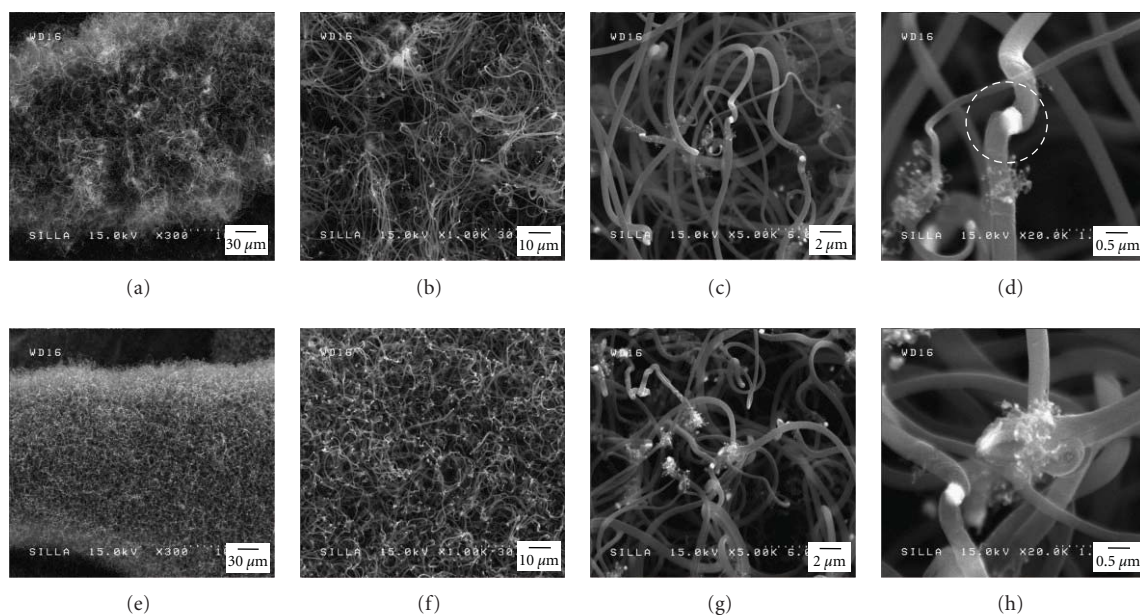
Figure 4: FESEM images for sample E under the magnification of (a) 300, (b) 1,000, (c) 5,000, and (d) 20,000 and for sample F under the magnification of (e) 300, (f) 1,000, (g) 5,000, and (h) 20,000.
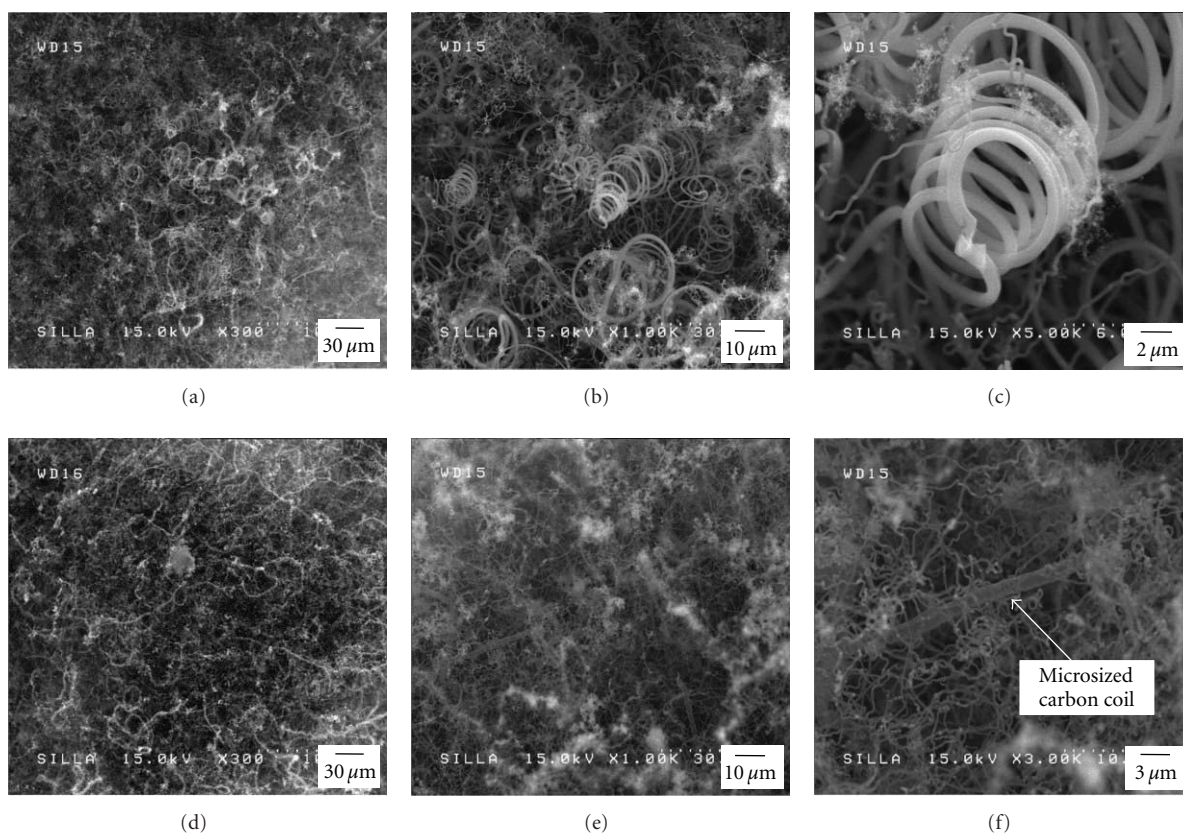


Figure 5: FESEM images for sample G under the magnification of (a) 300, (b) 1,000, and (c) 5,000 and for sample H under the magnification of (d) 300, (e) 1,000, and (f) 3,000.

(a)



(b)



(c)



(d)



(e)



Nanosized
carbon coil

(f)
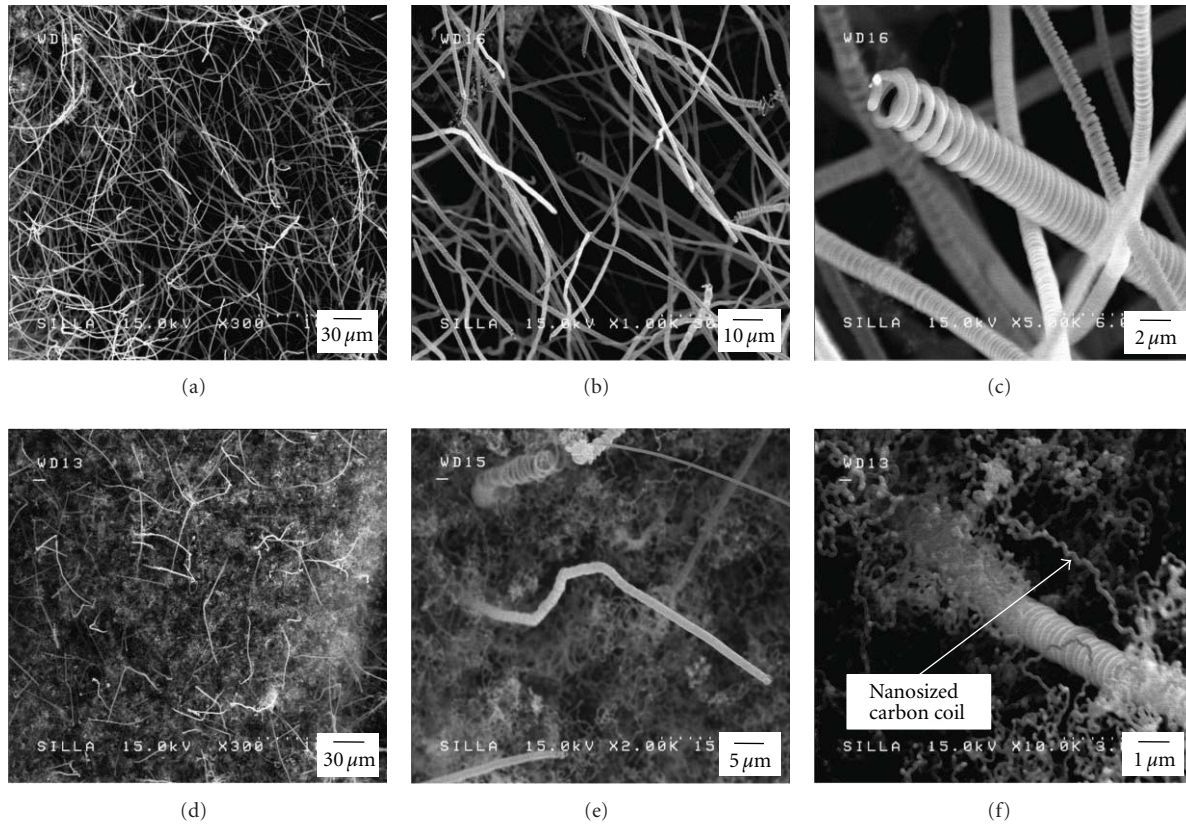
FIGURE 6: FESEM images for sample I under the magnification of (a) 300, (b) 1,000, and (c) 5,000 and for sample J under the magnification of (d) 300, (e) 2,000, and (f) 10,000.

diameters of the microsized carbon coils are in the range of a few tens nanometers to a few micrometers as shown in Figure 6(c). In case of $SiO_2$ substrate, however, the nanosized carbon coils were dominant on the surface of the substrate as shown in Figure 6(d). Occasionally, the microsized carbon coils were protruded among a lot of the nanosized carbon coils (see Figure 6(e)). As shown in Figure 6(f), several nanosized carbon coils were attached along the side of the microsized carbon coils.

The combined results of Figures 2–6 confirm that Si substrate favors the microsized type for the main geometry of as-grown carbon coils. In $SiO_2$ substrate case, however, the nanosized carbon coils were mostly developed on the substrate surface even under the same experimental condition. It may indicate the occurrence for the geometry change of carbon coils from the microsized type to the nanosized one simply by using the oxygen incorporated Si substrate. This result was also confirmed by the dominant formation of the microsized carbon coils on quartz substrate under the same experimental condition as shown in Figure 7.

The different thermal expansion coefficient between the Ni catalyst layer and the different substrates was proposed as the main cause for the geometry change of carbon coils according to the different substrates (Si or $SiO_2$). The difference of thermal expansion coefficient value between Ni catalyst layer and the different substrates was known to be higher in case of $SiO_2$ substrate compared with that

in case of Si substrate [20, 21]. The higher difference of thermal expansion coefficient between the metal layer and the substrate may induce the higher stress between them. Consequently, the metal layer will be more easily peeled off and eventually will be broken into very tiny nanosized pieces and scattered in surrounding area. Basically, the mechanism of carbon coils growth was based on the metal size and shape [10, 22]. So, the peeled-off tiny nanosized Ni pieces could be the seed of the nanosized carbon coils. Consequently, the as-grown nanosized carbon coils from the nanosized Ni pieces would deposit on the whole surface of the substrate. This is the reason why the density of the nanosized carbon coils from $SiO_2$ substrate is higher than that from Si substrate. Figure 8 shows FESEM images indicating the different situation of the peeled-off Ni layers from Si substrate (Figure 8(a)) and from $SiO_2$ substrate (Figure 8(b)) after cooling down the substrate from 750°C under vacuum. As shown in these images, $SiO_2$ substrate gives rise to the more readily peeled-off Ni layer, which may form the nanosized geometry for as-grown carbon coils.

In addition, the different etched characteristics of Si or $SiO_2$ substrate by $SF_6 + H_2$ flow was believed to be another cause for the geometry change of carbon coils according to the different substrates (Si or $SiO_2$). Figure 9 shows FESEM images indicating the different etched situation for Si substrate (Figure 9(a)) and $SiO_2$ substrate (Figure 9(b)) by $SF_6 + H_2$ flow for 1 minute under the condition of 100

(a)   (b)   (c)
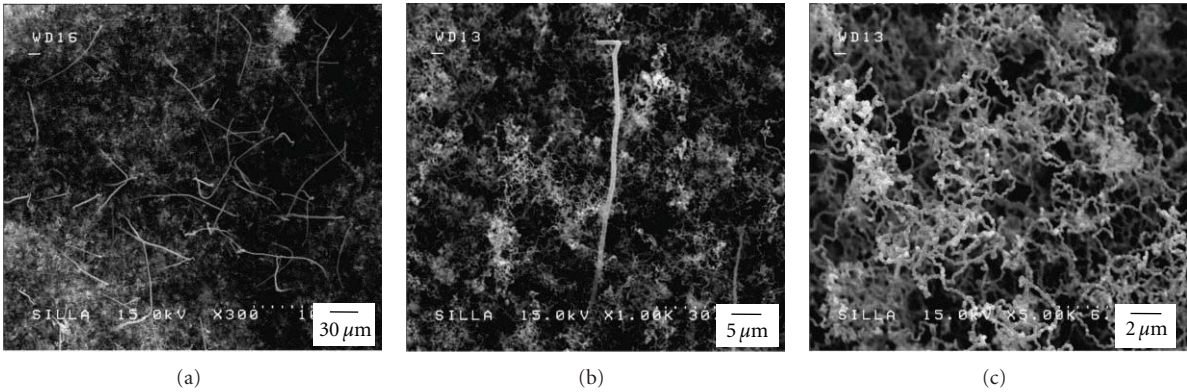
FIGURE 7: FESEM images for as-grown carbon coils on quartz substrate under the magnification of (a) 300, (b) 1,000, and (c) 5,000.



(a)   (b)
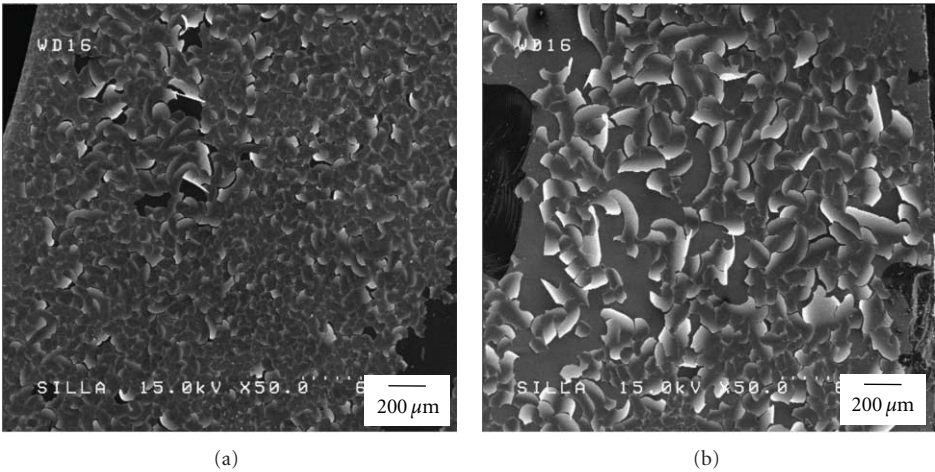
FIGURE 8: FESEM images for the peeled-Ni layers from (a) Si substrate and (b) SiO$_2$ substrate after cooling down the substrate from 750°C under vacuum.



(a)   (b)
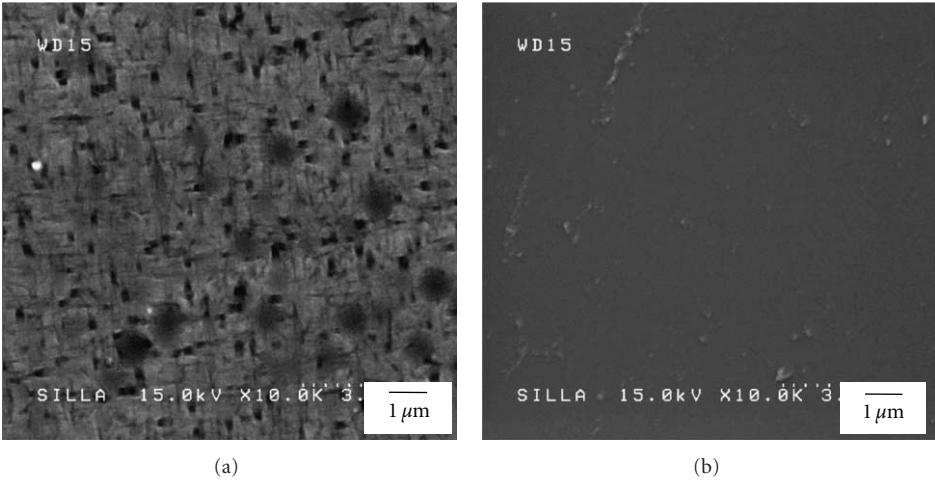
FIGURE 9: FESEM images for the etched surface of (a) Si substrate and (b) SiO$_2$ substrate by SF$_6$ + H$_2$ flow.

Torr and room temperature. As shown in these images, Si substrate would be more effectively etched by $SF_6$ flow, and the porous morphology would be formed on Si substrate. The porosity of the substrate was known to foster the coils geometry [19]. Previously, the microsized carbon coils were known to be come out by the joining of several nanosized coils [23]. Therefore, the well developing atmosphere of carbon coils by the porous morphology of Si substrate may eventually lead to the microsized geometry for as-grown carbon coils.

## 4. Conclusions

By exchanging the substrate from Si to $SiO_2$, the geometry of carbon coils was changed from the microsized type to the nanosized one even under the same experimental condition. The difference of thermal expansion coefficient values between Ni catalyst layer and the substrates was believed to be a main cause for this geometry change. In addition, the different etched characteristics for Si and $SiO_2$ substrates by $SF_6 + H_2$ flow during the reaction was suggested as another cause for the geometry change of as-grown carbon coils.

## References

[1] L. Pan, T. Hayashida, M. Zhang, and Y. Nakayama, "Field emission properties of carbon tubule nanocoils," *Japanese Journal of Applied Physics B*, vol. 40, no. 3, pp. L235–L237, 2001.

[2] S. Amelinckx, X. B. Zhang, D. Bernaerts, X. F. Zhang, V. Ivanov, and J. B. Nagy, "A formation mechanism for catalytically grown helix-shaped graphite nanotubes," *Science*, vol. 265, no. 5172, pp. 635–637, 1994.

[3] S. Hokushin, L. Pan, Y. Konishi, H. Tanaka, and Y. Nakayama, "Field emission properties and structural changes of a stand-alone carbon nanocoil," *Japanese Journal of Applied Physics*, vol. 46, no. 20–24, pp. L565–L567, 2007.

[4] K. Hernadi, L. Thiên-Nga, and L. Forró, "Growth and microstructure of catalytically produced coiled carbon nanotubes," *Journal of Physical Chemistry B*, vol. 105, no. 50, pp. 12464–12468, 2001.

[5] X. Chen, S. Yang, and S. Motojima, "Morphology and growth models of circular and flat carbon coils obtained by the catalytic pyrolysis of acetylene," *Materials Letters*, vol. 57, no. 1, pp. 48–54, 2002.

[6] X. Chen and S. Motojima, "Growth patterns and morphologies of carbon micro-coils produced by chemical vapor deposition," *Carbon*, vol. 37, no. 11, pp. 1817–1823, 1999.

[7] N. Okazaki, S. Hosokawa, T. Goto, and Y. Nakayama, "Synthesis of carbon tubule nanocoils using Fe-In-Sn-O fine particles as catalysts," *Journal of Physical Chemistry B*, vol. 109, no. 37, pp. 17366–17371, 2005.

[8] N. M. Rodriguez, M. S. Kim, F. Fortin, I. Mochida, and R. T. K. Baker, "Carbon deposition on iron-nickel alloy particles," *Applied Catalysis A*, vol. 148, no. 2, pp. 265–282, 1997.

[9] J. H. Eum, S. H. Kim, S. S. Yi, and K. Jang, "Large-scale synthesis of the controlled-geometry carbon coils by the manipulation of the $SF_6$ gas flow injection time," *Journal of Nanoscience and Nanotechnology*, vol. 12, no. 5, pp. 4397–4402, 2012.

[10] Q. Zhang, L. Yu, and Z. Cui, "Effects of the size of nano-copper catalysts and reaction temperature on the morphology of carbon fibers," *Materials Research Bulletin*, vol. 43, no. 3, pp. 735–742, 2008.

[11] S. Hokushin, L. Pan, and Y. Nakayama, "Diameter control of carbon nanocoils by the catalyst of organic metals," *Japanese Journal of Applied Physics A*, vol. 46, no. 8, pp. 5383–5385, 2007.

[12] N. Tang, J. Wen, Y. Zhang, F. Liu, K. Lin, and Y. Du, "Helical carbon nanotubes: catalytic particle size-dependent growth and magnetic properties," *ACS Nano*, vol. 4, no. 1, pp. 241–250, 2010.

[13] F. Du, J. Liu, and Z. Guo, "Shape controlled synthesis of Cu2O and its catalytic application to synthesize amorphous carbon nanofibers," *Materials Research Bulletin*, vol. 44, no. 1, pp. 25–29, 2009.

[14] S. Motojima, M. Kawaguchi, K. Nozaki, and H. Iwanaga, "Preparation of coiled carbon fibers by catalytic pyrolysis of acetylene, and its morphology and extension characteristics," *Carbon*, vol. 29, no. 3, pp. 379–385, 1991.

[15] M. Kawaguchi, K. Nozaki, S. Motojima, and H. Iwanaga, "A growth mechanism of regularly coiled carbon fibers through acetylene pyrolysis," *Journal of Crystal Growth*, vol. 118, no. 3-4, pp. 309–313, 1992.

[16] X. Chen, S. Motojima, and H. Iwanga, "Vapor phase preparation of super-elastic carbon micro-coils," *Journal of Crystal Growth*, vol. 237-239, no. 1–4, pp. 1931–1936, 2002.

[17] J. B. Bai, "Growth of nanotube/nanofibre coils by CVD on an alumina substrate," *Materials Letters*, vol. 57, no. 18, pp. 2629–2633, 2003.

[18] Z. Y. Huang, X. Chen, J. R. Huang, M. Q. Li, and J. H. Liu, "Synthesis of carbon nanocoils on surface morphology changed silicon substrates," *Materials Letters*, vol. 60, no. 17-18, pp. 2073–2075, 2006.

[19] M. Ch. Veziri, G. N. Karanikolos, G. Pilatos et al., "Growth and morphology manipulation of carbon nanostructures on porous supports," *Carbon*, vol. 47, no. 9, pp. 2161–2173, 2009.

[20] H. Tada, A. E. Kumpel, R. E. Lathrop et al., "Thermal expansion coefficient of polycrystalline silicon and silicon dioxide thin films at high temperatures," *Journal of Applied Physics I*, vol. 87, no. 9, pp. 4189–4193, 2000.

[21] T. G. Kollie, "Measurement of the thermal-expansion coefficient of nickel from 300 to 1000 K and determination of the power-law constants near the Curie temperature," *Physical Review B*, vol. 16, no. 11, pp. 4872–4881, 1977.

[22] D. W. Li, L. J. Pan, D. P. Liu, and N. S. Yu, "Relationship between geometric structures of catalyst particles and growth of carbon nanocoils," *Chemical Vapor Deposition*, vol. 16, no. 4–6, pp. 166–169, 2010.

[23] Y.-C. Jeon, S. I. Ahn, and S.-H. Kim, "Investigation the developing aspect of carbon coils formation during the beginning stage of the process," *Journal of Nanoscience and Nanotechnology*. In press.

*Research Article*

# Raman Spectroscopy of Isotactic Polypropylene-Halloysite Nanocomposites

**Elamin E. Ibrahim,[1] Dorina Magdalena Chipara,[2] Ram Thapa,[2] Karen Lozano,[3] and Mircea Chipara[2]**

[1] *Department of Chemistry, The University of Texas-Pan American, Edinburg, TX 78541, USA*
[2] *Department of Physics and Geology, The University of Texas-Pan American, 1201 West University Drive, Edinburg, TX 78541, USA*
[3] *Department of Mechanical Engineering, The University of Texas-Pan American, Edinburg, TX 78541, USA*

Correspondence should be addressed to Dorina Magdalena Chipara, dchipara@utpa.edu

Raman spectroscopy investigations on nanocomposites obtained by dispersing halloysite within isotactic polypropylene are reported. A detailed analysis of the modifications of the regularity band associated to the polymeric matrix is presented. The Raman lines assigned to the polymeric matrix are broadened and weakened as the loading with halloysite is increased. The analysis of Raman lines indicates that the polymeric matrix becomes less crystalline upon the loading with halloysite and that the nanofiller is experiencing a weak dehydration upon dispersion within the polymeric matrix, probably due to the related thermal processing used to achieve the dispersion of halloysite.

## 1. Introduction

The dispersion of carbon nanotubes within polymeric matrices resulted in important improvements of the mechanical properties (reflected in most cases by increases of the Young modulus [1–4]) and of the thermal stability [4] of polymeric matrices. Nevertheless, the electrical and thermal conductivity of one-dimensional carbon nanostructures [5, 6] added thermal and electrical conductivity to the typically insulating polymeric matrices (especially if the concentration of the nanofiller is at or above the percolation threshold [7, 8]). For some applications, such as electrical insulators or thermal barrier materials, such modifications are adverse. Detailed investigations on isotactic polypropylene filled with other one-dimensional materials (such as single-walled carbon nanotubes, multiwalled carbon nanotubes, and carbon nanofibers) have been reported elsewhere [9–13].

Halloysite (H) is an unique nanoclay [14], with a tubular morphology and low electrical and thermal conductivity. These features incited several investigations on the physical properties of polymer-halloysite nanocomposites [14–17].

Taking into account the above-mentioned characteristics, a detailed investigation on the physical properties of isotactic polypropylene-halloysite nanocomposite has been ignited.

There are several types of halloysites, corresponding to the degree of hydration. The extremes are represented by the so-called halloysite 10 A, and by halloysite 7 A. Halloysite 10 A is characterized by a monoclinic crystalline structure (with the cell parameters $a = 5.1$ A, $b = 8.9$ A, $c = 10.25$ A, and $\beta = 100°$), with the chemical formula $Al_2Si_2O_5(OH)_4\ 2H_2O$ and the unit cell volume of about 458 A$^3$. Halloysite 10 A is a nanotube with diameters ranging typically between 30 to 200 nm, a wall thickness of 20 nm, and lengths ranging between 500 nm to 10,000 nm obtained by rolling together kaolinite like sheets. It is known also as endelite, hydrated halloysite, or hydrohalloysite. It is typically unstable having a strong tendency to loose water. Halloysite 7 A (with amonoclinic crystal structure and cell parameters $a = 5.14$ A, $b = 8.9$ A, $c = 14.9$ A, and $\beta = 101.9°$) has an unit volume of about 667 A$^3$ and it is known as the dehydrated halloysite. During the dehydration process, the distance between layers decreases from about 1 nm to 0.7 nm.
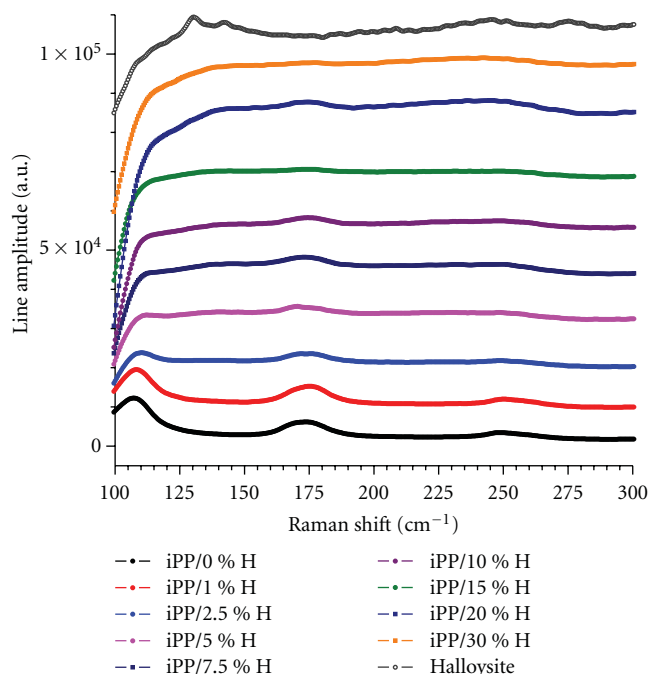
FIGURE 1: Raman spectra of iPPH nanocomposites for different loadings with H. From bottom to top: 0% H, 1.0% H, 2.5% H, 5.0% H, 7.5% H, 10.0% H, 15% H, 20% H, 30% H, and 100% H.



FIGURE 2: The effect of the loading with H on the position of Raman lines in the range from 100 to $300\,cm^{-1}$. iPP (or open symbols) identifies the Raman lines assigned to the matrix, and H the Raman lines due to the filler. Half-filled symbols represent overlapping lines due to iPP and H.

In halloysite, strong hydrogen interactions are responsible for the enhanced stability of hole water compared to associated water. Typically, the associated water is released at about $200°C$, while the hole water survives up to about $300°C$. The dehydrated halloysite is also known as metahalloysite. Several aluminosilicates (clays) have the same elemental composition $Al_2Si_2O_5(OH)_4$ as the dehydrated halloysite. Among them, the most important are (in alphabetical order) dickite, kaolinite, and nacrite. These compounds differ solely by the spatial distribution of atoms and consequently the discrimination between halloysite and any of these compounds is frequently difficult.

## 2. Experimental Methods

The structure and composition of naturally occurring H is expected to be intermediate between 7 A and 10 A, reflecting an $Al_2Si_2O_5(OH)_4 \cdot xH_2O$ chemical formula where $x$ is close to zero but not precisely zero due to some crystallization water eventually retained. This derives from the fact that most dehydrated halloysite (7 A) result from the dehydration of halloysite (10 A). Isotactic polypropylene-halloysite (iPPH) nanocomposites were obtained by high-shear mixing of isotactic polypropylene (iPP; Sigma Aldrich) with various amounts of halloysite ($Al_2Si_2O_5(OH)_4 \cdot xH_2O$; from Sigma Aldrich). Kaolinite, with a close chemical structure (missing, however, the two water molecules, i.e., $Al_2Si_2O_5(OH)_4$), is sometimes also referred to as a halloysite (see, e.g., the website of Sigma Aldrich http://www.sigmaaldrich.com/catalog/product/aldrich/685445?lang=en&region=US) or as meta-halloysite. The cylindrical symmetry of halloysite (H) is
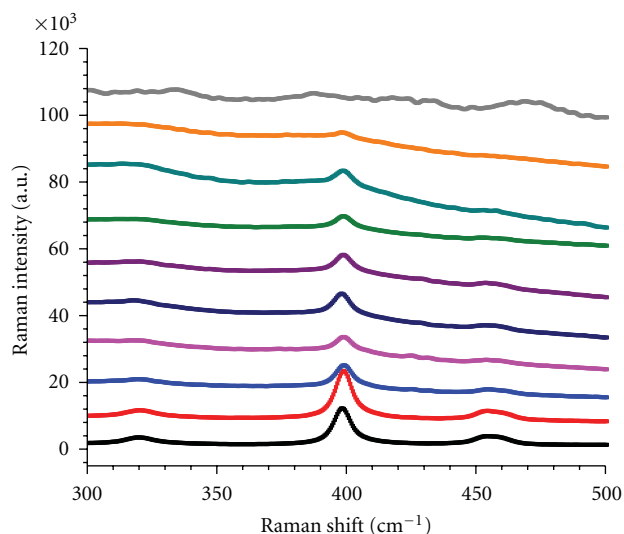


FIGURE 3: Raman spectra of iPPH nanocomposites for different loadings with H. From bottom to top: 0% H, 1.0% H, 2.5% H, 5.0% H, 7.5% H, 10.0% H, 15% H, 20% H, 30% H, and 100% H.

a consequence of a packing disorder. According to Sigma Aldrich, the external diameter of halloysite nanotubes is ranging between 30 and 70 nm (with an average of 50 nm), the average internal diameter is about 15 nm, and the length of halloysite is typically ranging between 1 to 3 $\mu$m. Hence, halloysite nanotubes are comparable to short-multiwalled carbon nanotubes. However, the Young modulus, the electrical conductivity, the thermal conductivity, and the thermal stability of halloysite are significantly lower than those

FIGURE 4: The effect of the loading with H on the position of Raman lines in the range from 300 to 500 cm$^{-1}$. iPP (or open symbols) identifies the Raman lines assigned to the matrix, and H the Raman lines due to the filler. Half-filled symbols represent overlapping lines due to iPP and H.



FIGURE 6: The effect of the loading with H on the position of Raman lines in the range 500 to 800 cm$^{-1}$. iPP (or open symbols) identifies the Raman lines assigned to the matrix, and H the Raman lines due to the filler. Half-filled symbols represent overlapping lines due to iPP, H, and A.



FIGURE 5: Raman spectra of iPPH nanocomposites for different loadings with H. From bottom to top: 0% H, 1.0% H, 2.5% H, 5.0% H, 7.5% H, 10.0% H, 15% H, 20% H, 30% H, and 100% H.



FIGURE 7: Raman spectra of iPPH nanocomposites for different loadings with H. From bottom to top: 0% H, 1.0% H, 2.5% H, 5.0% H, 7.5% H, 10.0% H, 15% H, 20% H, 30% H, and 100% H.

of multiwalled carbon nanotubes. The estimated Young modulus of halloysite is in the range from 150 to 300 GPa compared to 1000 GPa for a carbon nanotube [18]. The energy gap for halloysite is of about 9.7 eV compared to few eV (or zero) in semiconducting or metallic carbon nanotubes [18]. This classifies halloysite as an electric insulator.

The blending has been performed by utilizing a HAAKE Rheomix at 65 rpm and 180°C for 9 min followed by an additional mixing of 5 min at the same temperature and at 90 rpm. Composites loaded with various amounts of H ranging from 0% up to 30% wt. have been prepared. Raman investigations have been performed by using a Bruker Senterra dispersive confocal microscope spectrometer equipped with a 785 nm laser diode. Thermogravimetric analysis has been performed in nitrogen atmosphere by using a TA Instrument Equipment.
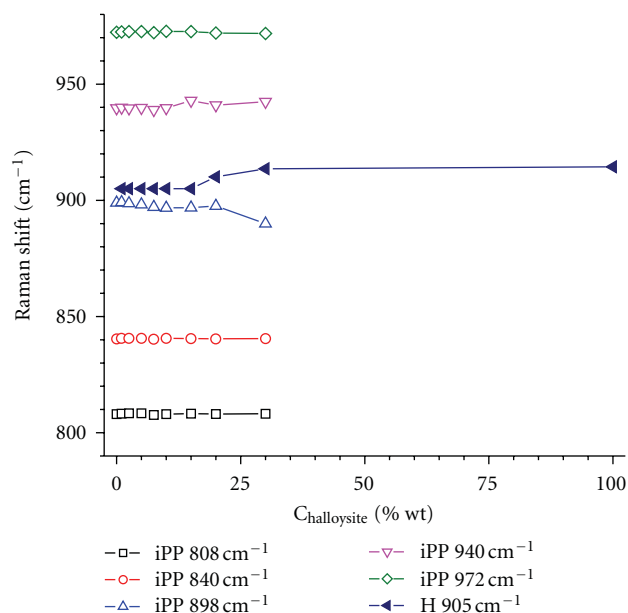
FIGURE 8: The effect of the loading with H on the position of Raman lines in the range from 800 to 1000 cm$^{-1}$. iPP (or open symbols) identifies the Raman lines assigned to the matrix, and H the Raman lines due to the filler.
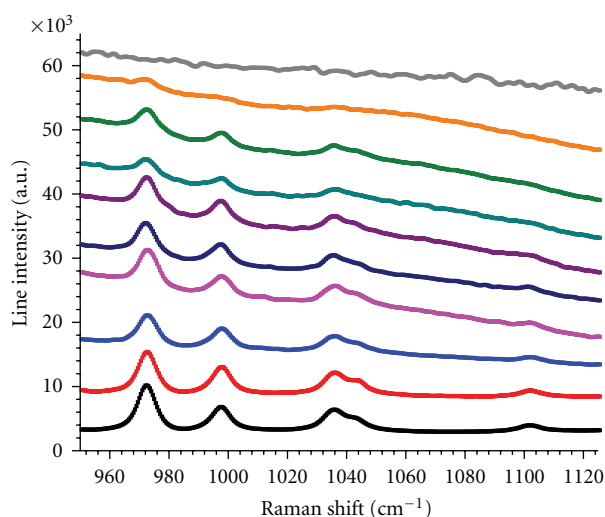


FIGURE 9: Raman spectra of iPPH nanocomposites for different loadings on the position of Raman lines in the range from 800 to 1000 cm$^{-1}$. iPP (or open symbols) identifies the Raman lines assigned to the matrix, and H the Raman lines due to the filler. Half-filled symbols represent overlapping lines due to iPP and H.

## 3. Experimental Results and Discussions

The Raman lines of pristine H are rather broad and weak, being superimposed on a very strong and wideband noticed at low Raman shifts (centered at about 125–150 cm$^{-1}$ and reported as a shoulder assigned to O–Si–O bending [19]). The Raman lines of iPP are typically narrow lines. As in the case of iPP-Vapor Grown Carbon Nanofiber (VGCNF) nanocomposites [11], the addition of the filler broadens the

Raman lines of the polymeric matrices up to their collapse in a very broad line. This behavior reflects the formation of an interface between the nanofiller and the polymeric chains and the final trapping of most macromolecular chains within these interfaces at loading concentrations above 20% wt.
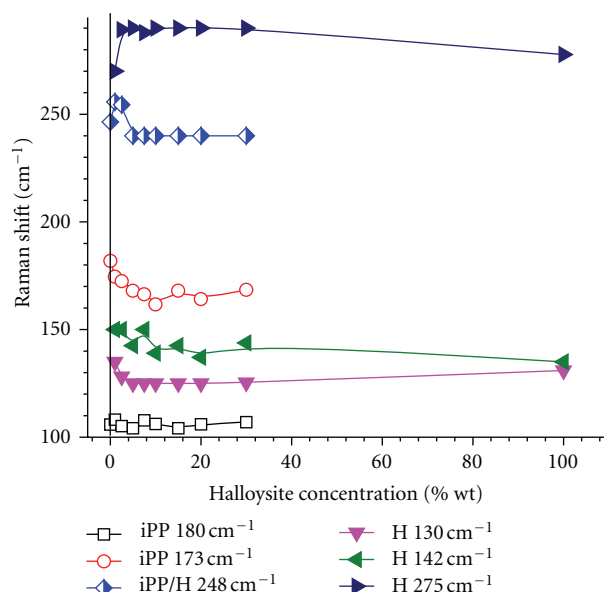
All Raman lines have been fitted by a superposition of modified Wigner-Breit-Fano lineshapes [20]; the general expression utilized for each line was

$$I(x) = \sum_{i=1}^{N} A_i \frac{[1 + D_i(x - P_i)/W_i]^2}{1 + [(x - P_i)/W_i]^2} + B + Sx + Qx^2, \quad (1)$$

where $I$ is the amplitude of the Raman spectral domain at a given Raman shift $x$ (in cm$^{-1}$), $N$ is the total number of lines for the spectral domain (including eventually both iPP and H lines), $B$ is the base line correction, $S$ is the slope correction, and $Q$ is a quadratic correction. For each line, labeled by $i$, $D_i$ is the shape deviation from a pure Lorentzian line, $P_i$ is the corresponding Raman peak position, and $W_i$ is the width of the line. For each spectral domain, an excellent agreement between fitted and recorded spectra was achieved, with correlation coefficients typically above 0.99. Each spectral domain involved at least 250 experimental points. The fit has been performed by using Origin Pro 8.6.

At low wavenumbers (spectral domain 100 to 300 cm$^{-1}$), the Raman spectrum shows the typical lines reported elsewhere (see Figure 1). The broad shoulder reported in the range from 110 to 130 cm$^{-1}$ is easily noticed in Figure 1. Raman spectra of halloysite confirm the line located at 130.8 cm$^{-1}$ identified as the line noticed at 134.7 cm$^{-1}$ and assigned to the symmetric (out of the plane) bending mode of $Si_2O_5$ [21, 22]. Tentatively, this can be associated to the line reported at 127 cm$^{-1}$ in the New Zeeland halloysite [23]. An intense line was noticed at 142.4 cm$^{-1}$ and identified as the line reported at 143 cm$^{-1}$ [23]. The origin of this line is under debate. Some authors are assigning this line to anatase impurities [19] while others are assigning this line to $AlO_6$ octahedron vibrations [22]. The Raman lines at 156 and 168 cm$^{-1}$ connected to inner surface hydroxyls are absent, suggesting a low degree of hydration [21]. However, the weak lines observed at 246 (O–H–O symmetric stretch in hydrated halloysite [24]) and 276 cm$^{-1}$ (O–H–O antisymmetric stretch in hydrated halloysite [24]) are connected to water's molecule vibrations [22].

For isotactic polypropylene, the lines located at 108 cm$^{-1}$, 173 cm$^{-1}$, and 248 cm$^{-1}$ are easily noticed. The Raman line located at 248 cm$^{-1}$ has been identified as the line located at 252 cm$^{-1}$ and assigned to wagging $CH_2$ and bending CH groups [25, 26]. An overlap between the iPP line located at 250 cm$^{-1}$ and the H line at 246 cm$^{-1}$ is possible in iPPH nanocomposites.

The dependence of the Raman lines position on the loading with halloysite is shown in Figure 2. Empty symbols are connected to the polymeric matrix and solid symbols to the filler. Half-solid symbol is assigned to the overlapping signals. It is noticed that the peak located at 275 cm$^{-1}$ is shifted towards larger Raman shift. The experimental data indicates a dehydration of the halloysite, expected during the thermal processing of the nanocomposite. It is important

to mention that in the case of halloysite, the Raman peaks were rather weak. At low concentration of halloysite, the water diffused within the polymer as moisture may hydrate weakly the filler. However, for samples containing 2.5% wt. H or a smaller amount of H, the intensity of this line is fairly low. From Figure 2 it is noticed that the position of the Raman lines of H are displaced towards smaller Raman shifts suggesting a weak dehydration of the nanofiller. This is consistent with the thermal blending and suggests a partial loss of water during the processing of the nanocomposites.

The second spectral domain, ranging between 300 and $500 \, cm^{-1}$, includes both iPP and H lines, as shown in Figure 3. The line noticed at $335 \, cm^{-1}$ can be assigned to uncomplexed kaolinite [19] or to water in nanoclays (responsible for another Raman line typically located at $332 \, cm^{-1}$ [24]) while the weak and broad line at $389 \, cm^{-1}$ confirms the presence of anatase impurities [19]. The line at $469 \, cm^{-1}$ is tentatively assigned to Al–O/Si–O vibrations [19] and labeled as the N line.

There are three main Raman lines, which are typically assigned to iPP in this spectral domain located at about $320 \, cm^{-1}$ [26, 27], $400 \, cm^{-1}$ [26, 27], and $455 \, cm^{-1}$ [28]. The line located at about $400 \, cm^{-1}$, assigned to the umbrella bending mode about the tertiary carbon atom [29], is the most intense one. The last line was assigned to wagging $CH_2$ and bending CH [28]. As noticed in Figure 4, the Raman lines of H are shifted towards lower Raman shifts as the H content is increased above 10% wt. halloysite. The position of the iPP line located at $399 \, cm^{-1}$ shows a weak shift towards larger values as the concentration of halloysite is increased. In the case of the line located at $400 \, cm^{-1}$, it was reported that the melting is shifting this line to $402 \, cm^{-1}$ [28]. This suggests a drop of the degree of crystallinity of iPP upon loading with H. The position of the iPP line located at $455 \, cm^{-1}$ is shifted to lower values as the H content is increased. The position of the other line assigned to iPP has a complex dependence of H content showing above 10% wt. halloysite a weak shift of the line to smaller Raman shifts as the H content is increased.

Figure 5 collects the line recorded in the spectral domain from $500 \, cm^{-1}$ to $800 \, cm^{-1}$. In this range, several Raman lines are expected. Water (in H) can contribute with a weak line located at $789 \, cm^{-1}$ [21, 22]. The line at $712 \, cm^{-1}$ is a rather weak resonance that confirms the presence of OH groups [24]. The line noticed at $754 \, cm^{-1}$ is labeled as the K line [19]. A single strong line due to iPP, located at $525 \, cm^{-1}$ and assigned to wagging $CH_2$, stretching $C–CH_3$, and rocking $CH_2$ [28]. The effect of the loading of iPP with H on the most important Raman lines observed in this spectral domain is shown in Figure 6. The position of the line located at $525 \, cm^{-1}$ is almost not modified by the loading with H. The position of the Raman lines assigned to H shows a complex dependence on the content of H (at low concentration of H) continuing by a weak shift towards larger values (versus H concentration) for samples containing between 10 and 30% wt. H.

Figure 7 collects the Raman lines in the spectral domain from 800 to $1000 \, cm^{-1}$. This spectral domain is dominated by the Raman lines due to iPP. The weak Al–OH libration

line [19, 24] located at $910–912 \, cm^{-1}$ and labeled as the I line is within the noise. The Raman lines originating from iPP have been observed at $808 \, cm^{-1}$ (regularity band associated with crystalline domains reflecting C–C stretching along backbone and rocking $CH_3$ [27, 28, 30]), $840 \, cm^{-1}$ (another regularity band due to $CH_3$ rocking and originating from amorphous regions [28]), $895 \, cm^{-1}$ (rocking $CH_2$, stretching $CH_3$, and bending CH [28]), and $940 \, cm^{-1}$. The line located at $895 \, cm^{-1}$ is typically observed in melts of iPP. This confirms that the loading of iPP with halloysite drops the degree of crystallinity of the polymeric matrix and agrees with experimental data on iPP filled with VGCNFs [11, 12]. Figure 8 shows the effect of the loading with H on the position of various Raman lines. The figure includes a single line assigned to H, which is weakly shifted towards larger values. The shift is stronger for H concentrations larger than 10% wt. (At low H concentrations the shift towards larger values is slightly above the experimental errors). The iPP lines included in Figure 8 are almost independent on the concentration of H.

The Raman spectra in the range from $1000 \, cm^{-1}$ to $1100 \, cm^{-1}$ are shown in Figure 9. This spectral domain is dominated by the strong lines originating from iPP and located at $972 \, cm^{-1}$ (regularity band due to $CH_3$ rocking [27, 28]), $997 \, cm^{-1}$ (another regularity band that does not disappear on melting [28]), $1033 \, cm^{-1}$ (which was reported as a structural defect [28]), $1041 \, cm^{-1}$, and $1100 \, cm^{-1}$. Halloysite is responsible for two weak lines located at $1172 \, cm^{-1}$ and $1180 \, cm^{-1}$ assigned to Si–O units [22]. The effect of loading with H on the position of the Raman lines is shown in Figure 10. The spectra assigned to iPP are shifted towards larger Raman shifts as the content of halloysite is increased. Nevertheless, these shifts are rather weak. The dependence of the position of the halloysite limes on the content of halloysite is complex and weak. The line located at $1033 \, cm^{-1}$ indicates the enhancement of structural defects in H-doped nanocomposites. Nevertheless, the broadening of this line makes difficult an accurate estimation of the dependence of disorder degree versus the concentration of halloysite.

The isotacticity was calculated as the ratio between the area of the peak located at $809 \, cm^{-1}$ and the area of the peak located at $974 \, cm^{-1}$ [27]. Figure 11 demonstrates the drop of the isotacticity index as the polymeric matrix is loaded with H, indicating a decrease of the degree of crystallinity, consistent with other features noticed within this study.

The thermal stability of halloysite is rather poor. As can be inferred from Figure 12, the TGA data of pristine halloysite are consistent with stepwise thermal degradations centered at $250°C$, $480°C$, and $680°C$. The first maxim is assigned to the loss of crystallization water and the second one is assigned to dehydroxilation towards kaolinite (actually metakaolin, $Al_2Si_2O_7$). Assuming that all crystallization data is lost at $300°C$, the corrected structure of the pristine halloysite is $Al_2Si_2O_5(OH)_4 \cdot x \, H_2O$, where $x = 0.5$.

Raman spectra of pristine and annealed halloysite shown in Figure 13 exibit small differences, probably because the main component is the dehydrated halloysite and the recorded spectra are actually convolutions over slightly
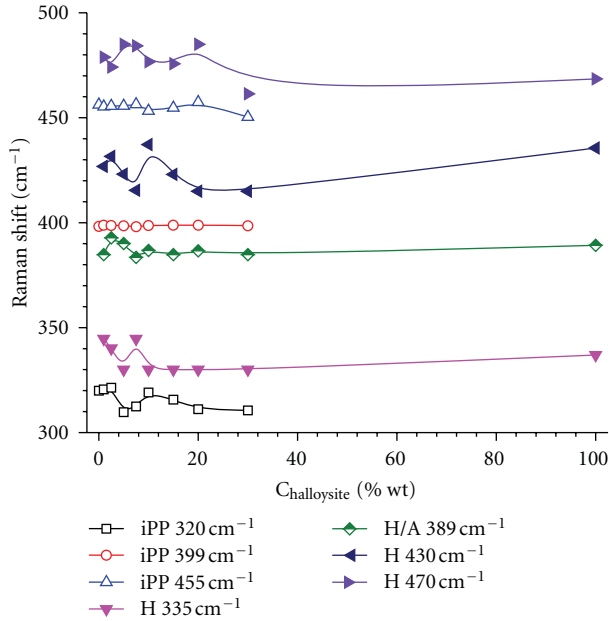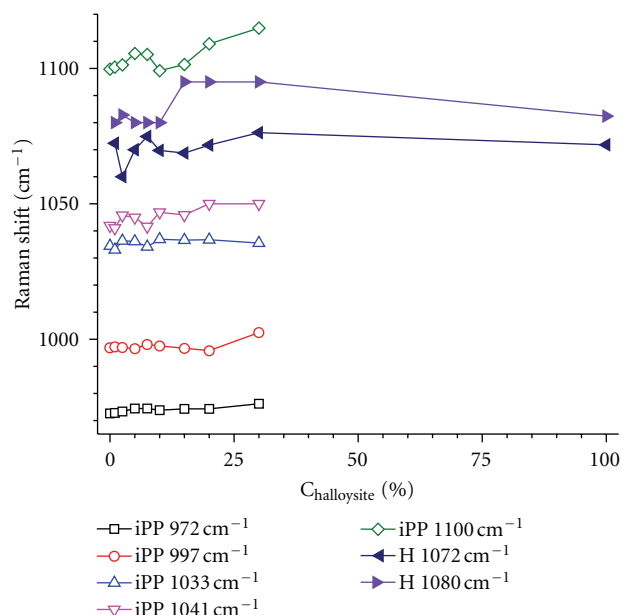
FIGURE 10: The effect of the loading with H on the position of Raman lines in the range from 1000 to 1100 $cm^{-1}$. iPP (or open symbols) identifies the Raman lines assigned to the matrix, and H the Raman lines due to the filler.
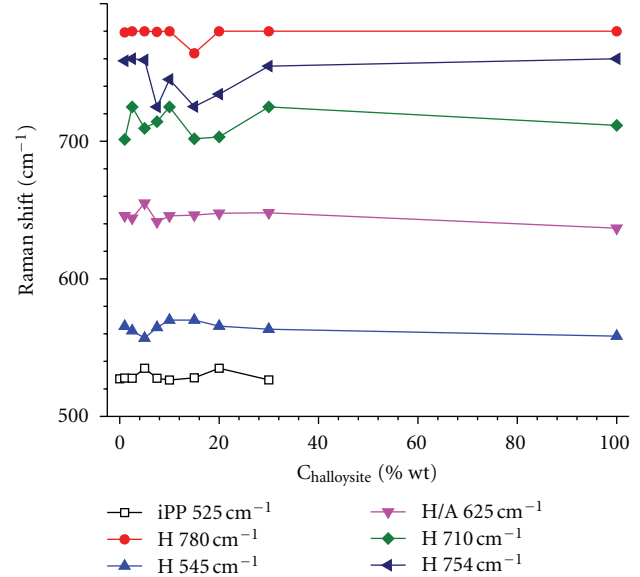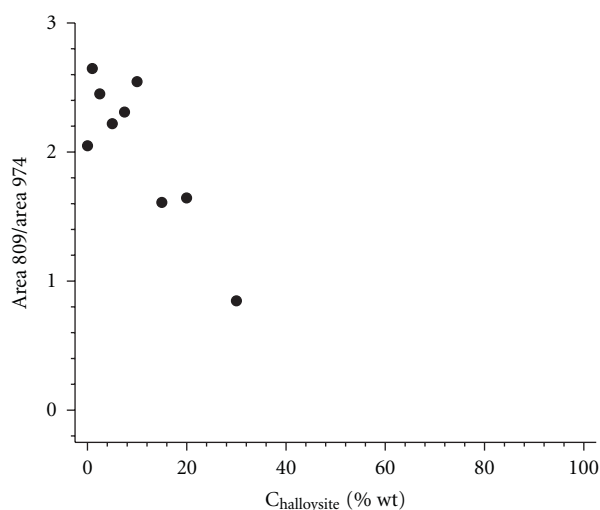


FIGURE 11: The dependence of the isotacticity index (i.e., of the ratio between the areas of the peaks located at 809 and 974 $cm^{-1}$ on the loading with halloysite).

different structures. **Figure 14** collects the Raman spectra of iPPH nanocomposites annealed at 250°C for 30 minutes. It is noticed that the annealing at 250°C (i.e., the dehydration of the halloysite) has a weak effect on the Raman spectra of iPPH nanocomposites.

## 4. Conclusions

Raman spectroscopy investigations on nanocomposites obtained by dispersing halloysite within iPP are reported.
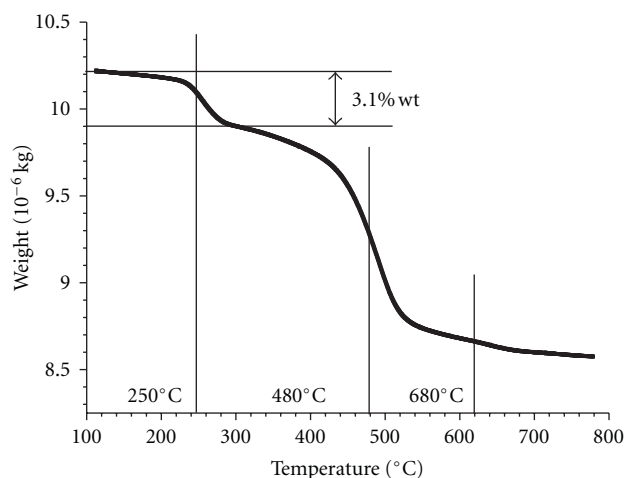


FIGURE 12: TGA data of pristine halloysite showing the main thermal degradation processes.
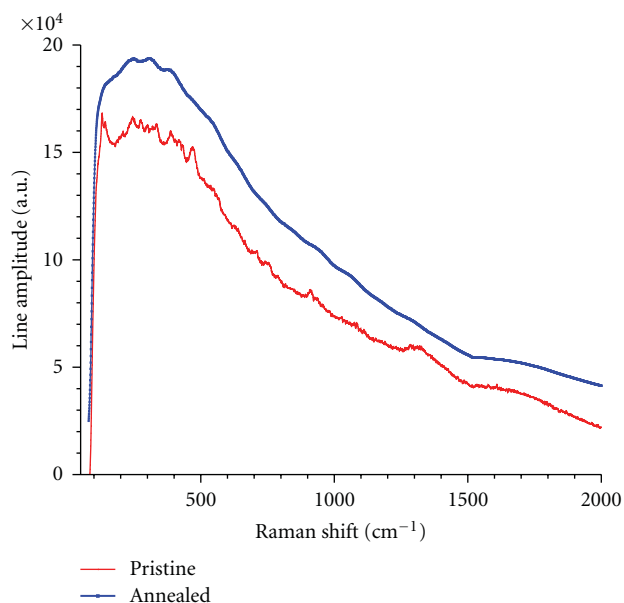


FIGURE 13: The Raman spectrum of pristine halloysite (narrow line) and of the halloysite annealed for 30 minutes at 250°C.

The Raman lines of halloysite are broad, as the experimental spectra are a convolution of spectra corresponding to molecules with various degrees of hydration. TGA data suggested that in average each two molecules of halloysite contain one molecule of water (or in other words there is one molecule of halloysite 10 A to every 4 molecules of halloysite 7 A). The existing literature suggests that the Young modulus of halloysite is three times smaller than the Young modulus of carbon nanotubes. For the same applied stress, the estimated strain should be three times larger than in carbon nanotubes. Hence, larger Raman shifts were expected in iPPH nanocomposites than in iPP-VGCNF composites. By comparing the Raman shifts reported here to the Raman shifts noticed in our previous study of iPP-VGCNF [11], it is
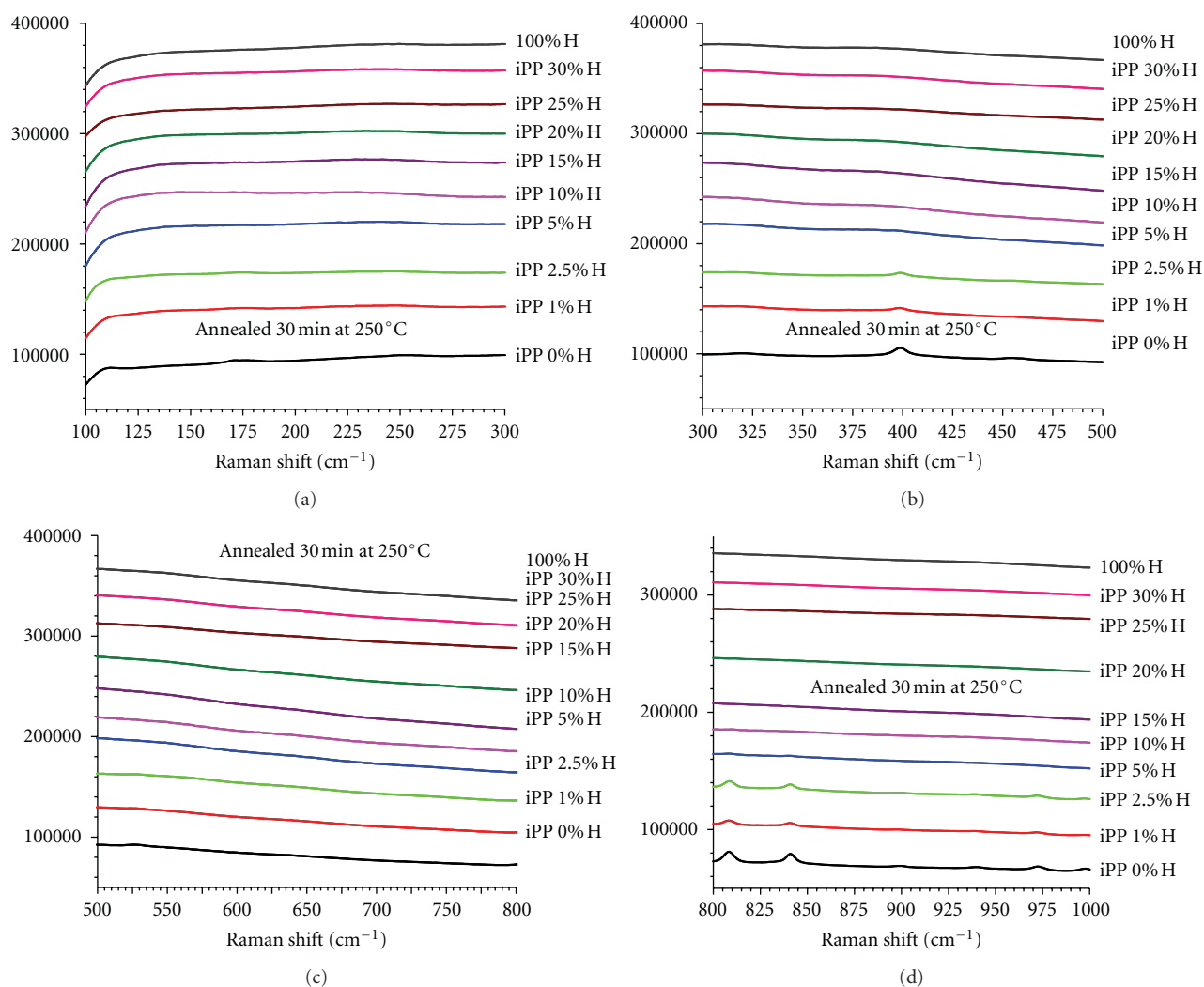
FIGURE 14: The Raman spectra of iPPH nanocomposites annealed at 250° for 30 minutes.

concluded that the shifts of the Raman peaks as a function of filler's concentration are weaker for halloysite (compared to VGCNF), and consequently the stress transfer between the polymeric matrix (same iPP) and the nanofiller is less efficient in the case of halloysite.

The experimental data are qualitatively analogous with the iPP-VGCNF nanocomposites; the nanofiller broadens and decreases the intensity of the Raman lines assigned to the polymeric matrix (iPP). However, due to the fact the nanofiller does not exhibit narrow and strong Raman lines, the analysis was also focused on the polymeric matrix. A detailed analysis of the modifications of the regularity band associated to the polymeric matrix is presented. The analysis of Raman lines indicates that the polymeric matrix becomes less crystalline upon the loading with halloysite and that the nanofiller is experiencing a weak dehydration upon dispersion within the polymeric matrix, probably due to the thermal processing. Raman spectroscopy failed to substantiate the growth of a gamma iPP phase due to the

loading of isotactic polypropylene with halloysite as reported in [14]. In conclusion, in iPP the loading with halloysite drops the isotacticity and decreases the degree of crystallinity, in contrast with the data reported in [14]. The drop of the isotacticity of iPP as the concentration of H is increased demonstrates interactions between the polymeric matrix and the halloysite nanotubes. As discussed previously, these interactions are weaker than in iPP-VGCNF nanocomposite. Further Differential Scanning Calorimetry and Wide Angle X-Ray Scattering experiments are in course to address the crystallinity and the crystallization of these nanocomposites.

## Acknowledgments

# References

[1] V. Chirila, G. Marginean, T. Iclanzan, C. Merino, and W. Brandl, "Method for modifying mechanical properties of carbon nano-fiber polymeric composites," *Journal of Thermoplastic Composite Materials*, vol. 20, no. 3, pp. 277–289, 2007.

[2] K. Suzuki and S. Nomura, "On elastic properties of single-walled carbon nanotubes as composite reinforcing fillers," *Journal of Composite Materials*, vol. 41, no. 9, pp. 1123–1135, 2007.

[3] K. T. Lau, M. Chipara, H. Y. Ling, and D. Hui, "On the effective elastic moduli of carbon nanotubes for nanocomposite structures," *Composites B*, vol. 35, no. 2, pp. 95–101, 2004.

[4] F. Hussain, M. Hojjati, M. Okamoto, and R. E. Gorga, "Review article: polymer-matrix nanocomposites, processing, manufacturing, and application: an overview," *Journal of Composite Materials*, vol. 40, no. 17, pp. 1511–1575, 2006.

[5] A. Allaoui, S. V. Hoa, and M. D. Pugh, "The electronic transport properties and microstructure of carbon nanofiber/epoxy composites," *Composites Science and Technology*, vol. 68, no. 2, pp. 410–416, 2008.

[6] J. Bernholc, D. Brenner, M. Buongiorno Nardelli, V. Meunier, and C. Roland, "Mechanical and electrical properties of nanotubes," *Annual Review of Materials Science*, vol. 32, pp. 347–375, 2002.

[7] J. Li and J. K. Kim, "Percolation threshold of conducting polymer composites containing 3D randomly distributed graphite nanoplatelets," *Composites Science and Technology*, vol. 67, no. 10, pp. 2114–2120, 2007.

[8] N. Li, Y. Huang, F. Du et al., "Electromagnetic Interference (EMI) shielding of single-walled carbon nanotube epoxy composites," *Nano Letters*, vol. 6, no. 6, pp. 1141–1145, 2006.

[9] A. R. Bhattacharyya, T. V. Sreekumar, T. Liu et al., "Crystallization and orientation studies in polypropylene/single wall carbon nanotube composite," *Polymer*, vol. 44, no. 8, pp. 2373–2377, 2003.

[10] E. Logakis, E. Pollatos, C. Pandis et al., "Structure-property relationships in isotactic polypropylene/multi-walled carbon nanotubes nanocomposites," *Composites Science and Technology*, vol. 70, no. 2, pp. 328–335, 2010.

[11] C. Mircea, J. R. Villarreal, M. D. Chipara, K. Lozano, A. C. Chipara, and D. J. Sellmyer, "Spectroscopic investigations on polypropylene-carbon nanofiber composites. I. Raman and electron spin resonance spectroscopy," *Journal of Polymer Science B*, vol. 47, no. 17, pp. 1644–1652, 2009.

[12] M. D. Chipara, K. Lozano, A. Hernandez, and M. Chipara, "TGA analysis of polypropylene-carbon nanofibers composites," *Polymer Degradation and Stability*, vol. 93, no. 4, pp. 871–876, 2008.

[13] M. Chipara, J. Hamilton, A. C. Chipara, T. George, D. M. Chipara, E. E. Ibrahim et al., "Fourier transform infrared spectroscopy and wide-angle X-ray scattering: investigations on polypropylene—vapor-grown carbon nanofiber composites," *Journal of Applied Polymer Science*, vol. 125, no. 1, pp. 353–360, 2012.

[14] M. Du, B. Guo, and D. Jia, "Newly emerging applications of halloysite nanotubes: a review," *Polymer International*, vol. 59, no. 5, pp. 574–582, 2010.

[15] Y. Tang, S. Deng, L. Ye et al., "Effects of unfolded and intercalated halloysites on mechanical properties of halloysite-epoxy nanocomposites," *Composites A*, vol. 42, no. 4, pp. 345–354, 2011.

[16] E. Horváth, J. Kristóf, R. Kurdi, É. Makó, and V. Khunová, "Study of urea intercalation into halloysite by thermoanalytical and spectroscopic techniques," *Journal of Thermal Analysis and Calorimetry*, vol. 105, no. 1, pp. 53–59, 2011.

[17] B. Lecouvet, M. Sclavons, S. Bourbigot, J. Devaux, and C. Bailly, "Water-assisted extrusion as a novel processing route to prepare polypropylene/halloysite nanotube nanocomposites: structure and properties," *Polymer*, vol. 52, no. 19, pp. 4284–4295, 2011.

[18] L. Guimarães, A. N. Enyashin, G. Seifert, and H. A. Duarte, "Structural, electronic, and mechanical properties of single-walled halloysite nanotube models," *Journal of Physical Chemistry C*, vol. 114, no. 26, pp. 11358–11363, 2010.

[19] K. H. Michaelian, S. L. Zhang, S. Yariv, and I. Lapides, "Low-frequency Raman spectra of kaolinite/alkali halide complexes," *Applied Clay Science*, vol. 13, no. 4, pp. 233–243, 1998.

[20] S. D. M. Brown, A. Jorio, P. Corio et al., "Origin of the Breit-Wigner-Fano lineshape of the tangential G-band feature of metallic carbon nanotubes," *Physical Review B*, vol. 63, no. 15, Article ID 155414, pp. 1554141–1554148, 2001.

[21] R. L. Frost and H. F. Shurvell, "Raman microprobe spectroscopy of halloysite," *Clays and Clay Minerals*, vol. 45, no. 1, pp. 68–72, 1997.

[22] R. L. Frost, T. H. Tran, and J. Kristof, "FT-Raman spectroscopy of the lattice region of kaolinite and its intercalates," *Vibrational Spectroscopy*, vol. 13, no. 2, pp. 175–186, 1997.

[23] R. L. Frost, "Fourier transform Raman spectroscopy of kaolinite, dickite and halloysite," *Clays and Clay Minerals*, vol. 43, no. 2, pp. 191–195, 1995.

[24] J. T. Kloprogge and R. L. Frost, "Raman microprobe spectroscopy of hydrated halloysite from a neogene cryptokarst from Southern Belgium," *Journal of Raman Spectroscopy*, vol. 30, no. 12, pp. 1079–1085, 1999.

[25] M. Arruebarrena de Báez, P. J. Hendra, and M. Judkins, "The Raman spectra of oriented isotactic polypropylene," *Spectrochimica Acta A*, vol. 51, no. 12, pp. 2117–2124, 1995.

[26] T. Hahn, W. Suen, S. Kang, S. L. Hsu, H. D. Stidham, and A. R. Siedle, "An analysis of the Raman spectrum of syndiotactic polypropylene. 1. Conformational defects," *Polymer*, vol. 42, no. 13, pp. 5813–5822, 2001.

[27] T. Sundell, H. Fagerholm, and H. Crozier, "Isotacticity determination of polypropylene using FT-Raman spectroscopy," *Polymer*, vol. 37, no. 15, pp. 3227–3231, 1996.

[28] R. M. Khafagy, "In situ FT-Raman spectroscopic study of the conformational changes occurring in isotactic polypropylene during its melting and crystallization processes," *Journal of Polymer Science B*, vol. 44, no. 15, pp. 2173–2182, 2006.

[29] V. M. Hallmark, S. P. Bohan, H. L. Strauss, and R. G. Snyder, "Analysis of the low-frequency isotropic Raman spectrum of molten isotactic polypropylene," *Macromolecules*, vol. 24, no. 14, pp. 4025–4032, 1991.

[30] D. E. Gen, K. A. Prokhorov, G. Y. Nikolaeva et al., "Raman spectra of various polymorphs of isotactic polypropylene," *Laser Physics*, vol. 21, no. 1, pp. 125–129, 2011.

*Research Article*

# Effects of Annealing Environments on the Solution-Grown, Aligned Aluminium-Doped Zinc Oxide Nanorod-Array-Based Ultraviolet Photoconductive Sensor

**Mohamad Hafiz Mamat,[1] Mohd Izzudin Che Khalin,[1] Nik Noor Hafizah Nik Mohammad,[2] Zuraida Khusaimi,[2] Nor Diyana Md Sin,[1] Shafinaz Sobihana Shariffudin,[1] Musa Mohamed Zahidi,[1] and Mohamad Rusop Mahmood[1, 2]**

[1] *NANO-ElecTronic Centre (NET), Faculty of Electrical Engineering, Universiti Teknologi MARA (UiTM), 40450 Shah Alam, Selangor, Malaysia*
[2] *NANO-SciTech Centre (NST), Institute of Science (IOS), Universiti Teknologi MARA (UiTM), 40450 Shah Alam, Selangor, Malaysia*

Correspondence should be addressed to Mohamad Hafiz Mamat, hafiz_030@yahoo.com

We have fabricated metal-semiconductor-metal- (MSM-) type ultraviolet (UV) photoconductive sensors using aluminium- (Al-) doped zinc oxide (ZnO) nanorod arrays that were annealed in different environments: air, oxygen, or a vacuum. The Al-doped ZnO nanorods had an average diameter of 60 nm with a thickness of approximately 600 nm that included the seed layer (with thickness ~200 nm). Our results show that the vacuum-annealed nanorod-array-based UV photoconductive sensor has the highest photocurrent value of $2.43 \times 10^{-4}$ A. The high photocurrent is due to the high concentration of zinc (Zn) interstitials in the vacuum-annealed nanorod arrays. In contrast, the oxygen-annealing process applied to the Al-doped ZnO nanorod arrays produced highly sensitive UV photoconductive sensors, in which the sensitivity reached 55.6, due to the surface properties of the oxygen-annealed nanorods, which have a higher affinity for oxygen adsorption than the other samples and were thereby capable of reducing the sensor's dark current. In addition, the sensor fabricated using the oxygen-annealed nanorod arrays had the lowest rise and decay time constants. Our result shows that the annealing environment greatly affects the surface condition and properties of the Al-doped ZnO nanorod arrays, which influences the performance of the UV photoconductive sensors.

## 1. Introduction

Recently, zinc oxide (ZnO) nanostructures have been widely studied because of their potential for various applications, including solar cells [1–3], light emitting devices [4], electron emitters [5, 6], photocatalysts [7], and sensors [8, 9]. The performance of devices containing one-dimensional (1D) ZnO nanostructures, such as nanobelts and nanorod arrays, has significantly improved because of the unique properties of these nanostructures, such as high mobility and a high surface-to-volume ratio [10, 11]. ZnO nanorod arrays are very promising materials for use as sensing elements in ultraviolet (UV) photoconductive sensor applications because these arrays exhibit a fast response and high

photocurrent and are highly sensitive to UV light [10, 12]. The use of ZnO nanorod arrays in UV photoconductive sensors is attractive for practical applications because of the diversity of fabrication methods for these nanorods, their large surface availability, and excellent physical and chemical properties. In addition, the high surface-to-volume ratio of ZnO nanorod arrays produces better sensitivity to UV light compared to conventional ZnO thin films because the photoconductivity mechanism in ZnO is strongly related to the surface reaction activities [13]. ZnO nanorod arrays can be successfully grown on substrates using various methods, such as chemical vapour deposition (CVD) [14], metal-organic chemical vapour deposition (MOCVD) [15], pulsed laser deposition (PLD) [16], and solution-based techniques

[17–20]. However, solution-based techniques offer many advantages over other synthesis methods capable of growing ZnO nanorod arrays at low temperature with low cost.

Generally, fabricated ZnO nanorod arrays, especially those prepared using solution-based techniques, contain a considerable number of defects, resulting in a low response to UV light. Because the UV photoconductivity is governed by the surface conditions of the nanorod arrays, effective fabrication methods should be developed to reduce the number of defects and improve the surface quality of the prepared ZnO nanorod arrays. A few approaches have been proposed that can enhance the performance of the ZnO-based UV photoconductive sensor by improving the ZnO surface condition and reducing the defects. These approaches include the use of polymer and metal surface coatings [13, 21–23] and plasma and chemical surface treatments [24–28]. These techniques facilitate efficient photogeneration processes in the ZnO under UV illumination, thereby contributing to improved performance of the device, such as a high and stable photocurrent, high sensitivity, and a fast photoresponse. However, annealing is also a ZnO surface treatment process that could remove surface defects and contamination, thereby improving the surface condition of ZnO [29–31]. Although the annealing temperature is widely reported to influence the performance of the UV photoconductive sensor [32–35], the effects of annealing under different environments have rarely been reported in terms of the performance of ZnO nanorod-array-based UV photoconductive sensors.

Herein, we reported on the performance of a UV photoconductive sensor developed using thin Al-doped ZnO nanorod arrays prepared using the sonicated sol-gel immersion method and annealed in different environments. The nanorod arrays were prepared in a very short immersion time, within 50 min, using sonicated sol-gel immersion method, which yield small and thin nanorod arrays with an average diameter of 60 nm and thickness of approximately 600 nm. We observed that annealing under different environments significantly influenced the surface conditions of the nanorod arrays, thereby affecting the performance of the UV photoconductive sensor.

## 2. Experimental Procedure

Al-doped ZnO nanorod arrays were grown on a glass substrate that was coated with an Al-doped ZnO seed layer using sonicated sol-gel immersion. The Al-doped ZnO thin film, which was used as a seeded catalyst, was prepared on the glass substrate using sol-gel spin-coating [36]. The solution for the seed layer was prepared using 0.4 M zinc acetate dihydrate $(Zn(CH_3COO)_2 \cdot 2H_2O$, 99.5% purity, Merck) as a precursor, 0.4 M monoethanolamine (MEA, $H_2NCH_2CH_2OH$, 99.5% purity, Aldrich) as a stabiliser, 0.004 M aluminium nitrate nonahydrate $(Al(NO_3)_3 \cdot 9H_2O$, 98% purity, Analar) as a doping source (to achieve approximately 1 at.% Al-doped ZnO), and 2-methoxyethanol as a solvent. The solution was then heated at 80°C and stirred using a hot plate magnetic stirrer for 3 h to yield a clear, homogeneous solution. The solution was further stirred at room temperature for 24 h for the ageing process. The seed layer was deposited onto

glass substrate using spin-coating technique. The prepared solution was dropped onto glass substrates while the substrates were spun at 3,000 rpm for 60 s. After the spin-coating process, the substrates were heated at 150°C for 10 min to evaporate the solvent and remove the organic component from the film. The coating was repeated five times to increase the film thickness to approximately 200 nm. The prepared films then were annealed in air using a furnace at 500°C for 1 h.

The solution for preparing the aligned Al-doped ZnO nanorod arrays contained 0.1 M zinc nitrate hexahydrate $(Zn(NO_3)_2 \cdot 6H_2O$, 98%, Systerm) as a precursor, 0.1 M hexamethylenetetramine (HMT, $C_6H_{12}N_4$, 99%, Aldrich) as a stabiliser, and 0.001 M aluminium nitrate nonahydrate $(Al(NO_3)_3 \cdot 9H_2O$, 98%, Analar) as a dopant, which were dissolved in deionised (DI) water. The solution was then sonicated at 50°C for 30 min using an ultrasonic water bath (Hwashin Technology Powersonic 405, 40 kHz) before being aged and stirred for 3 h at room temperature.

To deposit the aligned Al-doped ZnO nanorods, approximately 100 mL of the prepared solution was poured into a vessel that contained the horizontal glass substrates that were coated with the seeded catalyst at the bottom. The sealed vessel was immersed into a water bath deposition system at 95°C for 50 min. After the deposition process, the samples were removed from the vessel and cleaned with DI water. The resulting Al-doped ZnO nanorod arrays were heated at 150°C for 10 min to evaporate the water. Next, the samples were annealed at 500°C in an oxygen, air, or vacuum environment for 1 h using a furnace. Undoped ZnO nanorod arrays were also prepared using the same procedure and were annealed in air at 500°C for 1 h. In addition, the Al-doped ZnO nanorod arrays were prepared at different lengths of immersion time (i.e., 50, 100, and 150 min) and were annealed in air at 500°C for 1 h. To complete the metal-semiconductor-metal- (MSM-) type sensor structure, 60 nm thick Al-metal contacts were deposited onto the prepared nanorod arrays using a thermal evaporator at a deposition pressure of $4 \times 10^{-4}$ Pa. The distance between the two metal contacts was 2 mm.

The prepared nanorod arrays were characterised using field-emission scanning electron microscopy (FESEM, JEOL JSM-7600F), which was used to observe their surface morphology and the cross-section images. The crystallinity of the samples was characterised using X-ray diffraction (XRD, Panalytical X′pert PRO). The structural and selected area electron diffraction (SAED) of the air-annealed undoped and Al-doped ZnO nanorod arrays was investigated using transmission electron microscopy (TEM; JEOL JEM 3010). The transmittance and absorbance properties of the nanorod arrays were characterised using ultraviolet-visible-near-infrared (UV-vis-NIR) spectrophotometry (Perkin Elmer Lambda 750). The photoluminescence properties of the prepared samples were characterised using a photoluminescence (PL) spectrometer (Horiba Jobin Yvon 79 DU420A-OE-325) equipped with a helium-cadmium (He-Cd) laser excitation source at 325 nm. The current-voltage (I-V) characteristics of the UV photoconductive sensors were investigated using a two-probe I-V measurement system (Keithley 2400). The

UV photoresponse measurements of the fabricated sensor were conducted using a UV photocurrent measurement system (Keithley 2400) operating at 365 nm with a power density of 750 $\mu$W/cm$^2$ at a bias voltage of 10 V.

## 3. Results and Discussion

Figures 1(a)–1(d) present the FESEM images of the as-grown, oxygen-annealed, air-annealed, and vacuum-annealed Al-doped ZnO nanorod arrays prepared using the sonicated sol-gel immersion method. These images reveal that the nanorods were uniformly deposited on the glass substrate coated with the seed layer after immersion for 50 min. The FESEM images also reveal that the morphology of the Al-doped ZnO nanorod arrays did not exhibit a significant change after annealing in different environments. Based on the FESEM images, the average diameter of the Al-doped ZnO nanorod is approximately 60 nm. According to the EDS spectrum of as-grown Al-doped ZnO nanorod arrays shown in Figure 1(e), the peaks of Zn, Al, and O correspond to an atomic ratio of 49.21 : 0.64 : 50.16. Figures 2(a)–2(d) show the cross-sectional images of the Al-doped ZnO nanorod arrays that were annealed under different environments. These images indicated that the Al-doped ZnO nanorods were deposited perpendicular to the substrate with good alignment. The thicknesses of these films were estimated from the FESEM images to be approximately 600 nm.

Figure 3 presents the XRD patterns of the as-grown, oxygen-annealed, air-annealed, and vacuum-annealed Al-doped ZnO nanorod arrays. The nanorod arrays present diffraction peaks that can be indexed to the ZnO hexagonal phase with a wurtzite structure (Joint Committee on Powder Diffraction Standards (JCPDS) PDF number 36-1451). The XRD patterns reveal that the (002) peak of the nanorod is the most prevalent, which indicates that the nanorod preferentially grows along the $c$-axis (perpendicular to the substrate). The other weak diffraction peaks in the XRD patterns may be a result of imperfect nanorod alignment on the substrate [37]. According to this result, the relative intensities of the XRD peak from the (002) plane are oxygen-annealed > air-annealed > vacuum-annealed > as-grown. This ordering indicates that oxygen is a better annealing environment than the other annealing environments (i.e., air and vacuum) for improving the crystallinity of the Al-doped ZnO nanorod arrays. Annealing in oxygen promotes the reaction between oxygen and the Zn interstitials to form crystalline ZnO. Similarly, this process also occurred during annealing in air. However, due to the higher concentration of oxygen molecules in the oxygen-annealing process relative to air annealing, the oxidation rate in oxygen annealing is much faster due to the greater reduction in the free-surface energy. Therefore, the crystallinity of the oxygen-annealed nanorod arrays is better than that of the air-annealed nanorod arrays. The as-grown sample presented low-intensity XRD peaks, which were attributed to the high density of defects in the nanorod arrays, particularly the presence of hydroxyl (OH) groups on the nanorod surface. The presence of OH groups on the surface of the nanorod is commonly reported for low-temperature solution-based syntheses [29, 38, 39]. However,

the XRD pattern of the vacuum-annealed ZnO nanorod array presents the weakest peak intensity compared to the other annealed samples. In addition, the XRD pattern of the vacuum-annealed nanorod arrays shows the emergence of Zn metal peaks. This condition could be attributed to the desorption of OH groups from the ZnO nanorod array during annealing, which leaves a large amount of Zn or Zn interstitials in the nanorod. Because of the unavailability of oxygen molecules, the oxidation of Zn could not occur during the annealing process in the vacuum. As a result, the growth of ZnO was inhibited while maintaining a high concentration of Zn or Zn interstitials, thereby degrading the crystallinity of the Al-doped ZnO nanorod arrays.

Figure 4(a) shows the transmittance spectra of the Al-doped ZnO nanorod arrays prepared at different annealing environments in the wavelength ranges from 300 to 1500 nm. These spectra demonstrate that the nanorod arrays have good optical transmittance in the visible (400–800 nm) and near-infrared ranges (800–1500 nm). The spectra also reveal that upon the annealing process in the oxygen environment, the transmittance of the nanorod arrays improves relative to the as-grown sample. Note that the average transmittance of the as-grown Al-doped ZnO nanorod arrays in the visible region is approximately 72%. The average transmittance of the oxygen-annealed Al-doped ZnO nanorod arrays in the visible region was estimated to be 78%. However, the transmittance slightly decreased after annealing in air and vacuum, with average transmittances of 77 and 76%, respectively. We also observed that interference fringes appeared in the spectra, which indicated that the nanorod arrays are uniformly deposited on the substrate [40]. Figure 4(b) shows the absorbance spectra of the Al-doped ZnO nanorod arrays prepared using different annealing environments. The absorbance spectra reveal that all of the samples exhibit good UV absorption properties below 400 nm with an absorption edge of 380 nm. The sharp absorption edge observed at approximately 380 nm corresponds to the direct transition of electrons between the edges of the valence band and the conduction band. The high absorption properties in the UV region indicate that the prepared samples are suitable for UV photoconductive sensor applications.

Figure 5 shows the PL spectra of the as-grown, oxygen-annealed, air-annealed, and vacuum-annealed Al-doped ZnO nanorod arrays. Two emission peaks were detected in the PL measurement, located in the UV region and the visible region. The UV emission is due to the recombination of excitons, whereas the visible emission is caused by the emission of defects [41–43]. The as-grown nanorod arrays have a broad and low-intensity UV emission peak centred at 383 nm and a high-intensity visible emission peak centred at 573 nm. This visible peak is due to the high concentration of OH-groups on the nanorod surface [44]. For the oxygen-annealed nanorod arrays, the intensity of the UV emission peak that is centred at 379 nm increased relative to that of the as-grown nanorod arrays. However, the visible region exhibits a reduced intensity and shift to a higher wavelength. This visible emission peak was shifted to 630 nm and attributed to interstitial oxygen or excess oxygen at the nanorod surface [39, 45]. The oxygen adsorption in the nanorod arrays

(a)

(b)

(c)

(d)

| Element | App. conc. | Intensity corrn. | Weigh... | Weigh... sigma | Atomic (%) | Comp... | Formula | Number of ions |
|---------|-----------|------------------|----------|----------------|------------|---------|---------|----------------|
| Al K | 0.03 | 0.5226 | 0.42 | 0.11 | 0.64 | 0.8 | $Al_2O_3$ | 0.1 |
| Zn L | 7.81 | 0.8073 | 79.69 | 0.27 | 49.21 | 99.2 | ZnO | 7.85 |
| O | | | 19.88 | 0.26 | 50.16 | | | 8 |
| Totals | | | 100 | | | | | |
| | | | | | | | Cation... | 7.95 |

Full scale 16509 cts Cursor: 3.810 (137 cts)          (keV)

(e)
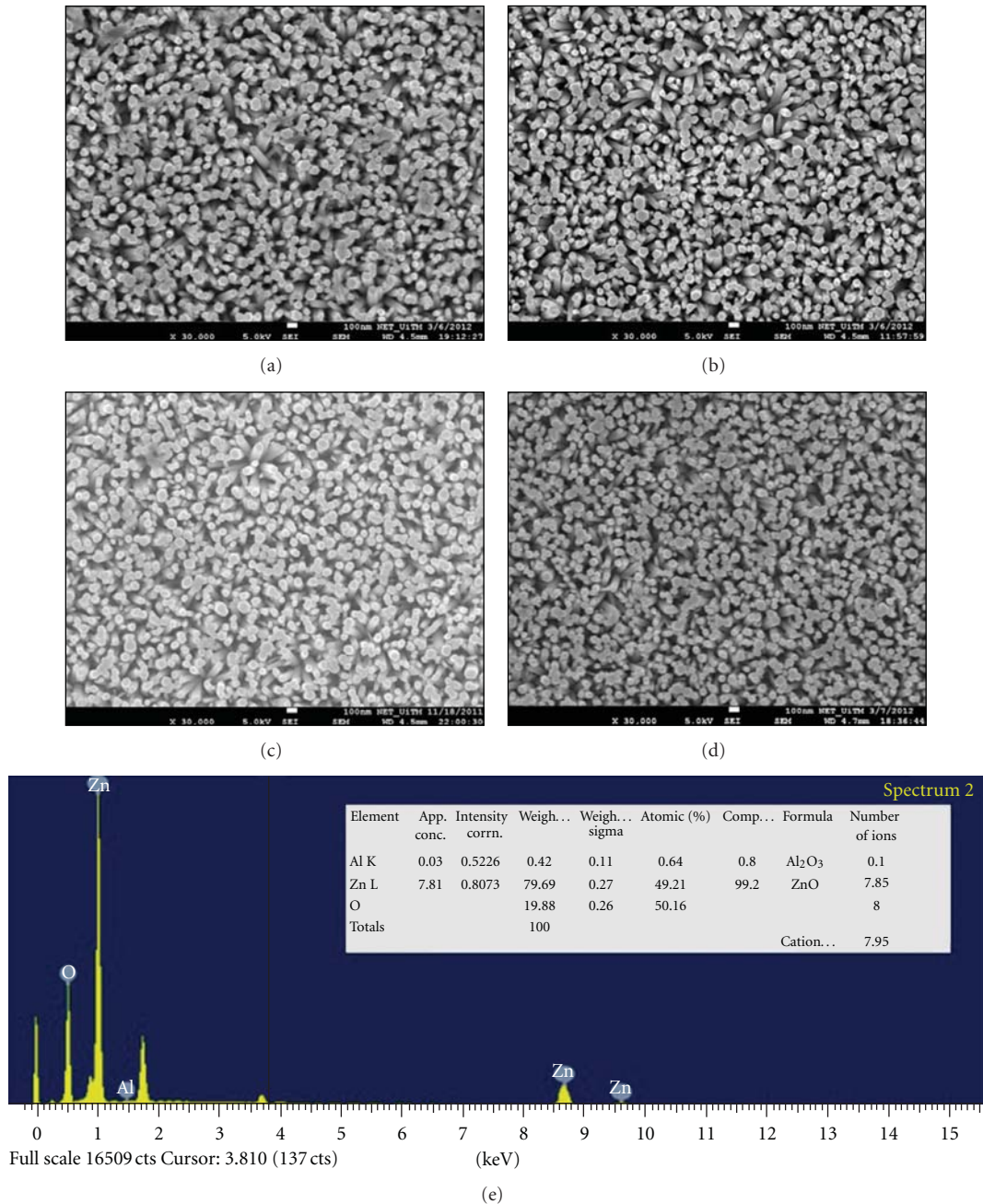
FIGURE 1: Surface morphology of (a) as-grown, (b) oxygen-annealed, (c) air-annealed, and (d) vacuum-annealed Al-doped ZnO nanorod arrays. (e) EDS spectrum of as-grown Al-doped ZnO nanorod arrays.

also decreases the excitonic recombination, as reported by other groups [39, 46]. However, the air-annealed and vacuum-annealed nanorod arrays show almost identical UV emission peak intensity of the peaks that are centred at 379 and 380 nm, respectively, but slightly different intensities in the visible emission peak. The visible emission peak intensity for the air-annealed nanorod arrays was slightly higher than that of the vacuum-annealed nanorod arrays. In addition, these visible emission peak centres for the air-annealed and vacuum-annealed Al-doped ZnO nanorod arrays are located at different wavelengths of 600 nm and 588 nm, respectively. We suspected that this condition is due to different defect conditions, which affected the visible emission of the nanorod arrays. For the air-annealed sample, the defect state may be dominated by oxygen adsorption, but with lower concentration compared to the oxygen-annealed nanorod arrays, whereas for the vacuum-annealed sample, the zinc interstitials and oxygen vacancies may be the prominent defects in the nanorod arrays.

Figure 6 presents the $I$-$V$ measurement spectra of the Al-doped ZnO nanorod arrays annealed in different environments. The $I$-$V$ curves indicate that all of the prepared

(a)



(b)



(c)



(d)
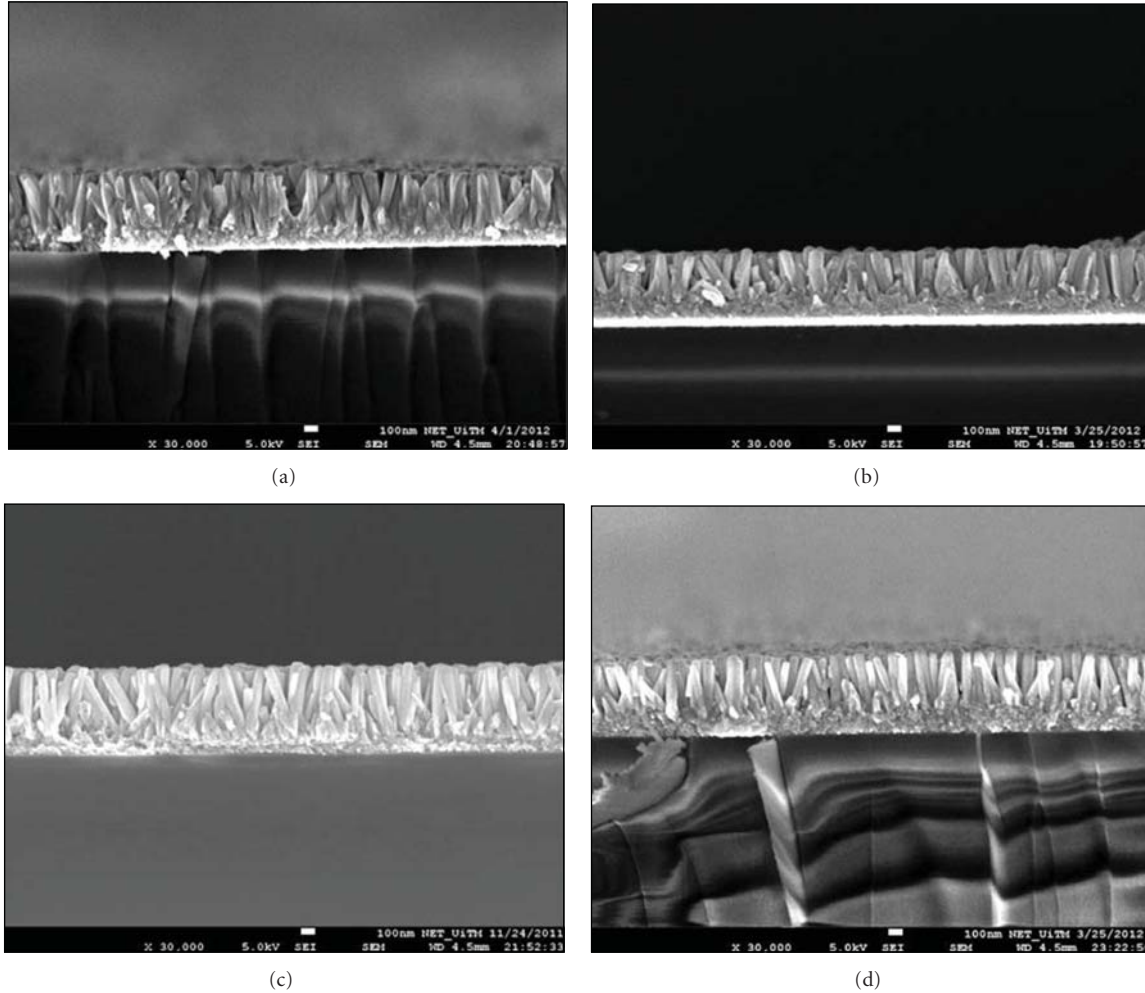
FIGURE 2: Cross-sectional images of (a) as-grown, (b) oxygen-annealed, (c) air-annealed, and (d) vacuum-annealed Al-doped ZnO nanorod arrays.
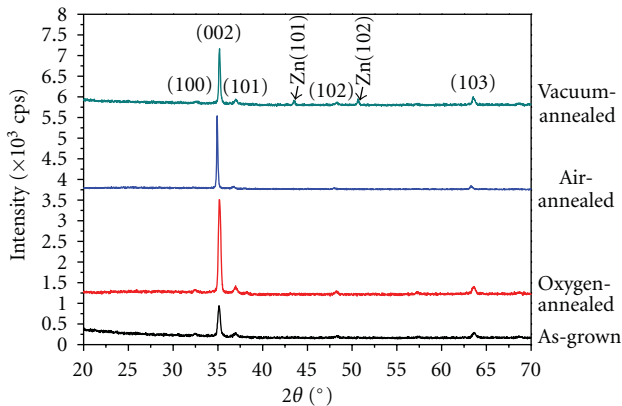


FIGURE 3: XRD patterns of the as-grown, oxygen-annealed, air-annealed, and vacuum-annealed Al-doped ZnO nanorod arrays.

Al-doped ZnO nanorod arrays formed ohmic contacts with the Al contacts. However, the current with respect to the supplied voltage shows different values for the as-grown,

oxygen-annealed, air-annealed, and vacuum-annealed Al-doped ZnO nanorod arrays. According to this spectra, the highest current value is exhibited by the vacuum-annealed sample, followed by the air-annealed sample, then by the as-grown sample, and finally, by the oxygen-annealed sample. From these results, the resistance of the samples were calculated to be 0.80, 1.59, 0.16, and 0.10 MΩ for the as-grown, oxygen-annealed, air-annealed, and vacuum-annealed Al-doped ZnO nanorod arrays, respectively. The lowest resistance of the vacuum-annealed nanorod arrays might be a result of the excess of free carriers due to the Zn interstitials and Al-doping. In addition, annealing in vacuum also removed the adsorbed oxygen on the nanorod surface, which decreased the resistance of the nanorod arrays [47]. However, annealing in oxygen significantly increased the resistance of the nanorod arrays, which is likely due to the large amount of oxygen adsorbed on the surface of the nanorod arrays. During the annealing process in oxygen, oxygen could also diffuse into the nanorod arrays, which induces a high density of acceptor-like defects (i.e., Zn vacancies, oxygen antisites) [48]. This condition results in

(a)

(b)
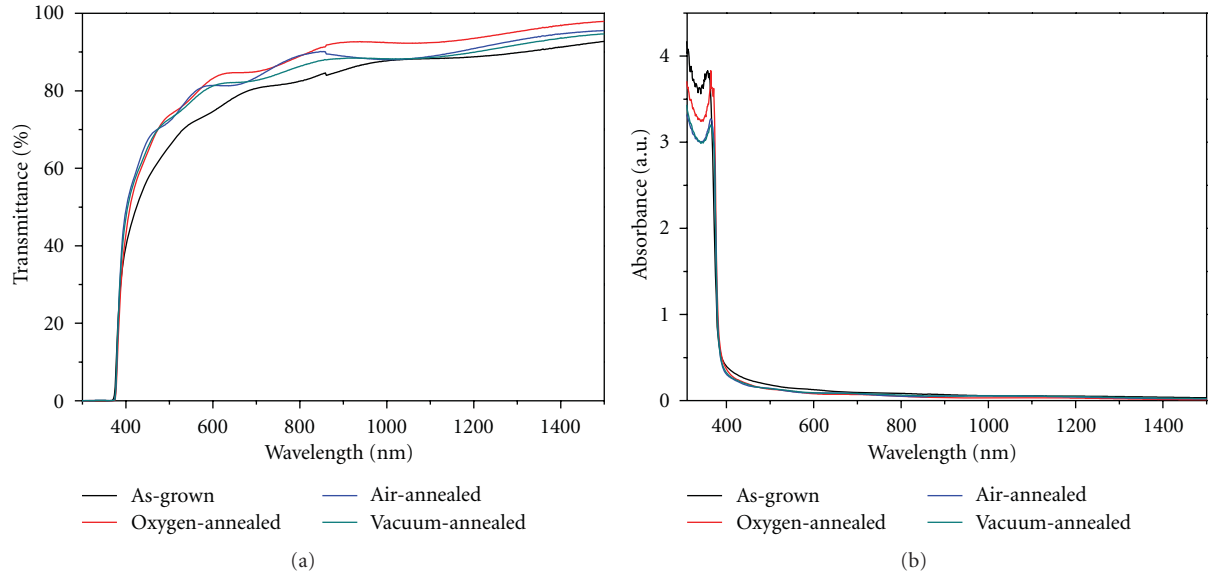
Figure 4: (a) Transmittance and (b) absorbance spectra of the as-grown and annealed Al-doped ZnO nanorod arrays.
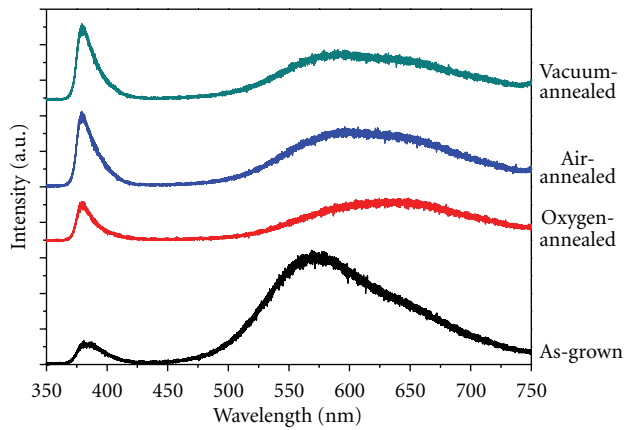


Figure 5: Room temperature PL spectra of the as-grown, oxygen-annealed, air-annealed, and vacuum-annealed Al-doped ZnO nanorod arrays.



Figure 6: Current-voltage ($I$-$V$) plots of the as-grown, oxygen-annealed, air-annealed, and vacuum-annealed Al-doped ZnO nanorod arrays.

the compensation of donor-like defects (i.e., oxygen vacancies, Zn interstitials) and depletion of the carrier density. Meanwhile, annealing the nanorod arrays in air produced the nanorod arrays with a moderate resistance, in which the resistance value was between that of the vacuum-annealed and oxygen-annealed nanorod arrays. This phenomenon is due to the decreased concentration of oxygen molecules in air compared to the concentration of oxygen molecules available during the oxygen annealing process, which reduces the amount of adsorbed oxygen. The as-grown sample presented the highest resistance due to its high defect concentrations and poor crystallinity properties, as shown in the XRD patterns.

Figure 7 depicts the time-resolved photoresponse of the UV photoconductive sensor prepared using the Al-doped ZnO nanorod arrays that were annealed in different environments. The measurements were performed using 365 nm

UV light with an optical power density of $750 \, \mu\text{W/cm}^2$ at a bias voltage of 10 V. Under UV illumination, the Al-doped ZnO nanorod-array-based UV photoconductive sensor showed good photoresponses; the current rapidly increased and then gradually became saturated. The current suddenly decreased when the UV illumination was turned off, eventually returning to its initial value.

The spectra indicate that the photocurrent properties of the sensors provide different responses with the use of Al-doped ZnO nanorod arrays that were annealed in different environments. The spectra reveal that the UV photoconductive sensor with the vacuum-annealed Al-doped ZnO nanorod arrays has the highest photocurrent value of $2.43 \times 10^{-4}$ A. The UV photoconductive sensor that uses
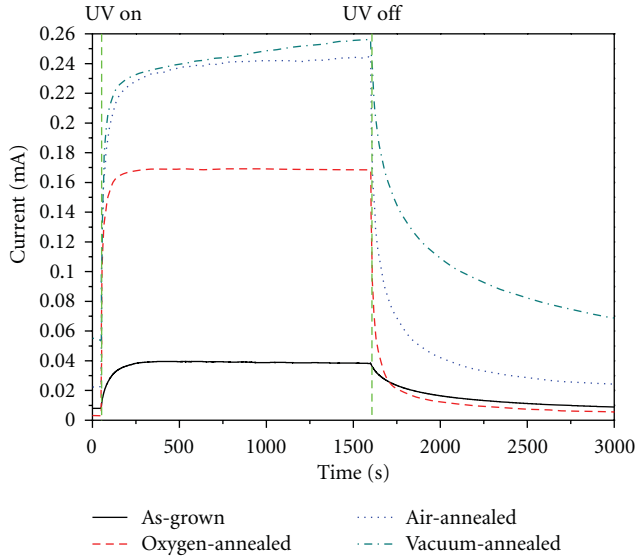
FIGURE 7: Photoresponse spectra of the UV photoconductive sensor using as-grown, oxygen-annealed, air-annealed, and vacuum-annealed Al-doped ZnO nanorod arrays under UV illumination (365 nm, 750 $\mu$W/cm$^2$) and a 10 V bias.

the air-annealed nanorod arrays also has a high photocurrent value ($2.39 \times 10^{-4}$ A) but it is slightly lower than that of the vacuum-annealed nanorod-arrays. However, the photocurrent value of the oxygen-annealed Al-doped ZnO nanorod-array-based UV photoconductive sensor was significantly reduced to $1.69 \times 10^{-4}$ A. Furthermore, the as-grown Al-doped ZnO nanorod array-based UV photoconductive sensor shows the lowest photocurrent value of $3.91 \times 10^{-5}$ A. The highest photocurrent value of the vacuum-annealed Al-doped ZnO nanorod-array-based UV photoconductive sensor could be attributed to the high concentration of Zn interstitials. According to Bera et al., when ZnO nanowires with a high concentration of Zn interstitials are irradiated with UV light, the photogenerated excitons could interact with the Zn interstitials, which results in ionisation of Zn interstitials [13]. When Zn interstitials are ionised, more free electrons are generated in the conduction band, which increases the photocurrent of the sensor. We also proposed that the photogenerated excitons also interact with Al-doping level to contribute more free electrons to the conduction band. However, annealing in air and oxygen results in an improvement of the ZnO stoichiometry, thereby decreasing the concentration of defects, including Zn interstitials. During the annealing process, vacant sites in the ZnO lattice, which resulted from the evaporation of OH groups from the nanorod surface, were immediately replaced by oxygen from the environment. Because of the excessive oxygen flow during the oxygen annealing process, oxygen molecules are easily adsorbed onto the nanorod surface, which results in the increase of the nanorod resistance. As a result, the photocurrents of the Al-doped ZnO nanorod array-based UV photoconductive sensors were reduced after annealing in air and oxygen. For the as-grown Al-doped ZnO nanorod-array-based UV photoconductive sensor, the photocurrent

is low because of the low concentration of photogenerated electrons in the conduction band. This condition is a result of the large concentration of OH-groups on the nanorod surface, which hinders efficient photogeneration during UV illumination. In addition, the as-grown nanorod arrays have a large number of structural defects, which is evident by the less intense XRD peaks compared to the annealed samples. This condition reduces the mobility of the nanorod arrays and induced the recombination of the photogenerated electrons with the defects, which decreased the number of photogenerated electrons in the conduction band.

Generally, the adsorption of oxygen on the nanorod surface causes the existence of a non-conductive barrier or a surface depletion region and thus, an upward band bending. However, the width of this barrier in nanorod arrays may differ after annealing in oxygen, air, and vacuum. According to our results, the band bending of the as-grown Al-doped ZnO nanorod arrays and the Al-doped ZnO nanorod arrays that were annealed in oxygen, air, and vacuum can be illustrated in Figure 8. In this case, among the annealed samples, the oxygen-annealed Al-doped ZnO nanorod arrays have the most depleted surface region due to the large amount of adsorbed oxygen, followed by the air-annealed sample and the vacuum-annealed sample. For this reason, the oxygen-annealed Al-doped ZnO nanorod arrays have lower photocurrent properties compared to the other annealed samples. This theory was also supported by our PL measurement result, in which the UV emission was suppressed and has lower intensity compared to the other annealed samples despite the oxygen-annealed nanorod arrays having the highest crystallinity. Meanwhile, for the as-grown nanorod arrays, the depletion region is primarily attributed to the OH-groups and other native defects of ZnO, such as oxygen vacancies and Zn interstitials.

From the photocurrent spectra, the responsivity of the sensors was estimated using the following equation [49]:

$$R = \frac{I_{\mathrm{ph}} - I_{\mathrm{dark}}}{P_{\mathrm{op}}}, \tag{1}$$

where $I_{\mathrm{ph}}$ is the photocurrent, $I_{\mathrm{dark}}$ is the dark current, and $P_{\mathrm{op}}$ is the optical power of the UV source. In this study, the $I_{\mathrm{dark}}$ values of the sensors fabricated using the as-grown, oxygen-annealed, air-annealed, and vacuum-annealed Al-doped ZnO nanorods are $6.29 \times 10^{-6}$, $3.03 \times 10^{-6}$, $2.26 \times 10^{-5}$, and $5.44 \times 10^{-5}$ A, respectively. From this calculation, the responsivity values of the sensors composed of the as-grown, oxygen-annealed, air-annealed, and vacuum-annealed Al-doped ZnO nanorods are 0.73, 3.69, 4.81, and 4.19 A/W, respectively. This result indicates that the sensor composed of air-annealed ZnO nanorod arrays had a higher responsivity than the other samples. Although the photocurrent value of the vacuum-annealed Al-doped ZnO nanorod-array-based UV sensor is the highest, the sensor exhibits a lower responsivity value than the air-annealed nanorod-based UV photoconductive sensor due to its high dark current value. We believed that this large dark current value of vacuum-annealed Al-doped ZnO nanorod-array-based UV photoconductive sensor is primarily contributed
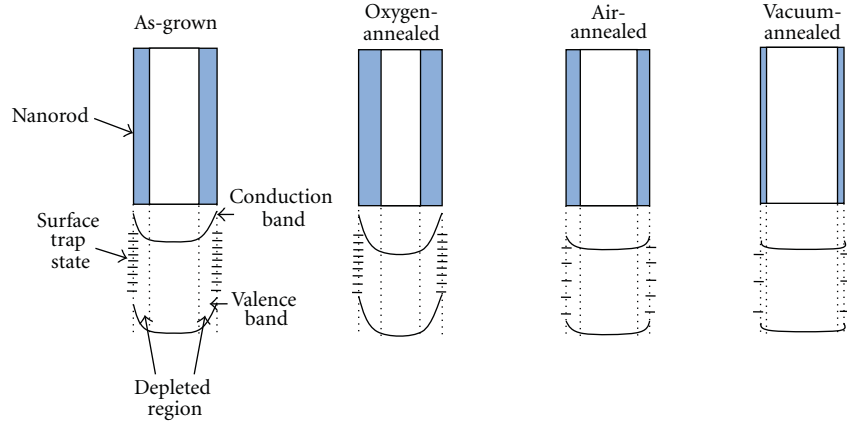
FIGURE 8: Schematic band diagram of the as-grown, oxygen-annealed, air-annealed, and vacuum-annealed Al-doped ZnO nanorod arrays illustrating the band bending due to oxygen adsorption and defects.

to high concentration of Zn interstitials and Al-doping. This condition improves the conductivity of the sensor, which results in significant enhancement of the dark current than that of the other samples.

The sensitivity of the sensors, which is defined as the photocurrent-to-dark-current ratio, was calculated for all of the devices. The sensitivity values of the sensors composed of the as-grown, oxygen-annealed, air-annealed, and vacuum-annealed Al-doped ZnO nanorod arrays are 6.2, 55.6, 10.6, and 4.6, respectively. The results indicate that the oxygen-annealed Al-doped ZnO nanorod array-based UV photoconductive sensors had the highest sensitivity. The improvement of the sensor sensitivity by oxygen annealing is due to the significant reduction of the dark current value as compared with the other samples. We suspect that the significant reduction in the dark current value is correlated with more adsorbed oxygen on the oxygen-annealed nanorod arrays, which increases the resistance of the film, as shown by the $I$-$V$ measurement results. In addition, annealing in oxygen improves the surface condition of the nanorod arrays, which increases their affinity for the oxygen molecules. The sensitivity of the sensor has been reported to be correlated with the oxygen adsorption and desorption processes [12, 33, 50]. In the dark, oxygen molecules tend to adsorb onto the nanorod surfaces by capturing free electrons and producing adsorbed oxygen ions, as shown by the following equation:

$$O_2 + e^- \longrightarrow O_2^-, \tag{2}$$

where $O_2$ is the oxygen molecule, $e^-$ is the free electron, and $O_2^-$ is the adsorbed oxygen ion on the nanorod surface. The adsorbed oxygen ions create a barrier near the surface, which generates a low current before UV illumination. When UV light is irradiated onto the nanorods, photogenerated electron-hole pairs are generated at the surface according to the following equation:

$$h\nu \longrightarrow h^+ + e^-, \tag{3}$$

where $h\nu$ is the photon energy of UV light, $h^+$ is the photo-generated hole in the valence band, and $e^-$ is the photogenerated electron in the conduction band. The photogenerated

holes recombine with the adsorbed oxygen ions on the surface, producing oxygen molecules; this reaction also eliminates the barrier near the nanorod surface. This process is described by the following equation:

$$O_2^- + h^+ \longrightarrow O_2. \tag{4}$$

At the same time, the desorption of adsorbed oxygen ions on the nanorod surface leaves photogenerated electrons in the conduction band, thereby increasing the film conductivity and contributing to the photocurrent. When the UV light is switched off, oxygen once again begins to adsorb onto the nanorod surface, thereby decreasing the conductivity of the sensor.

Using the photocurrent spectra, the rise and decay time constants of the fabricated sensors were calculated using the following equations:

$$I =$$

$$I_0 \left[ 1 - \exp\left( -\frac{t}{\tau_r} \right) \right] : \text{rise process with UV illumination on,}$$

$$I = I_0 \exp\left( -\frac{t}{\tau_d} \right) : \text{decay process with UV illumination off,}$$

$$\tag{5}$$

where $I$ is the magnitude of the current, $I_0$ is the saturated photocurrent, $t$ is the time $\tau_r$ is the rise time constant, and $\tau_d$ is the decay time constant. The calculation results indicate that the sensors constructed using the as-grown, oxygen-annealed, air-annealed, and vacuum-annealed Al-doped ZnO nanorod arrays have rise (decay) time constants of 38 (109), 3 (13), 10 (26), and 15 (52) s, respectively. Based on these results, it can be concluded that the oxygen-annealed Al-doped ZnO nanorod array-based UV photoconductive sensor exhibits the fastest response. This behaviour may be attributed to the surface condition of the oxygen-annealed Al-doped ZnO nanorod arrays, which can promptly adsorb and desorb oxygen during the switching on and off of the UV illumination, thereby resulting in sudden changes in the nanorod resistance. In addition,

(a)

(b)

(c)

(d)
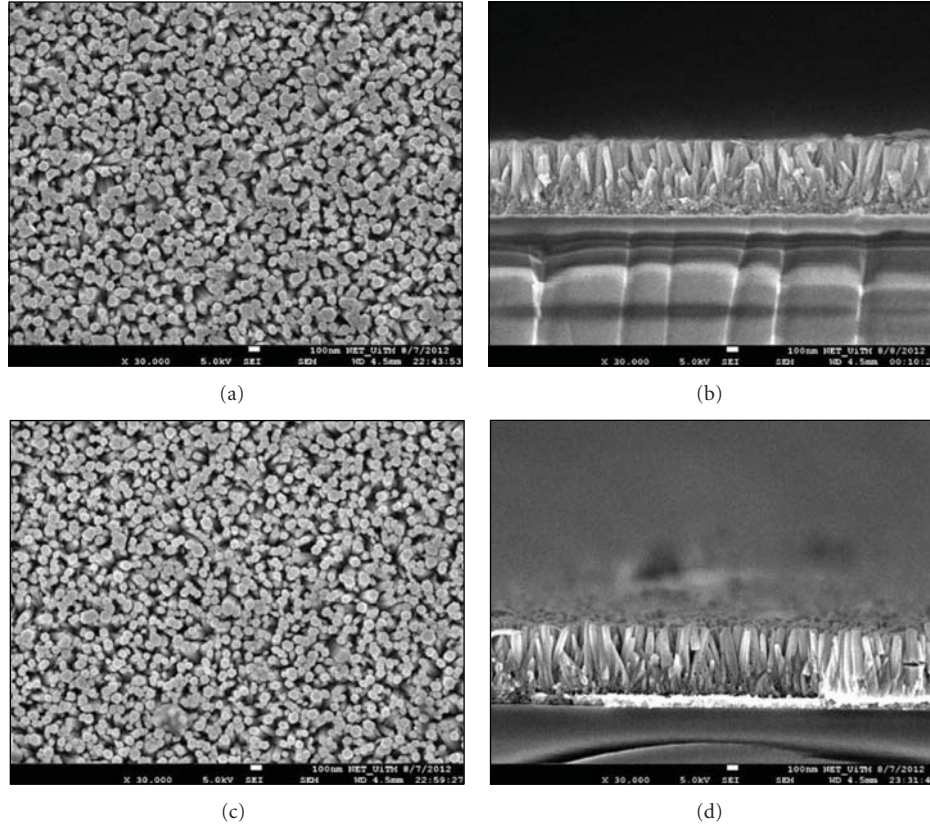
FIGURE 9: Surface morphology and cross-sectional images of Al-doped ZnO nanorod arrays as a function of immerse time: ((a)-(b)) 100 min and ((c)-(d)) 150 min.

TABLE 1: The characteristics of the as-grown, oxygen-annealed, air-annealed, and vacuum-annealed Al-doped ZnO nanorod-array-based UV photoconductive sensors.

| Sample | Resistance (MΩ) | Dark current (A) | Photocurrent (A) | Rise time constant (s) | Decay time constant (s) | Responsivity (A/W) | Sensitivity |
|---|---|---|---|---|---|---|---|
| As-grown | 0.80 | $6.29 \times 10^{-6}$ | $3.91 \times 10^{-5}$ | 38 | 109 | 0.73 | 6.2 |
| Oxygen-annealed | 1.59 | $3.03 \times 10^{-6}$ | $1.69 \times 10^{-4}$ | 3 | 13 | 3.69 | 55.6 |
| Air-annealed | 0.16 | $2.26 \times 10^{-5}$ | $2.39 \times 10^{-4}$ | 10 | 26 | 4.81 | 10.6 |
| Vacuum-annealed | 0.10 | $5.44 \times 10^{-5}$ | $2.43 \times 10^{-4}$ | 15 | 52 | 4.19 | 4.6 |

the oxygen-annealed Al-doped ZnO nanorod arrays possess better crystallinity than the other samples, which enhances the mobility of the photogenerated carriers in the nanorod arrays. In comparison, the vacuum-annealed nanorod arrays show a higher rise and decay time constant due to the prominent electron trapping at the positively charged Zn interstitial defect state, which has a large lifetime [51]. The characteristics of the as-grown, oxygen-annealed, air-annealed, and vacuum-annealed Al-doped ZnO nanorod-array-based UV photoconductive sensors are presented in Table 1.

We also investigate the UV photoconductive sensors performance using air-annealed Al-doped ZnO nanorod arrays that were prepared for longer immersion times of 100 and 150 min. Figures 9(a) and 9(c) show the surface morphologies of air-annealed Al-doped ZnO nanorod arrays

immersed for 100 and 150 min, respectively. In these FESEM images, dense nanorod arrays can be observed with high uniformity across all samples. However, the diameter of the nanorods is almost constant at 60 nm with further increase of immersion time up to 150 min. Figures 9(b) and 9(d) show the cross-sectional images of air-annealed Al-doped ZnO nanorod arrays prepared at immersion time of 100 and 150 nm, respectively. Based on the cross-sectional images, the thickness of the film increase, with the increase of immersion time. On the basis of the FESEM measurements, the thicknesses of the films prepared by immersion for 100 and 150 min are approximately 650 and 700 nm, respectively. Figure 10 depicts $I$-$V$ curves of Al-doped ZnO nanorod arrays prepared at different immersion times. The graphs reveal that the current intensity with respect to the voltage decrease when the immersion time was increased up to
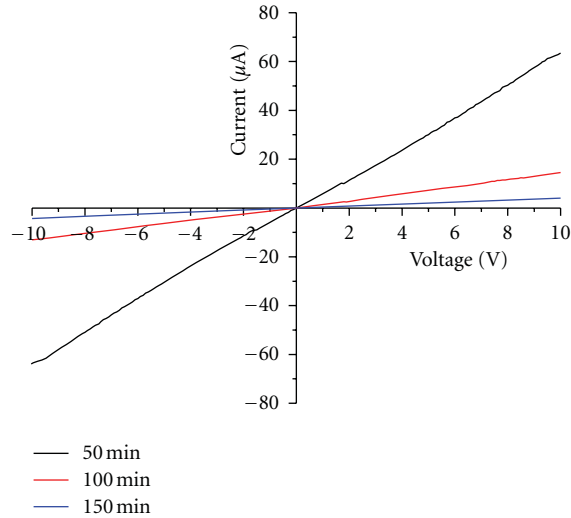
FIGURE 10: The *I-V* characteristic of air-annealed Al-doped ZnO nanorod arrays prepared for different immersion times.
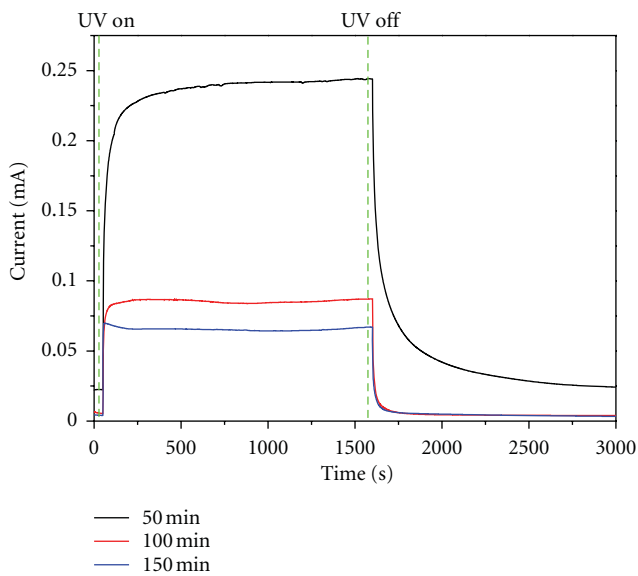


FIGURE 11: Photoresponse spectra of the UV photoconductive sensor using air-annealed Al-doped ZnO nanorod arrays prepared for different immersion times under UV illumination (365 nm, 750 $\mu$W/cm$^2$) and a 10 V bias.

150 min. The resistance of the samples was calculated to be 0.72 and 2.41 M$\Omega$ for the nanorod prepared at immersion time of 100 and 150 min, respectively.

Figure 11 shows the time-resolved photoresponse of the UV photoconductive sensor prepared using the air-annealed Al-doped ZnO nanorod arrays that were prepared at longer immersion times of 100 and 150 min. The results show that both photocurrent and dark current of the sensors were decreased with the increase of immersion time. The photocurrent/dark current values of the sensors are 8.41 $\times$ 10$^{-5}$/5.43 $\times$ 10$^{-6}$ and 6.50 $\times$ 10$^{-5}$/4.07 $\times$ 10$^{-6}$ A for the nanorod arrays prepared for immersion times of 100

and 150 min, respectively. The reduction in photocurrent value for sensors using nanorod arrays prepared for longer time influenced the responsivity of the devices; devices using nanorod arrays prepared for longer immersion time exhibited lower responsivity values. The responsivity values of the sensors are 1.75 and 1.36 A/W for the nanorod arrays prepared for immersion times of 100 and 150 min, respectively. In this case, we believed that the decrease of the photocurrent and responsivity values of the devices was affected by the increase of the resistance of the nanorod arrays after being immersed for longer times. However, the sensitivity of the devices is slightly increased using Al-doped ZnO nanorod arrays immersed for longer times. The sensitivity values of the devices are 15.5 and 16.0 using Al-doped ZnO nanorod arrays prepared for 100 and 150 min, respectively. This sensitivity increment may be attributed to decrease of the dark current and increase of the surface area for the devices using Al-doped ZnO nanorod arrays immersed for longer times.

In order to understand the effects of Al doping on ZnO nanorod array-based UV photoconductive sensor performance, air-annealed undoped and Al-doped ZnO nanorod-array-based UV photoconductive sensor were studied. Figure 12(a) shows FESEM image of air-annealed undoped ZnO nanorod arrays at magnification of 30,000x. The image reveals that undoped ZnO nanorods have been uniformly deposited on the seed-layer-coated glass substrate. The diameter of the undoped ZnO nanorod is estimated to be 100 nm, in which the size is larger than that of the air-annealed Al-doped ZnO nanorod and other samples. A cross-sectional image as shown in Figure 12(b) confirms that the nanorods grew perpendicular to the substrate with the thickness estimated to be approximately 600 nm. Figures 13(a)–13(d) show TEM images and SAED patterns of air-annealed undoped and Al-doped ZnO nanorods. These results indicate that both undoped and Al-doped ZnO nanorods are single crystals with wurtzite ZnO structure. The TEM images also reveal that the size of the Al-doped ZnO nanorod is smaller than the undoped ZnO, which attributed to the effect of the doped Al. The Al$^{3+}$ ions (0.054 nm) have smaller ionic radius than Zn$^{2+}$ ions (0.074 nm) and it is expected that this ionic radius difference may influence the diameter of ZnO nanorods when doped with Al [52, 53].

Figure 14 shows the *I-V* properties of the undoped and Al-doped ZnO nanorod arrays, which clearly show that the undoped ZnO nanorod arrays exhibit lower current value than that of Al-doped ZnO nanorod arrays with respect to the supplied voltage. From this *I-V* characteristic, the resistance of the undoped arrays was calculated to be 1.15 M$\Omega$. It is understood that this resistance value is higher than resistance value of air-annealed, vacuum-annealed, and as-grown Al-doped ZnO nanorod arrays but show lower values than that of oxygen-annealed Al-doped ZnO nanorod arrays.

Figure 15 shows the photoresponse spectra of the air-annealed undoped and Al-doped ZnO nanorod-array-based UV photoconductive sensors. The spectra reveal that both photocurrent and dark current of the undoped ZnO

(a)



(b)
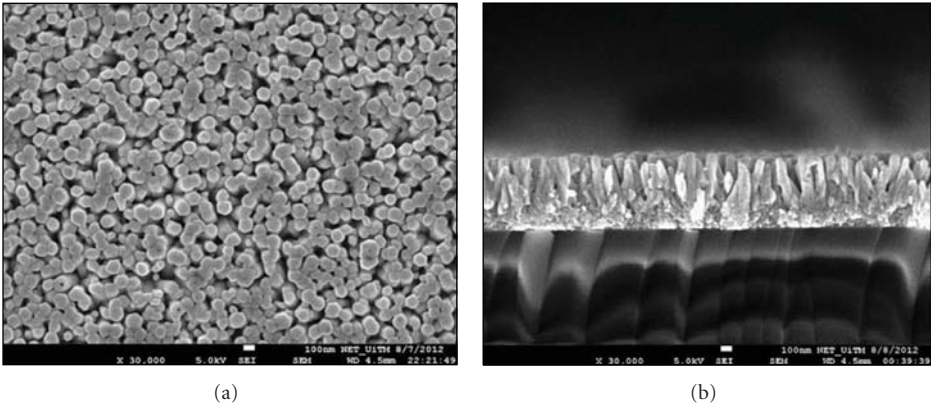
FIGURE 12: (a) Surface morphology and (b) cross-sectional images of undoped ZnO nanorod arrays.



(a)



(b)



(c)



(d)
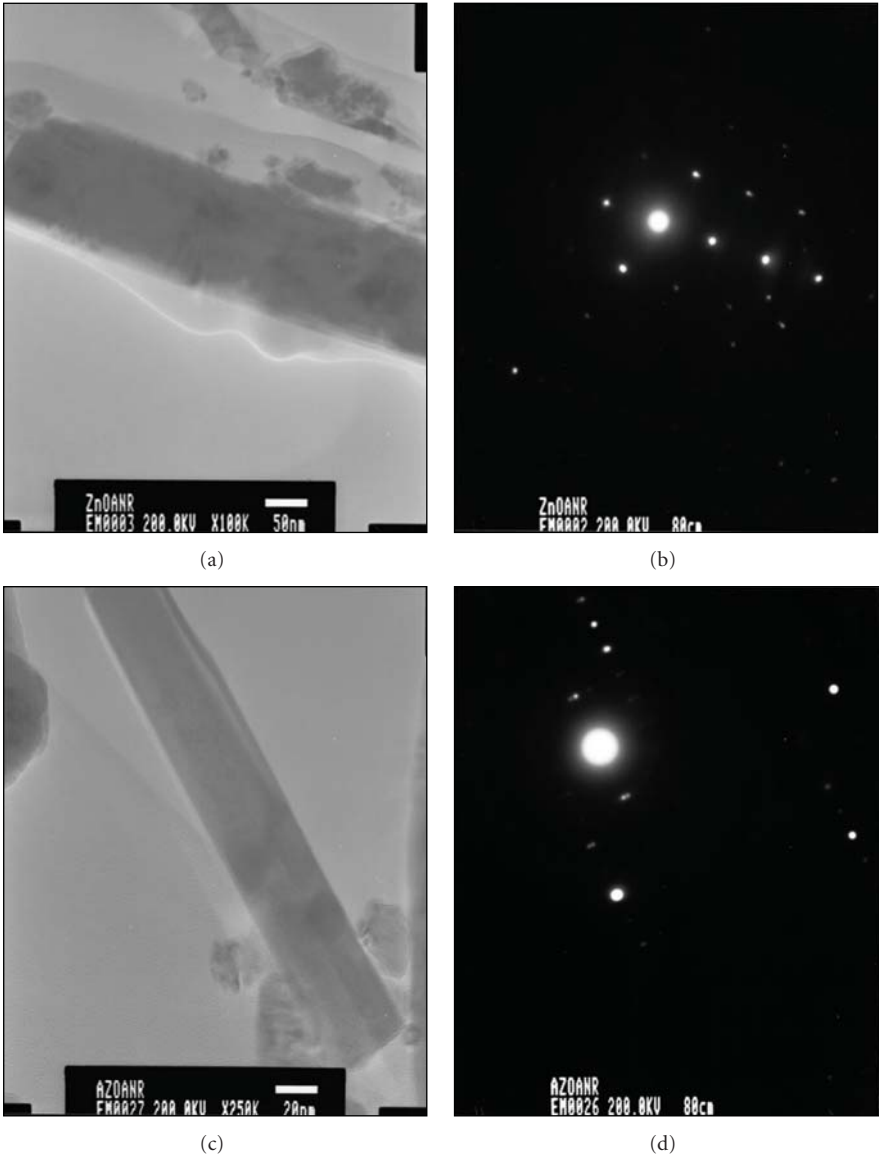
FIGURE 13: (a) TEM image and (b) SAED pattern of the undoped ZnO nanorod. (c) TEM image and (d) SAED pattern of the Al-doped ZnO nanorod.

FIGURE 14: The $I$-$V$ characteristic of air-annealed undoped and Al-doped ZnO nanorod arrays.



FIGURE 15: Photoresponse of undoped and Al-doped ZnO nanorod array-based UV photoconductive sensors under UV illumination (365 nm, 750 $\mu$W/cm$^2$) and a 10 V bias.

$Zn^{2+}$ ions in their sites in ZnO lattice to generate free electron in the process [8, 54, 55]. This condition increases the carrier concentration of the nanorod arrays and thus, improves the photocurrent and responsivity values of the Al-doped ZnO nanorod-array-based UV photoconductive sensors. Moreover, this phenomenon could also attributed to the higher surface to volume ratio of Al-doped ZnO nanorod-arrays compared to the undoped ZnO, which is contributed by smaller size of the Al-doped ZnO nanorod as can be observed in the FESEM and TEM images in Figures 12 and 13, respectively. Besides that, the doped Al was also reported to increase the stability and performance of the UV photoconductive sensor by decreasing the defect incident in ZnO such as Zn interstitials and oxygen vacancies [8, 56]. On the other hand, the sensitivity value of the undoped ZnO nanorod array-based UV photoconductive sensor was greater than that of the as-grown and vacuum-annealed Al-doped ZnO nanorod array-based devices but lower than that of air-annealed and oxygen-annealed Al-doped ZnO nanorod array-based UV photoconductive sensor. We believed that this condition is mainly attributed to the low dark current value of the undoped ZnO nanorod array-based UV photoconductive sensor, which increases the sensitivity value compared to that of the as-grown and vacuum-annealed Al-doped ZnO nanorod array-based devices. However, the undoped ZnO nanorod arrays lack free electron, which lower the photocurrent value of the device. As a result, the sensitivity of the undoped ZnO nanorod array-based UV photoconductive sensor is lower than that of the air-annealed and oxygen-annealed Al-doped ZnO nanorod array-based UV photoconductive sensors.

In comparison with our previous study, the Al-doped ZnO nanorod arrays show better UV sensing than that of the ZnO nanoparticle thin film especially in term of photocurrent and responsivity. The ZnO nanoparticles used in UV photoconductive sensors tend to exhibit sluggish photoresponses; this is likely the result of grain boundary effects and the presence of surface defects, which reduce the carrier mobility and increase carrier scattering within the thin film [49, 55, 57, 58]. The use of the nanorod arrays enhanced the UV photoconductive sensor performance due to their high mobility and high surface-to-volume ratio. Bera et al. emphasised that the UV photoconductivity of ZnO is strongly related to the surface reaction processes; thus, the high surface-to-volume ratios in the one-dimensional (1D) nanostructure (i.e., nanorod) enhance the sensitivity of the sensor beyond that of the ZnO nanoparticle thin film [13]. According to Soci et al., 1D structures have several advantages over bulk or thin films in UV sensor applications, including light scattering enhancements that reduce optical losses, improved light absorption, high photosensitivity due to the high gain, and the possibility to integrate functionalities within single 1D devices [59]. The prolonged photocarrier lifetime, which is due to charge separation promoted by surface states, and the reduction in carrier transit time, which can be achieved in high-quality, low-defect ZnO nanorods together with small gaps in the metal contacts, both contribute to the high gain in nanorod-based devices [59, 60].

nanorod-array-based UV photoconductive sensor show lower values than that of the Al-doped ZnO nanorod-array-based UV photoconductive sensor. The photocurrent/ dark current of the device is $2.98 \times 10^{-5}/2.97 \times 10^{-6}$ A, while the responsivity and sensitivity values were calculated to be 0.60 A/W and 10.0, respectively. When comparing the performance of the undoped and Al-doped ZnO nanorod-array-based UV photoconductive sensors (i.e., as-grown, oxygen-annealed, air-annealed, and vacuum-annealed Al-doped ZnO nanorod arrays), the undoped ZnO nanorod-array-based device shows the lowest photocurrent and responsivity values. From this result, it can be shown that the doped Al improved the photocurrent and responsivity of the devices by increasing the carrier concentration of the nanorod arrays. When ZnO is doped with Al, the $Al^{3+}$ ions substitute the

## 4. Conclusions

UV photoconductive sensors were successfully fabricated using Al-doped ZnO nanorod arrays that were annealed at 500°C in different environments. The nanorod arrays were prepared on seed-layer-coated glass substrates using sonicated sol-gel immersion. FESEM images reveal that the deposited nanorods have an average diameter of 60 nm with a thickness of approximately 600 nm including the seed layer. Interestingly, after annealing in different environments (i.e., oxygen, air, and vacuum), the morphology and thickness of the nanorod arrays remain almost unchanged. The XRD patterns indicate that the as-grown and annealed nanorod arrays have a prominent peak for the (002) orientation, with the oxygen-annealed nanorod arrays presenting the highest peak intensity, followed by the air-annealed, vacuum-annealed and as-grown nanorod arrays. For the vacuum-annealed nanorod arrays, the XRD measurement detected the appearance of Zn peaks, which indicates that the nanorod arrays are rich in Zn interstitial defects. The prepared nanorod arrays also show high transmittance properties in the visible region with an average transmittance of over 72%. According to the PL measurement spectra, the vacuum-annealed nanorod arrays have the highest UV emission peak intensity compared to the other samples. However, the air-annealed nanorod arrays show slightly lower UV emission peak intensity than those of the vacuum-annealed nanorod arrays, whereas for the oxygen-annealed nanorod arrays, the UV emission peak intensity is lower than that of the air-annealed arrays but higher than that of the as-grown nanorod arrays. Notably, we also observed that the oxygen-annealed nanorod arrays have visible emission that is centred at 630 nm, at which the intensity was almost similar with the UV emission. This visible emission was correlated with oxygen interstitials or adsorbed oxygen on the nanorod surface. The $I$-$V$ measurement spectra show that oxygen-annealed nanorod arrays have higher resistance values than the other samples, which was due to oxygen adsorption on the nanorod surface. In contrast, the vacuum-annealed nanorod arrays have low resistance values, which is due to the high concentration of Zn interstitials. The photocurrent measurement spectra indicate that the vacuum-annealed nanorod arrays exhibit the highest photocurrent, followed by the air-annealed, oxygen-annealed, and as-grown nanorod arrays. However, the oxygen-annealed nanorod-array-based UV photoconductive sensor shows the highest sensitivity value of 55.6. This result was due to the significant reduction of the dark current and suitable surface conditions of the nanorod arrays, which facilitates fast oxygen adsorption and desorption processes. In addition, the oxygen-annealed nanorod arrays also show lower rise and decay time constants compared to the other samples.

## Acknowledgments

## References

[1] J. Y. Chen and K. W. Sun, "Growth of vertically aligned ZnO nanorod arrays as antireflection layer on silicon solar cells," *Solar Energy Materials and Solar Cells*, vol. 94, no. 5, pp. 930–934, 2010.

[2] F. Xu, M. Dai, Y. Lu, and L. Sun, "Hierarchical ZnO nanowire-nanosheet architectures for high power conversion efficiency in dye-sensitized solar cells," *Journal of Physical Chemistry C*, vol. 114, no. 6, pp. 2776–2782, 2010.

[3] Z. X. Zhou, J. X. Gao, and Z. L. Wu, "Materials and Devices research of PPV-ZnO Nanowires for heterojunction solar cells," *Journal of Nanomaterials*, vol. 2012, Article ID 368236, 4 pages, 2012.

[4] S. P. Chang and T. H. Chang, "Use of the thermal chemical vapor deposition to fabricate light-emitting diodes based on zno nanowire/p-GaN heterojunction," , *Journal of Nanomaterials*, vol. 2011, Article ID 903176, 4 pages, 2011.

[5] J. Singh, S. S. Patil, M. A. More, D. S. Joag, R. S. Tiwari, and O. N. Srivastava, "Formation of aligned ZnO nanorods on self-grown ZnO template and its enhanced field emission characteristics," *Applied Surface Science*, vol. 256, no. 21, pp. 6157–6163, 2010.

[6] M. H. Mamat, Z. Khusaimi, M. F. Malik, M. M. Zahidi, and M. R. Mahmood, "Ultra-violet sensing characteristic and field emission properties of vertically aligned aluminum doped zinc oxide nanorod arrays," in *Proceedings of the International Conference on Enabling Science and Nanotechnology (ESciNano'10)*, Kuala Lumpur, Malaysia, December 2010.

[7] S. Moradi, P. A. Azar, S. R. Farshid, S. A. Khorrami, and M. H. Givianrad, "Effect of Additives on Characterization and Photocatalytic Activity of Tio$_2$/ZnO Nanocomposite Prepared via Sol-Gel Process," *International Journal of Chemical Engineering*, vol. 2012, Article ID 215373, 5 pages, 2012.

[8] M. H. Mamat, Z. Khusaimi, M. Z. Musa, M. F. Malek, and M. Rusop, "Fabrication of ultraviolet photoconductive sensor using a novel aluminium-doped zinc oxide nanorod-nanoflake network thin film prepared via ultrasonic-assisted sol-gel and immersion methods," *Sensors and Actuators, A*, vol. 171, pp. 241–247, 2011.

[9] O. Lupan, G. Chai, L. Chow et al., "Ultraviolet photoconductive sensor based on single ZnO nanowire," *Physica Status Solidi (A)*, vol. 207, no. 7, pp. 1735–1740, 2010.

[10] H. Jeong, K. S. Kim, Y. H. Kim et al., "A crossbar-type high sensitivity ultraviolet photodetector array based on a one hole—one nanorod configuration via nanoimprint lithography," *Nanotechnology*, vol. 22, no. 27, Article ID 275310, 2011.

[11] B. Yuan, X. J. Zheng, Y. Q. Chen, B. Yang, and T. Zhang, "High photosensitivity and low dark current of photoconductive semiconductor switch based on ZnO single nanobelt," *Solid-State Electronics*, vol. 55, no. 1, pp. 49–53, 2011.

[12] J. P. Kar, S. N. Das, J. H. Choi, Y. A. Lee, T. Y. Lee, and J. M. Myoung, "Fabrication of UV detectors based on ZnO nanowires using silicon microchannel," *Journal of Crystal Growth*, vol. 311, no. 12, pp. 3305–3309, 2009.

[13] A. Bera, T. Ghosh, and D. Basak, "Enhanced photoluminescence and photoconductivity of ZnO nanowires with sputtered Zn," *ACS Applied Materials and Interfaces*, vol. 2, no. 10, pp. 2898–2903, 2010.

[14] G. Y. Chai, L. Chow, O. Lupan et al., "Fabrication and characterization of an individual ZnO microwire-based UV photodetector," *Solid State Sciences*, vol. 13, no. 5, pp. 1205–1210, 2011.

[15] M. Rosina, P. Ferret, P. H. Jouneau et al., "Morphology and growth mechanism of aligned ZnO nanorods grown by catalyst-free MOCVD," *Microelectronics Journal*, vol. 40, no. 2, pp. 242–245, 2009.

[16] G. M. Fuge, T. M. S. Holmes, and M. N. R. Ashfold, "Ultrathin aligned ZnO nanorod arrays grown by a novel diffusive pulsed laser deposition method," *Chemical Physics Letters*, vol. 479, no. 1–3, pp. 125–127, 2009.

[17] M. H. Mamat, Z. Khusaimi, M. M. Zahidi et al., "Controllable growth of vertically aligned aluminum-doped zinc oxide nanorod arrays by sonicated sol-gel immersion method depending on precursor solution volumes," *Japanese Journal of Applied Physics*, vol. 50, no. 6, Article ID 06GH04, 2011.

[18] M. Mehrabian, R. Azimirad, K. Mirabbaszadeh, H. Afarideh, and M. Davoudian, "UV detecting properties of hydrothermal synthesized ZnO nanorods," *Physica E*, vol. 43, no. 6, pp. 1141–1145, 2011.

[19] M. H. Mamat, Z. Khusaimi, M. Z. Musa, M. Z. Sahdan, and M. Rusop, "Novel synthesis of aligned Zinc oxide nanorods on a glass substrate by sonicated sol-gel immersion," *Materials Letters*, vol. 64, no. 10, pp. 1211–1214, 2010.

[20] M. H. Mamat, M. Z. Sahdan, S. Amizam, H. A. Rafaie, Z. Khusaimi, and M. Rusop, "Properties of nanostructured zinc oxide by hydro-thermal aqueous chemical growth method," in *Proceedings of the International Conference on Nanoscience and Nanotechnology (Nano-SciTech'08)*, pp. 586–590, Selangor, Malaysia, November 2008.

[21] A. Bera and D. Basak, "Pd-nanoparticle-decorated ZnO nanowires: ultraviolet photosensitivity and photoluminescence properties," *Nanotechnology*, vol. 22, no. 26, Article ID 265501, 2011.

[22] A. Bera and D. Basak, "Effect of surface capping with poly(vinyl alcohol) on the photocarrier relaxation of ZnO nanowires." *ACS applied materials & interfaces*, vol. 1, no. 9, pp. 2066–2070, 2009.

[23] L. Qin, C. Shing, S. Sawyer, and P. S. Dutta, "Enhanced ultraviolet sensitivity of zinc oxide nanoparticle photoconductors by surface passivation," *Optical Materials*, vol. 33, no. 3, pp. 359–362, 2011.

[24] N. Chantarat, Y. W. Chen, S. Y. Chen, and C. C. Lin, "Enhanced UV photoresponse in nitrogen plasma ZnO nanotubes," *Nanotechnology*, vol. 20, no. 39, Article ID 395201, 2009.

[25] B. Angadi, H. C. Park, H. W. Choi, J. W. Choi, and W. K. Choi, "Oxygen plasma treated epitaxial ZnO thin films for Schottky ultraviolet detection," *Journal of Physics D*, vol. 40, no. 5, article no. 016, pp. 1422–1425, 2007.

[26] H. W. Ra, R. Khan, J. T. Kim, B. R. Kang, K. H. Bai, and Y. H. Im, "Effects of surface modification of the individual ZnO nanowire with oxygen plasma treatment," *Materials Letters*, vol. 63, no. 28, pp. 2516–2519, 2009.

[27] W. Park, G. Jo, W. K. Hong et al., "Enhancement in the photodetection of ZnO nanowires by introducing surface-roughness-induced traps," *Nanotechnology*, vol. 22, no. 20, Article ID 205204, 2011.

[28] S. P. Chang, R. W. Chuang, S. J. Chang, C. Y. Lu, Y. Z. Chiou, and S. F. Hsieh, "Surface HCl treatment in ZnO photoconductive sensors," *Thin Solid Films*, vol. 517, no. 17, pp. 5050–5053, 2009.

[29] D. Byrne, E. McGlynn, M. O. Henry, K. Kumar, and G. Hughes, "A novel, substrate independent three-step process for the growth of uniform ZnO nanorod arrays," *Thin Solid Films*, vol. 518, no. 16, pp. 4489–4492, 2010.

[30] T. G. G. Maffeis, M. W. Penny, A. Castaing, O. J. Guy, and S. P. Wilks, "XPS investigation of vacuum annealed vertically aligned ultralong ZnO nanowires," *Surface Science*, vol. 606, pp. 99–103, 2012.

[31] M. Z. Sahdan, M. H. Mamat, M. Salina, Z. Khusaimi, U. M. Noor, and M. Rusop, "Heat treatment effects on the surface morphology and optical properties of ZnO nanostructures," *Physica Status Solidi C*, vol. 7, no. 9, pp. 2286–2289, 2010.

[32] S. Dhara and P. Giri, "Enhanced UV photosensitivity from rapid thermal annealed vertically aligned ZnO nanowires," *Nanoscale Research Letters*, vol. 6, p. 504, 2011.

[33] K.-P. Kim, D. Chang, S. K. Lim, S. K. Lee, H. K. Lyu, and D. K. Hwang, "Thermal annealing effects on the dynamic photoresponse properties of Al-doped ZnO nanowires network," *Current Applied Physics*, vol. 11, pp. 1311–1314, 2011.

[34] M. H. Mamat, Z. Khusaimi, M. Z. Musa, M. F. Malek, and M. Rusop, "Ultraviolet sensing mechanism and characteristics of environmentally friendly aligned aluminium doped zinc oxide nanorod arrays prepared using low cost solution growth method," *Materials Research Innovations*, vol. 15, p. s148, 2011.

[35] H. Zhou, G.-J. Fang, N. Liu, and X. Z. Zhao, "Effects of thermal annealing on the performance of Al/ZnO nanorods/Pt structure ultraviolet photodetector," *Materials Science and Engineering B*, vol. 176, no. 9, pp. 740–744, 2011.

[36] M. H. Mamat, M. Z. Sahdan, Z. Khusaimi, A. Z. Ahmed, S. Abdullah, and M. Rusop, "Influence of doping concentrations on the aluminum doped zinc oxide thin films properties for ultraviolet photoconductive sensor applications," *Optical Materials*, vol. 32, no. 6, pp. 696–699, 2010.

[37] M. Qiu, Z. Ye, J. Lu et al., "Growth and properties of ZnO nanorod and nanonails by thermal evaporation," *Applied Surface Science*, vol. 255, no. 7, pp. 3972–3976, 2009.

[38] W. M. Kwok, A. B. Djurišić, Y. H. Leung et al., "Influence of annealing on stimulated emission in ZnO nanorods," *Applied Physics Letters*, vol. 89, no. 18, Article ID 183112, 2006.

[39] J. W. P. Hsu, D. R. Tallant, R. L. Simpson, N. A. Missert, and R. G. Copeland, "Luminescent properties of solution-grown ZnO nanorods," *Applied Physics Letters*, vol. 88, no. 25, Article ID 252103, 2006.

[40] J. Zhang and W. Que, "Preparation and characterization of solgel Al-doped ZnO thin films and ZnO nanowire arrays grown on Al-doped ZnO seed layer by hydrothermal method," *Solar Energy Materials and Solar Cells*, vol. 94, no. 12, pp. 2181–2186, 2010.

[41] M. K. Patra, K. Manzoor, M. Manoth, S. R. Vadera, and N. Kumar, "Studies of luminescence properties of ZnO and ZnO: Zn nanorods prepared by solution growth technique," *Journal of Luminescence*, vol. 128, no. 2, pp. 267–272, 2008.

[42] R. Xie, T. Sekiguchi, T. Ishigaki et al., "Enhancement and patterning of ultraviolet emission in ZnO with an electron beam," *Applied Physics Letters*, vol. 88, no. 13, Article ID 134103, 2006.

[43] Z.-M. Liao, H. Z. Zhang, Y. B. Zhou, J. Xu, J. M. Zhang, and D. P. Yu, "Surface effects on photoluminescence of single ZnO nanowires," *Physics Letters, Section A*, vol. 372, no. 24, pp. 4505–4509, 2008.

[44] J. Lee, J. Chung, and S. Lim, "Improvement of optical properties of post-annealed ZnO nanorods," *Physica E*, vol. 42, no. 8, pp. 2143–2146, 2010.

[45] Y. H. Leung, A. B. Djurišić, Z. T. Liu, D. Li, M. H. Xie, and W. K. Chan, "Defect photoluminescence of ZnO nanorods synthesized by chemical methods," *Journal of Physics and Chemistry of Solids*, vol. 69, no. 2-3, pp. 353–357, 2008.

[46] D. Wang and N. Reynolds, "Photoluminescence of Zinc Oxide nanowires: the effect of surface band bending," *ISRN Condensed Matter Physics*, vol. 2012, Article ID 950354, 6 pages, 2012.

[47] T. Ghosh and D. Basak, "Highly enhanced ultraviolet photoresponse property in Cu-doped and Cu-Li co-doped ZnO films," *Journal of Physics D*, vol. 42, no. 14, Article ID 145304, 2009.

[48] M. Li, G. Xing, L. F. N. Ah Qune et al., "Tailoring the charge carrier dynamics in ZnO nanowires: the role of surface hole/electron traps," *Physical Chemistry Chemical Physics*, vol. 14, pp. 3075–3082, 2012.

[49] J. H. Jun, H. Seong, K. Cho, B. M. Moon, and S. Kim, "Ultraviolet photodetectors based on ZnO nanoparticles," *Ceramics International*, vol. 35, no. 7, pp. 2797–2801, 2009.

[50] S. Mridha, M. Nandi, A. Bhaumik, and D. Basak, "A novel and simple approach to enhance ultraviolet photosensitivity: activated-carbon-assisted growth of ZnO nanoparticles," *Nanotechnology*, vol. 19, no. 27, Article ID 275705, 2008.

[51] A. Bera and D. Basak, "Role of defects in the anomalous photoconductivity in ZnO nanowires," *Applied Physics Letters*, vol. 94, no. 16, Article ID 163119, 2009.

[52] C. H. Ahn, W. S. Han, B. H. Kong, and H. K. Cho, "Ga-doped ZnO nanorod arrays grown by thermal evaporation and their electrical behavior," *Nanotechnology*, vol. 20, no. 1, Article ID 015601, 2009.

[53] A. F. Lotus, Y. C. Kang, J. I. Walker, R. D. Ramsier, and G. G. Chase, "Effect of aluminum oxide doping on the structural, electrical, and optical properties of zinc oxide (AOZO) nanofibers synthesized by electrospinning," *Materials Science and Engineering B*, vol. 166, no. 1, pp. 61–66, 2010.

[54] C.-H. Hsu and D.-H. Chen, "Synthesis and conductivity enhancement of Al-doped ZnO nanorod array thin films," *Nanotechnology*, vol. 21, no. 28, Article ID 285603, 2010.

[55] S. Mridha and D. Basak, "Aluminium doped ZnO films: electrical, optical and photoresponse studies," *Journal of Physics D*, vol. 40, no. 22, pp. 6902–6907, 2007.

[56] B. K. Sharma and N. Khare, "Stress-dependent band gap shift and quenching of defects in Al-doped ZnO films," *Journal of Physics D*, vol. 43, no. 46, Article ID 465402, 2010.

[57] X. G. Zheng, Q. S. Li, J. P. Zhao et al., "Photoconductive ultraviolet detectors based on ZnO films," *Applied Surface Science*, vol. 253, no. 4, pp. 2264–2267, 2006.

[58] J. M. Liu, Y. B. Xia, L. J. Wang, Q. F. Su, and W. M. Shi, "Effect of grain size on the electrical properties of ultraviolet photodetector with ZnO/diamond film structure," *Journal of Crystal Growth*, vol. 300, no. 2, pp. 353–357, 2007.

[59] C. Soci, A. Zhang, X. Y. Bao, H. Kim, Y. Lo, and D. Wang, "Nanowire photodetectors," *Journal of Nanoscience and Nanotechnology*, vol. 10, no. 3, pp. 1430–1449, 2010.

[60] C. Sheng-Po, L. Chien-Yuan, C. Shoou-Jinn, C. Yu-Zung, H. Ting-Jen, and H. Cheng-Liang, "Electrical and optical characteristics of UV photodetector with interlaced ZnO nanowires," *IEEE Journal of Selected Topics in Quantum Electronics*, vol. 17, pp. 990–995, 2011.

*Research Article*

# Characterization and Hydrogen Storage of Surface-Modified Multiwalled Carbon Nanotubes for Fuel Cell Application

## Kuen-Song Lin, Yao-Jen Mai, Shin-Rung Li, Chia-Wei Shu, and Chieh-Hung Wang

*Department of Chemical Engineering and Materials Science and the Fuel Cell Center, Yuan Ze University, Chungli 320, Taiwan*

Correspondence should be addressed to Kuen-Song Lin, kslin@saturn.yzu.edu.tw

The synthesis, identification, and $H_2$ storage of multiwalled carbon nanotubes (MWCNTs) have been investigated in the present work. MWCNTs were produced from the catalytic-assembly solvent (benzene)-thermal (solvothermal) route. Reduction of $C_6Cl_6$ with metallic potassium was carried out in the presence of Co/Ni catalyst precursors at 503–623 K for 12 h. XRD patterns indicated that the abstraction of Cl from hexachlorobenzene and the formation of KCl precipitates were involved in the early stage of the synthesis process of MWCNTs. This result offers further explanation for the formation of MWCNT structure and yield using the solvothermal route depending on the Co/Ni catalyst precursors. The diameter of MWCNTs ranged between 30 and 100 nm and the $H_2$ storage capacity of MWCNTs improved when 2.7–3.8 wt% Pd or $NaAlH_4$ were doped. The XANES/EXAFS spectra revealed that the Co/Ni catalyst precursors of the MWCNT synthesis were in metallic form and Pd atoms possessed a Pd–Pd bond distance of 2.78 Å with a coordination number of 9.08. Ti-$NaAlH_4$ or Pd nanoparticles were dispersed on MWCNTs and facilitated to improve the $H_2$ storage capacity significantly with the surface modification process.

## 1. Introduction

Carbon nanotubes (CNTs) have been predicted to possess novel mechanical and unique electrical properties due to their regular, periodic structure and quantum size [1–4]. The applications for CNTs have enormous potentials such as novel nanoscale electronic devices, tips for scanning probe microscopy, hydrogen storage media, reinforcing materials for carbon matrix composites, and catalyst supports [3–5]. MWCNTs have earned intensive interest in the past decade because of their role in the emerging environmental and energy-related applications. The synthesis of metal-catalyzed CNTs has been pursued by a variety of methods that included chemical vapor deposition (CVD), laser, or arc process [6–12]. However, these methods are associated with the formation of many undesired by products and low yields, and many other separation challenges [13–17]. In addition, neither method is readily scalable for bulk commercial production [18–20]. Conversely, a low-cost, mass-producible, effective, and novel benzene-solvothermal route that involves the reduction of hexachlorobenzene ($C_6Cl_6$) by metallic potassium (K) in the presence of Co/Ni catalyst precursors

has been conducted in the present work [7, 9]. However, the valency and fine structure of Co and Ni atoms also have not been well studied for the formation of CNTs. The concurrence of Co/Ni metal nanoparticles nucleation leads to create a complex transient chemical environment and thus makes it difficult to study the inception and growth process of CNTs [7, 9]. The $CoCl_2^{\bullet}$ and $NiCl_2^{\bullet}$ mixtures are reduced to Co/Ni catalyzed particles by metallic potassium (K), while $C_6Cl_6$ is also reduced by K through deleting chloride to form carbon clusters and KCl salts. Once the nucleation of CNTs from freshly reduced Co/Ni metal particles has finished, the hexagonal carbon clusters diffuse to the growth sites through constant surface diffusion, then assemble into CNTs and cause the axial growth [7, 9]. In addition, CNTs are known to possess significant catalytic activity via the $\pi$ and $\sigma$ bonds with sp$^2$ hybridization state and that affects the potential ability for hydrogen adsorption [21, 22].

Complex metal hydrides, with the form $ABH_4$ (where A is one of the alkali metals and B is a group III atom), have been widely studied in solution as proton acceptors for their ability to enhance $H_2$ adsorption [23–30]. From some literature and reports, the increasing interest in $NaAlH_4$ as

TABLE 1: Comparison of literatures and the present work on the hydrogen adsorption capacity of Ti-doped $NaAlH_4$ or Ti-$NaAlH_4$-doped CNTs composites.

| Samples | Adsorption conditions | $H_2$ adsorption capacity (wt%) |
|---|---|---|
| $NaAlH_4$ + 3 mol% Ti + 1 mol% Fe [29] | 473 K and 1 atm | 4.3 |
| $NaAlH_4$ + 4 mol% Ti [25] | 423 K and 1 atm | 3.5 |
| $NaAlH_4$ + 2 mol% Ti + 5 wt% Al + 10 wt% MWCNTs (SWCNTs) [54] | 473 K and 1 atm | 3.9 (4.2) |
| $NaAlH_4$ + 8 mol% MWCNTs [31] | 433 K and 1 atm | 4.2 |
| $TiO_2$-doped MWCNTs [51] | 298 K and 18 atm | 0.4 |
| Ti-coated SWCNTs [55] (first-principle total-energy calculations) | 200–900 K and 1 atm | 5.0–8.0 |
| 4 wt% Ti-$NaAlH_4$ + 5 wt% MWCNTs (this work) | 425 K and 30 atm | 3.8 |

a potential hydrogen storage material is arisen, particularly for being admixed with nonmetallic, lightweight, and high-surface-area CNTs [31–33]. Similarly, an alternative way of increasing the hydrogen adsorption capacities of MWCNTs is loading them with transition metals. Enormous progress has been made towards the development of metal-doped CNTs (Li, Ni, Pd, Fe, Pb, Pt, Al, Ti, V, or La) as a hydrogen gas storage material [34–51]. Nanoporous MWCNTs consisting of small transition metallic nanoparticles are exposed to the vicinity of pore volume and surface area and that can be a major concern for hydrogen storage abilities [19, 20, 23, 35, 41, 45, 46, 52, 53]. Additionally, Pd, Pt, or V nanoparticle dispersions onto MWCNTs lead to hydrogen loadings up to 0.5 wt% [34, 36, 38–45, 47, 53, 54]. Rather et al. [46] reported that the hydrogen adsorption of Pd-embedded CNTs possesses a maximum reversible hydrogen storage capacity of 0.18 wt% at 298 K and 1.6 MPa, which is nearly twice the storage capacity of pristine CNTs. According to Gundiah et al. [37] Pd-loaded MWCNTs showed enhanced hydrogen absorption kinetics on the storage system even though maximum adsorption was obtained of only 3.7 wt% at 300 K. Yildirim and Ciraci [55] have reported that a single Ti atom adsorbed on single-walled CNTs can strongly bind to up to four hydrogen molecules using a computational study. In other words, single-walled CNTs decorated with Ti can strongly adsorb up to 8 wt% hydrogen. In addition, such available metals are recognized to play a role in the dissociation of hydrogen, followed by atomic hydrogen spillover, and finally adsorption onto MWCNTs. Using MWCNTs decorated by nanophase metal particles seems to be a promising method to improve hydrogen adsorption abilities. Based on the above principles, comparison of literature or reports on Pd or Ti-loaded MWCNTs and $NaAlH_4$ composites is summarized in Table 1.

The XANES/EXAFS spectroscopy can be used to investigate the valency and fine structures of the complex metals (e.g., Ni, Co, Ti, or Pd) in as-synthesized MWCNTs. The XANES/EXAFS spectra offer a basic understanding of the oxidation states and fine structure of the metal-loaded MWCNTs for the characteristic nature of hydrogen adsorption. The XANES/EXAFS spectroscopy is also an excellent technique for characterizing the valency and local structure of Pd/Co/Ni metals in catalysts with short-range order [37, 56–58]. Thus, the main objective of the present study is to investigate the fine structure, oxidation states, or surface

chemical modification of MWCNTs and Pd/Co/Ni atoms dispersed in the catalyst using HR-TEM, XRD, FE-SEM/EDS, and XANES/EXAFS spectroscopy. In addition, the adsorptive $H_2$ storage capacity of as-synthesized MWCNTs, improved by adding Pd or Ti-$NaAlH_4$, was also studied using a high-pressure microgravimetric balance.

## 2. Experimental

### 2.1. Starting Materials for MWCNTs Synthesis.

The MWCNTs synthesis was conducted in a batch system. Benzene (100 mL) was placed into a 250 mL PTFE-lined 316 austenitic stainless steel autoclave. Then 15.0 g $C_6Cl_6$ and 20.0 g metallic potassium (K) were added under an argon-flowing glove box in order to prevent the metallic potassium species from oxidation. Subsequently, 70–80% of the volume of the autoclave was filled with 15 mL of benzene and 700 mg of catalyst precursors. The catalyst precursor was prepared by dissolving 1.0 g of $CoCl_2 \cdot 6H_2O$ and $NiCl_2 \cdot 6H_2O$ mixture (mole ratio Co/Ni = 1) in 100 mL of absolute ethanol, followed by drying at 353 K and calcining at 423 K in flowing air. All the chemicals used were high-purity (ACS grade). The sealed autoclave was heated in the furnace at 503–623 K for 8–12 h, and then cooled to room temperature. The obtained samples were repeatedly and sequentially washed and filtrated with absolute ethanol, dilute acid, and deionized double-distilled water to remove the residual impurities, such as chlorides and the remaining catalyst, by using the ultrasonic method. The liquid residues were also further dried overnight to form KCl salt powders. Finally, the samples were vacuum-dried at 343–353 K for 6–10 h.

### 2.2. Surface Modification/Functionalization and Metals Doping.

The surface modification process of as-synthesized MWCNTs was conducted by using a concentrated solution of $H_2SO_4/HNO_3$ (ratio = 3) reflux for 1 h at 393 K. The MWCNTs with a surface modification have lots of COOH, OH, or $NO_2$ functional groups that possibly enhance the hydrogen adsorption abilities. Moreover, the well-dispersed surface-modified 5 wt% Pd-doped MWCNTs were prepared by adding MWCNTs into $PdCl_{2(aq)}$ for well dispersion or impregnation and dried in alcohol solution at 323 K. Finally, the PdO/MWCNTs were reduced to form the active

Pd/MWCNTs with flowing hydrogen gases at 393–433 K for 6 h for the further measurement of hydrogen adsorption.

The two samples of 95 wt% Ti-NaAlH$_4$ (4 wt% Ti) + 5 wt% MWCNTs and 95 wt% NaAlH$_4$ + 5 wt% MWCNTs were mechanically admixed for the period of 30 min at milling speeds of 5,500 rpm under argon atmosphere by using a SPEX 8000 ball mill, respectively. A hardened steel crucible and six steel balls 12 mm in diameter were used for the milling. The ball to powder weight ratio was 12.5 : 1. The samples were then used for hydrogen adsorption capacity test and the microstructure characterization.

*2.3. Hydrogen Adsorption Capacity Measurement.* Dihydrogen isotherms were measured gravimetrically at different temperatures using a method previously described by Li et al. [59]. A Cahn Thermax 500 microgravimetric balance with a sensitivity of 1 g was used to measure the changes in mass of MWCNT samples suspended within a glass enclosure under a certain atmosphere. A pressure sensor, with a range of 0 to 68 atm and sensitivity of 0.011 atm (at 1,000°C), was used to measure the hydrogen pressure in the chamber. MWCNT samples were outgassed overnight until a constant mass was attained; these varied from 0.2 to 2.0 g. Prior to admittance of the analyte gas, the entire chamber and manifold were evacuated overnight. The system was purged at room temperature three times with the analyte gas and gases were passed through a molecular sieve trap immersed in liquid nitrogen to remove any condensable impurities and a two-step liquid nitrogen trap system was also conducted for the complete removal of moisture content in the flowing hydrogen gas (>99.999%, of high purity) before being exposed to the samples. Pressures were measured with the range covering 1 to 30 atm. Hydrogen was added incrementally, and data points were recorded when no further change in mass was observed. The dynamic and equilibrium hydrogen adsorption data were also taken at room temperature (298 K) to 425 K and different pressures. The adsorbed amount of hydrogen was calculated after the buoyancy correction. For the buoyancy correction [60, 61], the volume of the sample container and the samples were determined using a helium measurement assuming that helium adsorption at room temperature can be neglected.

*2.4. Characterization and Identification.* The average Co/Ni metal contents in the catalyst precursor were evaluated by atomic absorption spectroscopy (AAS, GBC model 908) and induced coupled plasma/mass spectroscopy (ICP/MS, ELAN model 5000). Each calibration curve was generated with its corresponding standard metal solution at ten different concentrations and that generated the expected Co/Ni metal concentrations in the catalyst. Then the concentration of Co/Ni in the catalyst precursor was calculated. The morphologies of the samples were observed with Zeiss 10C transmission electron microscope (TEM) at 200 kV, and the microstructures of MWCNTs were measured with a JEOL 2010 high-resolution transmission electron microscope (HR-TEM) also at 200 kV. Samples for the electron microscope were prepared by 1 h ultrasonic dispersion of 0.2 g of product with 50 mL of absolute ethanol in a 100 mL conical flask.

Then a drop of the solution was placed on a copper microgrid or carbon film and dried in air before observation. Further elemental microstructures of the MWCNTs were determined by FE-SEM/EDS (Hitachi, S-4700 Type II) with a resolution of 0.1 nm. Structures of the MWCNTs or Co/Ni precursors samples were measured by X-ray powder diffraction (XRD) scanned from 10 to 90°($2\theta$) with a scan rate of 4°($2\theta$) min$^{-1}$ with monochromatic CuK$_\alpha$ radiation (MAC Science, MXP18) at 30 kV and 20 mA. The specific peak intensities and $2\theta$ values recorded can be further identified by a computer database system (JCPDS). The surface area of the MWCNTs was measured by BET (Brunauer-Emmett-Teller) nitrogen adsorption (Micromeritics ASAP 2010 Instrument). For the BET surface area measurements, the catalyst was scraped from the tube substrate and powdered so as to avoid any influence from the steel tube. Prior to measurement, all samples were degassed at 423 K for 1 h. For the calculation of the BET surface areas, the relative pressure range $P/P_0$ of 0.05 to 0.2 was used. The pore radius distribution was determined by the Barrett, Joyner, and Halenda (BJH) method.

*2.5. XANES/EXAFS Measurement.* The XANES/EXAFS spectra were collected at 01C1 and the Wiggler 17C1 beamlines at the National Synchrotron Radiation Research Center (NSRRC) of Taiwan. The electron storage ring was operated with energy of 1.5 GeV and a current of 100–200 mA. A Si(111) DCM was used for providing highly monochromatized photon beams with energies of 1 to 15 keV and resolving power ($E/\Delta E$) of up to 7,000. Data were collected in fluorescence or transmission mode with a Lytle ionization detector [62] for Pd (26,711 eV), Co (7,709 eV), and Ni (8,333 eV) K-edge experiments at room temperature. The photon energy was calibrated by characteristic preedge peaks in the absorption spectra of Pd, Co, and Ni foil standards. The raw absorption data in the region of 50 to 200 eV below the edge position were fit to a straight line using the least-square algorithms [37, 46, 62]. The XANES extends to energy of the order of 50 eV above the edge. The EXAFS function was derived from the raw absorption data through the pre- and post-edge background subtraction and then normalized with respect to the edge jump by using the program package AUTOBK. The $k^2$- or $k^3$-weighted and EXAFS spectra were Fourier transformed to $R$ space over the range between 2.5 and 12.5 Å$^{-1}$. Local structural parameters such as the bond distance $R$, coordination number $N$, and Debye-Waller factor $\sigma$, for different coordination shells surrounding the absorbing atoms, were obtained through nonlinear least-square fitting routine. The EXAFS data were analyzed using the UWXAFS 3.0 program and FEFF 8.20 codes based on the crystallographic data of individual species [37, 56–58].

## 3. Results and Discussion

The MWCNTs were synthesized by Co/Ni catalyst precursors with metallic K and then doping of palladium on the surface was investigated to understand the morphological behaviors. The HR-TEM micrographs shown in Figure 1

(a)



(b)



(c)



(d)
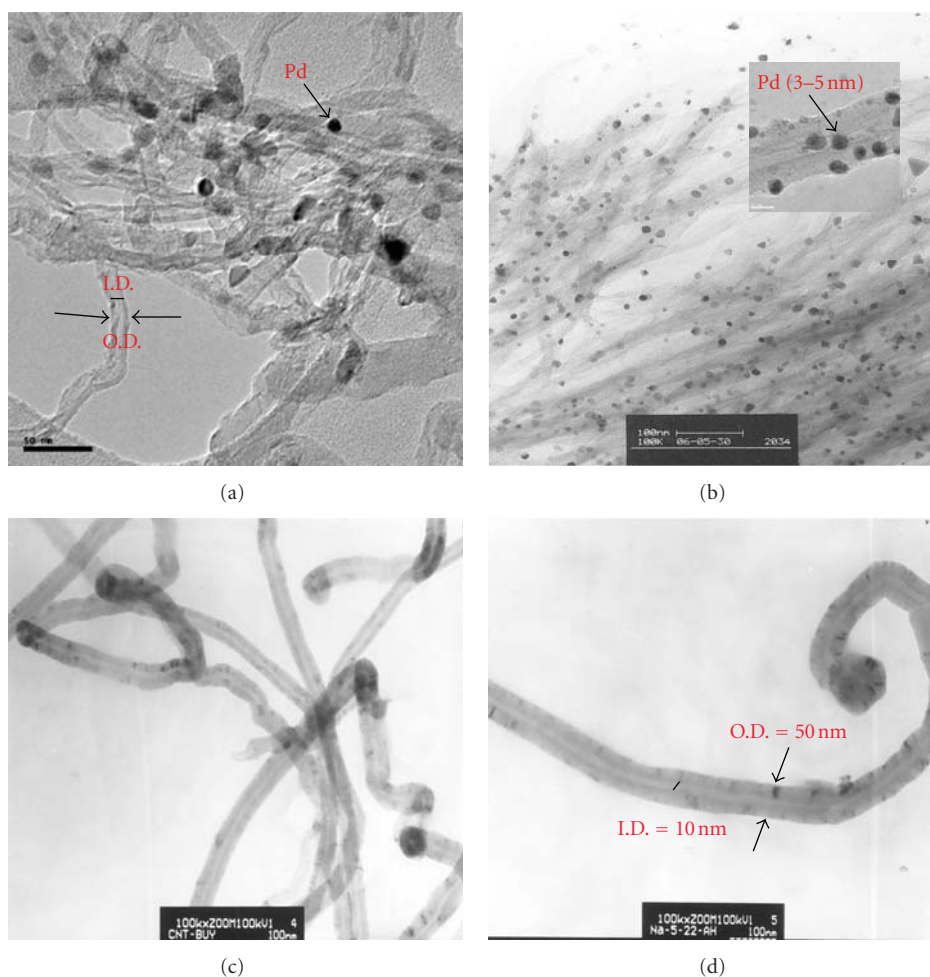
FIGURE 1: HR-TEM images of (a, b) well-dispersed Pd nanoparticles on the MWCNTs surfaces and (c, d) irregular-shaped of MWCNTs synthesized by Co/Ni catalyst precursors with metallic K at $T$ = 503–623 K for 12 h.

were used to investigate the crystallinity and microstructures of the as-synthesized MWCNTs. As shown in Figure 1, the MWCNTs have an irregularly shaped structure with an average length of 1–500 nm. Additionally, the inner and outer average diameters of the MWCNTs are around 20–40 and 45–100 nm, respectively, and clearly visible in Figures 1(b)–1(d). The inner tube is subdivided by a single or multigraphite layer, which is formed by the surface diffusion of carbon cluster on the larger Co/Ni catalytic nanoparticles [17, 46]. In addition, palladium metals are uniformly distributed throughout the surface of MWCNTs (Figures 1(a)-1(b)), thus leading to the formation of the metallic particles consisting of 5 to 10 nm and representing the porous cavities [17, 52]. The MWCNTs were attained with irregular shapes and shown in Figures 1(b)–1(d).

Pretreatment of MWCNTs was carried out with acid or ultrasonic purification and led to forming typically open ended nonamorphous carbon coating [52]. According to the energy dispersive spectrometer (EDS) analysis (Figure 2(a)), the K species are present in microcrystalline MWCNTs synthesized by Co/Ni catalyst precursors. Figure 2(b) revealed

that KCl solid residues were formed in the MWCNTs washing liquids after drying overnight. Therefore, the postulated equation and reaction mechanism of the MWCNTs synthesis may be described as follow:

$$nC_6Cl_6 + nK \longrightarrow 6nKCl + \text{polyaromatic hydrocarbons}$$

$$(+ \text{ benzene at 503–623 K}) \qquad (1)$$

$$\longrightarrow \text{MWCNTs } (+ \text{ Co/Ni for 8–12 h}).$$
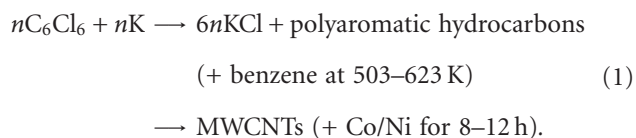
The structure of the MWCNTs compound was confirmed by structural refinement of X-ray diffraction patterns shown in Figure 3. The intensive peaks appearing at small $2\theta$ angles are characteristics of porous materials which possess numerous pores or cavities. In Figure 3, the XRD patterns indicate that the abstraction of Cl from hexachlorobenzene and the formation of KCl precipitates were involved in the early stage of the synthesis process of MWCNTs. Most of the KCl from the MWCNTs sample can be removed by washing with D.I. water (Figures 3(b) and 3(c)). KCl was the main component and over 95% of K$^+$ cations were transformed
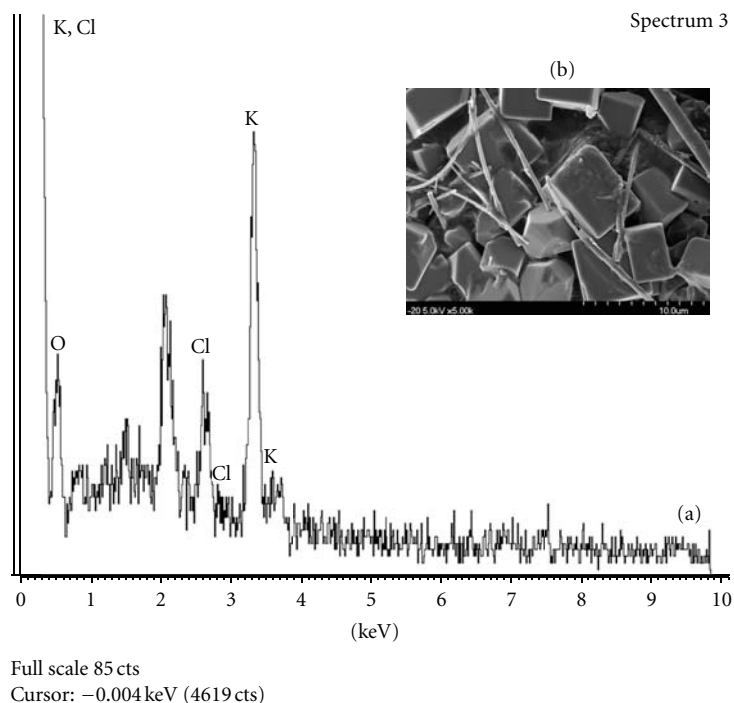
FIGURE 2: FE-SEM/EDS measurement of (a) the surface of MWCNTs synthesized using Co/Ni catalyst precursors with metallic K at $T =$ 503–623 K for 12 h and (b) KCl solid residues formed after drying overnight in the washing liquids of MWCNTs purification process.
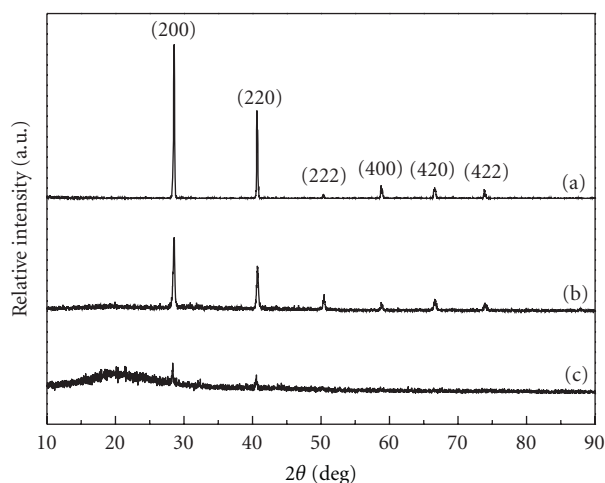


FIGURE 3: XRD patterns of (a) KCl standard, (b) unwashed MWCNTs with KCl crystals, and (c) washed MWCNTs with KCl contaminants synthesized by Co/Ni catalyst precursors at $T =$ 503–623 K for 12 h.
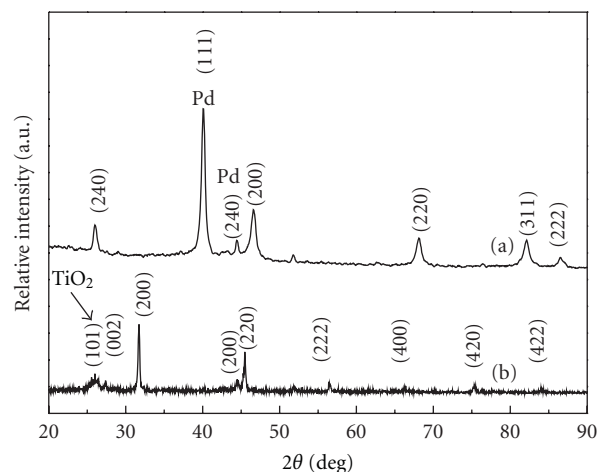


FIGURE 4: XRD patterns of (a) 5 wt% Pd-doped and (b) 4 wt% Ti-NaAlH$_4$-doped MWCNTs synthesized by Co/Ni catalyst precursors at $T =$ 503–623 K for 12 h.

into KCl in the synthesis process of the MWCNTs using Co/Ni catalyst precursors at $T =$ 503–623 K for 8–12 h.

Furthermore, the XRD patterns of Pd and Ti-NaAlH$_4$-doped MWCNTs indicate that the metallic particles have a crystalline structure (Figure 4) and therefore could enhance the surface area with their higher roughness as well as hydrogen-adsorption ability of the MWCNTs. According to FE-SEM, the dispersion of metallic Pd on the surface of

MWCNTs apparently facilitated similar consequences. The XRD patterns of Pd (Figure 4(a)) exhibit characteristic sharp peaks at $2\theta = 40.12$ and $46.77°$, which are consistent with 5–10 nm particle size. As shown in Figure 4(b), the peak at $2\theta = 26.3°$ of Ti-NaAlH$_4$-doped sample also indicates that the largely crystalline structure attributes the particle size as 80–120 nm [28, 51, 55, 63]. This particle size was roughly calculated using Scherrer's equation (with Warren's

TABLE 2: Fine structural parameters of Ni, Co, Pd or PdCl$_2$ powder standard, catalyst precursor residues, and non-surface- or surface-modified 5 wt% MWCNTs with hydrogen reduction analyzed using EXAFS technique.

| Samples | Shell | CN[a] ($\pm 0.05$) | $R$[b] ($\pm 0.05$ Å) | $\sigma^2$ (Å$^2$)[c] |
|---|---|---|---|---|
| Nickel powder standard | Ni–Ni | 3.01 | 2.43 | 0.0087 |
| Catalyst precursor residue (Ni) | Ni–Ni | 2.92 | 2.48 | 0.0058 |
| Cobalt powder standard | Co–Co | 6.02 | 2.45 | 0.0046 |
| Catalyst precursor residue (Co) | Co–Co | 5.96 | 2.49 | 0.0067 |
| Pd powder standard | Pd–Pd | 9.21 | 2.76 | 0.0058 |
| PdCl$_2$ powder standard | Pd–Cl | 2.13 | 2.25 | 0.0042 |
| NHR 5 wt% Pd-doped MWCNTs[d] | Pd–Pd | 8.98 | 2.80 | 0.0112 |
| HR 5 wt% Pd-doped MWCNTs[e] | Pd–Pd | 9.08 | 2.78 | 0.0093 |

[a] CN denotes "coordination number";
[b] $R$ denotes "bond distance";
[c] $\sigma$ denotes "Debye-Waller factor";
[d] NHR 5 wt% Pd-doped MWCNTs denotes "as-synthesized non-surface-modified 5 wt% multiwalled carbon nanotubes reduced at 453 K under flowing hydrogen gas for 6 h";
[e] HR 5 wt% Pd-doped MWCNTs denotes "as-synthesized surface-modified 5 wt% multiwalled carbon nanotubes reduced at 453 K under flowing hydrogen gas for 6 h".

correction for instrumental broadening) applied at half the height of the maximum intensity diffraction peak.

Generally, the XANES/EXAFS spectroscopy can provide the information on the atomic arrangement of sorbents in terms of bond distance, coordination number, and kind of neighbors. Since the valency and fine structures of Co and Ni atoms used as the catalyzer precursor of the MWCNTs formation have not been well studied, XANES and EXAFS spectra may determine the catalytic redox mechanisms for the growth of MWCNTs. By using XANES spectra, all metallic Co or Ni species of the solid residues were found in the MWCNTs as shown in Figure 5(a). XANES or EXAFS data indicate that in the presence of metallic potassium the chlorides of Co and Ni were reduced to Co/Ni catalyst particles. Simultaneously, hexachlorobenzene was also reduced by potassium through releasing chlorides to form carbon clusters and KCl.

A high reliability of the EXAFS data fitting for Pd species in MWCNTs was obtained. The data were collected several times and standard deviation also calculated from the average spectra. Fourier transformation (FT) was performed on $k^2$- or $k^3$-weighted oscillations over the range of 2.2–10 Å$^{-1}$. The radial structure function derived from the FT is shown in Figure 5(b) and Table 2. The EXAFS data of Co/Ni precursor residues revealed that the nanophase metallic Co or Ni particles had a central Co (or Ni) atom with a coordination number of $2.92 \pm 0.05$ (or $5.96 \pm 0.05$) and a primarily Co–Co bond distance of $2.49 \pm 0.05$ Å (or $2.48 \pm 0.05$ Å). The coordination number for Pd powder is $9.21 \pm 0.05$ with a Pd–Cl bond distance of $2.13 \pm 0.05$ Å. Moreover, Pd-doped surface-modified and nonmodified MWCNTs have the coordination numbers of 9.08 and $8.98 \pm 0.05$, respectively.

Hydrogen reduction occurs with the palladium particles on the central atom. These results obtained from XANES/EXAFS may offer further explanation of the yield and structure of MWCNTs formed using catalytic-assembly benzene-solvothermal route. However, the results combined with HR-TEM images (Figures 1(a) and 1(b)) may indicate that the Co/Ni metal particles are responsible for

the nucleation of the MWCNTs growth and belongs with some bending structures at close ends of the tubes. The concurrence of nucleation of the Co/Ni metal nanoparticles and MWCNTs growth within a reactive hydrocarbon atmosphere (e.g., benzene) create a complex transient chemical environment, making it difficult to study the inception and growth processes in MWCNTs synthesis.

Nonspecific physical adsorption of the nonmodified and 5 wt% Pd-doped MWCNTs was carried out to measure the total surface area and pore size distribution as shown in Figure 6. The surface area and total pore volume were calculated according to the adsorption data summarized in Table 3. A large surface area was generally observed for Pd-doped MWCNTs with the surface-modified processes. Most of the microcrystalline structures of Pd on the MWCNTs were confirmed from the HR-TEM analysis (Figure 1) and that was helpful to increase the surface area and hydrogen adsorption capacity. The adsorption-desorption isotherms exhibit a hysteresis behavior, indicating that the specimens were mainly mesoporous. Also, the type IV hysteresis isotherm was obtained and is represented in Figure 6. The adsorption hysteresis was observed in the region of a relative pressure $P/P_0$ above 0.8. A comparison between the shapes of the two isotherms in the pressure range of $P/P_0$ 0–0.9 (Figures 6(a) and 6(b)) reveals a more pronounced hysteresis in the Pd-doped MWCNTs belonging with the surface modification. In addition, BET N$_2$ adsorption for MWCNTs and Pd-doped MWCNTs were 79.4 and 114.2 m$^2$ g$^{-1}$ and pore volumes were 0.18 and 0.32 cm$^3$ g$^{-1}$, respectively. It also indicated that the resulting factor of surface enhancement depended on the surface modification of the Pd on the MWCNTs.

These results caused by the dispersion of the Pd on the MWCNTs surface were due to the surface modification using a concentrated solution of H$_2$SO$_4$/HNO$_3$ (ratio = 3) reflux for 1 h at 393 K. In general, microporosity of the MWCNTs exposed with the increase of hydrogen reduction at 453 K under flowing hydrogen gas for 6 h. According to Table 3, the BET surface area was increased notably with

(a)

(b)
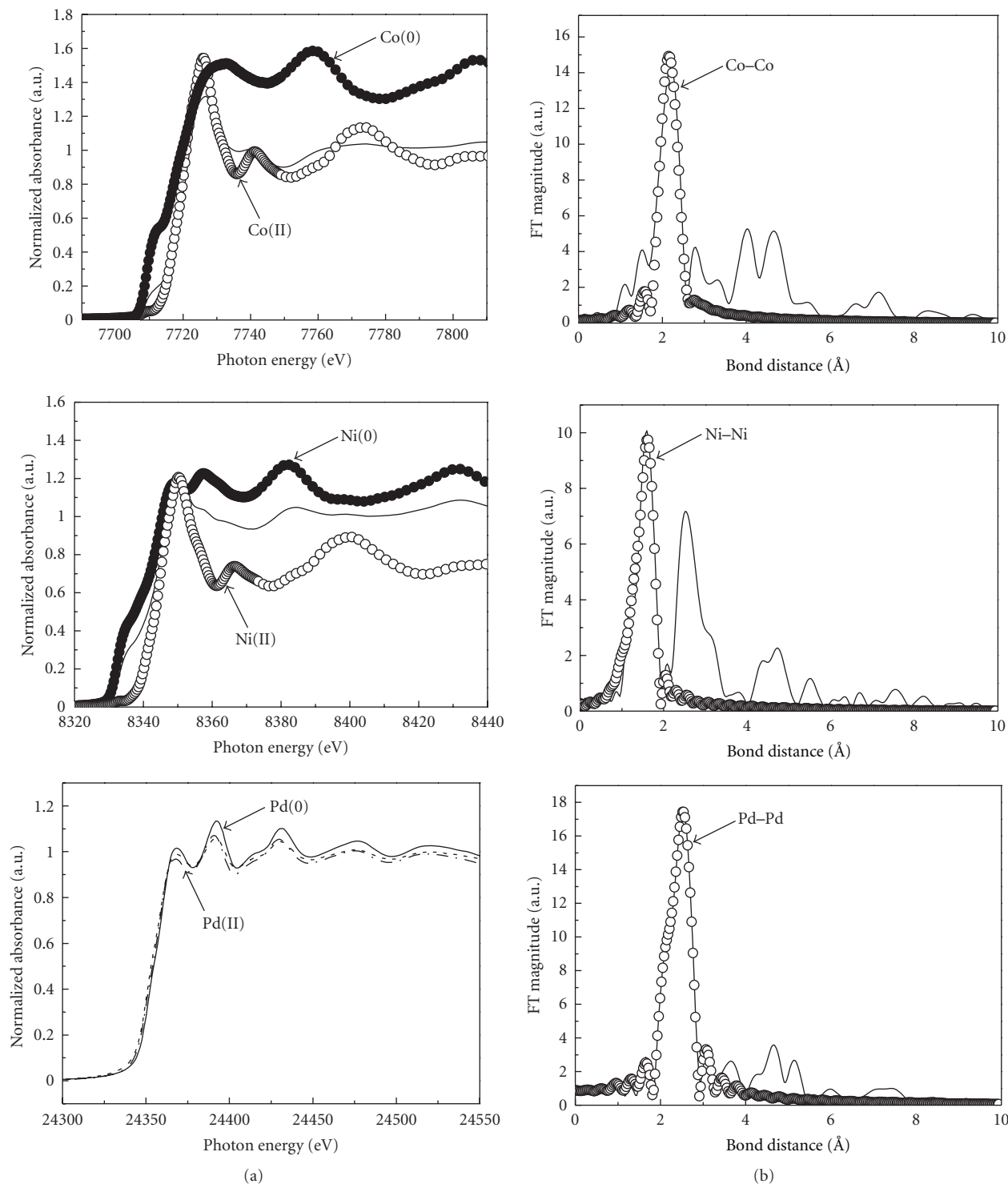
FIGURE 5: (a) XANES of Co/Ni precursor residue samples (solid lines) compared with Co(0, II), Ni(0, II), or Pd(0, II) standards and (b) Fourier transform (FT) of the metallic Co, Ni, or Pd K-edge EXAFS of the MWCNTs synthesized using Co/Ni catalyst precursors at $T =$ 603 K for 8–12 h. The best fitting of EXAFS spectra are expressed by the dotted and circled lines.

hydrogen reduction on the nonmodified and 5 wt% Pd-doped MWCNTs and was observed as 89.4 and 128.6 m$^2$ g$^{-1}$, where as the pore volumes were 0.24 and 0.84 cm$^3$ g$^{-1}$, respectively. Specific BET surface area of Pd-doped MWCNT sample started to increase due to the exposure of the nanophase Pd particles loaded on the surface of MWCNTs to hydrogen reduction, which might induce the microporosity and perfections in the carbon structures.

(a)



(b)



(c)
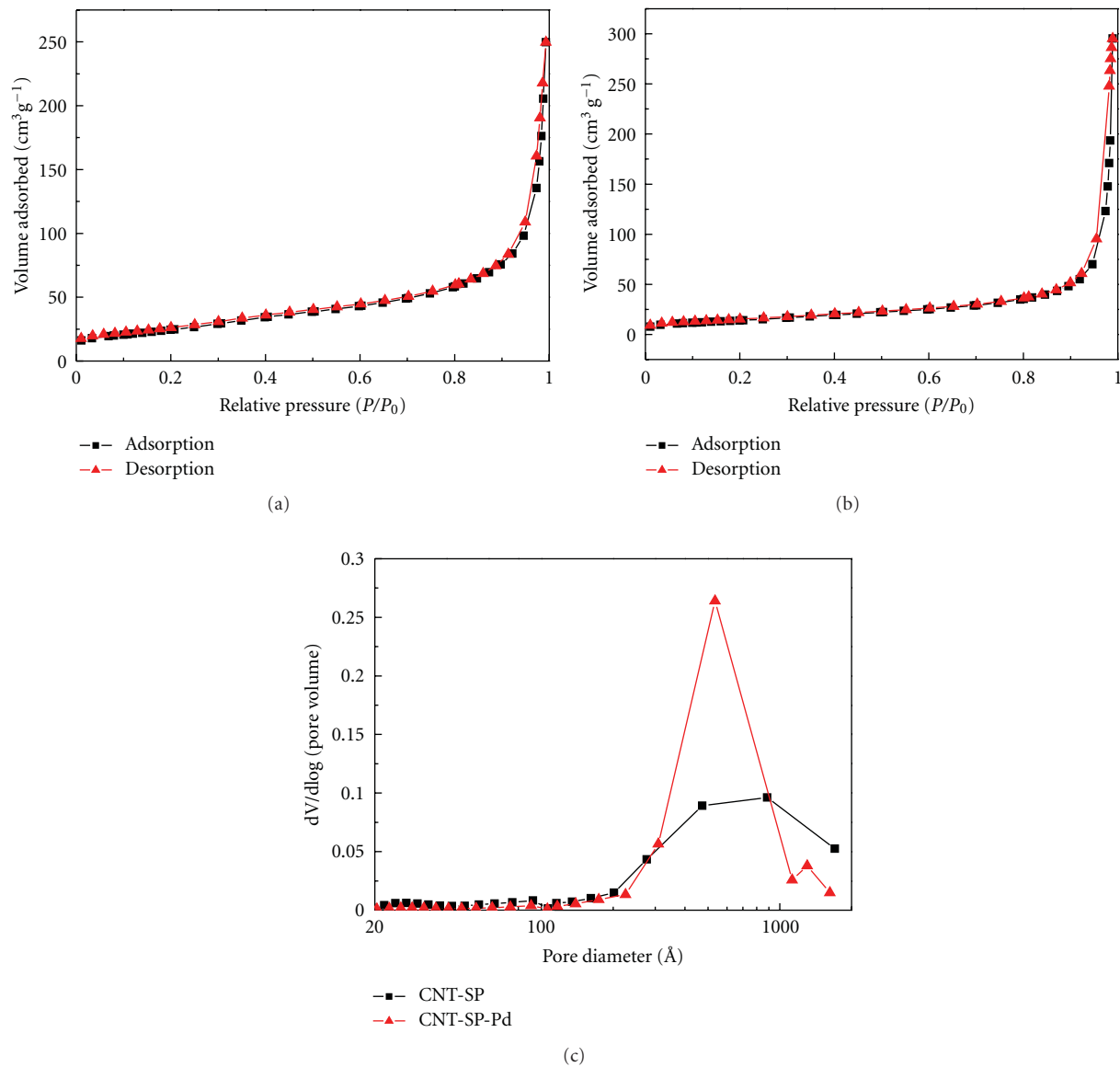
FIGURE 6: (a) Nitrogen adsorption/desorption isotherms of non-surface-modified 5 wt% Pd-doped MWCNTs and (b) surface-modified 5 wt% Pd-doped MWCNTs, and (c) pore size distributions of non- and surface-modified 5 wt% Pd-doped MWCNTs samples.

TABLE 3: Specific BET surface area and total pore volumes of nonsurface- or surface-modified MWCNTs and 5 wt% Pd-doped MWCNTs using $H_2SO_4/HNO_3$ (ratio = 3) reflux for 1 h at 393 K.

| Samples | BET surface area ($m^2 g^{-1}$) | Total pore volume ($cm^3 g^{-1}$) |
|---|---|---|
| Non-surface-modified MWCNTs | 79.4 | 0.18 |
| Surface-modified MWCNTs | 114.2 | 0.32 |
| NHR 5 wt% Pd-doped MWCNTs[a] | 89.4 | 0.24 |
| HR 5 wt% Pd-doped MWCNTs[b] | 128.6 | 0.38 |

[a]NHR 5 wt% Pd-doped MWCNTs denotes "as-synthesized non-surface-modified 5 wt% multiwalled carbon nanotubes reduced at 453 K under flowing hydrogen gas for 6 h".
[b]HR 5 wt% Pd-doped MWCNTs denotes "as-synthesized surface-modified 5 wt% multiwalled carbon nanotubes reduced at 453 K under flowing hydrogen gas for 6 h".
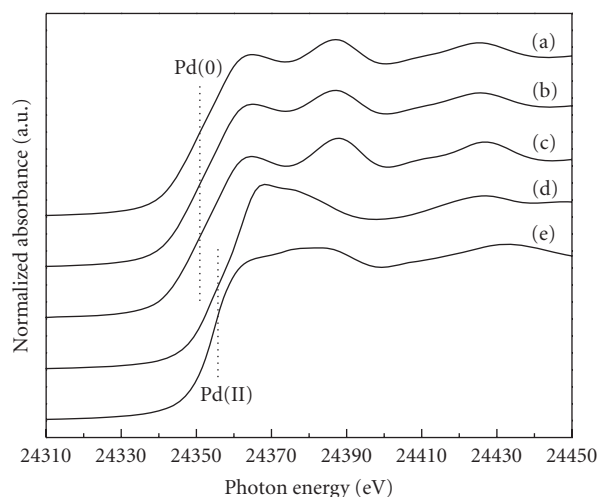
FIGURE 7: XANES spectra of (a) non-surface- and (b) surface-modified 5 wt% Pd-doped MWCNTs after $H_2$ reduction at 433 K for 6 h, (c) Pd, (d) PdO, and (e) $PdCl_2$ powder standards.



FIGURE 8: Fourier transform (FT) spectra of (a) Pd powder standard, (b) non-surface-modified 5 wt% Pd-doped MWCNTs after $H_2$ reduction at 433 K for 6 h, (c) fresh non-surface-modified 5 wt% Pd-doped MWCNTs, (d) surface-modified 5 wt% Pd-doped MWCNTs after $H_2$ reduction at 433 K for 6 h, and (e) fresh surface-modified 5 wt% Pd-doped MWCNTs. The best fitting of the EXAFS spectra are expressed by the circle lines.

The intensive peak of the Pd(0) K-edge region around 24,368 eV and the stronger 24,392 eV quantify the transition metals of Pd on the surface of MWCNTs and occurred due to the orbital $3d \rightarrow 5s$ or $4p$ hybridization caused by unoccupied $d$ bands as shown in Figures 7(a)–7(e) [53, 56, 64]. Therefore, the absorption was intensive at $3d \rightarrow 5s$ or $4p$ hybridization. The p-like density of states was notably enhanced and the absorption could increase like the second absorption peak in the XANES spectra of the Pd standards (Figure 7(a)). In addition, compared with the absorption cross section of the Pd standard, it might be extensively increased because of the $3d \rightarrow 4p$ hybridization of Pd(II) [8, 53, 56]. By using the EXAFS spectra shown in Figure 8, the Pd clusters possessed a Pd–Pd bond distance of $2.76 \pm 0.05$ Å with a coordination number around 9 and the $PdCl_2$ species had a Pd–Cl bond distance of $2.25 \pm 0.05$ Å with a coordination number of 2 [53, 64]. In the EXAFS data analyzed, the Debye-Waller factors ($\Delta\sigma^2$) were less than 0.015 (Å$^2$) indicating that the center Pd atoms were the coordinated by Pd–Pd bonding confirmatively. The apparent shortening of the bond distance with coordination number probably was caused by the random motion of surface atoms on the small Pd particles and that posed to increase the surface area of the Pd-doped MWCNT samples. Furthermore, this result also revealed that the Pd nanoparticles were well dispersed on the surface of the MWCNTs, which improved the amount of hydrogen storage efficiency significantly.

The unique adsorptive properties of carbon nanotubes suggest enormous potential applications for the fuel cell power generation systems. Laboratory-scale experiments were carried out to provide information concerning the feasibility for $H_2$ storage ability of MWCNTs, and to determine if further developments would be warranted. The chemical modification of MWCNTs surfaces was done for the hydrogen adsorption capacity enhancement using a concentrated solution of $H_2SO_4/HNO_3$ method. In order to know more detail about the hydrogen adsorption behavior
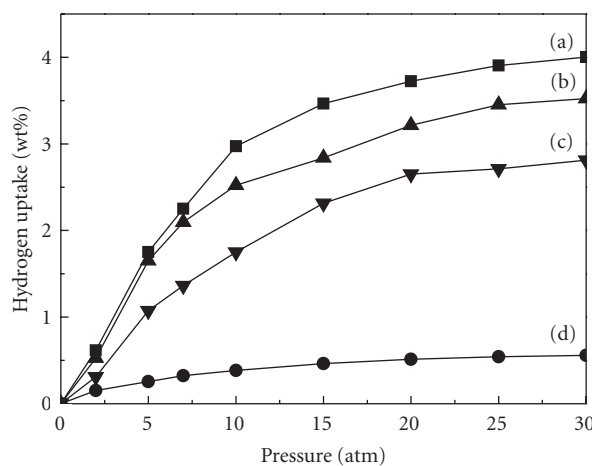


FIGURE 9: Hydrogen adsorption curves of (a) 4 wt% Ti-$NaAlH_4$ + 5 wt% MWCNTs (at 425 K), (b) $NaAlH_4$ + 5 wt% MWCNTs (at 425 K), (c) 5 wt% Pd-doped MWCNTs (at 298 K), and (d) MWCNTs (at 298 K). The adsorption pressures of as-synthesized hydrogen storage materials of MWCNTs were ranged of 1–30 atm.

and the efficiency of Pd-doped MWCNTs, the hydrogen adsorption was carried out and represented in Figure 9. The fine particle size and the crystalline structure of the Pd-doped MWCNTs are responsible for higher sorption of $H_2$ as shown in Figure 9(c), compared with the as-synthesized MWCNTs without metal doping shown in Figure 9(d). In addition, antidispersive force and the expected specific interaction with Pd sites also played an important role in case of the Pd-doped MWCNTs [46, 53]. The addition of Pd or Ti-$NaAlH_4$ nanoparticles increased the amount of hydrogen adsorption on the surface of MWCNTs.

The hydrogen storage capacity of MWCNTs improved by doping of Pd or Ti-NaAlH$_4$ of about 2.7–3.8 wt% measured at 30 atm and 298 to 425 K which makes it more feasible to apply into the fuel cell power generation system [46, 53]. Experimentally, the hydrogen adsorption selectivity of Pd or Ti-NaAlH$_4$-doped MWCNTs was increased due to the dispersion of the Pd or Ti-NaAlH$_4$ nanomaterial, respectively. The surface roughness and abundance of metallic dispersion on the MWCNTs surface helped to increase the hydrogen adsorption performance. This result was also followed through the EXAFS analysis that surface atoms of the Pd nanoparticles exhibited random motion and posed to enhance the hydrogen adsorption behavior.

## 4. Conclusions

The potential synthesis route of MWCNTs with catalytic hexachlorobenzene in the presence of Co/Ni catalyst precursors at 503–623 K for 12 h was investigated. The identified characteristics of as-synthesized or metallic doped MWCNTs as well as H$_2$ storage capacity for the fuel cell application were also studied. TEM micrographs show that the MWCNTs have a bamboo-like structure with an average length of 1–500 nm. The inner and outer diameters of MWCNTs were 20 and 45 nm in average, respectively. The XRD patterns indicated that the abstraction of Cl from hexachlorobenzene and the formation of the KCl precipitate were involved in the early stage of the synthesis process of MWCNTs. XANES spectra showed that the Co/Ni catalyst precursors of the MWCNTs were all metallic Co or Ni species. Furthermore, the EXAFS spectra of Co/Ni precursor residues revealed that the metallic Co or Ni nanoparticles have a central Co (or Ni) atom with a coordination number of 2.92 ± 0.05 (or 5.96 ± 0.05) and with a Co–Co bond distance of 2.49 ± 0.05 Å (or 2.48 ± 0.05 Å). In addition, Pd or PdCl$_2$ possessed a Pd–Pd or Pd–Cl bond distance as 2.76 or 2.25 Å with a coordination number of around 9 or 2, respectively. The capacity of H$_2$ storage of the MWCNTs improved by Pd or Ti-NaAlH$_4$ was ranged of 2.7–3.8 wt%. This result revealed that the Ti-NaAlH$_4$-dopant or Pd nanoparticles were well dispersed on MWCNTs and that improved the H$_2$ storage capacity significantly. Moreover, surface-modified or Pd- and Ti-NaAlH$_4$-doped MWCNTs are some of the potential hydrogen adsorption materials. The safe storage of high purity hydrogen fed to the proton exchange membrane fuel cells (PEMFC) stack for power generation makes surface-modified MWCNTs utilization systems economically and environmentally attractive.

## Acknowledgment

## References

[1] S. Iijima, "Helical microtubules of graphitic carbon," *Nature*, vol. 354, no. 6348, pp. 56–58, 1991.

[2] M. S. Dresselhaus, G. Dresselhaus, and R. Saito, "Physics of carbon nanotubes," *Carbon*, vol. 33, no. 7, pp. 883–891, 1995.

[3] A. C. Dillon, K. M. Jones, T. A. Bekkedahl, C. H. Kiang, D. S. Bethune, and M. J. Heben, "Storage of hydrogen in single-walled carbon nanotubes," *Nature*, vol. 386, no. 6623, pp. 377–379, 1997.

[4] J. Hone, M. Whitney, and A. Zettl, "Thermal conductivity of single-walled carbon nanotubes," *Synthetic Metals*, vol. 103, no. 1–3, pp. 2498–2499, 1999.

[5] Y. Tong, C. Liu, P. X. Hou, H. M. Cheng, N. S. Xu, and J. Chen, "Field emission from aligned multi-walled carbon nanotubes," *Physica B*, vol. 323, no. 1–4, pp. 156–157, 2002.

[6] T. Guo, P. Nikolaev, A. Thess, D. T. Colbert, and R. E. Smalley, "Catalytic growth of single-walled manotubes by laser vaporization," *Chemical Physics Letters*, vol. 243, no. 1-2, pp. 49–54, 1995.

[7] Y. Jiang, Y. Wu, S. Zhang et al., "A catalytic-assembly solvothermal route to multiwall carbon nanotubes at a moderate temperature," *Journal of the American Chemical Society*, vol. 122, no. 49, pp. 12383–12384, 2000.

[8] Y. P. Sun, K. Fu, Y. Lin, and W. Huang, "Functionalized carbon nanotubes: properties and applications," *Accounts of Chemical Research*, vol. 35, no. 12, pp. 1096–1104, 2002.

[9] X. Wang, J. Lu, Y. Xie, G. Du, Q. Guo, and S. Zhang, "A novel route to multiwalled carbon nanotubes and carbon nanorods at low temperature," *Journal of Physical Chemistry B*, vol. 106, no. 5, pp. 933–937, 2002.

[10] J. Liu, M. Shao, X. Chen, W. Yu, X. Liu, and Y. Qian, "Large-scale synthesis of carbon nanotubes by an ethanol thermal reduction process," *Journal of the American Chemical Society*, vol. 125, no. 27, pp. 8088–8089, 2003.

[11] J. Liu, M. Shao, Q. Xie, L. Kong, W. Yu, and Y. Qian, "Single-source precursor route to carbon nanotubes at mild temperature," *Carbon*, vol. 41, no. 11, pp. 2101–2104, 2003.

[12] A. Reyhani, S. Z. Mortazavi, A. Z. Moshfegh, A. N. Golikand, and M. Amiri, "Enhanced electrochemical hydrogen storage by catalytic Fe-doped multi-walled carbon nanotubes synthesized by thermal chemical vapor deposition," *Journal of Power Sources*, vol. 188, no. 2, pp. 404–410, 2009.

[13] J. Chen, M. A. Hamon, H. Hu et al., "Solution properties of single-walled carbon nanotubes," *Science*, vol. 282, no. 5386, pp. 95–98, 1998.

[14] S. S. Wong, A. T. Woolley, E. Joselevich, C. L. Cheung, and C. M. Lieber, "Covalently-functionalized single-walled carbon nanotube probe tips for chemical force microscopy," *Journal of the American Chemical Society*, vol. 120, no. 33, pp. 8557–8558, 1998.

[15] M. A. Hamon, H. Hu, P. Bhowmik et al., "End-group and defect analysis of soluble single-walled carbon nanotubes," *Chemical Physics Letters*, vol. 347, no. 1–3, pp. 8–12, 2001.

[16] J. Zhang, H. Zou, Q. Qing et al., "Effect of chemical oxidation on the structure of single-walled carbon nanotubes," *Journal of Physical Chemistry B*, vol. 107, no. 16, pp. 3712–3718, 2003.

[17] C. Branca, F. Frusteri, V. Magazù, and A. Mangione, "Characterization of carbon nanotubes by TEM and infrared spectroscopy," *Journal of Physical Chemistry B*, vol. 108, no. 11, pp. 3469–3473, 2004.

[18] Y. Xing, L. Li, C. C. Chusuei, and R. V. Hull, "Sonochemical oxidation of multiwalled carbon nanotubes," *Langmuir*, vol. 21, no. 9, pp. 4185–4190, 2005.

[19] A. Ansón, E. Lafuente, E. Urriolabeitia et al., "Preparation of palladium loaded carbon nanotubes and activated carbons for hydrogen sorption," *Journal of Alloys and Compounds*, vol. 436, no. 1-2, pp. 294–297, 2007.

[20] S. Kocabas, T. Kopac, G. Dogu, and T. Dogu, "Effect of thermal treatments and palladium loading on hydrogen sorption characteristics of single-walled carbon nanotubes," *International Journal of Hydrogen Energy*, vol. 33, no. 6, pp. 1693–1699, 2008.

[21] O. Gülseren, T. Yildirim, and S. Ciraci, "Tunable adsorption on carbon nanotubes," *Physical Review Letters*, vol. 87, no. 11, Article ID 116802, pp. 116802/1–116802/4, 2001.

[22] Y. Wang, W. Deng, X. Liu, and X. Wang, "Electrochemical hydrogen storage properties of ball-milled multi-wall carbon nanotubes," *International Journal of Hydrogen Energy*, vol. 34, no. 3, pp. 1437–1443, 2009.

[23] J. Moc, D. G. Musaev, and K. Morokuma, "Activation and adsorption of multiple $H_2$ molecules on a Pd5 cluster: a density functional study," *Journal of Physical Chemistry A*, vol. 107, no. 24, pp. 4929–4939, 2003.

[24] D. J. Ross, M. D. Halls, A. G. Nazri, and R. F. Aroca, "Raman scattering of complex sodium aluminum hydride for hydrogen storage," *Chemical Physics Letters*, vol. 388, no. 4-6, pp. 430–435, 2004.

[25] P. Wang and C. M. Jensen, "Preparation of Ti-doped sodium aluminum hydride from mechanical milling of NaH/AI with off-the-shelf Ti powder," *Journal of Physical Chemistry B*, vol. 108, no. 40, pp. 15827–15829, 2004.

[26] S. Chaudhuri and J. T. Muckerman, "First-principles study of Ti-catalyzed hydrogen chemisorption on an Al surface: a critical first step for reversible hydrogen storage in NaAlH$_4$," *Journal of Physical Chemistry B*, vol. 109, no. 15, pp. 6952–6957, 2005.

[27] E. H. Majzoub, J. L. Herberg, R. Stumpf, S. Spangler, and R. S. Maxwell, "XRD and NMR investigation of Ti-compound formation in solution-doping of sodium aluminum hydrides: Solubility of Ti in NaAlH$_4$ crystals grown in THF," *Journal of Alloys and Compounds*, vol. 394, no. 1-2, pp. 265–270, 2005.

[28] J. Wang, A. D. Ebner, T. Prozorov, R. Zidan, and J. A. Ritter, "Effect of graphite as a co-dopant on the dehydrogenation and hydrogenation kinetics of Ti-doped sodium aluminum hydride," *Journal of Alloys and Compounds*, vol. 395, no. 1-2, pp. 252–262, 2005.

[29] J. Wang, A. D. Ebner, R. Zidan, and J. A. Ritter, "Synergistic effects of co-dopants on the dehydrogenation kinetics of sodium aluminum hydride," *Journal of Alloys and Compounds*, vol. 391, no. 1-2, pp. 245–255, 2005.

[30] V. J. Surya, K. Iyakutti, M. Rajarajeswari, and Y. Kawazoe, "Functionalization of single-walled carbon nanotube with borane for hydrogen storage," *Physica E*, vol. 41, no. 7, pp. 1340–1346, 2009.

[31] D. Pukazhselvan, B. K. Gupta, A. Srivastava, and O. N. Srivastava, "Investigations on hydrogen storage behavior of CNT doped NaAlH$_4$," *Journal of Alloys and Compounds*, vol. 403, no. 1-2, pp. 312–317, 2005.

[32] P. A. Berseth, A. G. Harter, R. Zidan et al., "Carbon nanomaterials as catalysts for hydrogen uptake and release in NaAIH4," *Nano Letters*, vol. 9, no. 4, pp. 1501–1505, 2009.

[33] C. Liu, Y. Chen, C. Z. Wu, S. T. Xu, and H. M. Cheng, "Hydrogen storage in carbon nanotubes revisited," *Carbon*, vol. 48, no. 2, pp. 452–455, 2010.

[34] D. Lin and B. Xing, "Tannic acid adsorption and its role for stabilizing carbon nanotube suspensions," *Environmental Science and Technology*, vol. 42, no. 16, pp. 5917–5923, 2008.

[35] Z. T. Liu, C. X. Wang, Z. W. Liu, and J. Lu, "Selective hydrogenation of cinnamaldehyde over Pt-supported multi-walled carbon nanotubes: insights into the tube-size effects," *Applied Catalysis A*, vol. 344, no. 1-2, pp. 114–123, 2008.

[36] A. Lueking and R. T. Yang, "Hydrogen spillover from a metal oxide catalyst onto carbon nanotubes—implications for hydrogen storage," *Journal of Catalysis*, vol. 206, no. 1, pp. 165–168, 2002.

[37] G. Gundiah, A. Govindaraj, N. Rajalakshmi, K. S. Dhathathreyan, and C. N. R. Rao, "Hydrogen storage in carbon nanotubes and related materials," *Journal of Materials Chemistry*, vol. 13, no. 2, pp. 209–213, 2003.

[38] E. Yoo, L. Gao, T. Komatsu et al., "Atomic hydrogen storage in carbon nanotubes promoted by metal catalysts," *Journal of Physical Chemistry B*, vol. 108, no. 49, pp. 18903–18907, 2004.

[39] S. Dag, Y. Ozturk, S. Ciraci, and T. Yildirim, "Adsorption and dissociation of hydrogen molecules on bare and functionalized carbon nanotubes," *Physical Review B*, vol. 72, no. 15, pp. 155404–155411, 2005.

[40] A. Lan and A. Mukasyan, "Hydrogen storage capacity characterization of carbon nanotubes by a microgravimetrical approach," *Journal of Physical Chemistry B*, vol. 109, no. 33, pp. 16011–16016, 2005.

[41] A. Ansón, E. Lafuente, E. Urriolabeitia et al., "Hydrogen capacity of palladium-loaded carbon materials," *Journal of Physical Chemistry B*, vol. 110, no. 13, pp. 6643–6648, 2006.

[42] F. H. Yang, A. J. Lachawiec, and R. T. Yang, "Adsorption of spillover hydrogen atoms on single-wall carbon nanotubes," *Journal of Physical Chemistry B*, vol. 110, no. 12, pp. 6236–6244, 2006.

[43] V. Gayathri and R. Geetha, "Hydrogen adsorption in defected carbon nanotubes," *Adsorption*, vol. 13, no. 1, pp. 53–59, 2007.

[44] C. T. Hsieh, Y. W. Chou, and J. Y. Lin, "Fabrication and electrochemical activity of Ni-attached carbon nanotube electrodes for hydrogen storage in alkali electrolyte," *International Journal of Hydrogen Energy*, vol. 32, no. 15, pp. 3457–3464, 2007.

[45] M. K. Kumar and S. Ramaprabhu, "Palladium dispersed multiwalled carbon nanotube based hydrogen sensor for fuel cell applications," *International Journal of Hydrogen Energy*, vol. 32, no. 13, pp. 2518–2526, 2007.

[46] S. U. Rather, R. Zacharia, S. W. Hwang, M. U. D. Naik, and K. S. Nahm, "Hydrogen uptake of palladium-embedded MWCNTs produced by impregnation and condensed phase reduction method," *Chemical Physics Letters*, vol. 441, no. 4-6, pp. 261–267, 2007.

[47] R. Zacharia, S. U. Rather, S. W. Hwang, and K. S. Nahm, "Spillover of physisorbed hydrogen from sputter-deposited arrays of platinum nanoparticles to multi-walled carbon nanotubes," *Chemical Physics Letters*, vol. 434, no. 4–6, pp. 286–291, 2007.

[48] K. M. Brieño-Enriquez, J. Ledesma-García, J. J. Perez-Bueno, L. A. Godinez, H. Terrones, and C. Ángeles-Chavez, "Bonding titanium on multi-walled carbon nanotubes for hydrogen storage: an electrochemical approach," *Materials Chemistry and Physics*, vol. 115, no. 2-3, pp. 521–525, 2009.

[49] K. Iyakutti, Y. Kawazoe, M. Rajarajeswari, and V. J. Surya, "Aluminum hydride coated single-walled carbon nanotube as a hydrogen storage medium," *International Journal of Hydrogen Energy*, vol. 34, no. 1, pp. 370–375, 2009.

[50] W. Liu, Y. H. Zhao, Y. Li, Q. Jiang, and E. J. Lavernia, "Enhanced hydrogen storage on li-dispersed carbon nanotubes," *Journal of Physical Chemistry C*, vol. 113, no. 5, pp. 2028–2033, 2009.

[51] S. U. Rather, N. Mehraj-ud-din, R. Zacharia, S. W. Hwang, A. R. Kim, and K. S. Nahm, "Hydrogen storage of nanostructured TiO$_2$-impregnated carbon nanotubes," *International Journal of Hydrogen Energy*, vol. 34, no. 2, pp. 961–966, 2009.

[52] R. Zacharia, K. Y. Kim, A. K. M. Fazle Kibria, and K. S. Nahm, "Enhancement of hydrogen storage capacity of carbon nanotubes via spill-over from vanadium and palladium nanoparticles," *Chemical Physics Letters*, vol. 412, no. 4–6, pp. 369–375, 2005.

[53] Y. Suttisawat, P. Rangsunvigit, B. Kitiyanan et al., "Investigation of hydrogen storage capacity of multi-walled carbon nanotubes deposited with Pd or V," *International Journal of Hydrogen Energy*, vol. 34, no. 16, pp. 6669–6675, 2009.

[54] J. Wang, A. D. Ebner, and J. A. Ritter, "Kinetic behavior of Ti-doped $NaAlH_4$ when cocatalyzed with carbon nanostructures," *Journal of Physical Chemistry B*, vol. 110, no. 35, pp. 17353–17358, 2006.

[55] T. Yildirim and S. Ciraci, "Titanium-decorated carbon nanotubes as a potential high-capacity hydrogen storage medium," *Physical Review Letters*, vol. 94, no. 17, Article ID 175501, pp. 175501–175504, 2005.

[56] S. D. Conradson, "Application of X-ray absorption fine structure spectroscopy to materials and environmental science," *Applied Spectroscopy*, vol. 52, no. 7, pp. 252A–279A, 1998.

[57] G. Vlaic, D. Andreatta, and P. E. Colavita, "Characterisation of heterogeneous catalysts by EXAFS," *Catalysis Today*, vol. 41, no. 1–3, pp. 261–275, 1998.

[58] D. Koningsberger, B. Mojet, J. Miller, and D. Ramaker, "XAFS spectroscopy in catalysis research: AXAFS and shape resonances," *Journal of Synchrotron Radiation*, vol. 6, no. 3, pp. 135–141, 1999.

[59] H. Li, M. Eddaoudi, M. O'Keeffe, and O. M. Yaghi, "Design and synthesis of an exceptionally stable and highly porous metal- organic framework," *Nature*, vol. 402, no. 6759, pp. 276–279, 1999.

[60] X. Li, H. Zhu, C. Xu, Z. Mao, and D. Wu, "Measuring hydrogen storage capacity of carbon nanotubes by tangent-mass method," *International Journal of Hydrogen Energy*, vol. 28, no. 11, pp. 1251–1253, 2003.

[61] H. Z. Geng, T. H. Kim, S. C. Lim et al., "Hydrogen storage in microwave-treated multi-walled carbon nanotubes," *International Journal of Hydrogen Energy*, vol. 35, no. 5, pp. 2073–2082, 2010.

[62] F. W. Lytle, "The EXAFS family tree: a personal history of the development of extended X-ray absorption fine structure," *Journal of Synchrotron Radiation*, vol. 6, no. 3, pp. 123–134, 1999.

[63] B. Bogdanović and M. Schwickardi, "Ti-doped $NaAlH_4$ as a hydrogen-storage material—preparation by Ti-catalyzed hydrogenation of aluminum powder in conjunction with sodium hydride," *Applied Physics A*, vol. 72, no. 2, pp. 221–223, 2001.

[64] S. D. Lin, Y. H. Hsu, P. H. Jen, and J. F. Lee, "Probing Pd-carbon interaction in Pd/C catalysts by EXAFS," *Journal of Molecular Catalysis A*, vol. 238, no. 1-2, pp. 88–95, 2005.

*Research Article*

# Micromechanism and Kinetic Formulation of Vertically Aligned ZnO Nanorods Grown on Catalytic Bilayers

## Dong-Hau Kuo and Jheng-Yu He

*Department of Materials Science and Engineering, National Taiwan University of Science and Technology, Taipei 10607, Taiwan*

Correspondence should be addressed to Dong-Hau Kuo, dhkuo@mail.ntust.edu.tw

Vertically aligned ZnO nanorods were grown at 700°C for 2 h on sapphire substrates with catalysts in bilayer configurations of Sn (top)/Ni (bottom) and Sn/In, where the top layer is formed by sputtering and the bottom one is deposited by spin coating. The effects of bilayer catalysts on growth kinetics of nucleation and growth, growth micromechanism, and vertical alignment of growing ZnO nanorods have been investigated. The vertical alignment of the Sn/Ni-catalyzing ZnO nanorods is determined at the initial nucleation stage, where the nuclei are formed as regular candlestick-like platforms. The reason for the formation of the candlestick-like nuclei is due to the contribution of strain energy built in the underlying catalyst bilayers. The variations of axial and radial dimensions with growth duration for the growth of ZnO rods were explained and data fitting with the aids of kinetic growth equations, which are based upon the well-known ledge model for crystal growth from vapor and diffusion kinetics.

## 1. Introduction

Zinc oxide (ZnO) is a direct bandgap semiconductor with a wide bandgap of 3.37 eV and large exciton binding energy (60 meV). This semiconductor has been attractive for optoelectronic applications in light-emitting diodes and laser diodes at room temperature. Nanometer scale, one-dimensional (1D) materials, such as nanowires, nanorods, and nanotubes, have become of great interest due to their potential applications in nanolaser, field emission devices, photovoltaic, piezoelectric transducers, photocatalysts, chemical, and biosensors, and so forth.

The vapor-phase growth of 1D ZnO has been widely conducted with Zn and (ZnO + graphite) powders as reactants. The most uniform and vertically aligned (VA) ZnO nanorods with a diameter of 50–150 nm have been grown by using the carbothermal reaction above 850°C on Au catalyst-patterned sapphire substrates with the aids of submicrometer sized polystyrene balls [1] and laser-hardening lithography technology [2, 3] or by using the Zn source at 750°C on sapphire substrates covered with a *c* axis-oriented ZnO buffer layer [4]. Because no droplets on the tips of flat-ended nanorods have been observed, the self-catalytic growth

mechanism or the vapor-solid mechanism is used to explain the growth behaviors. However, the self-catalytic mechanism needs to consider the oxidation of catalysts during the growth period. The vapor-liquid-solid growth mechanism has been applied for nanowires with dome-shaped droplets on its tips. The formation of catalyst droplets and its durability through the growth process without oxidation or nitridation are the major concerns.

Gold has been the most important and reliable catalyst for growing 1D ZnO, because it has demonstrated the capability to grow uniform and aligned nanorods. The preference of Au catalyst is related to its high-temperature stability in oxidizing atmosphere. Other catalysts such as Ni, Sn, Cu, have also been examined, but their uniformity and size in diameter need to be improved. ZnO rods grown by thermal evaporation on the Ni-coated silicon had a large size of 300–350 nm in diameter [5]. By using Sn catalyst, a liquid Sn droplet was located on the tip of ZnO nanorods to assist the orientation-aligned growth [6, 7]. Catalyst has been recognized as a requisite to perform the 1D catalyst-confined growth. In order to understand the growth micromechanisms, we ever used Au-containing bilayer catalysts of Au/Al, Au/Ni, and Au/In to grow randomly oriented

ZnO rods on silicon wafer substrates with diameters of ~100, 400, and 800 nm, respectively [8]. To make a further progress in order to grow well-aligned ZnO nanorods instead of micrometer sized and randomly oriented ZnO rods on the bilayer catalyst-covered substrates without using Au as a catalyst, we had investigated different unilayer or bilayer configurations made by mixed-solution coating, sputtering, polymer dispersant in coating solution, substrate etching techniques [9–11]. The one with the promising result is the ZnO rods grown on the Fe-covered [9] and Sn/Ni bilayer substrates [11]. We have continued efforts on the growth of ZnO nanorods by using the bilayer configurations. There were few works to grow ZnO nanorods with a bilayer catalyst. With our variations in the bilayer configurations, we demonstrate in this paper with different growth modes and different micromechanisms.

From our systematic works, I have a better control in growing the well-aligned ZnO rods. *Without the better growth control, the measurements of rod dimensions in repeated experiments with different growth durations will be very difficult and not reliable, which is the reason for the difficulty and limited reports in kinetic study.* After we can provide reliable and controllable techniques to grow the uniform and vertically aligned ZnO nanorods with a size of ~110 nm in diameter by utilizing the bilayer catalysts of Sn/Ni and Sn/In, we intend to investigate the ZnO nanorods grown at different growth periods to explore the growth kinetics and the relations among the bilayer catalysts, the initial nucleation stage, and the subsequent growth stage. Kinetic growth equations are derived, which are based upon the variations of the axial and radial dimensions with the growth duration, and they are fitted well to our growth data. Some of works had measured the length/diameter changes with growth period, but only the interpretations were mentioned without rate equations to explain and fit their growth data individually in the axial and radial directions.

## 2. Experimental

ZnO nanowires were grown at 700°C for 2 h on the catalyst-coated Si wafer or sapphire substrates by thermal evaporation under a mixture flow of 10-sccm (standard cubic centimeter per minute) $O_2$ and 200-sccm $N_2$ with a Zn mixture of Zn and ZnO at a weight ratio of 1.0 g : 1.0 g or 1 : 1. The Zn mixture together with substrate was loaded on a graphite support. The preparation of catalyst layers involved spin coating and direct current (d.c.) sputtering. A similar experimental approach is listed in [9]. The spin coatings of Sn, In, and Ni catalysts involved the 0.01 M solutions of tin chloride, indium nitrate, and nickel nitrate, respectively, followed by pyrolysis at 650°C for 30 min and reduction at 850°C for 30 min in an (Ar + 7% $H_2$) mixed gas. Each pyrolyzed oxide had a film thickness of ~0.1 μm. For d.c. sputtering, Sn, In, and Ni films were deposited at output powers of 20 and 70 watts for 1 min for coating Sn and Ni, respectively, and of 5 watts for 3.5 min for depositing indium. These metallic catalyst layers had a thickness of 30–60 nm for each. In addition to the single-layered catalysts,

bilayer catalysts of Sn/Ni and Sn/In were also prepared. The bilayer catalysts were constituted by spin coating a bottom layer followed by sputtering a top layer. The symbol of Sn/Ni, as an example, represented a Sn-sputtered coating on top of a Ni-spin coated layer. After spin coating and pyrolysis of the Ni layer, the reduction reaction was executed after the Sn layer was sputtered on the nickel oxide. The sapphire substrates for the Sn/Ni system were etched by a 0.1 M NaOH solution. The substrate for the Sn/In system was not etched. The etching did not change the vertical alignment but was beneficial for obtaining slender 1D ZnO. To study the growth kinetics, ZnO nanorods were grown at 700°C for different durations of 1 min, 5 min, 30 min, and 120 min on Sn/Ni and Sn/In sapphire substrate. Before heating, the growth chamber was pumped down by mechanical pump. During the heating stage, the system was under argon and the Zn vapor generated as temperature approached 700°C. When the temperature reached 700°C, the mixed ($O_2$ + $N_2$) gas flowed into this system. Therefore, the oxide growth started at the $O_2$-added stage. Scanning electron microscopes (SEM, JEOL JSM 6500F, Japan; Cambridge S360, UK) were used to observe the growth morphology. A field-emission scanning electron microscope (FESEM, JEOL JSM 6500F, Japan) was used to observe the growth morphology and to measure the rod dimensions in length and diameter. Phase identification, composition analysis, and microstructural characterization of nanowires were conducted by a transmission electron microscope (TEM, JEOL 3010, Japan) equipped with energy dispersive spectroscopy (EDS). Room-temperature photoluminescence (PL) measurements were performed using a 325 nm He-Cd laser as the excitation source.

## 3. Results

*3.1. ZnO Growth on Catalytic Unilayers.* Figure 1 shows SEM images of one-dimensional ZnO grown at 700°C for 2 h on (a), (b) Sn, (c), (d) In, and (e), (f) Ni (a), (c), (e) sputter or (b), (d), (f) spin coated silicon wafer substrates by thermal evaporation with a Zn mixture of Zn and ZnO in a weight ratio of 1.0 g : 1.0 g. The Sn-catalyzing 1D ZnO was in the form of nanowires with smaller diameters of 100 nm (Figure 1(a)) and 200 nm (Figure 1(b)). The In-catalyzing growth contained nonuniform ZnO crystals including rods of 200–300 nm in size and larger leaf-like crystals (Figures 1(c) and 1(d)). The Ni-catalyzing 1D ZnO grown on Si wafer substrates were in the form of inclined and hexagonal-shaped rods with a larger diameter of 800 nm–1.5 μm for those spin coated (Figure 1(f)) and in the form of leafs with a large dimension in 600 nm–1.2 μm for those sputtered (Figure 1(e)). There is no difference for ZnO from the Sn catalyst, which can be attributed to its melt state at different catalyst size. However, the difference in the ZnO shape from the Ni catalyst can be related to the catalyst size, which in the solid state has led to different crystallinities. Catalysts of Sn, In, Ni spin coated with nitrate or chloride solutions can be reduced to form metallic droplets for Sn and Ni but it remains as an oxide layer for In catalysts. No matters of metallic indium or indium oxide, the grown ZnO had no
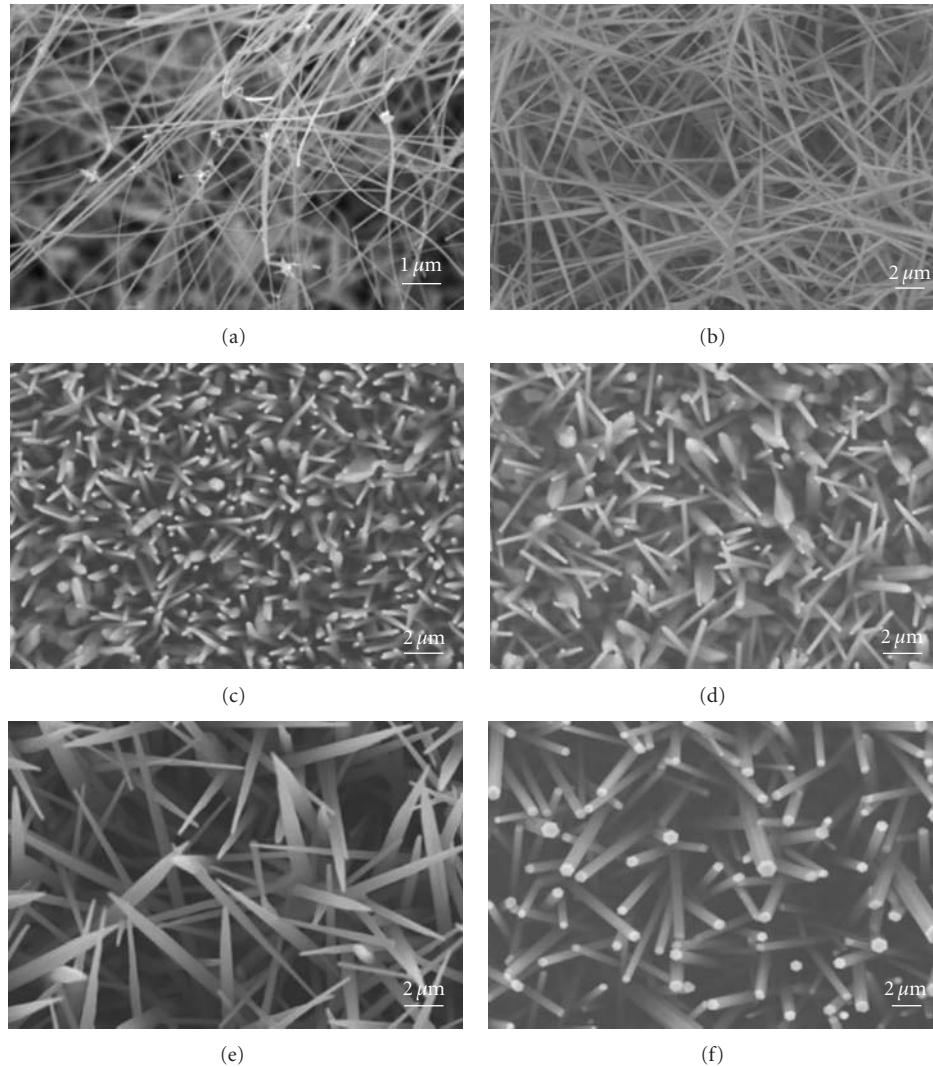
Figure 1: SEM images of one-dimensional ZnO grown at 700°C for 2 h on (a), (b) Sn, (c), (d) In, and (e), (f) Ni (a), (c), (e) sputter- or (b), (d), (f) spin coated silicon wafer substrates by thermal evaporation with a Zn mixture of Zn and ZnO in a weight ratio of 1.0 g : 1.0 g.

big differences for the sputtered and the spin coated ones. From these experiments, the Sn catalyst generates the finest nanowires and the spin coated Ni catalyst favors to form ZnO nanorods with a hexagonal cross-section. However, the size of these hexagonal-shaped ZnO was in a sub-micrometer scale. 1D ZnO rods grown with the Ni catalyst have constantly suffered the problem of large diameters [5].

*3.2. ZnO Growth on Catalytic Bilayers.* Two types of bilayer catalysts used to assist the 1D ZnO growth include Sn/Ni and Sn/In. **Figure 2** displays surface morphologies of ZnO nanorods grown at 700°C for (b) 1 min, (c) 5 min, (d) 30 min, and (e) 120 min on Sn sputter/Ni spin coated sapphire substrates. After growing for 1 min, no 1D formed and only nuclei were observed. ZnO nanorod arrays with a hexagonal cross-section had formed with a length of 0.4 ± 0.1 μm and a diameter of 100 ± 20 nm in 5 min from pyramid platforms, which behaved like a candle rod sits

on a candlestick. These pyramid platforms were examined at higher magnifications, as can be seen in the inset of **Figure 2(c)**. With increasing growth time, nanorods increase apparently on its length but not on its diameter. After a 2-h growth duration, the grown ZnO rods had a length of 30 ± 10 μm and a diameter of 110 ± 25 nm. The image of as-fabricated Sn/Ni bilayer catalyst, after pyrolysis at 650°C for 30 min and reduction at 850°C in an Ar-5% $H_2$ mixture gas for 30 min, is shown in **Figure 2(a)**. Before the ZnO growth, the Sn/Ni bilayer catalyst had become spheroidal. After the 1-min growth, the spheroidal catalysts disappear and the substrates were covered with the oxidized Zn-covering layers. The 2D growth on 1D-ZnO had been observed by metal-organic chemical vapor deposition [12].

**Figure 2(f)** shows the PL spectra of the VA-ZnO nanorods shown in **Figure 2(e)**. From the PL spectra, it can be seen that the vertically aligned ZnO nanorods only show a sharp and strong peak at approximately 383.3 nm (3.24 eV), which corresponds to the near-band-edge peak that is

(a)



(b)



(c)



(d)



(e)



(f)

FIGURE 2: Surface morphologies of ZnO nanorods grown at 700°C for (b) 1 min, (c) 5 min, (d) 30 min, and (e) 120 min on Sn sputter-/Ni spin coated sapphire substrates by thermal evaporation with a Zn mixture of Zn and ZnO in a weight ratio of 1 : 1. (a) SEM image of Sn sputter-/Ni spin coated bilayer catalysts after pyrolysis at 650°C for 30 min and reduction at 850°C in a Ar-5% $H_2$ mixture gas for 30 min. (f) Photoluminescence spectra for the vertically aligned ZnO nanorods in (e). The substrates were etched by a 0.1 M NaOH solution for 15 s. The inset in (c) was enlarged from the white square-selected area.

responsible for the recombination of free excitons through an exciton-exciton collision process [13–15]. A full width at half maxima value of 145 meV for this excitonic emission was obtained [16]. The appearance of a sharp and strong near-band-edge emission in the UV region without any deep level emission in the visible region indicates that the as-grown ZnO nanorods showed good crystallinity with a good optical property and few structural defects such as oxygen vacancies and interstitials of zinc. Therefore, based upon the bilayer catalyst-assisting growth, VA-ZnO nanorods with a good ultraviolet emission quality can be grown from pyramidal platforms or nuclei with parallel (0001) planes to the substrate surface.

Figure 3 displays surface morphologies of ZnO nanorods grown at 700°C for (b) 1 min, (c) 5 min, (d) 30 min, and (e) 120 min on Sn/In bilayer-coated sapphire substrates. The Sn/In catalysts remained as a layer on substrates (Figure 3(a)). The sputtered Sn layer inhibited by the underlying $In_2O_3$ layer did not become spheroidal after 850°C annealing. ZnO nuclei formed after the 1-min growth duration (Figure 3(b)). The ZnO nanorods directly grown from the catalytic buffer layer had a length of 0.75 ± 0.25 $\mu$m and a diameter of 250 ± 30 nm in 5 min without the platform nuclei available (Figure 3(c)). With the increase in the growth duration, the length and diameter of nanorods apparently increased. After a 2-h growth duration, the grown ZnO
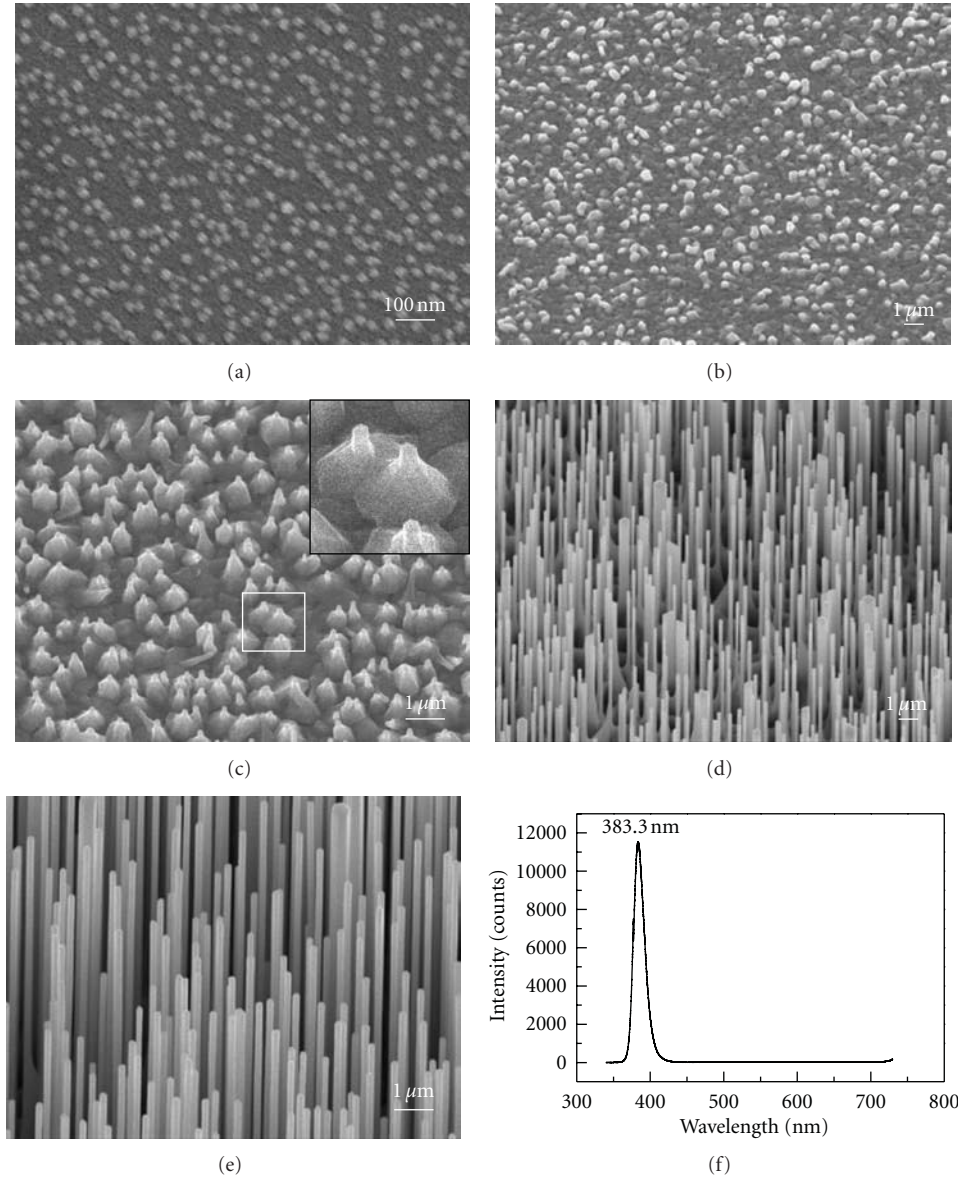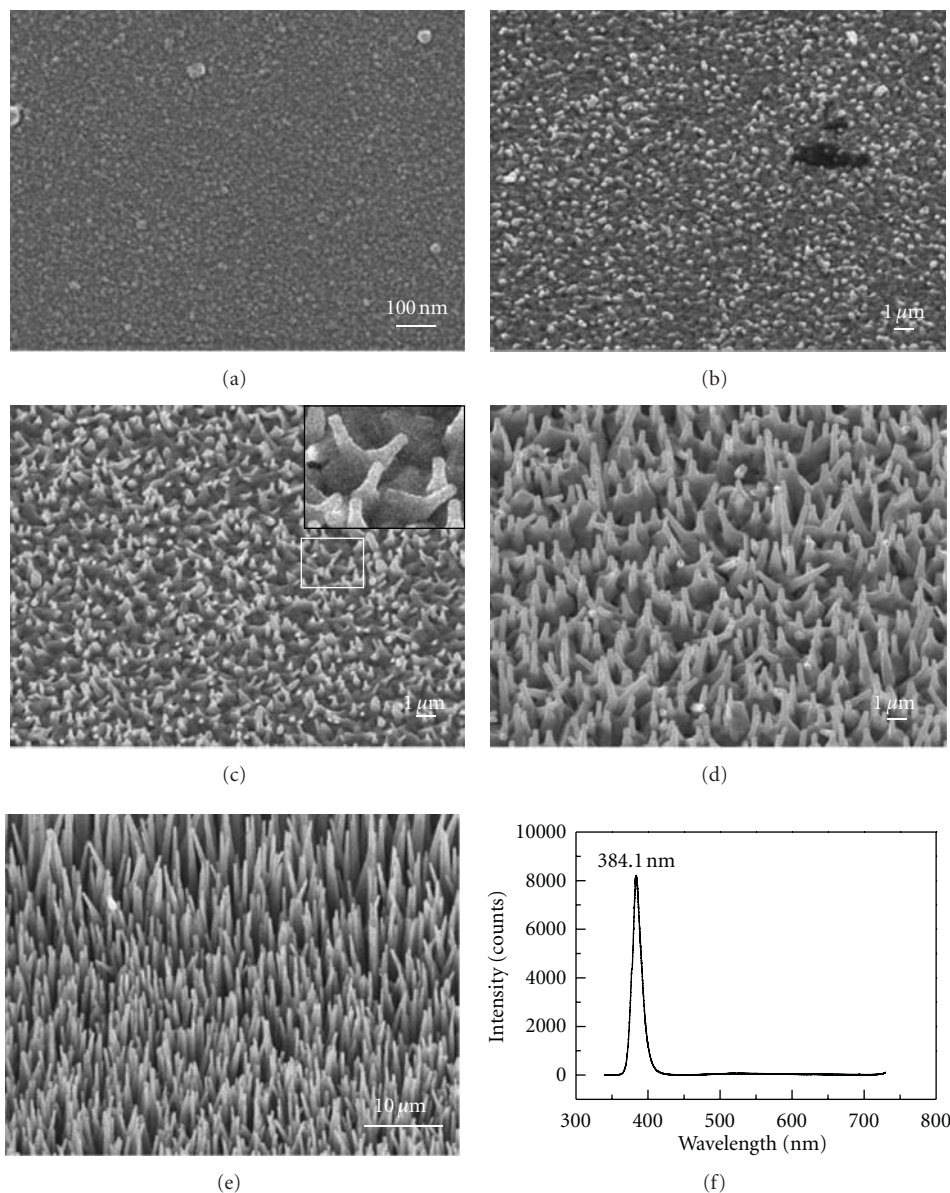
FIGURE 3: Surface morphologies of ZnO nanorods grown at 700°C for (b) 1 min, (c) 5 min, (d) 30 min, and (e) 120 min on Sn sputter-/In spin coated sapphire substrates by thermal evaporation with a Zn mixture of Zn and ZnO in a weight ratio of 1 : 1. (a) SEM image of Sn sputter-/In spin coated bilayer catalysts after pyrolysis at 650°C for 30 min and reduction at 850°C in an Ar-5% $H_2$ mixture gas for 30 min. (f) Photoluminescence spectra for the vertically aligned ZnO nanorods in (e). The inset in (c) was enlarged from the white square-selected area.

rods had a length of $25 \pm 5 \mu m$ and a diameter of $400 \pm 55$ nm (Figure 3(e)). Although the Sn/In-catalyzing ZnO rods had a hexagonal shape in cross-section, but these rods were not aligned. The inset in Figure 3(c) shows an enlarged image to observe the initial growth stage of ZnO nanorods. There were no larger, well-defined, and isolated pyramid platforms spreading on the ZnO-covering substrate surface. Figure 3(f) shows the PL spectra of the VA0-ZnO nanorods shown in Figure 3(e). The aligned ZnO nanorods display a sharp and strong peak at approximately 384.1 nm (3.23 eV). This nanorod showed a similar result in photoluminescence measurement as that shown for ZnO obtained

from the Sn/Ni catalyst (Figure 2(f)). The similar performance indicates the different catalyst configurations only change the growth behaviors but do not introduce growth defects.

*3.3. Dimensional Changes in the Axial and Radial Directions.* The growth kinetic study of 1D ZnO is executed by measuring the changes of the axial and radial dimensions with the growth duration. Figures 4(a) and 4(b) show the variations of the diameter and length of ZnO nanorods grown at 700°C for different durations of 1, 5, 30, 120 min on (a) Sn/Ni- and (b) Sn/In-coated sapphire substrates. Both of the systems
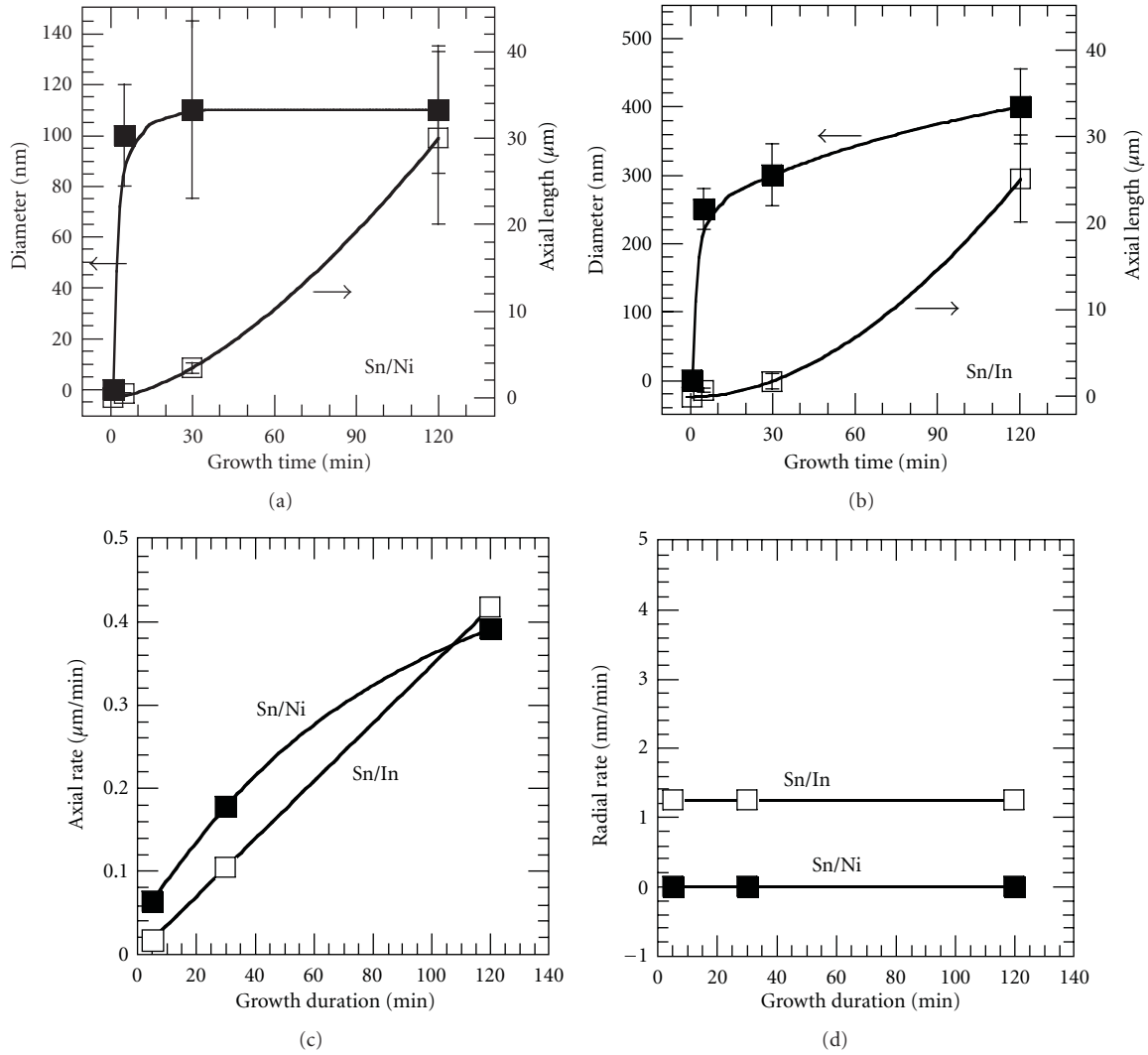
FIGURE 4: Growth behaviors in terms of the diameter and length of ZnO nanorods grown at 700°C for different durations of 1, 5, 30, 120 min on (a) Sn/Ni- and (b) Sn/In-coated sapphire substrates by a thermal evaporation-oxidation method with a Zn mixture of Zn and ZnO in a weight ratio of 1 : 1. The variations of axial and radial rates, obtained by curve fitting the 5-, 30, and 120-min data followed by retrieving from the derivatives of the best-fitting equations, with growth duration are shown in (c) and (d), respectively.

display a slight different trend. The Sn/Ni-catalyzing rods after growing for 5 min and 2 h have diameters of 100 ± 20 and 110 ± 25 nm, respectively, and lengths of 0.4 ± 0.1 and 30 ± 10 um. The stage for the first few minutes belongs to nucleation. The growth stage began apparent after a 5-minute growth period. The axial and radial growth rates can be derived at different periods, excluding the nucleation stage, as shown in Figures 4(c) and 4(d), by curve fitting the wire length-growth duration plot, followed by retrieving from the derivatives of the curve-fitting equations to obtain growth rates at the durations of 5, 30, and 120 min. *This approach needs to be emphasized, because the growth rate is not obtained from the measured length divided by our growth duration. The conventional approach is related to an average growth rate during a growth period, but our approach is to obtain an instantaneous rate.* For the Sn/Ni system, the lengthening rate was proportional to the time exponent of

1/2 and the thickening rate is zero. The lengthening and thickening rates were proportional to the time exponents of 1 and 0 for the Sn/In system.

## 4. Discussion

*4.1. ZnO Growth.* From the previous experimental data, two comparable systems of Sn/Ni and Sn/In have been obtained. The Sn/Ni system has grown the vertically aligned ZnO nanorods from the regularly aligned candlestick-like nuclei. The growth of ZnO rods from this system is a nucleus-confined growth. It only grows in the axial direction. The Sn/In system has grown the incompletely aligned rods from the ZnO-covering buffer layer. It does not show the apparent nuclei, as the candlestick-like nuclei do. These rods grow in both the axial and radial directions. By using the apparently
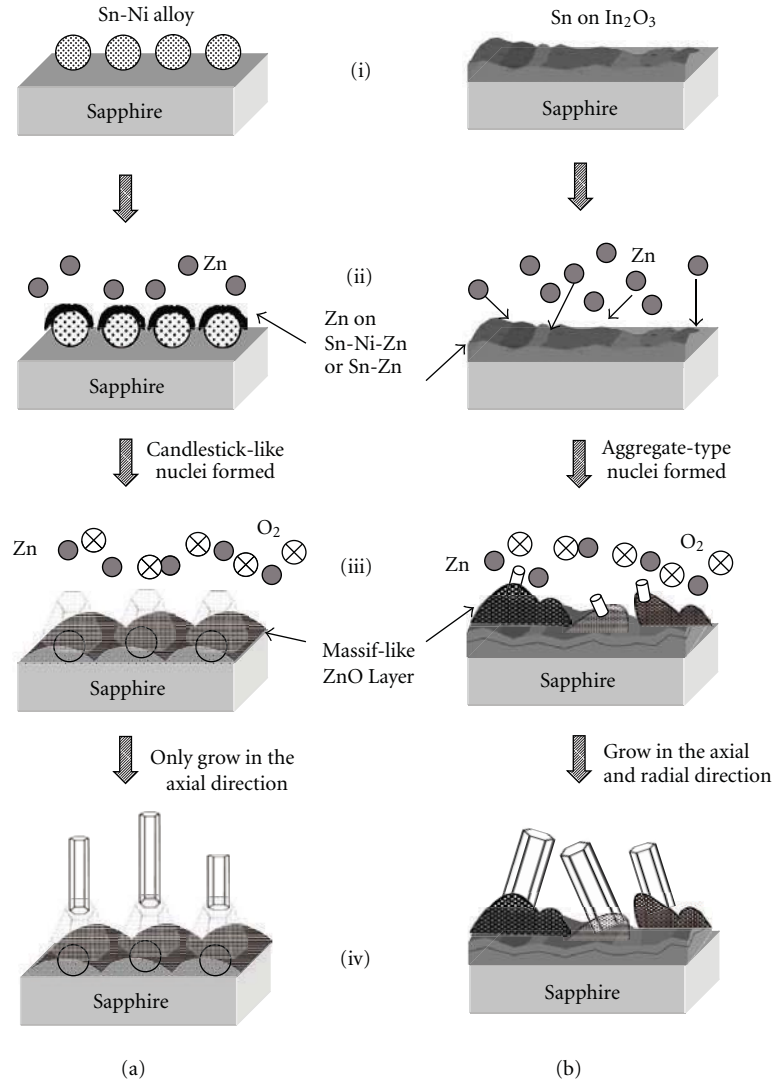
FIGURE 5: Schematic growth micromechanisms for (a) vertically aligned ZnO nanorod array grown on the Sn sputter/Ni spin coated sapphire substrates and for (b) slightly slant ZnO nanorods grown on the Sn/In coated substrates.

different systems for comparative purposes, the reasons for the growth behavior and dimensional change need to be explained and embodied by a formulated equation.

*4.2. Our Proposed Growth Micromechanisms.* From the observations of Figures 2 and 3, it is observed that the style of nuclei formed at the early stage of nucleation determines the vertical alignment of 1D ZnO. Figure 5 shows the schematic diagrams of the growth micromechanisms of the bilayer-catalyzing ZnO nanorods with the (a) vertically aligned and (b) slightly slant modes. The nuclei can be easily distinguished in the Sn/Ni system, where the flat-end pyramid-shaped islands form as candlestick-like platforms to provide the sites for growing ZnO nanorods with a hexagonal cross-section. On the other hand, the Sn/In system does not show the well-defined nuclei or the candlestick-like platforms and has grown slightly slant ZnO nanorods directly from the large-grained ZnO buffer layer by aggregating the adsorbed

adatoms through a short-range diffusion to form the nuclei. Briefly speaking, the Sn/Ni system has the platforms on the massif-like ZnO-covering layer but the Sn/In system only has the ZnO rods grown from the massif-like layer. The different nucleation behaviors can lead to the different inclination in alignment. The obvious reason for the differences of these two systems is related to the different components of nickel in the Sn/Ni system and indium in the Sn/In system. For the as-fabricated catalyst images in Figures 2(a) and 3(a), isolated catalyst droplets have formed in the Sn/Ni system, but it is not the case for the Sn/In system (Figure 5(i)). The nonreducible $In_2O_3$ films inhibit the spheroidization of metallic Sn in the Sn/In system (Figure 5(b-i)). Before oxygen enters the reactor at 700°C, zinc vapor liberates during the heating cycle. The vaporized Zn will condense and cover on substrates (Figure 5(ii)), react with the spheroidal catalysts (Figure 5(a-ii)), and be oxidized once oxygen is introduced (Figure 5(a-iii)) [17]. For the Sn/Ni system, the

ZnO buffer layers embedded inside with reacted spheroidal catalysts are composed of large grains and favor to nucleate flat-end or (0001) plane-oriented pyramid platforms. The flat ends of those platforms orient parallel to the (0001) plane-oriented sapphire substrates in order to establish the well-aligned nanorods. After a 1-minute growth period (Figure 2(b)), the nuclei or platforms are not obvious. After a 5-minute growth period, the pyramidal nuclei have formed with protruded nanorods of $0.4\,\mu$m in length. It can be induced that the nucleation step is accomplished within the first five minutes. After a 2-h growth duration, our nucleus platforms behave as candlesticks regularly sitting on the massif-like table ready for growing VA-ZnO nanorods with a diameter of ~110 nm.

For the Sn/In system, the ZnO buffer layers underlying with flat Sn/In$_2$O$_3$ catalyst layers (Figures 5(b-ii) and 3(b)). Nucleation occurs randomly and does not form the flat-end pyramid platforms. Once the nuclei grow to a critical size, the ZnO nanorods are directly grown from the massif-like ZnO layers in an inclined orientation via the reactant adsorption from vapor, surface diffusion of adatoms, zinc-oxygen reactions, and the desorption for the surplus reactants (Figure 5(b-iii)). As the ZnO growth continues, the rods increase its dimensions in length and diameter (Figure 5(b-iv)). However, the formation of isolated catalyst droplets cannot guarantee the vertical alignment of ZnO nanorods. To have regularly aligned ZnO nanorods, the formation of the candlestick-like platforms is the critical factor. Therefore, the choice of the catalyst combination is very important, which can lead to different catalyst properties, reactions, and stress states. Based on the nucleation and growth theory for crystal growth, the extra built-in strain energy in the Sn/Ni system assists nucleation by overcoming the formation energy of pyramidal nuclei. There is no sufficient built-in strain energy for the Sn/In system due to the softness of Sn metal in the form of flat layer. Growth mechanisms of randomly oriented 1D ZnO with nanopen-, nanonail-, or nanopencil-like structure on pyramids have been proposed in literatures, however, their pyramids had a comparatively large dimension to form the pen-like shape [18, 19]. Kim et al. have been aware that the nanosheets with several facet planes play a significant role in the evolution of ultraslim and vertical ZnO nanowire arrays [20]. However, their nanosheets are similar to the previously proposed self-catalyzing ZnO buffer layers.

### 4.3. Kinetics and Kinetic Model.
Our candlestick-like nuclei restrict the thickening of ZnO nanorods. When the axial dimensions of ZnO rods increase exponentially with the growth duration, their radial dimensions do not change for the Sn/Ni system but have a big change for the Sn/In system (Figure 4(b)). The irrelevance of our radial dimension in the Sn/Ni system with growth time is similar with the growth of carbon nanotubes (CNTs) and can be attributed to the nucleus-confined growth behavior. The reported diameters of 1D ZnO increased with growth time [21, 22]. Tsao et al. reported a linear relation. For the axial dimension, it increases fast but levels off at long durations for CNTs [23]. A

linear relation between the length of nanowires and growth time for 1D ZnO has been reported [21, 24]. Reports with experimental growth data in the axial and radial directions simultaneously changed with growth duration are rare. The trends of rod length or diameter in the growth kinetics have been mentioned, but the explanations and data fitting with *kinetic equations* are much difficult. What the relevance is between the changes of rod length and diameter needs more understanding, regardless to say the data fitting for the rod length and diameter together with kinetic equations. However, we will use kinetic equations to fit and explain the growth rates in radial and axial directions together. The systematical dimension measurements at different durations for kinetic understanding are our major approach to probe the growth kinetic problems. This work is totally different from our previous work on the developments of aligned and well-controlled ZnO rods, but they provide the basis for our progress in kinetics [8–11].

To analytically formulate the vapor-solid growth rates, the kinetic of the well-known ledge model (Figure 6(a)) and the surface diffusion (Figure 6(b)) needs to be considered [25, 26]. *Although this mechanism has been well developed, there are no reported data referring or fitting to the equations derived from such a ledge mechanism.* The reactants from vapors will gas-phase diffuse through a boundary layer to surface and become adatoms. The adatoms will propagate on surface through surface diffusion to execute reactions and find stable sites to reside. There are two directions on the step ledge, one is for ledge lengthening and the other is for thickening (Figure 6(a)). Li et al. proposed the growth mechanisms of tapered ZnO nanowire arrays with the aids of step velocity and radial growth rate [27]. They mentioned only the concept of the ledge velocity and radial velocity for the tapering angle. Shi et al. proposed the lattice step ledges as preferred places for nucleation of ZnO by the oxidation of Zn on step ledges [28]. Both of them did not present the experimental data in growth rates. Based upon the conservation of mass transporting from the vapor and migrating on the surface, the ledge velocity for a multiple-growth step condition is formulated as [25]

$$
\begin{aligned}
v_{\text{ledge}} &= \frac{\sqrt{2}(C_\infty - C_e)\lambda}{N^* \cdot \tau} \times \tanh\left(\frac{d}{\sqrt{2}\lambda}\right) \\
&= \frac{\sqrt{2}(S-1)Z_e\lambda}{N^*} \times \tanh\left(\frac{d}{\sqrt{2}\lambda}\right),
\end{aligned}
\tag{1}
$$

where $C_\infty$ is the concentration of reactants in the gas phase far away from the growing interface, $C_e$ the equilibrium concentration at vapor-solid interface, $C_i$ the interface concentration, $C_p$ the concentration of ZnO crystal, $d$ the distance between steps, $Z_e$ the stream of colliding reactants per unit time in equilibrium on interfaces, $\lambda$ the mean diffusion distance between adsorption and evaporation, $N^*$ the number of sites per unit area on crystal surface, $\tau$ the mean time of stay for adatoms, $S$ the supersaturation ($C_\infty/C_e$), and $C_e$ defined as $Z_e \cdot \tau$. In the ledge mechanism, the adsorbed reactant vapor will evaporate if it resides far away from steps. Although this equation is derived from a
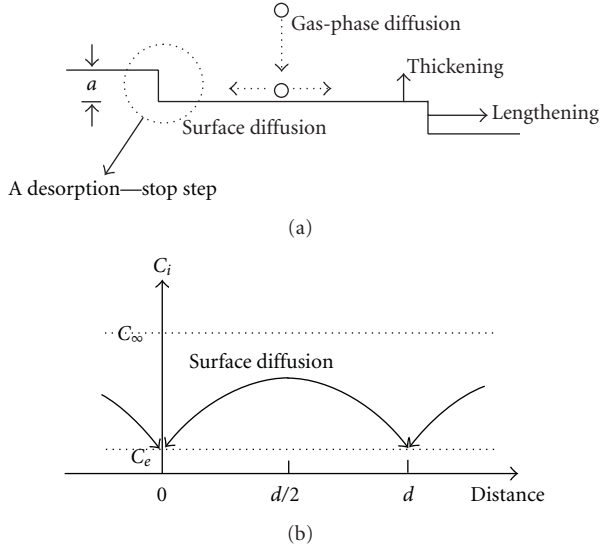
(a)



(b)

FIGURE 6: (a) Schematic configuration of the vapor-phase growth of ZnO rods *via* the combination of the ledge mechanism and diffusion processes, which involves the surface diffusion-controlled mechanism nearby the growing steps and the gas phase diffusion-controlled mechanism nearby the solid-vapor interface. The concentration profile for the surface diffusion-controlled growth mechanism is shown in (b).

well-known model, its utilization together with the growth data of one-dimensional crystals is rare.

Based upon the two-dimensional nucleation, $d$ is proportional to the critical size of nuclei and inversely proportional to the formation energy of the nanorods $(\Delta G_f)$. $\Delta G_f$ related to the free energies of the gas-phase state and the equilibrium solid state is proportional to the $\mathrm{RT} \cdot \ln(C_\infty/C_e)$. Therefore, the step spacing can be related to supersaturation of $(S-1)$ as shown in (2) provided $(C_\infty - C_e) \ll C_e$ in a dilute gas phase [25]:

$$
\begin{aligned}
d \propto \frac{1}{\Delta G_f} &= \frac{1}{\mathrm{RT} \cdot \ln(C_\infty/C_e)} \\
&\approx \frac{1}{\mathrm{RT} \cdot (C_\infty - C_e)/C_e} \\
&= \frac{1}{\mathrm{RT} \cdot (S-1)}.
\end{aligned}
\tag{2}
$$

Under a constant reactant flux, the apparent flux at the growth front of crystal gradually becomes increased because the crystal becomes longer. Therefore, one assumption is made here to have supersaturation $(S-1)$ proportional to $t^{1/2}$, that is, $(S-1) = k_1 t^{1/2}$ with $k_1$ a constant.

Our two systems with completely different behaviors in growth rates are discussed in the following sections with the viewpoint of kinetic formulation for the growth stage.

*4.3.1. ZnO Nanorods Grown on Sn/Ni-Coated Substrates.* These ZnO NRs grow faster at the axial direction but do not increase its dimension in diameter. The ZnO growth is confined by the candlestick-like nuclei to grow only in the

axial direction (Figure 4(a)). It is assumed that the axial growth of smooth growing fronts of ZnO NRs is assisted by the "ledge mechanism." These ledges form on nuclei and on the flat-end top surface under a supersaturation growth condition in order to initiate the two-dimensional nucleation and growth processes. With the ledge growth mechanism, the lengthening rate can be expressed as

$$
\frac{d\ell}{dt^{\mathrm{Sn/Ni}}_{\mathrm{axial}}} = \frac{a}{d} \times v_{\mathrm{ledge}}.
\tag{3}
$$

As higher strain energy is embedded in the Zn vapor-covering Sn/Ni layer, the ledges formed on the nuclei under supersaturation are a lot and their step spacing of $d$ is quite smaller than the mean diffusion distance. With the condition of $d \ll \lambda$, (1) can be simplified as

$$
\begin{aligned}
\frac{d\ell}{dt^{\mathrm{Sn/Ni}}_{\mathrm{axial}}} &\approx \frac{a}{d} \times \frac{\sqrt{2}(S-1)Z_e\lambda}{N^*} \times \left(\frac{d}{\sqrt{2}\lambda}\right) \\
&= \frac{a \cdot Z_e}{N^*}(S-1) \\
&\approx \frac{a \cdot Z_e}{N^*} \cdot k_1 \sqrt{t}.
\end{aligned}
\tag{4}
$$

With this derivation, the axial rate of the Sn/Ni system is proportional to $t^{1/2}$, which is consistent with our experimental data in Figure 4(c).

As for a nil growth rate in diameter, it indicates the reactant vapor can only form nuclei on the flat-end cones. The nucleation on the smooth sides of hexagonal cones is difficult. The accommodation factor of reactant vapors for this system except on the flat-end top surface is almost negligible. The inability to build a radial rate can be related to the taller nuclei with steep edges, which is difficult to build the desorption-stop steps (Figure 6(a)) on nuclei. The desorption-stop step is the step in the ledge mechanism with the emphasis on its function to hold the adatoms. The adatoms without the desorption-stop steps cannot stick to that interface and will slip away or desorb from substrates.

Here, we need to clarify that the higher supersaturation due to larger strain energy can nucleate the growth steps with a short spacing (2). From the Sn/Ni system with a nil radial growth rate, we understand that supersaturation in vapor surrounding NRs is not helpful in building the heterogeneous nuclei on the NR sides. This behavior is also applied to the other system due to the same reactant flux. To differentiate these systems, the types of the desorption-stop steps on nuclei is important.

*4.3.2. ZnO Nanorods Grown on Sn/In-Coated Substrates.* These ZnO NRs have grown with a linearly increasing rate in the axial direction (Figure 4(c)) in addition to a constant thickening rate (Figure 4(d)). Our NR lengthening is analyzed with the similar equation of (1), but the condition becomes $d \gg \lambda$ and $\tanh(d/\sqrt{2} \cdot \lambda) \approx 1$. This hypothesis can

be supported by the smallest strain energy in the buffer layer. Therefore, (1) for the axial growth rate becomes

$$
\begin{aligned}
\frac{d\ell}{dt}\Big|_{\text{axial}}^{\text{Sn/In}} &\approx \frac{a}{d} \times \frac{\sqrt{2}(S-1)Z_e\lambda}{N^*} \times 1 \\
&= k_2 a\text{RT}(S-1) \times \frac{\sqrt{2}(S-1)Z_e\lambda}{N^*} \\
&= k_3(S-1)^2 \\
\frac{d\ell}{dt}\Big|_{\text{axial}}^{\text{Sn/In}} &\approx k_3\left(k_1 \cdot t^{1/2}\right)^2 = kt,
\end{aligned}
\tag{5}
$$

where $k$, $k_2$, and $k_3$ are the proportional constants. With this derivation, the axial rate of the Sn/In system is proportional to $t$, which is consistent with the growth rate data in Figure 4(c).

Our NRs were thickened at the same time of the axial growth but with a slower rate. In order to increase the NR diameter, new absorbing adatoms need to arrive on the growing-stop steps of nuclei. Due to the smaller strain energy or the larger step distance, the attachment of reactant adatoms on the steps of nuclei is more difficult. In this situation, the ZnO growth on the desorption-stop steps of nuclei becomes a rate-determining factor, the NR thickening is controlled by the reactant reactions on the buffer layer-covering substrates, or the radial growth is an surface diffusion-controlled process (Figure 6(b)). For the interface-controlled growth, the growth rate or the thickening rate, proportional to the difference in chemical potentials ($\Delta\mu$) of reactions at interface and at equilibrium or approximately to the off-balance concentration ($C_i - C_e$) at moving interfaces (Figure 6(b)), can be expressed as

$$
\begin{aligned}
v_{\text{radial}}^{\text{Sn/In}} &= M \cdot (\text{force}) = M \cdot \frac{\Delta\mu}{V_m} \\
&= \frac{M\text{RT}}{V_m} \cdot \ln\left(\frac{C_i}{C_e}\right) \\
&\approx \frac{M\text{RT}}{V_m} \cdot \frac{C_i - C_e}{C_e},
\end{aligned}
\tag{6}
$$

where $M$ is the interface mobility, $C_i$ is the concentration between steps, and $V_m$ the molar volume of materials. Therefore, the thickening rate of the Sn/In system is almost constant, which is consistent with the experimental data in Figure 4(d).

Our proposed growth formulations are applied only for 1D ZnO grown by a vapor-solid mechanism. For the growth *via* a vapor-liquid-solid process, the diffusion in liquid droplets becomes the rate-determining step for lengthening as the wire diameter is determined by the catalyst size [29].

Growth behaviors of one-dimensional ZnO nanorods grown with a vapor-solid process are determined by the nucleus states of the buffer layer on substrates. With different surface modifications to generate different residual stress states in the buffer layers, the nucleation and growth behaviors for the rod growth become different, which reveal in the different growth behaviors in the axial and radial directions. With the successful equation formulations applied to different growth modes by using the basic kinetic model for crystals growing from vapor, the ZnO growth behaviors can be better elucidated and understood. Although some assumptions have been made and some considerations may not be complete, this work is trying to curve fit the experimental data with rate equations and to find the relevance between the axial and radial growth behaviors. In the Sn/Ni system, the ZnO growth occurs with the aid of the ledges on the flat-end top surface of the candlestick-like nuclei. No rod thickening is caused by the difficulty in the attachment of reactants on the side surface of camdlestick-like nuclei. For the Sn/In system, growths in the axial and radial directions simultaneously occur. Their lengthening provided by a ledge mechanism is determined by the step configuration. Their thickening is attributed to the attachment of reactant vapors to steps on nuclei through a surface diffusion-controlled process.

## 5. Conclusions

Vertically aligned ZnO nanorods were successfully grown on the bilayer catalyst-covered sapphire substrates with a length of $30 \pm 10\,\mu$m and a diameter of $110 \pm 25$ nm by thermal evaporation at $700°$C for 2h in the atmospheres of oxygen and nitrogen. The bilayer catalysts included Sn/Ni and Sn/In with the top and bottom layers prepared by sputtering and spin coating, respectively. Sn/Ni system shows a promising potential to grow vertically aligned ZnO nanorod arrays with a good ultraviolet emission from the regular and candlestick-like pyramid nuclei, which is aided by the strain energy built in the underlining catalyst layer. Without the pyramidal nuclei, slightly inclined nanorods in the Sn/In sytem were grown. The kinetic data of the growth rates in axial and radial directions for the Sn/Ni and Sn/In systems can be successfully curve fitted, correlated, and interpreted by kinetic equations, based upon the ledge mechanism for the vapor-solid crystal growth and diffusion kinetics.

## Acknowledgment

## References

[1] H. J. Fan, B. Fuhrmann, R. Scholz et al., "Well-ordered ZnO nanowire arrays on GaN substrate fabricated via nanosphere lithography," *Journal of Crystal Growth*, vol. 287, no. 1, pp. 34–38, 2006.

[2] X. Wang, C. J. Summers, and Z. L. Wang, "Large-scale hexagonal-patterned growth of aligned ZnO nanorods for nano-optoelectronics and nanosensor arrays," *Nano Letters*, vol. 4, no. 3, pp. 423–426, 2004.

[3] D. S. Kim, R. Ji, H. J. Fan et al., "Laser-interference lithography tailored for highly symmetrically arranged ZnO nanowire arrays," *Small*, vol. 3, no. 1, pp. 76–80, 2007.

[4] L. Wang, X. Zhang, S. Zhao, G. Zhou, Y. Zhou, and J. Qi, "Synthesis of well-aligned ZnO nanowires by simple physical

vapor deposition on *c*-oriented ZnO thin films without catalysts or additives," *Applied Physics Letters*, vol. 86, no. 2, Article ID 024108, 3 pages, 2005.

[5] A. Umar, B. Karunagaran, E. K. Suh, and Y. B. Hahn, "Structural and optical properties of single-crystalline ZnO nanorods grown on silicon by thermal evaporation," *Nanotechnology*, vol. 17, no. 16, pp. 4072–4077, 2006.

[6] P. X. Gao, Y. Ding, and Z. L. Wang, "Crystallographic orientation-aligned ZnO nanorods grown by a tin catalyst," *Nano Letters*, vol. 3, no. 9, pp. 1315–1320, 2003.

[7] Y. Ding, P. X. Gao, and Z. L. Wang, "Catalyst-nanostructure interfacial lattice mismatch in determining the shape of VLS grown nanowires and nanobelts: a case of Sn/ZnO," *Journal of the American Chemical Society*, vol. 126, no. 7, pp. 2066–2072, 2004.

[8] D. H. Kuo and B. J. Chang, "From preannealing of bilayer catalysts to explore the growth micromechanisms of ZnO nanorods," *Crystal Growth and Design*, vol. 10, no. 2, pp. 977–982, 2010.

[9] D. H. Kuo, J. F. Fang, R. S. Chen, C. A. Chen, and Y. S. Huang, "ZnO nanomaterials grown with Fe-based catalysts," *Journal of Physical Chemistry C*, vol. 115, no. 25, pp. 12260–12268, 2011.

[10] D.-H. Kuo and B.-J. Chang, "Growth behaviors of ZnO nanorods grown with the Sn-based bilayer catalyst-covered substrates," *Journal of Nanomaterials*, vol. 2011, Article ID 603098, 9 pages, 2011.

[11] D.-H. Kuo, J.-Y. He, and Y.-S. Huang, "Synthesis of vertically aligned ZnO nanorods on Ni-based buffer layers using a thermal evaporation process," *Journal of Electronic Materials*, vol. 41, no. 3, pp. 451–456, 2012.

[12] S. H. Park, S. H. Kim, and S. W. Han, "Growth of homoepitaxial ZnO film on ZnO nanorods and light emitting diode applications," *Nanotechnology*, vol. 18, no. 5, Article ID 055608, 2007.

[13] S. C. Lyu, Y. Zhang, H. Ruh et al., "Low temperature growth and photoluminescence of well-aligned zinc oxide nanowires," *Chemical Physics Letters*, vol. 363, no. 1-2, pp. 134–138, 2002.

[14] E. M. Wong and P. C. Searson, "ZnO quantum particle thin films fabricated by electrophoretic deposition," *Applied Physics Letters*, vol. 74, no. 20, pp. 2939–2941, 1999.

[15] V. Srikant and D. R. Clarke, "On the optical band gap of zinc oxide," *Journal of Applied Physics*, vol. 83, no. 10, pp. 5447–5451, 1998.

[16] W. I. Park, G. C. Yi, M. Kim, and S. J. Pennycook, "ZnO nanoneedles grown vertically on Si substrates by non-catalytic vapor-phase epitaxy," *Advanced Materials*, vol. 14, no. 24, pp. 1841–1843, 2002.

[17] X. Q. Meng, D. X. Zhao, J. Y. Zhang et al., "Growth temperature controlled shape variety of ZnO nanowires," *Chemical Physics Letters*, vol. 407, no. 1–3, pp. 91–94, 2005.

[18] H. Tang, J. C. Chang, Y. Shan et al., "Growth mechanism of ZnO nanowires via direct Zn evaporation," *Journal of Materials Science*, vol. 44, no. 2, pp. 563–571, 2009.

[19] G. Shen, Y. Bando, B. Liu, D. Golberg, and C. J. Lee, "Characterization and field-emission properties of vertically aligned ZnO nanonails and nanopencils fabricated by a modified thermal-evaporation process," *Advanced Functional Materials*, vol. 16, no. 3, pp. 410–416, 2006.

[20] D. C. Kim, S. K. Mohanta, and H. K. Cho, "Vertically aligned ultraslim zno nanowires formed by homobuffer: growth evolution and emission properties," *Crystal Growth and Design*, vol. 9, no. 11, pp. 4725–4729, 2009.

[21] F. C. Tsao, J. Y. Chen, C. H. Kuo et al., "Residual strain in ZnO nanowires grown by catalyst-free chemical vapor deposition on GaN/sapphire (0001)," *Applied Physics Letters*, vol. 92, no. 20, Article ID 203110, 3 pages, 2008.

[22] W. Mai, P. Gao, C. Lao et al., "Vertically aligned ZnO nanowire arrays on GaN and SiC substrates," *Chemical Physics Letters*, vol. 460, no. 1–3, pp. 253–256, 2008.

[23] H. Cui, G. Eres, J. Y. Howe et al., "Growth behavior of carbon nanotubes on multilayered metal catalyst film in chemical vapor deposition," *Chemical Physics Letters*, vol. 374, no. 3-4, pp. 222–228, 2003.

[24] H. J. Fan, F. Fleischer, W. Lee et al., "Patterned growth of aligned ZnO nanowire arrays on sapphire and GaN layers," *Superlattices and Microstructures*, vol. 36, no. 1–3, pp. 95–105, 2004.

[25] R. H. Doremus, *In Rates of Phase Transformation*, Academic Press, Orlando, Fla, USA, 1985.

[26] D. A. Porter and K. E. Eastering, *In Phase Transformations In Metals and Alloys*, CRC Press, 2nd edition, 1992.

[27] S. Li, X. Zhang, and L. Zhang, "$Sb_2O_3$-induced tapered ZnO nanowire arrays: the kinetics of radial growth and morphology control," *Journal of Physical Chemistry C*, vol. 114, no. 23, pp. 10379–10385, 2010.

[28] J. Shi, S. Grutzik, and X. Wang, "Zn cluster drifting effect for the formation of ZnO 3D nanoarchitecture," *ACS Nano*, vol. 3, no. 6, pp. 1594–1602, 2009.

[29] D. H. Kuo and M. Y. Su, "Growth and kinetic modeling of $Fe(CO)_5$-catalyzed carbon nanotubes grown by chemical vapor deposition," *Journal of the Electrochemical Society*, vol. 153, no. 4, pp. J21–J25, 2006.

*Research Article*

# Figures of Merit for High-Performance Transparent Electrodes Using Dip-Coated Silver Nanowire Networks

## Sergio B. Sepulveda-Mora[1] and Sylvain G. Cloutier[2]

[1] *Department of Electrical & Computer Engineering, University of Delaware, Newark, DE 19716, USA*
[2] *Department of Electrical Engineering, École de Technologie Supérieure, Montréal, QC, Canada H3C 1K3*

Correspondence should be addressed to Sergio B. Sepulveda-Mora, sergiosm@udel.edu

Homogeneous, highly conductive, and transparent silver nanowire thin films were fabricated using a simple dip-coating technique and a subsequent annealing step. Silver nanowires with two different average lengths (11 $\mu$m and 19 $\mu$m) were used in the sample preparation to analyze the dependence of the sheet resistance on the length of the one-dimensional nanostructures. The best sample had a sheet resistance of 10.2 $\Omega/\square$ with optical transmittance of 89.9%. Two figures of merit, the electrical to optical conductivity ratio ($\sigma_{DC}/\sigma_{OP}$) and $\phi_{TC}$, were obtained for all the samples in order to measure their performance as transparent conductive materials.

## 1. Introduction

Transparent conductive electrodes (TCE) are unique materials that manifest both high electrical conductivity and high optical transmittance. Such materials are an essential component in optoelectronic devices which require to extract electrons from the active layer while allowing the light to pass through. Some applications of TCE are organic solar cells, thin film solar cells, light-emitting diodes (LEDs), liquid crystal displays (LCDs), touch screens, antistatic coatings, and electromagnetic shielding, among others [1]. Transparent conductive thin films are of special interest in the solar energy industry [2], mainly for their application in the new generation of low-cost photovoltaic devices.

The performance of TCE films can be assessed through two crucial parameters, namely, the sheet resistance ($R_{sh}$) and the optical transmittance ($T$). It is always desirable to have a low $R_{sh}$ with a high value of $T$. Nevertheless, there is an inherit relation between these variables. Lower values of $R_{sh}$ leads to a decrease in the optical transmittance and vice versa.

Metal oxides are currently the most widely used material for TCE. Aluminum-doped Zinc Oxide is used in amorphous silicon solar cells, fluorine doped tin oxide (FTO), and indium-doped tin oxide (ITO) are used in organic solar cells and

LEDs [3]. During the last five decades, ITO has dominated the market as the most commonly used TCE in optoelectronic applications owing to its high optical transparency at very low sheet resistance (typical values are $T = 80\%$ and $R_{sh} = 10 \, \Omega/\square$ in glass substrate [4]).

Although ITO has demonstrated to work very well in optoelectronic applications in the last years, it also has some drawbacks which are leading to search for alternative materials. First, the fabrication of ITO is costly and complex because of the high vacuum required in the sputtering process. Second, indium is becoming scarcer with the pass of time, which in turn produces an increment in the price of ITO. Finally, ITO is completely unsuitable for flexible devices owing to its brittle nature [5].

Recently, emerging candidates have been proposed as replacement for metal oxides, specially for applications in flexible devices. Random carbon nanotubes (CNTs) networks [6–8] and graphene [9] have been characterized as TCE thin films. In fact, organic solar cells have been successfully implemented and tested using CNTs [10, 11] and graphene [12, 13] as the front transparent contact. In general, CNTs and graphene have shown stable flexibility but still with inferior performance than that of ITO with regard to $R_{sh}$ and $T$.

A new paradigm to achieve both high conductivity and high transparency is to use a mesh of highly conductive metal nanowires covering only a small fraction of a surface. Copper [14] and silver [3, 4, 15–20] nanowire networks have been reported to behave as TCE with comparable performance to ITO and also with bending and stretching stability.

Other approaches include the preparation of TCE thin films using hybrid composite materials such as silver nanowires with metal oxides [21, 22], a mixture of silver and gold nanowires [23], and silver nanowires with polymer [24–26].

Silver nanowire networks stand out among all the other candidates to replace ITO in optoelectronic devices due not only to their electrical and optical characteristics (comparable and in some cases better than ITO [19]) but also because of the constant $R_{\text{sh}}$ while the film is being bent or stretched [3, 15, 16, 18, 20]. Furthermore, silver nanowire meshes have been proven to effectively replace ITO in organic solar cells [4, 22, 24, 27, 28], sound emitting devices [29], touch screens [17], organic LEDs [25, 26], and electrical conductive adhesives [30] applications.

While different deposition techniques of silver nanowires on rigid and flexible substrates have been already demonstrated [3, 15–17, 19, 20], most of them showed an inferior performance than that of ITO on rigid substrates. In this paper, we report the fabrication of uniform silver nanowire thin films using a straightforward dip-coating technique and a subsequent annealing step. In our best sample, we obtained a very low sheet resistance ($R_{\text{sh}} = 10.2\,\Omega/\square$) with an outstanding optical transmittance (89.9%). We fabricated and characterized silver nanowire networks with two different average lengths leading to analyse the influence of nanowire morphology in the overall performance of the film as a transparent conductive electrode. Two figures of merit defined in the literature were used to determine the quality of the films.

## 2. Experimental

Silver nanowires in ethanol solution were purchased from two different companies, namely, Blue nano (product no. SLV-NW-90) and Nanogap (product number NF Ag-3101-E). The first one with a concentration of 10 mg/mL and the second one with 0.87 mg/mL. Further SEM analysis of the morphology showed an average diameter of 103 nm and average length of 19 $\mu$m for the Blue nano sample; the average diameter and length for the Nanogap nanowires were 108 nm and 11 $\mu$m, respectively.

### 2.1. Sample Preparation.
Microscope slides with dimensions $25 \times 75 \times 1.0$ mm were obtained from Fisher Scientific and used as glass substrate. Each slide was carefully divided into two halves with a glass cutter yielding a glass substrate of dimensions $25 \times 37.5 \times 1.0$ mm.

The glass slides were thoroughly cleaned with detergent and washed out with deionized water. All of the glass substrate was then treated with acetone and isopropanol baths in the sonicator during 15 min each.

Silver nanowires in ethanol solutions from both sources were prepared with concentrations of 5 mg/mL, 10 mg/mL,

and 20 mg/mL. Uniform $25 \times 25$ mm thin films of silver nanowires were fabricated by dip coating the glass slide on the aforementioned solutions. Sticker paper was attached to the rear side of the substrate to prevent the formation of a silver nanowire mesh on the backside of the sample. Different coverage densities were achieved by dip coating several layers of the same solution, allowing a 2 min waiting time between layers to let the ethanol evaporate. After the last layer, the sticker paper was peeled off the glass and the rear side of the sample was carefully cleaned up with ethanol to remove any remaining residues. Then the sample was cut again to form a $25 \times 25$ mm square thin film of silver nanowires on glass substrate as shown in Figure 1(a). The dip coater (Dip Master 50 from Chemat inc.) was set up at a with draw speed of 200 mm/min and a still time of 1 s for all the samples made in this study.

The use of extra material has to be considered when using the dip-coating technique since an undesired layer will be formed in the rear side of the substrate. A lower withdraw speed yields a thinner layer and therefore less wasted material.

After the dip-coating step, the samples were annealed at 250°C during 30 min in a tube furnace to improve the contact between nanowires. A mechanical pump was used to extract the air of the tube furnace in order to prevent oxidation of the samples.

Commercially available ITO and FTO were purchased and characterized for comparison purposes. ITO on glass with dimensions of $25 \times 25 \times 0.7$ mm was acquired from Delta Technologies (product number CG-61IN) with a sheet resistance range of 15–30 $\Omega/\square$.

### 2.2. Characterization.
An e-beam evaporator was utilised to place two circular electrode pads of silver on opposite corners of each sample (see Figure 1(a)). The evaporator was set up to deposit the pads with a thickness of 100 nm, and the masks were custom designed to set the diameter of the pads in 3 mm. Then the sheet resistance of the silver nanowire films was determined using a Keithley 236 source measure unit.

The transmittance was measured with a light source coupled through an optical fiber to a silicon-biased detector with a wavelength range of 350–1100 nm. A tungsten halogen lamp (LS-1) from Ocean Optics was employed as the light source. The samples were placed orthogonal to the incident light. Transmittance was calculated as the ratio of the light intensity detected after the sample and the light intensity detected after a glass slide which was used as reference.

The morphology of the silver nanowires was characterized with a scanning electron microscope (SEM) JEOL JSM 7400F.

Coverage density was calculated from imaging the samples with an optical microscope at 100x magnification. First, 10 images were taken from each sample. Then, the color depth of the images was decreased to 1 bit per pixel. The modified image was read bit by bit, and the coverage density was defined as the ratio of the number of fewer pixels to the total number of pixels contained in the image. The coverage density data presented in Figure 4 is the average of the 10 images.

(a)      (b)
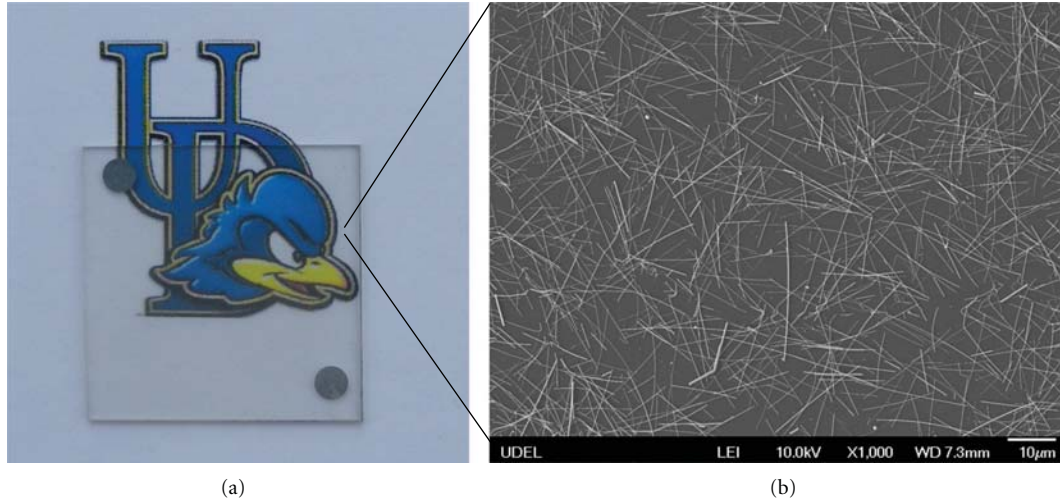
FIGURE 1: (a) Photograph of a typical sample with $R_{sh} = 24\,\Omega/\square$ and $T = 90\%$ (Nanogap $\langle L \rangle = 11\,\mu m$) on top of the University of Delaware logo. (b) SEM image of the same sample showing the random distribution of silver nanowires throughout the surface of the glass substrate.



(a)      (b)
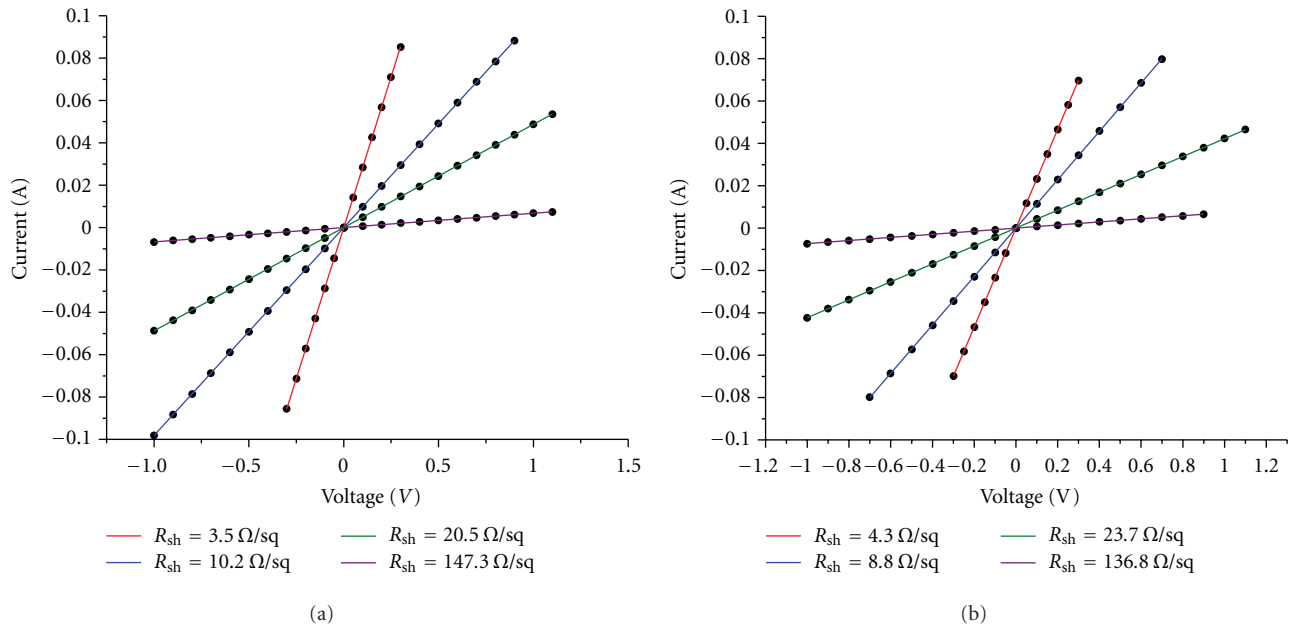
FIGURE 2: $I$-$V$ curves of different samples for (a) long nanowires (Blue nano) and (b) short nanowires (Nanogap).

The adhesion properties were measured by using a well-known test. The AgNW samples did not pass the scotch tape test, and hence encapsulation is required to guarantee a high adhesion of the nanowires to the substrate.

The stability of the samples in ambient conditions was tested by repeating the characterization process after a certain period of time. The samples did not oxidize, and both the electrical and optical properties remained unchanged after 3 months of fabrication.

## 3. Results and Discussion

One can see from Figure 1(a) that the dip-coated samples are highly uniform and transparent, since the logo

underneath is clearly visible. The SEM image displayed in Figure 1(b) demonstrates the even distribution of the nanowires throughout the surface of the substrate. Using the dip-coating technique, the one-dimensional structures are placed in random directions creating an arbitrary network where charge carriers have different paths to go through.

The current-voltage characteristics of the samples with different sheet resistance for the long and the short nanowires are shown in Figure 2. The straight lines demonstrate the linear response and the quality of the films as electrodes.

The nanowire-nanowire contact resistance is notably improved by the annealing process. When the silver nanowires mesh undergoes relatively high temperatures, the junction of the nanowires starts to melt increasing the

FIGURE 3: SEM image of a silver nanowire network after annealing ($250°C \sim 30$ min).

conductivity of the film, as shown in the inset of Figure 3. Lee et al. [4] reported a decrease of one order of magnitude on $R_{sh}$ after heating treatment. We observed similar results in our experiments.

Every transparent conductive material presents a fundamental tradeoff between electrical conductivity and optical transmittance. In order to elucidate this phenomenon, we consider three parameters, the sheet re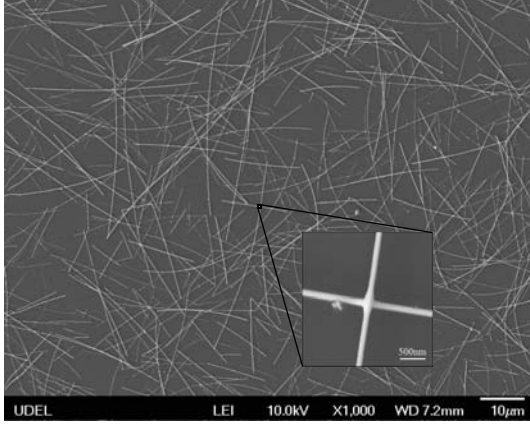sistance ($R_{sh}$), the optical transmittance ($T$), and the coverage density ($D$). Figure 4 shows how these variables are mutually related. As $R_{sh}$ becomes higher, the values of $T$ are increased as well. Conversely, a higher $D$ produces lower $R_{sh}$ values.

The plots shown in Figure 4 are the experimental data (filled dots) and a nonlinear fit (smooth lines) obtained using the curve fitting tool available in Matlab. The mathematical model for the long nanowires (Blue nano) is displayed in

$$T = f(R_{sh}) = 0.96 - 1.03R_{sh}^{-1.18}, \qquad R^2 = 0.99, \quad (1)$$

$$D = f(R_{sh}) = 11.78 + 105.7R_{sh}^{-1.46}, \qquad R^2 = 0.95. \quad (2)$$

Equations (3) and (4) model the behavior of $T$ and $D$ as a function of $R_{sh}$ for the short nanowires (Nanogap)

$$T = f(R_{sh}) = 0.92 - 16.06R_{sh}^{-2.77}, \qquad R^2 = 0.99, \quad (3)$$

$$D = f(R_{sh}) = 7.75 + 24.65R_{sh}^{-0.48}, \qquad R^2 = 0.94. \quad (4)$$

The values of $R$-squared in all of the previous equations are very close to the unity which indicates a good fit of the model with the experimental data.

Figure 4(a) is a plot of $T$ and $D$ as a function of $R_{sh}$ for the long nanowires (Blue nano), while Figure 4(b) is the same plot for the short nanowires (Nanogap). The sheet resistance and optical transmittance data for commercial samples of ITO and FTO on glass substrate are also shown for comparison purposes. Both nanowires samples have a superior performance than that of FTO by far. The long nanowires (Blue nano) show better results than ITO, while the short nanowires (Nanogap) have a slight inferior performance in comparison with ITO. This will be further discussed later when we explain the figures of merit.



(a)



(b)
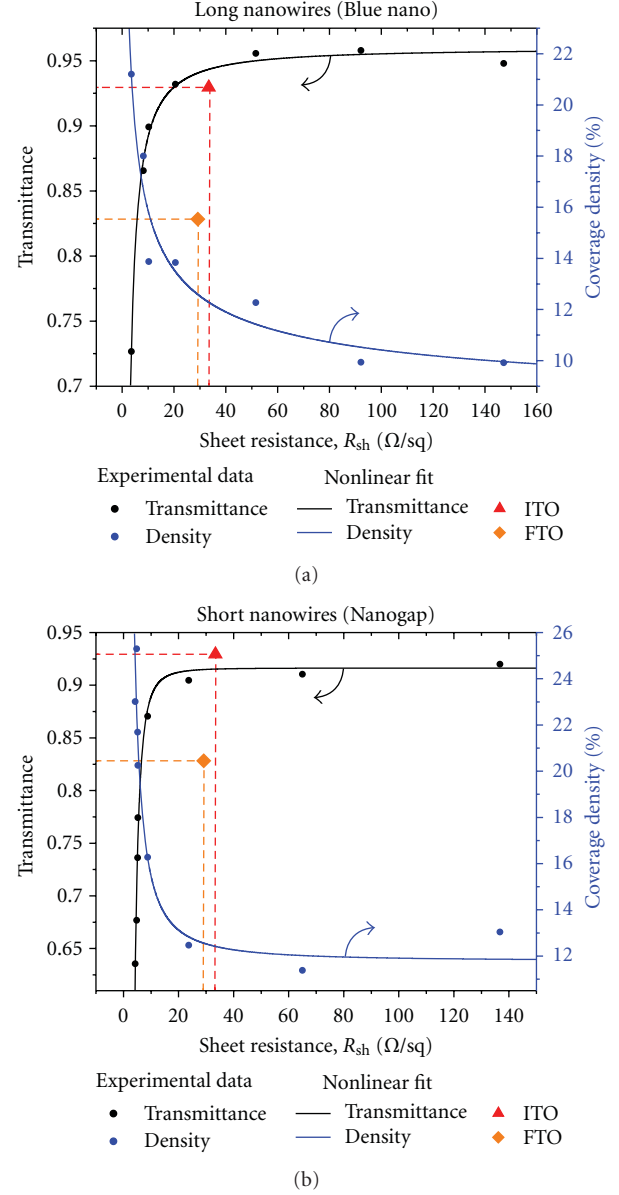
FIGURE 4: Optical transmittance and coverage density versus $R_{sh}$ for (a) Blue nano AgNWs ($\langle L \rangle = 11\,\mu m$) and (b) Nanogap AgNWs ($\langle L \rangle = 19\,\mu m$).

Different coverage densities are obtained by increasing the number of dip-coated layers deposited on the glass substrate. Higher coverage density values are achieved by increasing the concentration of the silver nanowires in the ethanol solution. The correlation of the three important parameters ($R_{sh}$, $T$, and $D$) is conspicuously depicted in Figure 5. The microscopy analysis is in good agreement with the data shown in the Figure 4. A smaller empty space between the silver nanowires leads to a higher coverage density and a lower sheet resistance, which in turn results in a lower transmittance.

In order to determine which combinations of $R_{sh}$ and $T$ are the optimal, we need to use some figures of merit defined

(a)



(b)



(c)



(d)
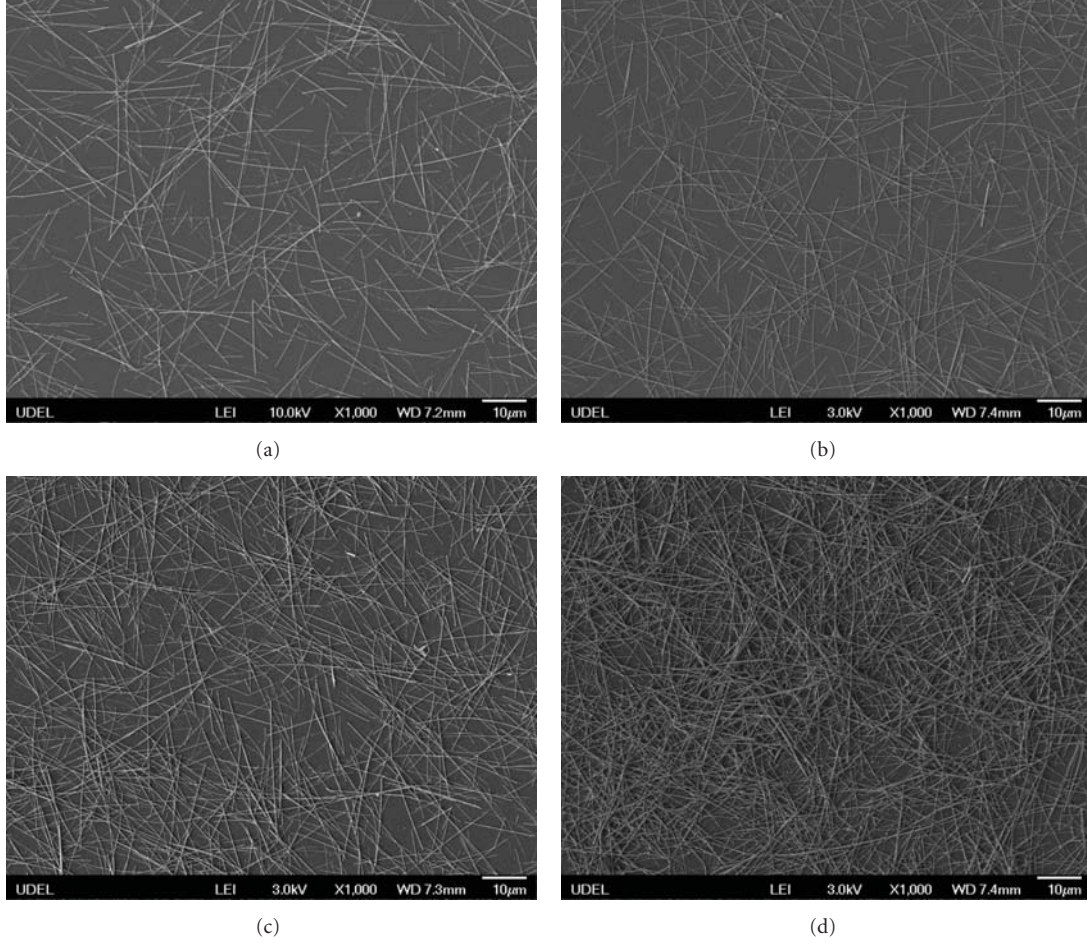
FIGURE 5: SEM images of Blue nano AgNWs ($\langle L \rangle = 19\,\mu$m) samples with different sheet resistance ($R_{sh}$), optical transmittance ($T$), and coverage density ($D$) (a) $R_{sh} = 147\,\Omega/\square$, $T = 94.8\%$, $D = 9.9\%$. (b) $R_{sh} = 20.5\,\Omega/\square$, $T = 93.2\%$, $D = 13.8\%$. (c) $R_{sh} = 10.2\,\Omega/\square$, $T = 89.9\%$, $D = 13.9\%$. (d) $R_{sh} = 3.5\,\Omega/\square$, $T = 72.7\%$, $D = 21.2\%$.

in the literature. The first one is the electrical to optical conductivity ratio used by some authors [19, 20, 31]:

$$T = \left(1 + \frac{188.5}{R_{sh}} \cdot \frac{\sigma_{OP}}{\sigma_{DC}}\right)^{-2}, \tag{5}$$

or

$$\frac{\sigma_{DC}}{\sigma_{OP}} = \frac{188.5}{R_{sh} \cdot (T^{-1/2} - 1)}. \tag{6}$$

From (6), we can easily determine the electrical to optical conductivity ratio from the $R_{sh}$ and $T$ parameters. This figure of merit will help us to judge how well the silver nanowire network behaves as a transparent conductive electrode. The higher the $\sigma_{DC}/\sigma_{OP}$, the better the TCE.

We can deduce a model for the electrical to optical conductivity by using the nonlinear fits presented before. If we solve (1) and (3) for $R_{sh}$ and then replace it on (6), we will obtain the figure of merit $\sigma_{DC}/\sigma_{OP}$ as a function of the

transmittance $T$ for the long nanowires (7) and for the short ones (8):

$$\frac{\sigma_{DC}}{\sigma_{OP}} = \frac{188.5}{T^{-1/2} - 1} \cdot \left(\frac{0.96 - T}{1.03}\right)^{1/1.18}, \tag{7}$$

$$\frac{\sigma_{DC}}{\sigma_{OP}} = \frac{188.5}{T^{-1/2} - 1} \cdot \left(\frac{0.92 - T}{16.06}\right)^{1/2.77}. \tag{8}$$

Figure 6(a) shows a plot of the electrical to optical conductivity ratio as a function of the optical transmittance for both the long (Blue nano) and the short (Nanogap) silver nanowires. The scattered dots represent the experimental data while the smooth lines depict the plot of (7) and (8).

It turned out that the longer nanowires present a better performance than the short nanowires. The highest values of $\sigma_{DC}/\sigma_{OP}$ were $339\,\Omega^{-1}$ and $300\,\Omega^{-1}$ for the long (Blue nano) and the short (Nanogap) nanowires, respectively; that is, an increase of 73% in the length of the silver nanowires will yield to an increment of 13% in the electrical to optical conductivity ratio.
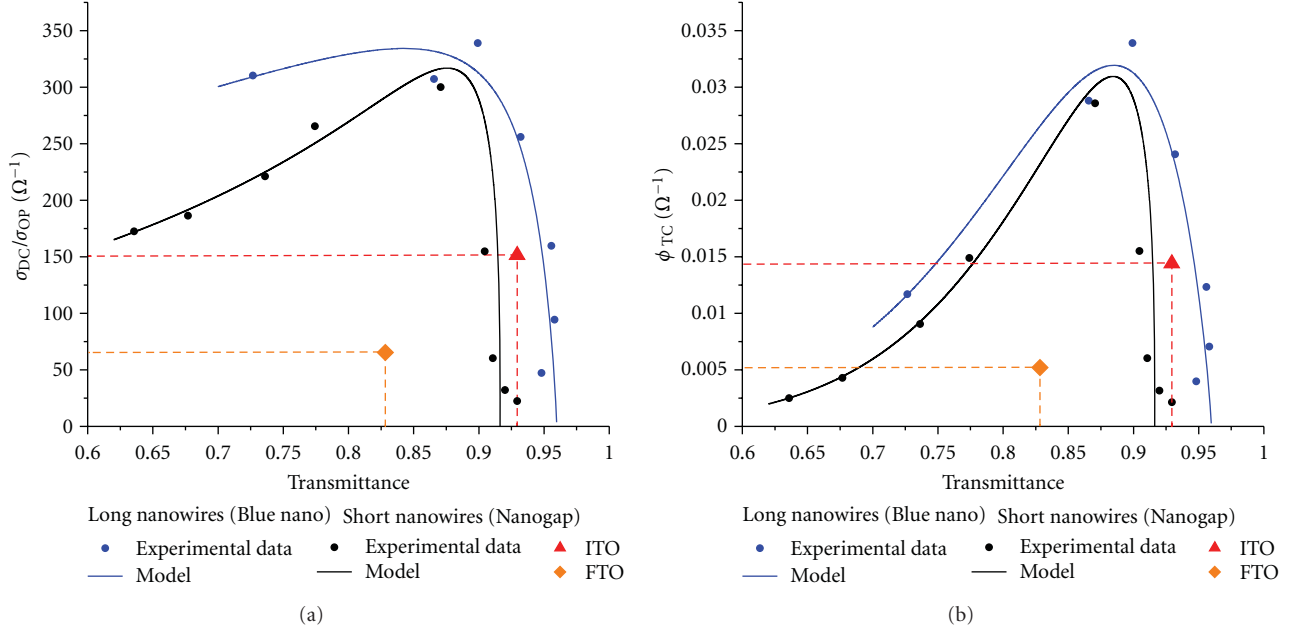
FIGURE 6: Figures of merit versus optical transmittance (a) $\sigma_{DC}/\sigma_{OP}$ and (b) $\phi_{TC}$.

Another figure of merit for transparent conductive materials was defined by Haacke [32]:

$$\phi_{TC} = \frac{T^{10}}{R_{sh}}. \tag{9}$$

Analogously to the procedure we did for the electrical to optical conductivity ratio, we determined a model for the figure of merit $\phi_{TC}$. This model is described by (10). The model is displayed in Figure 6(b):

$$\phi_{TC} = T^{10} \cdot \left( \frac{0.96 - T}{1.03} \right)^{1/1.18},$$
$$\phi_{TC} = T^{10} \cdot \left( \frac{0.92 - T}{16.06} \right)^{1/2.77}. \tag{10}$$

The superior performance of the long nanowires (Blue nano) is confirmed in Figure 6(b), where $\phi_{TC}$ is plotted as a function of the optical transmittance for the short and the long silver nanowires. The figures of merit for ITO and FTO are plotted as well. Lee et al. [4] and Hu et al. [3] reported that longer nanowires will cause a lower $R_{sh}$ which is in accordance with our results. The long nanowires can interconnect to each other with lower coverage density, allowing a higher transmittance with the same $R_{sh}$. The highest values of $\phi_{TC}$ for our samples were $0.034\,\Omega^{-1}$ and $0.029\,\Omega^{-1}$ for the long and the short nanowires, respectively. These values are better than the ones corresponding to the commercial samples of metal oxides (FTO and ITO). In the same way, an increment of 73% in the average length of the nanowires (from 11 $\mu$m to 19 $\mu$m) produces a raise in $\phi_{TC}$ of 17%.

The relative high diameter of the silver nanowires produces a rough surface. This might be an issue for organic devices with typical thickness of 100 nm or less. In the other hand, the rough surface improves the light trapping in photovoltaic devices, making these electrodes an appealing material for organic solar cell fabrication.

## 4. Conclusions

In summary, we fabricated uniform silver nanowire thin films on glass substrate using a straightforward dip-coating technique. We used short and long silver nanowires, and we demonstrated that longer nanowires lead to a higher performance of transparent conductive electrodes. Our best sample had a $R_{sh} = 10.2\,\Omega/\square$, $T = 0.899$, $D = 13.9\%$, $\sigma_{DC}/\sigma_{OP} = 339\,\Omega^{-1}$, and $\phi_{TC} = 0.034\,\Omega^{-1}$. We showed the dependence between sheet resistance, optical transmittance, and coverage density. We made use of two figures of merit to determine the performance of our samples and to compare them with metal oxides. We conclude that random networks of silver nanowires can immediately replace metal oxides such as ITO and FTO in any optoelectronic application owing to their electrical, optical, and mechanical properties which made them suitable for a great variety of devices.

## References

[1] G. Haacke, "Transparent conducting coatings," *Annual Review of Materials Science*, vol. 7, pp. 73–93, 1977.

[2] C. G. Granqvist, "Transparent conductors as solar energy materials: a panoramic review," *Solar Energy Materials and Solar Cells*, vol. 91, no. 17, pp. 1529–1598, 2007.

[3] L. Hu, H. S. Kim, J. Y. Lee, P. Peumans, and Y. Cui, "Scalable coating and properties of transparent, flexible, silver nanowire electrodes," *ACS Nano*, vol. 4, no. 5, pp. 2955–2963, 2010.

[4] J. Y. Lee, S. T. Connor, Y. Cui, and P. Peumans, "Solution-processed metal nanowire mesh transparent electrodes," *Nano Letters*, vol. 8, no. 2, pp. 689–692, 2008.

[5] Z. Chen, B. Cotterell, and W. Wang, "The fracture of brittle thin films on compliant substrates in flexible displays," *Engineering Fracture Mechanics*, vol. 69, no. 5, pp. 597–603, 2002.

[6] H. Z. Geng, K. K. Kim, K. P. So, Y. S. Lee, Y. Chang, and H. L. Young, "Effect of acid treatment on carbon nanotube-based flexible transparent conducting films," *Journal of the American Chemical Society*, vol. 129, no. 25, pp. 7758–7759, 2007.

[7] T. M. Barnes, J. Van De Lagemaat, D. Levi et al., "Optical characterization of highly conductive single-wall carbon-nanotube transparent electrodes," *Physical Review B*, vol. 75, no. 23, Article ID 235410, 2007.

[8] M. H. Andrew Ng, L. T. Hartadi, H. Tan, and C. H. Patrick Poa, "Efficient coating of transparent and conductive carbon nanotube thin films on plastic substrates," *Nanotechnology*, vol. 19, no. 20, Article ID 205703, 2008.

[9] A. Vollmer, X. L. Feng, X. Wang et al., "Electronic and structural properties of graphene-based transparent and conductive thin film electrodes," *Applied Physics A*, vol. 94, no. 1, pp. 1–4, 2009.

[10] N. Pimparkar, M. Chowalla, and M. A. Alam, "Device optimization for organic photovoltaics with cnt networks as transparent electrode," in *Proceedings of the Photovoltaic Specialists Conference*, 2008.

[11] M. A. Contreras, T. Barnes, J. Van De Lagemaat et al., "Replacement of transparent conductive oxides by single-wall carbon nanotubes in Cu(In,Ga)Se2-based solar cells," *Journal of Physical Chemistry C*, vol. 111, no. 38, pp. 14045–14048, 2007.

[12] X. Wang, L. Zhi, and K. Müllen, "Transparent, conductive graphene electrodes for dye-sensitized solar cells," *Nano Letters*, vol. 8, no. 1, pp. 323–327, 2008.

[13] J. Wu, H. A. Becerril, Z. Bao, Z. Liu, Y. Chen, and P. Peumans, "Organic solar cells with solution-processed graphene transparent electrodes," *Applied Physics Letters*, vol. 92, no. 26, Article ID 263302, 2008.

[14] H. Wu, L. Hu, M. W. Rowell et al., "Electrospun metal nanofiber webs as high-performance transparent electrode," *Nano Letters*, vol. 10, no. 10, pp. 4242–4248, 2010.

[15] Y. Wang, T. Feng, K. Wang, M. Qian, Y. Chen, and Z. Sun, "A facile method for preparing transparent, conductive, and paper-like silver nanowire films," *Journal of Nanomaterials*, vol. 2011, Article ID 935218, 5 pages, 2011.

[16] A. R. Madaria, A. Kumar, F. N. Ishikawa, and C. Zhou, "Uniform, highly conductive, and patterned transparent films of a percolating silver nanowire network on rigid and flexible substrates using a dry transfer technique," *Nano Research*, vol. 3, no. 8, pp. 564–573, 2010.

[17] A. R. Madaria, A. Kumar, and C. Zhou, "Large scale, highly conductive and patterned transparent films of silver nanowires on arbitrary substrates and their application in touch screens," *Nanotechnology*, vol. 22, no. 24, Article ID 245201, 2011.

[18] T. Akter and W. S. Kim, "Reversibly stretchable transparent conductive coatings of spray-deposited silver nanowires," *ACS Applied Materials & Interfaces*, vol. 4, pp. 1855–1859, 2012.

[19] J. van de Groep, P. Spinelli, and A. Polman, "Transparent conducting silver nanowire networks," *Nano Letters*, vol. 12, no. 6, pp. 3138–3144, 2012.

[20] S. De, T. M. Higgins, P. E. Lyons et al., "Silver nanowire networks as flexible, transparent, conducting films: extremely high DC to optical conductivity ratios," *ACS Nano*, vol. 3, no. 7, pp. 1767–1774, 2009.

[21] F. S. F. Morgenstern, D. Kabra, S. Massip et al., "Ag-nanowire films coated with zno nanoparticles as a transparent electrode for solar cells," *Applied Physics Letters*, vol. 99, Article ID 183307, 2011.

[22] R. Zhu, C.-H. Chung, K. C. Cha et al., "Fused silver nanowires with metal oxide nanoparticles and organic polymers for highly transparent conductors," *ACS Nano*, vol. 5, no. 12, pp. 9877–9882, 2011.

[23] D. Azulai, T. Belenkova, H. Gilon, Z. Barkay, and G. Markovich, "Transparent metal nanowire thin films prepared in mesostructured templates," *Nano Letters*, vol. 9, no. 12, pp. 4246–4249, 2009.

[24] Z. Yu, L. Li, Q. Zhang, W. Hu, and Q. Pei, "Silver nanowire-polymer composite electrodes for efficient polymer solar cells," *Advanced Materials*, vol. 23, pp. 4453–4457, 2011.

[25] L. Li, Z. Yu, W. Hu, C. h. Chang, Q. Chen, and Q. Pei, "Efficient flexible phosphorescent polymer light-emitting diodes based on silver nanowirepolymer composite," *Advanced Materials*, vol. 23, pp. 5563–5567, 2011.

[26] X. Y. Zeng, Q. K. Zhang, R. M. Yu, and C. Z. Lu, "A new transparent conductor: silver nanowire film buried at the surface of a transparent polymer," *Advanced Materials*, vol. 22, no. 40, pp. 4484–4488, 2010.

[27] D.-S. Leem, A. Edwards, M. Faist, J. Nelson, D. D. C. Bradley, and J. C. de Mello, "Efficient organic solar cells with solution-processed silver nanowire electrodes," *Advanced Materials*, vol. 23, pp. 4371–4375, 2011.

[28] J. Y. Lee, S. T. Connor, Y. Cui, and P. Peumans, "Semitransparent organic photovoltaic cells with laminated top electrode," *Nano Letters*, vol. 10, no. 4, pp. 1276–1279, 2010.

[29] H. Tian, D. Xie, and Y. Yang, "Flexible, ultrathin, and transparent sound-emitting devices using silver nanowires film," *Applied Physics Letters*, vol. 99, Article ID 253507, 2011.

[30] Z. Zhang, X. Chen, H. Yang, H. Fu, and F. Xiao, "Electrically conductive adhesives with sintered silver nanowires," in *Proceedings of the International Conference on Electronic Packaging Technology and High Density Packaging (ICEPT-HDP '09)*, pp. 834–837, August 2009.

[31] M. Dressel and G. Gruner, *Electrodynamics of Solids: Optical Properties of Electrons in Matter*, Cambridge University Press, Cambridge, UK, 2002.

[32] G. Haacke, "New figure of merit for transparent conductors," *Journal of Applied Physics*, vol. 47, no. 9, pp. 4086–4089, 1976.

*Research Article*

# Orientation of One-Dimensional Silicon Polymer Films Studied by X-Ray Absorption Spectroscopy

**Md. Abdul Mannan,[1,2] Yuji Baba,[1] Tetsuhiro Sekiguchi,[1] Iwao Shimoyama,[1] Norie Hirao,[1] Masamitsu Nagano,[2] and Hideyuki Noguchi[2]**

[1] *Quantum Beam Science Directorate, Japan Atomic Energy Agency, Tokai-mura, Naka-gun, Ibaraki 319-1195, Japan*
[2] *Department of Chemistry and Applied Chemistry, Faculty of Science and Engineering, Saga University, Honjo-1, Saga 840-8502, Japan*

Correspondence should be addressed to Yuji Baba, baba.yuji@jaea.go.jp

Molecular orientations for thin films of one-dimensional silicon polymers grown by vacuum evaporation have been assigned by near-edge X-ray absorption fine structure (NEXAFS) using linearly polarized synchrotron radiation. The polymer investigated was polydimethylsilane (PDMS) which is the simplest stable silicon polymer, and one of the candidate materials for one-dimensional molecular wire. For PDMS films deposited on highly oriented pyrolytic graphite (HOPG), four resonance peaks have been identified in the Si $K$-edge NEXAFS spectra. Among these peaks, the intensities of the two peaks lower-energy at 1842.0 eV and 1843.2 eV were found to be strongly polarization dependent. The peaks are assigned to the resonance excitations from the Si 1s to $\sigma^*$ p$_{yz}$ and $\sigma^*$ p$_x$ orbitals localized at the Si–C and Si–Si bonds, respectively. Quantitative evaluation of the polarization dependence of the NEXAFS spectra revealed that the molecules are self-assembled on HOPG surface, and the backbones of the PDMS are oriented nearly parallel to the surface. The observed orientation is opposite to the previously observed results for PDMS on the other surfaces such as oxide (indium tin oxide) and metal (polycrystalline copper). The flat-lying feature of PDMS observed only on HOPG surface is attributed to the interaction between CH bonds in PDMS and $\pi$ orbitals in HOPG surface.

## 1. Introduction

Polysilanes composed of silicon-silicon backbone have excellent properties in comparison with carbon-based polymers [1]. Polysilanes are considered to be an ideal one-dimensional (1D) molecular wire with high electric conductivity since the $\sigma$ electrons in polysilanes are delocalized comparable to those of $\pi$ electrons in the conjugated carbon-based polymers. It has also been predicted that the polysilanes possess electronic structure similar to direct band-gap semiconductor [2].

Among polysilanes, polydimethylsilane (PDMS) is the most fundamental stable silane and considered to be one of the candidate materials in the future nanotechnology with high quality. One of the features of PDMS is the high electric conductivity along the 1D chain due to the smaller HOMO-LUMO band gaps [3]. Thus PDMS and its derivatives are

expected to be used as extremely thin wires in molecular electronics. Furthermore, thin films of PDMS possess outstanding physical properties such as photoconductivity and ultraviolet electroluminescence [4–6]. It should be noted that the electric and optical properties in thin films of 1D polymer depend on the configuration of the molecular skeleton. Especially for ultrathin films around monolayer or thinner than monolayer, electric conductivity would become anisotropic depending on the molecular orientation. So it is much important to precisely determine the molecular orientation of polymers on solid surfaces.

It has been found that thin films of silicon polymers synthesized by vacuum evaporation are sometimes self-ordered on solid surfaces. It has been reported that the direction of the backbone of silicon polymers on silicon becomes perpendicular to the surface at high substrate temperature and low evaporation rate [7, 8]. On the other hand, the direction

becomes parallel to the surface at low substrate temperature with high evaporation rate [9–12]. In these works, X-ray diffraction was mainly used to determine the structures of the film, so the thickness of the layer is fairly thick in the order of $\mu$m. These works provide bulk crystal structures rather than molecular orientations in a thin film. Scanning tunnelling microscopy (STM) study confirmed the formation of self-assembled PDMS films of which the silicon backbone chain was perpendicular in respect to the basal plan of graphite substrate [13]. However, STM images gave information about the image of the surface morphology, so the precise titled angle of the PDMS molecules with respect to the backbone configuration and substrate surface has not thoroughly been investigated yet.

In the previous paper, we have investigated the molecular orientation of PDMS films grown on indium tin oxide (ITO) surface which practically used transparent substrate with high electric conductivity. We found that the backbone of the Si–Si bond of PDMS molecules is perpendicularly oriented on the ITO surface, and the polymer has a helical conformation rather than zigzag structure with polar angle around 40° [14].

In this paper, we present the results for the orientation of PDMS films grown on highly oriented pyrolytic graphite (HOPG) substrate which is one of the ideal materials with completely flat and inert surface. The results are compared with the previously obtained ones on the different substrates, and the origin of the difference in the orientation is discussed.

## 2. Experimental Method

*2.1. Experimental Setup.* All the experiments were performed *in situ* at the end station of beam line 27A (BL-27A) of the Photon Factory, High Energy Accelerator Research Organization (KEK-PF). Details of the BL-27A were reported elsewhere [15]. Briefly, double crystals of In Sb(111) were used as a monochromator. The total energy resolution of this monochromator was 0.90 eV at 1.84 keV (Si $K$-edge). The synchrotron radiation (SR) beam was generated from the bending magnet, and it was linearly polarized in the horizontal direction. The typical photon flux was $\sim 10^{10}$ photons·cm$^{-2}$·s$^{-1}$.

The end station of the BL-27A has two ultrahigh vacuum chambers: (i) a main chamber for X-ray photoelectron spectroscopy (XPS) and NEXAFS measurements and (ii) a preparation chamber for vacuum evaporation. The base pressure of both the chambers was in the order of $1 \times 10^{-8}$ Pa. The main chamber consisted of a five-axis manipulator, a hemispherical electron energy analyzer (VSW Co. Class-100) for XPS measurements. In the preparation chamber, a vacuum evaporator and a sample transfer systems were installed. For XPS measurements, the X-rays were irradiated at 55 degree from surface normal, and a take-off direction of photoelectrons was surface normal.

The vacuum evaporator consisted of a quartz crucible surrounded by spiral-type tungsten filament. The crucible was floated at +1.5 kV while the filament was grounded.

Therefore, the crucible was heated by the electron bombardment. The distance between the crucible and the substrate was 15 cm. A shutter electrically isolated from the ground was equipped with it in order to control the evaporation rate of the source material. Since some of the evaporated molecules are ionized due to the surface ionization, a positive current was observed at the shutter. Thickness of the films was precisely determined by the product of the shutter current and the evaporation time which was calibrated by XPS measurements.

*2.2. Film Synthesis.* The source powder material purchased from GELEST Inc. was polydimethylsilane (PDMS) [Si(CH$_3$)$_2$]$_n$. The average molecular weight of the PDMS is 2000 so the number of silicon atoms in a PDMS molecule was about 28. Fresh surface of the HOPG was obtained by cleaving in atmosphere, and it was attached on a sample holder by carbon tape and then immediately transferred into the preparation chamber.

The PDMS powder was put in the quartz crucible where the crucible was heated by the bombardment of 1.5 keV electrons from the backside. It was confirmed that the evaporation temperature of the crucible measured by a thermocouple was 250°C. The evaporation was performed for 5 min to 15 min at the working pressure of $2.2 \times 10^{-5}$ Pa. The filament current was 4.1 A, whereas the shutter current was 500 pA. The substrate was kept at room temperature during deposition. We have measured the Si 1s and C 1s peaks in the XPS spectrum for the deposited samples, and then the thickness was calculated by the peak intensity ratio using photoionization cross-section [16] and inelastic mean free-paths (IMFP's) [17] (see Section 3.1).

The electronic structure and molecular orientation were investigated by XPS and NEXAFS measurements. The NEXAFS spectra were taken with the total electron yield mode by recording the sample current. The total electron yields were normalized by the photon flux that was monitored by the current of aluminium foil located in front of the sample. The sample was horizontally located, and it was rotated around the vertical axis for the measurements of the polarization dependences.

Irradiation of intense X-rays on organic molecules would sometimes induce the decomposition. In order to check the radiation-induced decomposition, we have irradiated the PDMS films by SR X-rays for one day (total photon fluence was about $10^{15}$ photons·cm$^{-2}$). However, neither XPS nor NEXAFS spectra changed probably because of the low photoabsorption cross-sections of silicon and carbon (in the order of $10^4$ barn). So we can ignore the radiation-induced decomposition of molecules in the present experiments.

## 3. Results and Discussion

*3.1. Electronic Structure and Film Thickness by XPS Analysis.* Figure 1 shows XPS wide scan spectra for the PDMS films with two different deposition times. The XP spectrum for a clean HOPG surface before the deposition is also shown as a
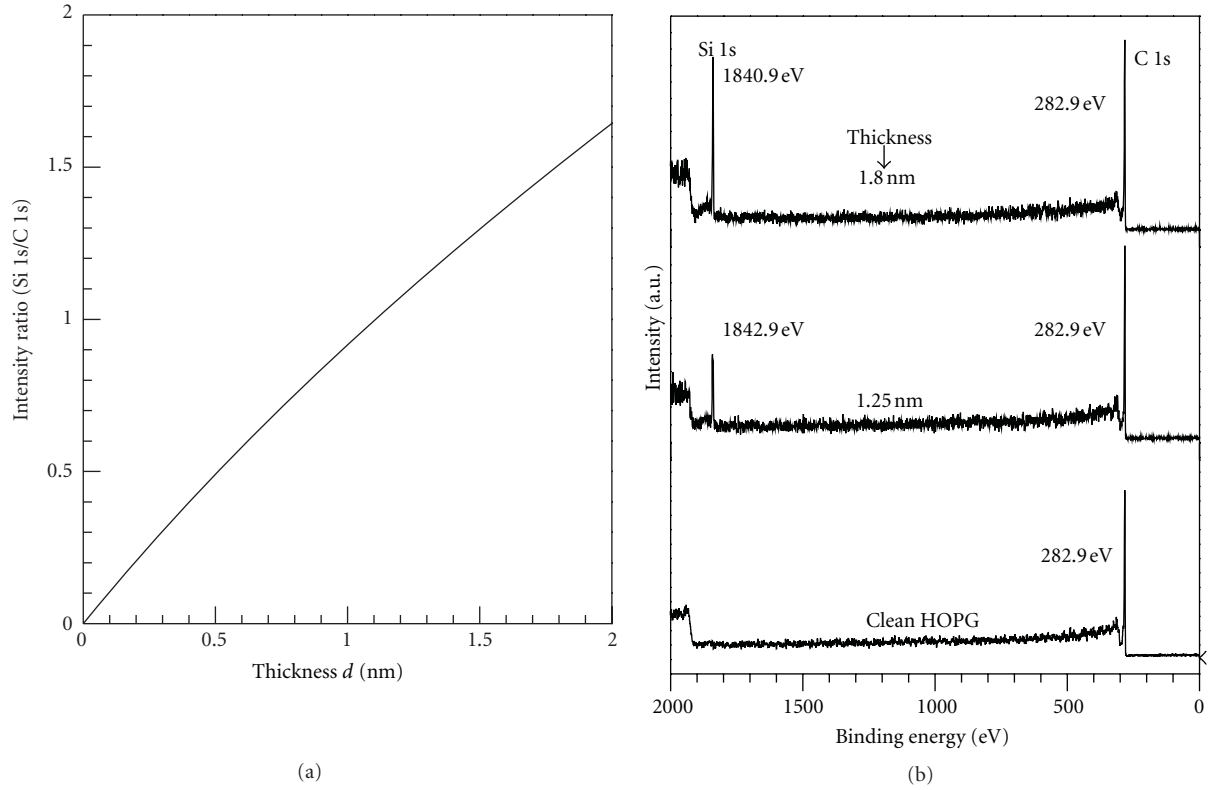
FIGURE 1: XPS wide scan spectra for the PDMS films with different thickness evaporated on HOPG surface at ambient temperature. The sample surface was irradiated with the SR beam of 2.2 keV photons as an excitation source. The spectra were taken at the step energy of 1.0 eV. The relationship between the film thickness and the intensity ratio of Si 1s/C 1s calculated by (1) is (a).

bottom spectrum. First, the thicknesses of the PDMS films is determined on the basis of the XPS peak intensities.

The intensities of Si 1s photoelectrons ($I_{\text{Si 1s}}$) and C 1s photoelectrons ($I_{\text{C 1s}}$) were calculated by using the following two equations [18] supposing that the film is homogeneous:

$$I_{\text{Si 1s}} = K\sigma_{\text{Si 1s}} \times \lambda_{\text{Si 1s in PDMS}} \times n_{\text{Si 1s in PDMS}}$$
$$\times \left[ 1 - \exp\left( \frac{-d}{\lambda_{\text{Si 1s in PDMS}}} \right) \right], \tag{1}$$

$$I_{\text{C 1s}} = K\sigma_{\text{C 1s}} \times \lambda_{\text{C 1s in HOPG}} \times n_{\text{C in HOPG}}$$
$$\times \exp\left( \frac{-d}{\lambda_{\text{C 1s in PDMS}}} \right) + K\sigma_{\text{C 1s}} \times \lambda_{\text{C 1s in PDMS}} \tag{2}$$
$$\times n_{\text{C in PDMS}} \times \left[ 1 - \exp\left( \frac{-d}{\lambda_{\text{C 1s in PDMS}}} \right) \right],$$

where $K$ is the constant depending on detection efficiency of the electron energy analyser, $\sigma$ (barn) is photoionization cross-section, $\lambda$ (nm) is IMFP of the photoelectrons of the respective elements, $n$ is the atomic concentration of the element in the material indicated as subscripts, and $d$ (nm) is the thickness of the PDMS film. The values used for the calculation of $\sigma$ for Si 1s and C 1s at 2.2 keV photons were $1.02 \times 10^5$ and $5.0 \times 10^3$ barns, respectively [16]. The Figure 1(a) shows the relationship between the thickness $d$ (nm) and the peak intensity ratio of Si 1s/C 1s. From the

experimentally obtained Si 1s/C 1s values, the thicknesses of the PDMS films for two samples are determined to be 1.25 nm (middle spectrum) and 1.80 nm (upper spectrum).

Figure 2 shows the Si 1s XPS narrow scan for the samples with the different thickness. The sample surface was excited by the SR beam of 2.2 keV photons, and the spectra were taken at the step energy of 0.07 eV. Two sharp peaks at the binding energy of 1842.9 eV and 1840.7 eV are observed for the thin sample with the thickness of 1.25 nm. The intensity of the peak observed at 1842.9 eV becomes significantly low with the thickness (sample with the thickness of 1.80 nm). The energy of the main peak at 1840.7 eV is the same as the previously reported values for multilayered PDMS films [14]. Also the binding energies of the C 1s peak for these two layers are located around 282.8 eV, which is similar to those for the SiC layer [19–21]. Thus the main peak observed at 1840.7 eV is surely attributed to the silicon atoms in PDMS molecules. One of the biggest questions is that why two peaks are found in the Si 1s spectra. We confirmed that the peak splitting is not due to the decomposition of PDMS by X-ray irradiation because the peak structures have never changed even after long-time irradiation. It was reported that the peaks for the low-dimensional Si always stay at the higher binding energy region than that for the bulk-Si [22, 23]. We consider that low-dimensional feature for thin film might be one of the reasons for the peak found at 1842.9 eV [23]. So the possible explanations are that (i) the peak energy at 1842.9 eV is due
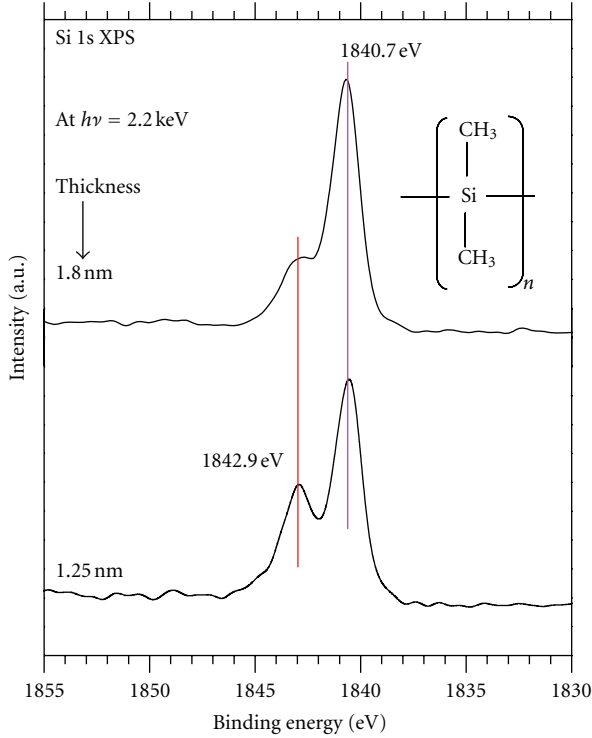
FIGURE 2: Si 1s narrow scan XP spectra for the PDMS films evaporated on HOPG surface with different thickness. The molecular formula of the PDMS is also shown in the figure in which the molecular weight is around 2000, and the number of silicon atoms ($n$) is about 28. The sample surface was excited by the SR beam of 2.2 keV photons as an excitation source and the spectra were taken at the step energy of 0.07 eV.

to the formation of monolayer and (ii) the peak energy at 1840.7 eV is due to the formation of multilayer of the PDMS molecules.

Since XPS could not provide information regarding molecular orientation of chemical bonds, NEXAFS has been applied in order to elucidate molecular orientation and quantitative evaluation of polar angle with respect to the backbone configuration of PDMS in the subsequent section.

*3.2. Quantitative Evaluation of Molecular Orientation by Si K-Edge NEXAFS Analyses.* Figures 3(a) and 3(b) show Si $K$-edge NEXAFS spectra for the PDMS films with different thickness. The spectra were recorded at different incidence angles $\theta$ of the SR beam. In the spectra, polarization dependence of NEXAFS has been clearly observed for both samples. At the nearly normal incidence ($\theta = 80°$) of the SR, four peaks marked by A, B, C, and D are observed. The photon energies of the four peaks are located at 1842.0, 1843.2, 1845.2, and 1848.6 eV, all of which are found to be the same as those observed for the samples deposited on ITO surface [14].

Among the four peaks, the peaks A and B are strongly polarization dependent. The intensity of the peak A is increased while the intensity of peak B is decreased at the small incidence angle of the SR beam ($\theta = 10°$). For comparison, Si $K$-edge NEXAFS spectra for the PDMS films

on ITO surface with different thickness are shown in Figure 4 [14]. It has been observed that the intensity of peak A decreased and the intensity of peak B increased when the incident angle becomes low ($\theta = 10°$). In the previous paper, we have concluded that the backbone of the PDMS, that is, the Si–Si bond is perpendicularly oriented on the ITO surface [14]. The present result for the polarization dependence of PDMS on HOPG is really opposite to that of PDMS on ITO. The result suggests that the Si–Si bond is parallel to the HOPG surface.

Let us go back to Figure 3. As to the peaks in Si $K$-edge NEXAFS spectra for Si polymer, the origin of the resonance peaks for PDMS or similar compounds has been experimentally and theoretically assigned [3, 24]. According to McCrary et al., the low-energy resonance peak A at 1842.0 eV is due to the resonance excitation from the Si 1s to $\sigma^* p_{yz}$ orbital localized at the Si–C bond, and the high-energy resonance peak B at 1843.2 eV is attributed to the resonance excitation from the Si 1s to $\sigma^* p_x$ orbital along the Si–Si bond [24]. Since higher-energy peaks C and D are not apparently polarization dependent, we shall hereafter concentrate on the polarization dependences of the peaks A and B.

To our knowledge, there have been no experimental works for precise determination of the angle for silicon polymer films on solid surface. Concerning this fact, it is very important to elucidate the exact polar angle of the PDMS molecule. As seen, a remarkable feature observed in the peaks A and B is the clear polarization dependence of their intensity. The peak intensity $I$ for the NEXAFS spectra using SR beam of the electric field $\mathbf{E}$ could be expressed by the following equation [25]:

$$\mathbf{I} \propto |\mathbf{E} \cdot \mathbf{O}|^2 \propto \cos^2\delta, \tag{3}$$

where $\mathbf{O}$ is the direction of the final state orbital, and $\delta$ is the angle between $\mathbf{E}$ and $\mathbf{O}$. Therefore, considering the polarization dependences as found in the Figure 3, we can suppose that the final state orbitals represented by the peak A are perpendicular while those represented by the peak B are parallel to the basal plane of the HOPG. In this viewpoint, the $\sigma^*$ orbitals localized at the Si–C bond (hereafter we denote $\sigma^*_{Si-C}$) are almost perpendicular, and the $\sigma^*$ orbitals localized at the Si-Si bond (hereafter we denote $\sigma^*_{Si-Si}$) are parallel to the HOPG substrate surface.

In order to get more quantitative clarification of the tilted angles, we estimate the angles of $\sigma^*_{Si-C}$ and $\sigma^*_{Si-Si}$ with respect to the silicon backbone configuration and the substrate surface. In that case, the resonance intensity in the NEXAFS spectrum could be simplified by the following equation:

$$I(\theta) = A\left[P \cdot I_p + (1 - P) \cdot I_v\right], \tag{4}$$

where $I_p$ and $I_v$ are the transition intensities associated with the angle-dependent matrix elements parallel and vertical to the electric field vector, respectively, A is the normalization, and P is the polarization factor [25]. The polarization factor of the SR beam under the present experimental condition was estimated to be about 0.95. The PDMS molecule on
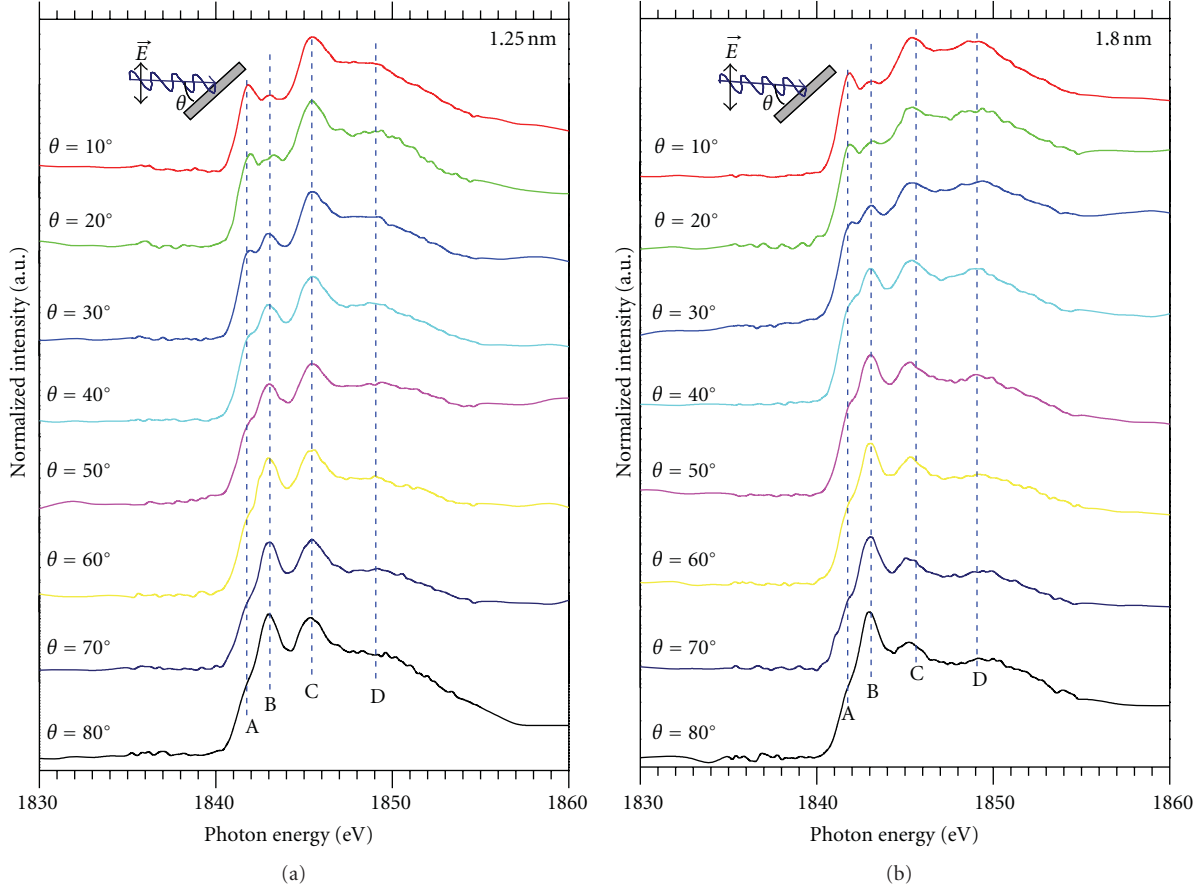
FIGURE 3: Si $K$-edge NEXAFS spectra for the samples deposited on HOPG substrate with different thickness: (a) 1.25 nm and (b) 1.80 nm. The NEXAFS spectra were recorded by the total electron yield mode at the different incident angles $\theta$ of the SR beam. Definition of the incidence angle $\theta$ is shown inside of this figure.

the HOPG surface has symmetry higher than threefold, so the intensities can be simply expressed by the following four equations: in the case of vector type orbital, the equation becomes

$$\mathbf{I}_v^{\parallel} = \left(\frac{1}{3}\right) \cdot \left[1 + \left(\frac{1}{2}\right) \cdot (3\cos^2\theta - 1) \cdot (3\cos^2\alpha - 1)\right], \quad (5)$$

$$\mathbf{I}_v^{\perp} = \left(\frac{1}{2}\right) \cdot \sin^2\alpha. \quad (6)$$

In the case of plane type orbital, the equation becomes

$$\mathbf{I}_p^{\parallel} = \left(\frac{2}{3}\right) \cdot \left[1 - \left(\frac{1}{4}\right) \cdot (3\cos^2\theta - 1) \cdot (3\cos^2\gamma - 1)\right], \quad (7)$$

$$\mathbf{I}_p^{\perp} = \left(\frac{1}{2}\right) \cdot [1 + \cos^2\gamma], \quad (8)$$

where $\alpha$ is the polar angle, that is, the angle between the surface normal and the vector-type $\sigma^*_{Si-Si}$ orbital (peak B). It should be noted that $\alpha$ is the same as the angle between surface and the Si–Si bond. $\gamma$ is also the polar angle that is, the angle between the surface normal and the normal direction of the plane-type $\sigma^*_{Si-C}$ orbital (peak A). The value of $\gamma$ is the same as the angle between surface and Si–C bond. The definition of the polar angles $\alpha$ and $\gamma$ is shown in the Figure 5.

Figures 6(a) and 6(b) show the normalized peak intensity **I** of the peaks A and B of the NEXAFS spectra as a function of the incident angle ($\theta$) of the SR beam. The details of the normalization procedure have been described in the caption of Figure 6. The spectrum taken at the small incidence angle ($\theta = 10°$) shows broad feature. It is seen that the intensity of the peak A decreased, while the intensity of the peak B increased when the spectra were taken at the incidence angle $\theta = 80°$ (See Figure 3). Therefore, the areas of the peaks A and B found strongly polarization dependent are calculated by peak deconvolution using Gaussian-curve fitting technique. The normalized intensities of the peaks A and B are plotted as filled circles with solid line which are shown in Figure 6.

It has been observed that the experimental data for both the samples almost follow the line with the polar angle ~65°. We already discussed the standing-up orientation in more detail on the basis of the zigzag and helical conformation of the PDMS films grown on ITO surface [14]. We proposed that the multilayer film composed of helix structure was perpendicularly oriented on the ITO surface with the polar angle of around 40°. Present results confirmed that the experimental values of the polar angle for both the vector and plane type orbitals follow the theoretical line around 65° (See Figures 6(a) and 6(b)).
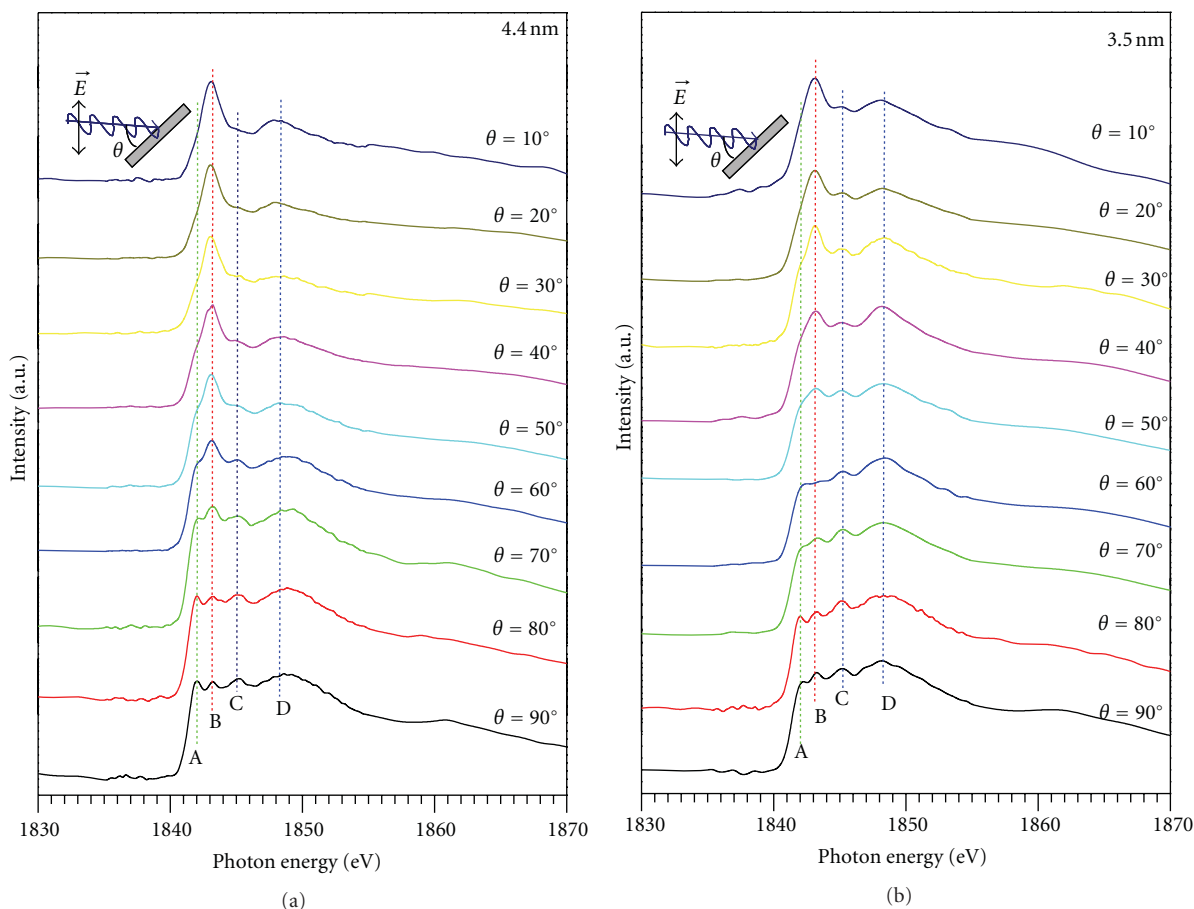
FIGURE 4: Si $K$-edge NEXAFS spectra for the samples deposited on ITO substrate with different thickness: (a) 4.4 nm and (b) 3.5 nm [14]. The NEXAFS spectra were recorded by the total electron yield mode at the different incident angles $\theta$ of the SR beam. Definition of the incidence angle $\theta$ is shown inside of this figure.

If the structure is flat-lying helical, $\alpha$ equals 48.5 degree, and $\gamma$ equals 41.5 degree. These angles are just complementarily angles of those of the standing-up helical configuration. On the other hand, for the flat-lying zigzag configuration, there are roughly two cases. One is that the Si–C plane is perpendicular to the surface. In this case, Si atoms locate close and far from the surface one by one. For this configuration, the $\alpha$ equals 54.5° and $\gamma$ equals 0°. The second case is that the Si–Si bond is parallel to the surface. In this case, all of the Si atoms are close to the surface. For this configuration, $\alpha$ equals 90° and $\gamma$ equals 0°.

The experimental data show that $\alpha$ equals 65°, and $\gamma$ equals 65°. It is wonder that the values are not exactly the same as those of the flat-lying helical structure. But if the configuration is flat-lying zigzag, then at least $\gamma$ value should be nearly 0 for both the cases. So we can suppose that the configuration is flat-lying helical structure with the polar angle of around 65°.

A question might be raised as why the orientations of the PDMS molecules are opposite between HOPG and ITO surfaces. At present, we cannot give a definite answer to this interesting phenomenon. One plausible speculation about standing-up configuration is as follows.

We have also investigated the orientation of PDMS on other substrates such as polycrystalline copper, and it was found that the backbones are perpendicular to the surface. As to the flatness of the surface, we observed that the ITO surface is vertically undulated in the order of 10 nm [26]. The surface of copper seems to be also undulated in larger scale. Therefore, the first layer of PDMS on the ITO and Cu surfaces cannot lie down due to the stress in the molecular backbone. This is the reason why the PDMS molecules stand up on a rough surface. On the other hand, HOPG has perfectly flat surface without defects and steps, so the first layer of PDMS can lie flat along the surface. It is considered that the succeeding over layers follows the orientation of the first layer.

As to the question why PDMS molecules lie flat only on HOPG surface, one plausible explanation is the relatively strong interaction between CH bonds in PDMS and $\pi$ orbitals (CH/$\pi$ interaction) at the HOPG surface. The CH/$\pi$ interaction is a kind of hydrogen bond operating between a soft acid CH and a soft base $\pi$-system like not only benzenes but graphites, fullerenes, and nanotubes. Nishio et al. have reported that the CH/$\pi$ interaction exists as ubiquitous force and stressed the importance of the CH/$\pi$ interaction in
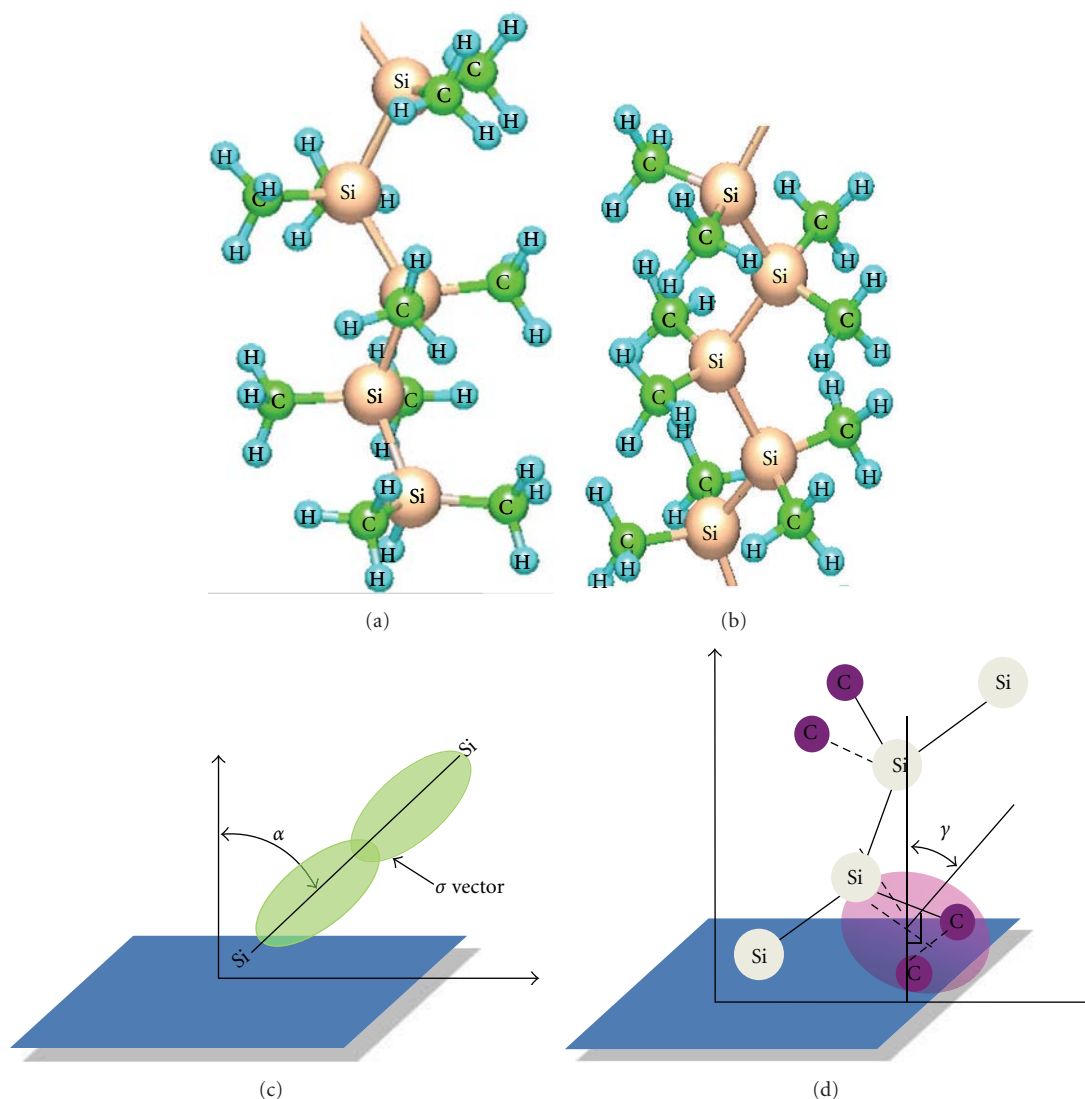
FIGURE 5: Sketch of the PDMS molecule in which only five silicon atoms are considered: (a) zigzag configuration, (b) helical configuration, (c) definition of the polar angle $\alpha$ in respect to the Si–Si $\sigma$ vector, and (c) definition of the polar angle $\gamma$ in respect to the Si–C plane. The structures (a) and (b) are sketched by the WinMOPAC3.9 version of the computer program.

various fields of chemistry [27–29]. As to the solid surface, Linares et al. reported the configuration of a porphyrin derivatives on graphite by scanning tunneling microscopy and molecular simulation, and they have shown that methyl groups point toward the surface of graphite, suggesting the occurrence of CH/$\pi$ hydrogen bonds [30]. In the present case, a PDMS molecule has six CH bonds in each silicon atom, and one of the CH bonds would contribute to bind with HOPG surface through the CH/$\pi$ interaction.

In summary, we have investigated the molecular configuration of PDMS films deposited on HOPG surface and demonstrated that the molecular skeleton of the polymer is just parallel to the basal plane of HOPG. More detailed analysis revealed that the PDMS molecules lie flat on the HOPG surface showing helical structure with the polar angle of around 65°. Since polysilanes composed of silicon-silicon backbone are one of the candidate materials as 1D

molecular wire with high electric conductivity, the present results will shed light on the future applications of polysilanes to molecular electronic devices with high quality.

## 4. Conclusions

We have analysed the self-assembling, electronic structure, and molecular orientation of 1D PDMS films by XPS and NEXAFS spectroscopy using linearly polarized synchrotron radiation as an excitation source. XPS confirmed the formation of monolayer and multilayer films in the samples. In the Si $K$-edge NEXAFS, four resonance peaks are identified of which two peaks are found to be strongly polarization dependent. On the basis of the polarization dependence of NEXAFS, finally, we found that the backbones of the PDMS molecules are nearly parallel in respect to the HOPG surface. The results are just opposite to those for our previous
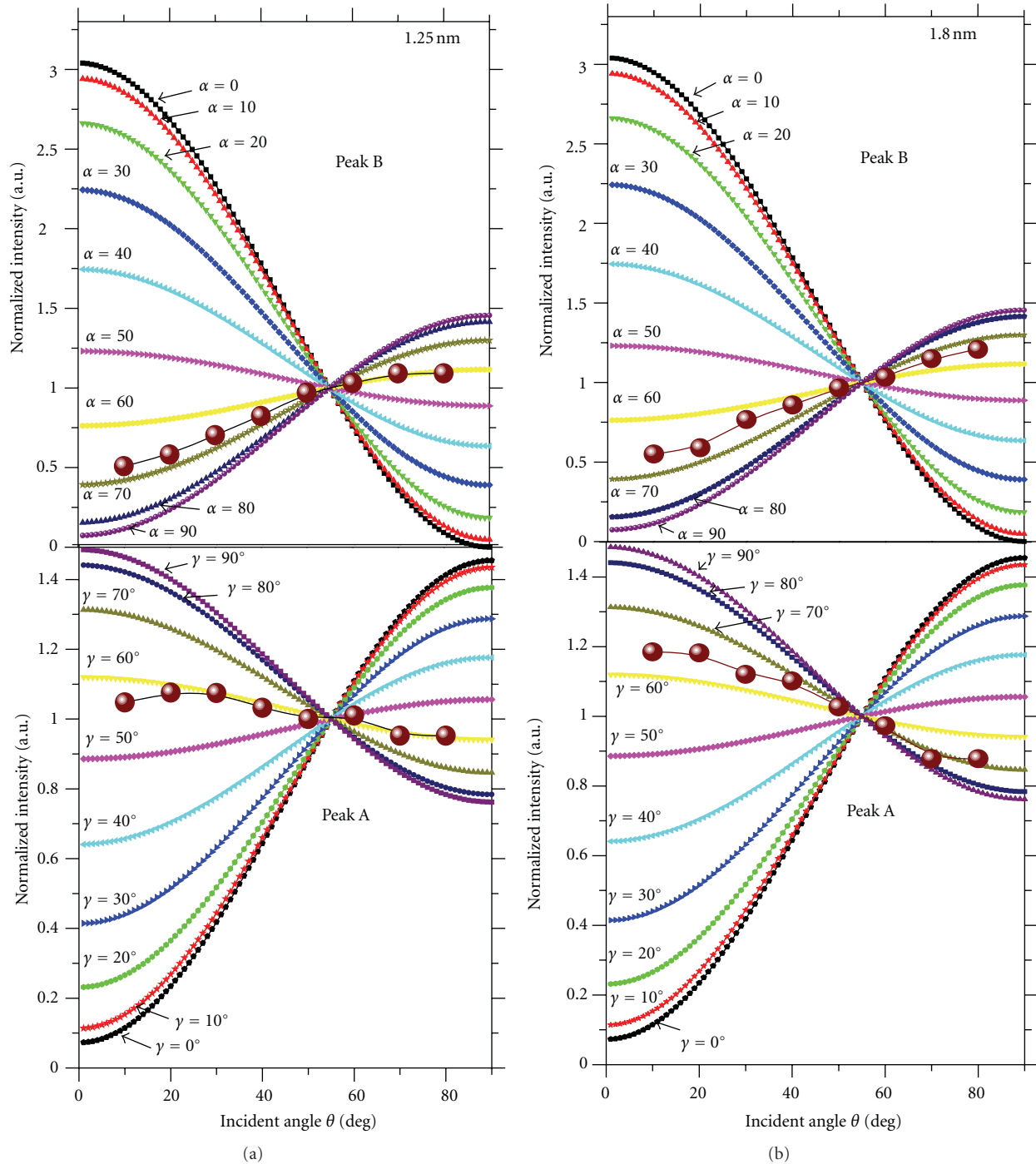
FIGURE 6: Normalized peak intensity **I** of the NEXAFS spectra as a function of the incident angle $\theta$ of the SR beam for the samples deposited on HOPG substrate with different thickness: (a) 1.25 nm and (b) 1.80 nm. The filled circles are the experimental values. The intensities are normalized such that $\mathbf{I} = 1$ at $\theta = 54.7°$ corresponding to the magic angle. The intensities of the peaks A and B were normalized by the total electron yields at 1890 eV for the respective incident angles where no polarization dependences existed. The coloured lines in the upper section of Figure 6 are theoretically calculated values at various $\alpha$ using (4), (5), and (6), while the coloured lines in the lower section of the Figure 6 are those obtained at various $\gamma$ values using (4), (7), and (8) shown in the text.

study which described that the backbones of the PDMS are perpendicular in respect to the ITO surface. The flat-lying feature of PDMS observed only on HOPG surface is attributed to the interaction between CH bonds in PDMS and $\pi$ orbitals in HOPG surface.

## Acknowledgments

# References

[1] R. West, "The polysilane high polymers," *Journal of Organometallic Chemistry*, vol. 300, no. 1-2, pp. 327–346, 1986.

[2] J. W. Mintmire, "Conformational effects in organopolysilanes: a first-principles approach," *Physical Review B*, vol. 39, no. 18, pp. 13350–13357, 1989.

[3] K. Seki, H. Ishii, A. Yuyama et al., "Electronic structures of polysilanes and related compounds," *Journal of Electron Spectroscopy and Related Phenomena*, vol. 78, pp. 403–406, 1996.

[4] J. F. Rabolt, D. Hofer, R. D. Miller, and G. N. Fickes, "Studies of chain conformational kinetics in poly(di-n-alkylsilanes) by spectroscopic methods. 1. Poly(di-n-hexylsilane), poly(di-n-heptylsilane), and poly(di-n-octylsilane)," *Macromolecules*, vol. 19, no. 3, pp. 611–616, 1986.

[5] V. M. Hallmark, R. Sooriyakumaran, R. D. Miller, and J. F. Rabolt, "Studies of chain conformational kinetics in poly(di-n-alkylsilanes) by spectroscopic methods. III. Fourier transform Raman studies of unsymmetric side chain substitution," *The Journal of Chemical Physics*, vol. 90, no. 4, pp. 2486–2491, 1989.

[6] F. C. Schilling, A. J. Lovinger, J. M. Zeigler, D. D. Davis, and F. A. Bovey, "Solid-state structures and thermochromism of poly(di-n-butylsilylene) and poly(di-n-pentylsilylene)," *Macromolecules*, vol. 22, no. 7, pp. 3055–3063, 1989.

[7] S. Furukawa and K. I. Takeuchi, "Structure and orientation of polydimethylsilane films," *Solid State Communications*, vol. 87, no. 10, pp. 931–934, 1993.

[8] S. Furukawa, K. Takeuchi, T. Nomura, T. Yasuda, and M. Tamura, "Estimation of the physical constants of a polydimethylsilane crystal and its evaporated film," *Journal of Physics*, vol. 5, no. 27, pp. 4729–4736, 1993.

[9] S. Furukawa, M. Obana, T. Nakamine, Y. Shirakawa, A. Sorai, and M. Tamura, "Structure and optical properties of ternary Si:C:H films prepared by evaporation of organo-polysilane," *Journal of Physics*, vol. 4, no. 22, pp. 5167–5172, 1992.

[10] K. I. Takeuchi, M. Mizoguchi, M. Kira, M. Shimana, S. Furukawa, and M. Tamura, "Orientation of films prepared by the evaporation of poly(dimethyl silane)," *Journal of Physics*, vol. 6, no. 49, pp. 10705–10712, 1994.

[11] S. Furukawa, "Structure and orientation control of organopolysilanes and their application to electronic devices," *Thin Solid Films*, vol. 331, no. 1-2, pp. 222–228, 1998.

[12] S. Furukawa and H. Ohta, "Structure and orientation of vacuum-evaporated poly(di-methyl silane) film," *Thin Solid Films*, vol. 438-439, pp. 48–55, 2003.

[13] M. Gröppel, W. Roth, N. Elbel, and H. von Seggern, "Self-assembly of organopolysilanes on graphite: a scanning tunneling microscopy study," *Surface Science*, vol. 323, no. 3, pp. 304–310, 1995.

[14] M. A. Mannan, Y. Baba, T. Sekiguchi et al., "Self-ordering of silicon polymer thin film grown on indium tin oxide surface investigated by X-ray absorption spectroscopy," *Journal of Electron Spectroscopy and Related Phenomena*, vol. 181, no. 2-3, pp. 242–248, 2010.

[15] H. Konishi, A. Yokoya, H. Shiwaku et al., "Synchrotron radiation beamline to study radioactive materials at the Photon Factory," *Nuclear Instruments and Methods in Physics Research A*, vol. 372, no. 1-2, pp. 322–332, 1996.

[16] J. H. Scofield, "Theoretical photoionization cross section from 1 to 1500 keV," Livermore UCRL 51326, Lawrence Livermore Laboratory, Livermore, Calif, USA, 1973.

[17] M. P. Seah and W. A. Dench, "Quantitative electron spectroscopy of surfaces: a standard data base for electron inelastic mean free paths in solids," *Surface and Interface Analysis*, vol. 1, no. 1, pp. 2–11, 1979.

[18] Y. Baba, T. Sekiguchi, I. Shimoyama, and K. G. Nath, "Structures of sub-monolayered silicon carbide films," *Applied Surface Science*, vol. 237, no. 1–4, pp. 176–180, 2004.

[19] K. Sakamoto, D. Kondo, Y. Ushimi et al., "Temperature dependence of the electronic structure of $C_{60}$ films adsorbed on Si(001)-(2x1) and Si(111)-(7x7) surfaces," *Physical Review B*, vol. 60, no. 4, pp. 2579–2591, 1999.

[20] T. M. Parrill and Y. W. Chung, "Surface analysis of cubic silicon carbide (001)," *Surface Science*, vol. 243, no. 1–3, pp. 96–112, 1991.

[21] G. Dufour, F. Rochet, F. C. Stedile et al., "SiC formation by reaction of Si(001) with acetylene: electronic structure and growth mode," *Physical Review B*, vol. 56, no. 7, pp. 4266–4282, 1997.

[22] K. G. Nath, I. Shimoyama, T. Sekiguchi, and Y. Baba, "Chemical-state analysis for low-dimensional Si and Ge films on graphite," *Journal of Applied Physics*, vol. 94, no. 7, pp. 4583–4588, 2003.

[23] K. G. Nath, I. Shimoyama, T. Sekiguchi, and Y. Baba, "Synchrotron radiation photoabsorption and photoemission spectroscopy for thermal-induced reoriented Si polymer," *Journal of Electron Spectroscopy and Related Phenomena*, vol. 144-147, pp. 323–326, 2005.

[24] V. R. McCrary, F. Sette, C. T. Chen et al., "Polarization effects in the valence and inner-shell spectra of poly(di-n-hexylsilane)," *The Journal of Chemical Physics*, vol. 88, no. 9, pp. 5925–5933, 1988.

[25] J. Stöhr, *NEXAFS Spectroscopy*, vol. 25 of *Springer Series in Surface Sciences*, Springer, Berlin, Germany, 1996.

[26] J. Deng, Y. Baba, T. Sekiguchi, N. Hirao, and M. Honda, "Effect of substrates on the molecular orientation of silicon phthalocyanine dichloride thin films," *Journal of Physics Condensed Matter*, vol. 19, no. 19, Article ID 196205, 2007.

[27] M. Nishio, "CH/$\pi$ hydrogen bonds in crystals," *CrystEngComm*, vol. 6, pp. 130–158, 2004.

[28] M. Nishio, Y. Umezawa, K. Honda, S. Tsuboyama, and H. Suezawa, "CH/$\pi$ hydrogen bonds in organic and organometallic chemistry," *CrystEngComm*, vol. 11, no. 9, pp. 1757–1788, 2009.

[29] M. Nishio, "The CH/$\pi$ hydrogen bond in chemistry. Conformation, supramolecules, optical resolution and interactions involving carbohydrates," *Physical Chemistry Chemical Physics*, vol. 13, no. 31, pp. 13873–13900, 2011.

[30] M. Linares, P. Iavicoli, K. Psychogyiopoulou et al., "Chiral expression at the Solid-Liquid interface: a joint experimental and theoretical study of the self-assembly of chiral porphyrins on graphite," *Langmuir*, vol. 24, no. 17, pp. 9566–9574, 2008.

*Research Article*

# Transitional Failure of Carbon Nanotube Systems under a Combination of Tension and Torsion

## Byeong-Woo Jeong

*Department of Guided Weapon Engineering, Daeduk College, Daejeon 305-715, Republic of Korea*

Correspondence should be addressed to Byeong-Woo Jeong, bwoojeong@gmail.com

Transitional failure envelopes of single- and double-walled carbon nanotubes under combined tension-torsion are predicted using classical molecular dynamics simulations. The observations reveal that while the tensile failure load decreases with combined torsion, the torsional buckling moment increases with combined tension. As a result, the failure envelopes under combined tension-torsion are definitely different from those under pure tension or torsion. In such combined loading, there is a multitude of failure modes (tensile failure and torsional buckling), and the failure consequently exhibits the feature of transitional failure envelopes. In addition, the safe region of double-walled carbon nanotubes is significantly larger than that of single-walled carbon nanotubes due to the differences in the onset of torsional buckling.

## 1. Introduction

Carbon nanotubes (CNTs) have the unique properties including high stiffness, high covalent bond strength, large elastic instability, low density, tubular shape, and large aspect ratio. They have consequently been proposed for use as key elements in applications such as nanometer scale devices [1–5] and composite materials [6]. In these CNT-based applications, combined tensile and torsional loads on the CNTs are widely expected to occur. For instance, CNTs may be used as drive shafts [2], torsion springs [4], and torsional oscillators [7] that can experience torsion as well as tension. Thus, characterizing and understanding the mechanical responses of CNTs undergoing this type of loading are important to optimize their use in new materials and devices. While numerous studies have examined some aspects of the mechanical responses of CNTs, such as their strength [8, 9], buckling instability [10, 11], and elastic modulus [12, 13], there is much that is still unknown about other aspects of the mechanical responses of CNTs in combined tensile and torsional loading, especially concerning the details of transitional failure envelopes.

In the most general terms, failure refers to any actions leading to an inability of a part to function in the intended manner. It follows that permanent deformation (yielding) or

fracture may be regarded as modes of failure. Another way in which a part may fail is through instability by undergoing large displacements when the applied load reaches the buckling value. Here, while the permanent deformation or fracture indicates the elastic-plastic yield transition of parts, buckling instability is an effect of overall geometry rather than only material instability. Therefore, the beginnings of failure occur prior to the onset of any high levels of stress and the buckled systems are totally elastic. While the CNTs have their highest rigidity along the direction of the nanotube axis due to the $sp^2$ bonding between the carbon atoms, they are much more compliant in their radial direction [14, 15]. Therefore, the CNTs are readily collapsed in their radial direction without breaking any in-plane bonding [10, 16]. This characterizes the buckling instability which occurs in the CNTs under torsional load [10]. However, the CNTs under tensile load exhibit the elastic-plastic yield transition or fracture behavior [8, 14]. When tension or torsion is applied to CNTs in a uniaxial manner, tensile load and torsional moment can be compared directly with tensile failure load and torsional buckling moment, respectively, to estimate whether or not the CNTs will fail. However, the problem becomes more complex under combined tension-torsion. In such cases, there is a multitude of failure modes (tensile failure and torsional buckling), and the failure

consequently may exhibit the feature of transitional failure. Therefore, this requires that the failure under combined tension-torsion is characterized with transitional failure envelopes.

The particular focus of this work is the identification of transitional failure envelope (TFE) for failure of single-walled carbon nanotubes (SWCNTs) and double-walled carbon nanotubes (DWCNTs) under combined tensile-torsional loads using classical molecular dynamics (MD) simulations. The efficiency of the design approach relies in great measure on our ability to predict the circumstances under which failure is likely to occur. The results are therefore expected to provide new insights that will enhance the design of CNT-based devices and materials to better function under combined tensile-torsional loading.

## 2. Methods

The classical MD simulations numerically integrate Newton's equations of motion with a third-order Nordsieck predictor corrector using a time-step of 0.2 fs [17]. The forces on the atoms are calculated using methods that vary with interatomic distance. In particular, the short-range covalent interactions are modeled using the many-body, second-generation reactive empirical bond-order (REBO) hydrocarbon potential [18]. It has been previously demonstrated that the cut-off functions of the REBO potential overestimate the force needed to break a carbon-carbon covalent bond [9]. In order to prevent this overestimation, we have used the modified cut-off function for distances between 1.7 and 2.0 Å in the same way as the literature which was previously published [9]. In addition, long-range van der Waals interactions are included in the form of a Lennard-Jones potential [17] that is only active at distances greater than the covalent bond lengths. The system temperature is maintained at 300 K using a velocity-rescaling thermostat that has been shown to have negligible effects on the mechanical behavior of CNTs [19]. The particular nanotubes that are considered are (10,10) SWCNTs and (10,10) at (5,5) DWCNTs. An axial-strain-induced torsion has been shown to be negligible for these armchair CNTs [20], and thus such effect was not considered for this work. The nanotubes are about 9.5 nm long, and only defect-free nanotubes are considered here.

The CNTs were prepared by minimizing the potential energy of the entire nanotubes. The external loads are then applied to one end of SWCNTs and the outer wall of DWCNTs, while the other end is held fixed. In applications such as nanoelectromechanical paddle oscillators, it has been shown that only the outermost walls of the multiwalled CNTs (MWCNTs) carry the applied torques as torsion springs while the inner walls only slide against them [1, 5, 21, 22]. Therefore, applying torsional moment to the outer wall of DWCNTs is reasonable to optimize their use in the devices. In particular, the combined tensile-torsional loads are applied simultaneously during the simulations, and the various loading types are shown in Table 1. In the simulations to obtain the tensile failure envelope, the tensile loading rate is fixed but the torsional loading rate is varied (Table 1). On the other hand, in the simulations to obtain the torsional

TABLE 1: Loading cases considered for the simultaneous tension-torsion simulations. The tensile load (tension) and torsional moment (torque) are applied simultaneously in a proportional and quasistatic manner.

| Tensile failure analysis | | Torsional failure analysis | |
|---|---|---|---|
| Loading type | Loading ratio (torque/tension) | Loading type | Loading ratio (tension/torque) |
| A0[a] | 0.000[a] | B0[b] | 0.000[b] |
| A1 | 0.060 | B1 | 0.500 |
| A2 | 0.100 | B2 | 1.250 |
| A3 | 0.160 | B3 | 2.000 |
| A4 | 0.200 | B4 | 2.750 |
| A5 | 0.240 | B5 | 3.571 |
| A6 | 0.280 | B6 | 4.167 |
| A7 | 0.440 | B7 | 5.000 |

[a] Pure tension (tensile load).
[b] Pure torque (torsional moment).

failure envelope, the torsional loading rate is fixed but the tensile loading rate is varied (Table 1). It should be notified that the MD simulations are based on the quasistatic and load-control method, in which the applied loads are incremented quasistatically to the CNTs and then their displacements are obtained during the simulations. Therefore, this approach is similar to the quasistatic testing of macroscopic materials and structures that especially adopts the load control method. The applied tensile and torsional loading rates during MD simulations correspond to a deformation rate of 10 m/s and 10 Grad/s, respectively. These loading rates are low enough to avoid adverse effect on the failure loads.

## 3. Results and Discussion

Figure 1 presents tension versus tensile strain curves of a SWCNT under pure tension and different combinations of tension-torsion. The flat regime represents a sudden increase of bond elongation which is interpreted by us as failure [8, 9]. Thus, failure is not triggered on the boundary where external loads are applied because the rate of applied loads used in the simulations is low enough to avoid such adverse effect on the boundary. The tensile strength of the SWCNT under pure tension is found to be about 100 GPa, in good agreement with published theoretical predictions [8, 9], but this value is higher than the tensile strength of about 50 GPa obtained from experiments [23, 24]. This discrepancy between experimental measurements and theoretical predictions is thought to be caused mainly by the wall defects and other imperfections in the experimental CNT samples that are not present in the CNTs examined computationally [25].

For combined loading types, A1–A3, the failure of a SWCNT is governed by the tensile failure but not by torsional buckling (Figure 1 and Table 1). Therefore, the torsional failure (buckling) does not occur for the loading types. However, for combined loading types, A4–A7, for which higher torsion (higher loading ratio) is applied, the torsional buckling
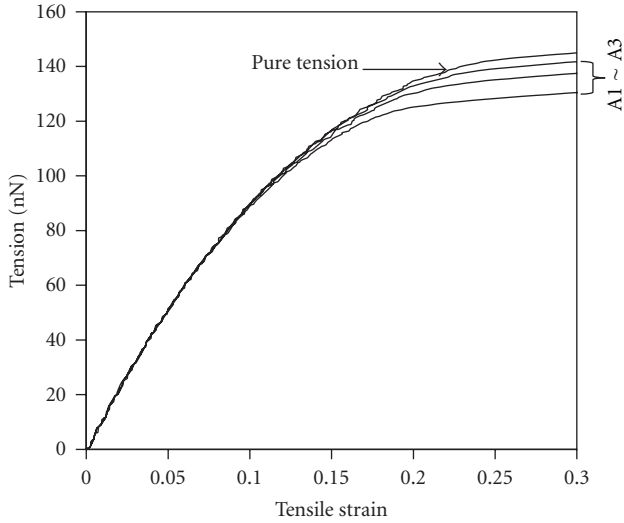
FIGURE 1: Tension versus tensile strain curves of a (10, 10) SWCNT under pure tension and combined tension-torsion. A1~A3 indicates the combined loading types shown in Table 1.
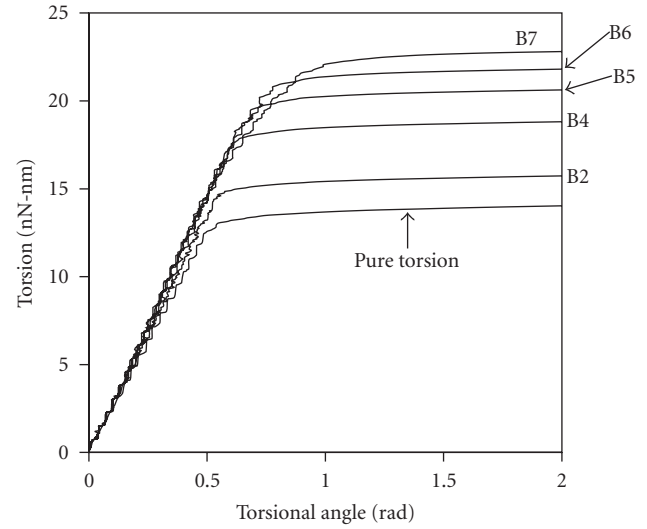


FIGURE 2: Torsion versus torsional angle curves of a (10, 10) SWCNT under pure torsion and combined tension-torsion. B2 and B4~B7 indicate the combined loading types shown in Table 1.

occurs but not tensile failure as mentioned in the following (Table 1). From Figure 1, we can see that the tensile failure loads substantially decrease with the increase of applied torsion (or the loading ratio of torsion and tension). In the other word, the tensile strength of SWCNTs under combined tensile-torsional loading is definitely different from their tensile strength under pure tension. This is because the tensile behaviors of SWCNTs under combined tension-torsion are affected by the combination between tensile (normal) stress and torsional shear stress acting on them. In addition, the figure indicates that the tensile stiffness (elastic modulus) within the linear elastic limit is almost the same for different loading types. This means that applied torsion does not affect the tensile elastic modulus of the SWCNT.

When the torsional moment is applied, the SWCNTs are rapidly contracted in the radial direction after the buckling onset, so that their buckled configuration exhibits a substantial kink [10, 26] and a constant torque is sufficient to further deform the tubes. Consequently, the effective torsional stiffness is decreased to nearly zero after the buckling onset, indicating torsional buckling (Figure 2). This buckling instability under torsional moment is an effect of overall geometry rather than only material instability. Therefore, it should be noted that the beginnings of failure occur prior to the onset of any high levels of stress [27]. Figure 2 shows the effects of combined tension on torsional buckling in terms of a torsional angle which are the results simulated for a SWCNT. The data of Figure 2 are obtained from simulations where torsional buckling occurs but not tensile failure. In other words, the tensile failure does not occur in the system until the combined loading type, B7 (Table 1). The failure of SWCNT is therefore governed by torsional buckling but not by tensile failure until the loading type, B7 (Table 1). The figure illustrates that the torsional buckling moment significantly increases in proportion to the loading ratio of tension and torsion (or the value of combined tension).

This result is because the combined tension influences the progress of torsional shear strain and the opposite of the trend for tensile failure load, which decreases with combined torsion, as shown in Figure 1. In addition, the figure also indicates that the torsional stiffness (or shear modulus) significantly varies with combined tension relative to what happens under pure torsion. As shown in the figure, the torsional stiffness increases in proportion to the loading ratio of tension and torsion. This result is different from the trend for tensile stiffness, which does not vary when torsion is combined (Figure 1). Here, the fact that the torsional stiffness is changed by combined tension indicates nonlinear effects due to mechanical coupling between torsional shear strain and tensile strain. This unusual behavior is thought to be caused mainly by the ability of the CNTs to endure relatively large axial elongation.

As mentioned above, the combined tension and torsion affect the torsional buckling moment and tensile failure load of a SWCNT, respectively. As a result, the failure envelopes under the combined tension-torsion would be different from those under the pure tension or torsion. Figure 3 presents the failure envelopes of SWCNT under the combined tension-torsion which are obtained from the results of Figures 1 and 2. From the figure, we can see that while the tensile failure load decreases with combined torsion, the torsional buckling moment increases with combined tension. In other words, the figure shows that the failure envelopes under the combined tension-torsion are definitely different from those under the pure tension or torsion. Therefore, when the SWCNTs are considered for the use under the combined tension-torsion, the particular failure envelopes obtained under the combined loading condition should be carefully utilized. The figure also indicates that the tensile failure would be transitioned to the torsional buckling for the loading ratio higher than the loading type, A3. In contrast, the torsional buckling would be transitioned to the tensile
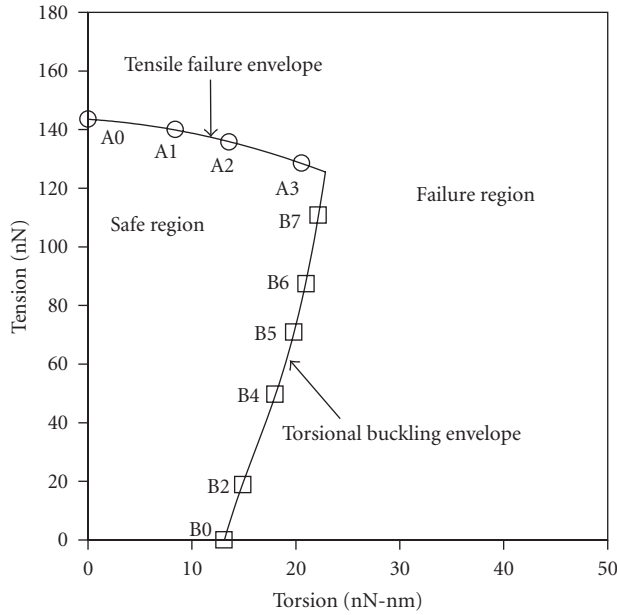
Figure 3: Failure envelopes of a (10, 10) SWCNT under combined tension-torsion. A0 and B0 indicate the pure tension and torsion, respectively. A1~A3, B2, and B4~B7 indicate the combined loading types shown in Table 1.



Figure 4: Tension versus tensile strain curves of a (10, 10) at (5,5) DWCNT under pure tension and combined tension-torsion. A2~ A7 indicates the combined loading types shown in Table 1.



Figure 5: Torsion versus torsional angle curves of a (10, 10) at (5,5) DWCNT under pure torsion and combined tension-torsion. B1~B3 indicate the combined loading types shown in Table 1.

failure for the loading ratio higher than the loading type, B7. Consequently, the failure envelopes of SWCNT under combined tension-torsion consist of both tensile and torsional failure envelopes which depend on the loading ratio (torsion/tension or tension/torsion).

Figure 4 illustrates tension versus tensile strain curves of a DWCNT under pure tension and combined tension-torsion. The tensile failure load of the DWCNT under pure tension is found to be not different from the value for SWCNT. This is because the tensile load is applied to the outer wall of DWCNT and the inner CNT does not affect the tensile failure due to the relatively weak van der Waals shear interactions between CNT walls [28]. Until combined loading types A7, the torsional buckling does not occur and thus the failure of DWCNT is governed by the tensile failure but not by torsional buckling (Table 1 and Figure 4). This result is due to the torsional buckling moment of DWCNT which is significantly higher than that of the SWCNT [10]. However, for the combined loading ratio that is higher than the value of A7, the torsional buckling occurs in the system. From Figure 4, we can see that the tensile failure loads substantially decrease with the increase of the loading ratio of torsion and tension (or the increase of combined torsion) in the same way as Figure 1. In addition, the figure also indicates that the tensile stiffness (elastic modulus) within the linear elastic limit is almost the same for different loading types. This means that applied torsion does not affect the tensile elastic modulus of DWCNT in the same way as SWCNT.

Figure 5 shows that the torsional buckling moment of a DWCNT is affected by the combined tension. The data of Figure 5 are obtained from simulations where torsional buckling occurs, but not tensile failure which occurs in
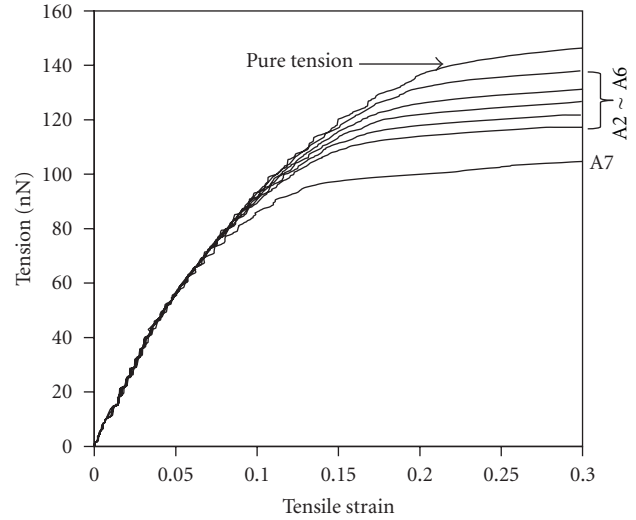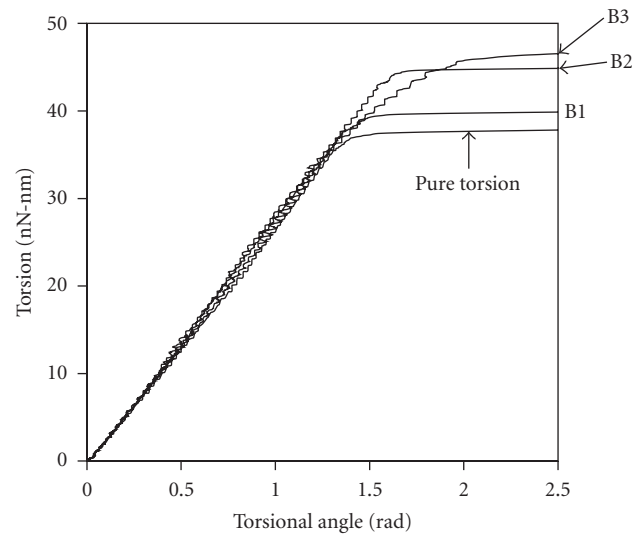
the loading ratio higher than the value of loading type, B3. As shown in the figure, the torsional buckling moment significantly increases in proportion to the loading ratio in the same way as the case of SWCNT (Figure 2). In addition, Figure 5 also illustrates that the torsional stiffness (or shear modulus) significantly varies with combined tension relative to what happens under pure torsional loading. This is same as the result for SWCNT (Figure 2). This might be because mechanical coupling between tensile strain and torsional shear strain influences torsional responses, which is probably caused primarily by tensile strain energy that is much larger than torsional shear strain energy.

As described above on DWCNT, the combined tension affects the torsional buckling moment, and the combined
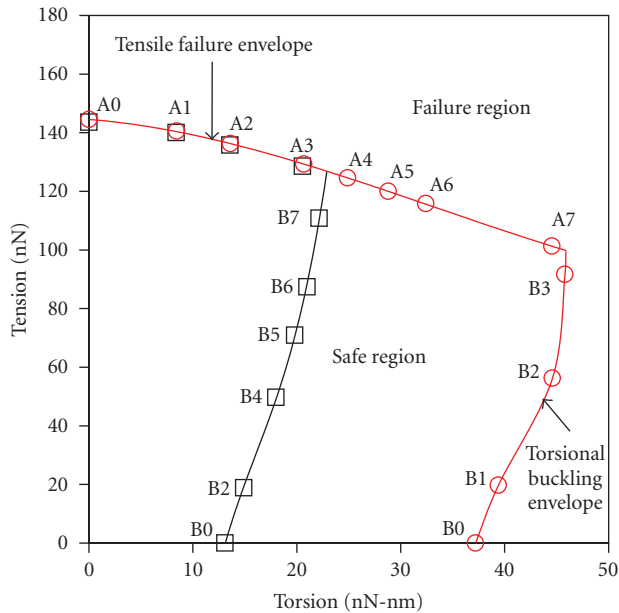
FIGURE 6: Failure envelopes of SWCNT and DWCNT under combined tension-torsion. A0 and B0 indicate the pure tension and torsion, respectively. A1~A7 and B1~B7 indicate the combined loading types shown in Table 1.

torsion affects the tensile failure loads. This implies that the failure envelopes under the combined tension-torsion would be different from those under the pure tension or torsion. Figure 6 presents the failure envelopes of DWCNT under the combined tension-torsion which are obtained from the results of Figures 4 and 5. The tensile failure loads are unaffected by the presence of an inner tube in DWCNT, and thus the tensile failure envelopes of SWCNT and DWCNT are nearly identical until combined loading type, A3. However, when the loading ratio remains above A3, the tensile failure of SWCNT is transitioned to the torsional buckling, while the failure of DWCNT is still governed by the tensile failure until the loading type, A7, without the torsional buckling phenomena. This is because the value of torsional buckling moment of DWCNT is significantly larger than that of SWCNT [10, 27]. Consequently, the tensile failure envelopes between SWCNT and DWCNT show significant differences as shown in Figure 6. Here, when the combined loading ratio remains higher than A7, the tensile failure of DWCNT is transitioned to the torsional buckling in similar manner with SWCNT. In contrast, the torsional buckling of SWCNT and DWCNT is transitioned to the tensile failure for the loading ratios above the loading type, B7 and B3, respectively. From Figure 6, we can also see that the safe region between SWCNT and DWCNT is definitely different, and the safe region of DWCNT is significantly larger than that of SWCNT. This result is due to the torsional buckling moment of DWCNT which is higher than that of SWCNT.

## 4. Conclusions

This work has predicted the transitional failure envelopes of SWCNT and DWCNT under combined tension-torsion,

using classical MD simulations. The observations reveal that while the tensile failure load decreases with combined torsion, the torsional buckling moment increases with combined tension. As a result, the failure envelopes under combined tension-torsion are definitely different from those under pure tension or torsion. In such combined loading condition, there is a multitude of failure modes (tensile failure and torsional buckling), and the failure consequently exhibits the feature of transitional failure envelopes which consist of both tensile and torsional failure envelopes and depend on the loading ratio (torsion/tension or tension/torsion). In addition, the safe region of DWCNT is significantly larger than that of SWCNT due to the differences in the onset of torsional buckling. The efficiency of the design approach relies in great measure on our ability to predict the circumstances under which failure is likely to occur. The results are therefore expected to provide new insights that will enhance the design of CNT-based devices and materials to better function under combined tensile-torsional loading.

## References

[1] T. Cohen-Karni, L. Segev, O. Srur-Lavi, S. R. Cohen, and E. Joselevich, "Torsional electromechanical quantum oscillations in carbon nanotubes," *Nature Nanotechnology*, vol. 1, no. 1, pp. 36–41, 2006.

[2] A. M. Fennimore, T. D. Yuzvinsky, W. Q. Han, M. S. Fuhrer, J. Cumings, and A. Zetti, "Rotational actuators based on carbon nanotubes," *Nature*, vol. 424, no. 6947, pp. 408–410, 2003.

[3] A. R. Hall, M. R. Falvo, R. Superfine, and S. Washburn, "A self-sensing nanomechanical resonator built on a single-walled carbon nanotube," *Nano Letters*, vol. 8, no. 11, pp. 3746–3749, 2008.

[4] J. C. Meyer, M. Paillet, and S. Roth, "Materials science: single-molecule torsional pendulum," *Science*, vol. 309, no. 5740, pp. 1539–1541, 2005.

[5] S. J. Papadakis, A. R. Hall, P. A. Williams et al., "Resonant oscillators with carbon-nanotube torsion springs," *Physical Review Letters*, vol. 93, no. 14, Article ID 146101, 4 pages, 2004.

[6] R. H. Baughman, A. A. Zakhidov, and W. A. De Heer, "Carbon nanotubes—the route toward applications," *Science*, vol. 297, no. 5582, pp. 787–792, 2002.

[7] V. Sazonova, Y. Yalsh, I. Üstünel, D. Roundy, T. A. Arlas, and P. L. McEuen, "A tunable carbon nanotube electrochemical oscillator," *Nature*, vol. 431, no. 7006, pp. 284–287, 2004.

[8] T. Belytschko, S. P. Xiao, G. C. Schatz, and R. S. Ruoff, "Atomistic simulations of nanotube fracture," *Physical Review B*, vol. 65, no. 23, Article ID 235430, 8 pages, 2002.

[9] B. W. Jeong, J. K. Lim, and S. B. Sinnott, "Tensile mechanical behavior of hollow and filled carbon nanotubes under tension

or combined tension-torsion," *Applied Physics Letters*, vol. 90, no. 2, Article ID 023102, 3 pages, 2007.

[10] B. W. Jeong, J. K. Lim, and S. B. Sinnott, "Elastic torsional responses of carbon nanotube systems," *Journal of Applied Physics*, vol. 101, no. 8, Article ID 084309, 7 pages, 2007.

[11] B. I. Yakobson, C. J. Brabec, and J. Bernholc, "Nanomechanics of carbon tubes: instabilities beyond linear response," *Physical Review Letters*, vol. 76, no. 14, pp. 2511–2514, 1996.

[12] J. P. Lu, "Elastic properties of carbon nanotubes and nanoropes," *Physical Review Letters*, vol. 79, no. 7, pp. 1297–1300, 1997.

[13] D. Srivastava, C. Wei, and K. Cho, "Nanomechanics of carbon nanotubes and composites," *Applied Mechanics Reviews*, vol. 56, no. 2, pp. 215–229, 2003.

[14] M. A. L. Marques, H. E. Troiani, M. Miki-Yoshida, M. Jose-Yacaman, and A. Rubio, "On the breaking of carbon nanotubes under tension," *Nano Letters*, vol. 4, no. 5, pp. 811–815, 2004.

[15] B. Ni, S. B. Sinnott, P. T. Mikulski, and J. A. Harrison, "Compression of carbon nanotubes filled with $C_{60}$, $CH_4$, or Ne: predictions from molecular dynamics simulations," *Physical Review Letters*, vol. 88, no. 20, Article ID 205505, 4 pages, 2002.

[16] A. Kutana and K. P. Giapis, "Transient deformation regime in bending of single-walled carbon nanotubes," *Physical Review Letters*, vol. 97, no. 24, Article ID 245501, 4 pages, 2006.

[17] M. P. Allen and D. J. Tildesley, *Computer Simulation of Liquids*, Clarendon Press, Oxford, UK, 1987.

[18] D. W. Brenner, O. A. Shenderova, J. A. Harrison, S. J. Stuart, B. Ni, and S. B. Sinnott, "A second-generation reactive empirical bond order (REBO) potential energy expression for hydrocarbons," *Journal of Physics Condensed Matter*, vol. 14, no. 4, pp. 783–802, 2002.

[19] S. Heo and S. B. Sinnott, "Investigation of the influence of thermostat configurations on the mechanical properties of carbon nanotubes in molecular dynamics simulations," *Journal of Nanoscience and Nanotechnology*, vol. 7, no. 4-5, pp. 1518–1524, 2007.

[20] H. Liang and M. Upmanyu, "Axial-strain-induced torsion in single-walled carbon nanotubes," *Physical Review Letters*, vol. 96, no. 16, Article ID 165501, 4 pages, 2006.

[21] P. A. Williams, S. J. Papadakis, A. M. Patel, M. R. Falvo, S. Washburn, and R. Superfine, "Torsional response and stiffening of individual multiwalled carbon nanotubes," *Physical Review Letters*, vol. 89, no. 25, Article ID 255502, 4 pages, 2002.

[22] P. A. Williams, S. J. Papadakis, A. M. Patel, M. R. Falvo, S. Washburn, and R. Superfine, "Fabrication of nanometer-scale mechanical devices incorporating individual multiwalled carbon nanotubes as torsional springs," *Applied Physics Letters*, vol. 82, no. 5, pp. 805–807, 2003.

[23] M. F. Yu, B. S. Files, S. Arepalli, and R. S. Ruoff, "Tensile loading of ropes of single wall carbon nanotubes and their mechanical properties," *Physical Review Letters*, vol. 84, no. 24, pp. 5552–5555, 2000.

[24] M. F. Yu, O. Lourie, M. J. Dyer, K. Moloni, T. F. Kelly, and R. S. Ruoff, "Strength and breaking mechanism of multiwalled carbon nanotubes under tensile load," *Science*, vol. 287, no. 5453, pp. 637–640, 2000.

[25] S. L. Mielke, D. Troya, S. Zhang et al., "The role of vacancy defects and holes in the fracture of carbon nanotubes," *Chemical Physics Letters*, vol. 390, no. 4–6, pp. 413–420, 2004.

[26] B. W. Jeong, J. K. Lim, and S. B. Sinnott, "Torsional stiffening of carbon nanotube systems," *Applied Physics Letters*, vol. 91, no. 9, Article ID 093102, 3 pages, 2007.

[27] B. W. Jeong, J. K. Lim, and S. B. Sinnott, "Multiscale-failure criteria of carbon nanotube systems under biaxial tension-torsion," *Nanotechnology*, vol. 18, no. 48, Article ID 485715, 2007.

[28] M. Huhtala, A. V. Krasheninnikov, J. Aittoniemi, S. J. Stuart, K. Nordlund, and K. Kaski, "Improved mechanical load transfer between shells of multiwalled carbon nanotubes," *Physical Review B*, vol. 70, no. 4, Article ID 045404, 8 pages, 2004.

*Research Article*

# Influence of Electrostatic Forces on the Growth of One-Dimensional Nanostructures

## Michael Cross and Walter Varhue

*School of Engineering, University of Vermont, Burlington, VT 05405, USA*

Correspondence should be addressed to Michael Cross, mcross@cems.uvm.edu

The growth of crystalline ruthenium oxide square nanorods was considered on numerous substrate materials. The nanorods were found to grow easily on insulating substrates, while their growth on electrically conducting and grounded substrates was inhibited. The transfer of electrons from the plasma discharge to the developing nanorods caused the nanorods to be negatively charged and obtain a floating potential relative to ground. The electrical charging of the nanorod played a key role in their development.

## 1. Introduction

The growth of nanomaterial structures in general has attracted a great deal of interest and excitement over the past decade and a half with recent attention to the growth of one-dimensional nanorods [1–4]. Special interest has been given to $RuO_2$ nanostructures because of their attractive chemical and physical properties [5]. Ruthenium dioxide is a rutile-type tetragonal oxide that exhibits low electrical resistivity ($\sim 40\,\mu\Omega$-cm) and high catalytic activity [6]. As a result of these properties, nanostructured $RuO_2$ materials are of great interest to those working on field emission displays [7] and catalyst in heterogeneous electrochemical reactors including fuel cells and electrolyzers [8]. Nanorods (NRs) of $RuO_2$ have been successfully produced by MOCVD [9] as well as reactive sputtering [5, 10]. The reactive sputtering technique is attractive as it can be easily incorporated as a single-step process in the fabrication of integrated circuits. Also possible is the use of sputtering to deposit large area coatings on a variety of nonplanar surfaces such as automobile parts. In previous papers [11, 12], it was proposed that Ru hyperoxides, formed in the reactive sputtering process, are the high-vapor-pressure species that permit the synthesis of $RuO_2$ nanorods, at a low substrate temperature. The species $RuO_4$ has been proposed as an ideal precursor for the CVD growth of Ru-containing thin films [13, 14]. This high-vapor-pressure precursor is credited with having the surface mobility required to supply chemical reactions that produce highly faceted nanostructures. In this paper, a high plasma density, reactive sputtering process was used to grow $RuO_2$ NRs on a variety of substrate surfaces, with special attention paid to the electrical conductivity of the substrate material. The substrate materials used included a Si wafer substrate piece with various preexisting thin film coatings and metal sheets such as stainless steel and Ti. The nanorods have previously been found to be single crystal by X-ray diffraction analysis but randomly oriented relative to one another as displayed by the SEM pattern shown in Figure 1. The main difference in the growth process used by our group, and that used in other papers involving a sputter process, is that our process utilized a high plasma density ($10^{10}$ cm$^{-3}$ versus $10^8$ cm$^{-3}$) [13, 15–17] and a lower mole fraction of oxygen in the reactor ambient gas mixture (5% versus 50%) [12].

## 2. Experimental

The $RuO_2$ nanorod materials were formed by self-assembly through a reactive sputtering process onto a heated substrate surface. The process used to grow these nanomaterials on a Si substrate was described in earlier papers [11, 16, 17]. The $RuO_2$ nanorod samples were prepared by reactive sputtering
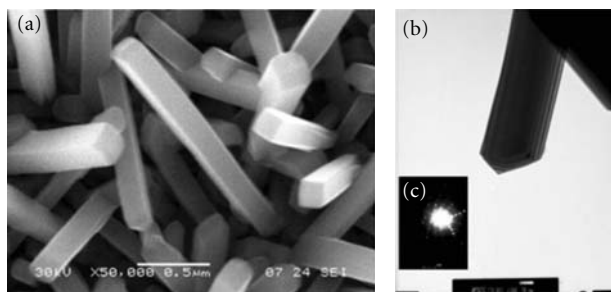
FIGURE 1: SEM and TEM images showing the single-crystal nature of the RuO$_2$ nanorods. (a) SEM image displaying smooth planar sidewalls. (b) TEM image showing atomically sharp nanorod tip. (c) TEM diffraction pattern, verifying nanorod crystallinity.



FIGURE 2: XRD diffraction pattern of the RuO$_2$ nanorods grown on a Si substrate.

from a Ru metal target operated at an RF frequency of 13.56 MHz and a power level of 50 W. In addition to the RF-driven discharge, an electron cyclotron resonant (ECR) plasma was generated above the sputter target/substrate assembly increasing the plasma density to $\sim 10^{10}$ cm$^{-3}$. The ambient in the reactor was obtained by flowing 100 sccm of a 5/95% O$_2$/Ar gas mixture, throttled to a pressure of 15 mTorr. The samples were heated radiatively from behind with a resistive BN-coated pyrolytic graphite heater to a temperature of 460°C. The resulting nanorod samples were then removed and observed with a JEOL JSM 6060 SEM.

Multiple substrates were used in this paper, including a Si wafer, an Al evaporation-coated Si wafer, a polished Ti sheet, and a Si$_3$N$_4$-coated Si wafer. Strongly conducting substrate materials included a stainless steel sheet, a stainless steel sheet coated with RuO$_2$, AZO on BSG (aluminum-doped zinc oxide on borosilicate glass), and ITO on BSG (indium tin oxide on borosilicate glass).

Electrical characterization was performed while the nanorod-coated substrates were submerged in an electrolyte solution (KOH in water) to ensure adequate contact to the nanorods. All measurements were performed at room temperature. A more detailed description of the apparatus and procedure was published earlier [18].

## 3. Results and Discussion

The deposited RuO$_2$ nanorods were randomly spaced and oriented with an average length of 1 $\mu$m for the growth conditions used. Characterization of the nanorods films by XRD suggests that the dominant growth phase is in the (200) direction, as evident by the peak at 40° in Figure 2.

The substrates in all successful NR growth cases were insulating and amorphous, and no crystalline insulating substrates were tried. The preference for the growth of the (200) phase is not obtained from the crystal orientation of the substrate, but the preferred growth from that phase is normal to the substrate. As the nanorod grows in the axial direction, only one crystal orientation can survive as a consequence of the high aspect ratio of the nanorods. Previous papers have shown a preferential growth of selected phases on insulating crystalline substrates over that on
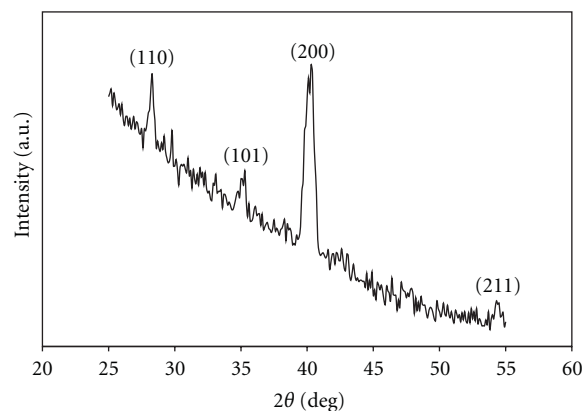
amorphous insulating substrates [19]. The current paper considers the growth of RuO$_2$ nanorods on insulating or conducting substrates.

In an earlier communication, the length was described to be strongly dependent on substrate temperature used during the growth process [11]. In that earlier paper, the RuO$_2$ nanorods were grown on Si substrates that had previously been coated with Au nanodots, which were assumed at that time to be required as nucleation sites for the subsequent growth of the RuO$_2$ NRs. Although no mechanism describing the involvement of the Au nanodots was given, the paper left the impression that these were required for RuO$_2$ nanorod growth. In other papers [5], and explicitly in the present paper, it has been found that Au nanodots are not required and will not serve as the nucleation sites for the growth of RuO$_2$ NRs. In our previous communication [11] the following was stated:

> Once formed the RuO$_4$ molecules migrate across the wafer surface and nucleate to form RuO$_2$ clusters. The clusters grow very rapidly into square nanorods with a length of 1.4 $\mu$m and width of 30 nm at a substrate temperature of 600°C. This process occurs on a very short timescale, and may be regarded as nearly instantaneous.

We have remained baffled by what appeared to be an almost instantaneous formation of the RuO$_2$ NRs. In the earlier communication [11], it was also stated that the growth proceeds by the following:

> Some combination of thermal diffusion of surface species and an electrostatic trapping mechanism that collects sputtered Ru ions from the plasma beam.

Although adatom migration across the substrate surface is still assumed to contribute to the nutrient feed of Ru species to the developing NR, the electrostatic trapping or adatom contribution directly from the discharge was poorly defined and left as speculation.

Experimental evidence gathered in this paper now permits us to state that electrostatic trapping contributes directly
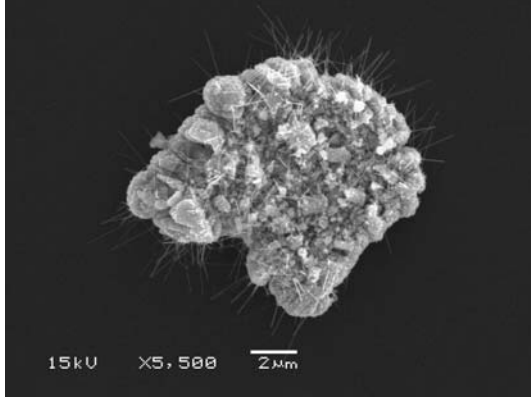
FIGURE 3: SEM image showing a piece of foreign matter decorated with RuO$_2$ NRs.

to the formation of RuO$_2$ NRs. It has been observed that dense nanorod formation originates on poorly connected fragments of foreign matter (FM) that clings onto the substrate. An SEM image of such an NR-decorated piece of FM is shown in Figure 3. It is safe to assume that pieces of FM are weakly bound to the substrate surface and therefore represent at best poor electrical connection to that substrate. Furthermore, movement of adatom species across the substrate surface and onto the object of FM is unlikely and made difficult by the required movement from the substrate surface up onto the FM particle. An electrostatic mediated collection of Ru species from the gas phase discharge is the only possibility.

Through a trial-and-error process, it was found that RuO$_2$ NRs grow easily on the following substrates: (a) Si wafer, (b) Al evaporation-coated Si, (c) polished Ti sheet, and (d) a Si$_3$N$_4$-coated Si wafer. SEM images of the RuO$_2$ NRs grown on these substrates are shown in Figure 4.

All of these substrates were highly polished, and it was initially assumed that this was affecting the surface mobility of the Ru adatoms that contributed to RuO$_2$ NR formation. The goal was to extend the above process to the growth of RuO$_2$ NRs on a stainless steel surface. Stainless steel substrates were tried, with both rough and smooth surface finishes, without effect [20]. On further consideration, the difference between the SS substrate and the group of substrates that gave successful results was the electrical resistance of the surface. In the case of the Si, Al, and Ti substrates, each of these elements reacts strongly with the oxygen contained in the air ambient and creates a surface of SiO$_2$, Al$_2$O$_3$, and TiO$_2$. The next step was to further verify that RuO$_2$ NRs could not be grown on conductive surfaces. A sampling of four different substrate materials unaffected by the oxygen-containing ambient was tried: (a) stainless steel, (b) stainless steel coated with RuO$_2$, (c) AZO on BSG (aluminum-doped zinc oxide on borosilicate glass), and (d) ITO on BSG (indium tin oxide on borosilicate glass). During the growth process, the top surface of the substrate was electrically grounded with a conducting stainless steel retaining clip. Each of these samples recorded a sheet resistance of $<1 \times 10^{-6}$ $\Omega$/cm$^2$. SEM images of these four

TABLE 1: Total resistance values.

| Electrode material | $R_{\text{total}}$ ($\Omega$) |
| --- | --- |
| Si | 1007 |
| Ti | 494 |
| Al | 381 |

substrate surfaces following a similar process sequence used to grow the RuO$_2$ NRs shown in Figure 4 are shown in Figure 5. There is a very low density of RuO$_2$ NRs present on these conductive surfaces. The few RuO$_2$ NRs that are present could be the result of insulating defects on these surfaces, perhaps resulting from FM or structural damage in the substrate surface.

The growth of the RuO$_2$ NRs on the Si, Al, and Ti surfaces can be explained as a consequence of the native oxide that exists on these substrate surfaces. Further confirmation that an insulating layer exists between the conducting RuO$_2$ NRs and the Si, Al-coated Si, and/or Ti substrates was obtained from an electrical resistance measurement of these three systems. Electrical contact to the top of the RuO$_2$ NR film was made with an electrolyte solution (KOH in water). The measured V-J curves for the RuO$_2$ NRs on these three different substrate materials are shown in Figure 6. The full curve in Figure 6 was used previously in a paper into the use of RuO$_2$ NR-coated electrodes as cathodes in the electrolysis of an aqueous solution of KOH [18].

The production of hydrogen at the cathode does not begin till a voltage less than $-0.5$ V is applied to the cathode. The portion of the V-J curve less than this value results from the electron and ion transport across the electrolyte and is shown in Figure 7.

The voltage drop measured from the solution to the substrate electrode is the result of resistive losses: (1) across the substrate, (2) at the oxide interface between the RuO$_2$ NR and the substrate surface, (3) across the RuO$_2$ NR length, and (4) at the interface between the RuO$_2$ NR and the liquid electrolyte. A circuit diagram representing this proposed model is sketched in Figure 8.

The total resistance for one NR, $r_{\text{total}}$, submerged in an electrolytic solution can be expressed with the following relationship:

$$r_{\text{total}} = r_{\text{sub}} + r_{\text{sub int oxide}} + r_{\text{NR}} + r_{\text{sol int}}. \tag{1}$$

The total resistance $R_{\text{total}}$ measured between the electrode substrate and the solution can be calculated from the slope of the V-J curves shown in Figure 7. The measured values are summarized in Table 1.

The resistance measured for the electrode fabricated with the Si substrate is higher than the other two, and this is a result of the higher resistivity of the Si substrate relative to Al and Ti substrates, which are assumed to be negligible. In the case of the Si electrode, with a resistivity of 50 $\Omega$ cm, there is a voltage drop across the substrate portion of the electrode, calculated to be 700 $\Omega$. The nanorods for all samples are approximately the same size and shape and are assumed to be of similar consistency. Therefore, the resistances for
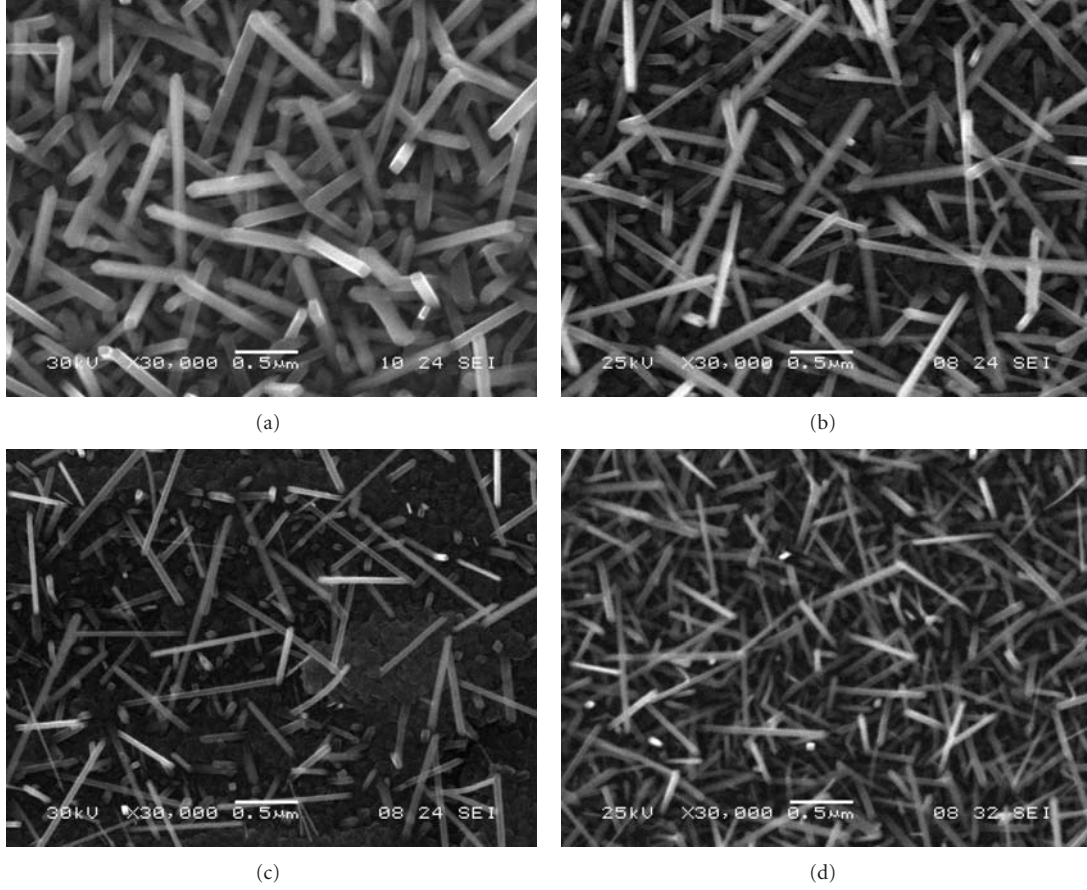
(a)



(b)



(c)



(d)

FIGURE 4: SEM images of $RuO_2$ nanorods grown on insulating substrates, including (a) Si, (b) Al-coated Si, (c) Ti, and (d) $Si_3N_4$-coated Si.

TABLE 2: Measured resistance (corrected for substrate).

| Material | $R_{\text{sub int oxide}} + R_{\text{sol int}}$ ($\Omega$) |
| --- | --- |
| Si | 307 |
| Ti | 494 |
| Al | 381 |

TABLE 3: Native oxide characteristics.

| Material | $T_{\text{ox}}$ (nm) | $\rho$ ($\Omega$ cm) | $r_{\text{sub int oxide}}$ ($\Omega$) |
| --- | --- | --- | --- |
| $SiO_2$ | 1 | $1 \times 10^{15}$ | $1 \times 10^8$ |
| $TiO_2$ | 8 | $1 \times 10^{10}$ | $8 \times 10^3$ |
| $Al_2O_3$ | 5 | $1 \times 10^{14}$ | $5 \times 10^7$ |

a nanorod, $r_{\text{NR}}$, should be the same in all cases and should be small with the resistivity of $\sim 40 \, \mu\Omega$ cm.

The relationship between the resistance measured experimentally $R_{\text{total}}$ and $r_{\text{total}}$ for an individual NR can be expressed as

$$\frac{1}{R_{\text{total}}} = N\left(\frac{1}{r_{\text{total}}}\right), \tag{2}$$

where $N$ is the surface density of $RuO_2$ NRs per cm$^2$. Using the above assumptions, the sum of measured resistances at the base of the nanorod connecting to the substrate $R_{\text{sub int oxide}}$ and at the interface with the electrolyte solution $R_{\text{sol int}}$ for the three samples is estimated to be as shown in Table 2.

All measured resistance values are reported per cm$^2$ of substrate or electrode area. It is assumed that an insulating film on the above substrates, that permitted the growth

of the $RuO_2$ NRs, is the characteristic native oxide layers commonly associated with these materials. Much is known about the native oxide layers on these material substrates, including thickness ($T_{\text{ox}}$) and resistivity ($\rho$) [21–23]. These characteristic values are summarized in Table 3.

Assuming these characteristic thickness and resistivity values for what was proposed as the nucleation sites for the $RuO_2$ NRs, the resulting resistance for conduction through a single nanorod would be the product of $T_{\text{ox}}$ and $\rho$. It is not possible herein to assign a specific portion of the total resistance value to either the contact resistance with the substrate or the electrolyte solution, but it is possible to assign an upper limit on either of these values. Assuming that the $r_{\text{sol int}} = 0 \, \Omega$, then the values given in Table 2 are equal to the resistance at the interface between the $RuO_2$ NR and its substrate, $R_{\text{sub int oxide}}$ per cm$^2$ of electrode area. The equivalent circuit for the NR-coated electrode is a parallel combination of resistance values assigned to
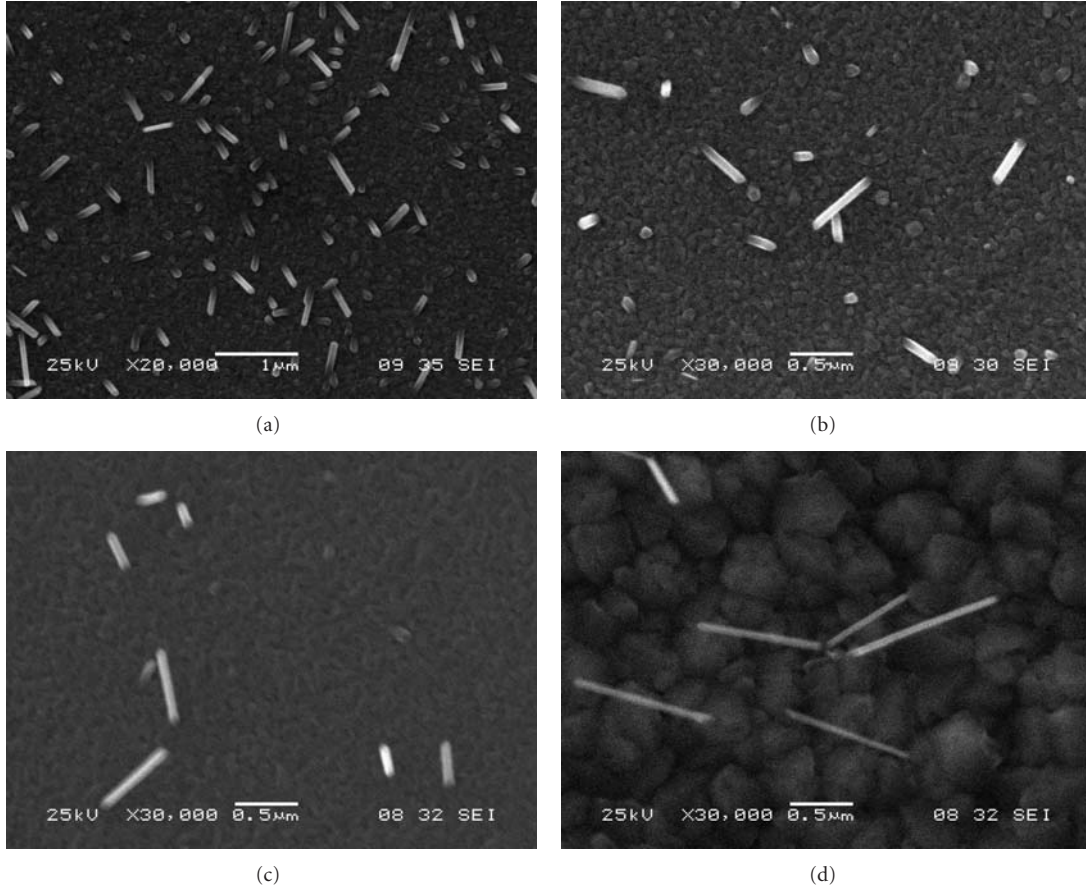
(a)



(b)



(c)



(d)

Figure 5: SEM images of RuO$_2$ nanorods grown on conducting substrates, including (a) stainless steel, (b) stainless steel coated with RuO$_2$, (c) AZO, and (d) ITO.

Table 4: Parallel combination of NRs.

| Material | $R_{\text{sub int oxide}} + R_{\text{sol int}}$ ($\Omega$) | $r_{\text{total}}$ ($\Omega$) | NR density (cm$^{-2}$) |
|---|---|---|---|
| Si | 307 | $1 \times 10^{15}$ | $3.2 \times 10^5$ |
| Ti | 494 | $1 \times 10^{10}$ | $1.6 \times 10^2$ |
| Al | 381 | $1 \times 10^{14}$ | $1.3 \times 10^5$ |

a single NR, $r_{\text{total}}$. The results of this analysis are organized in Table 4. The calculated surface density of nanorods by this analysis ia acceptable for the Si and Al/Si electrodes, but is an underestimation of those observed on the Ti substrate. The initial assumption that $r_{\text{sol int}} = 0 \, \Omega$ may be an oversimplification and may in fact be larger than $r_{\text{sub int oxide}}$. Further investigation into this discrepancy is required.

The plasma discharge in the ECR-enhanced sputter process that is used in the current investigation was the subject of an earlier study that used a Langmuir probe to characterize the physical nature of the plasma stream [24]. The electron temperature of the Ar discharge was found to be less than 2 eV. This value is physically credible and can be used to calculate other parameters that can describe the discharge used. It was proposed above that the growth

of the RuO$_2$ NRs occurs as a result of an electrostatic trapping phenomenon. A more complete description of this mechanism requires a proposed nucleation site that is electrically insulated from the grounded substrate. The nucleation site can consist of an island of insulating material on what can be a conducting substrate. In the case of the Si, Al/Si, and Ti substrates, this was accomplished by the formation of SiO$_2$, Al$_2$O$_3$, and TiO$_2$ nucleation sites. The RuO$_2$ NR will nucleate at this site and will be assisted by the fact that the conducting RuO$_2$ mass acts as a body that will attain the floating potential of the plasma discharge. A plasma discharge is a collection of an equal number of electrons and ions. The mass of the electrons is significantly less than that of the ions, and therefore, they travel at significantly higher velocities and will escape the plasma and charge any body in its vicinity. The conducting body as a result of this high-mobility electron flux will develop a negative bias with respect to ground, which is known as the floating potential, $V_f$. An expression relating the electron and ion temperatures and masses is shown as follows [24]:

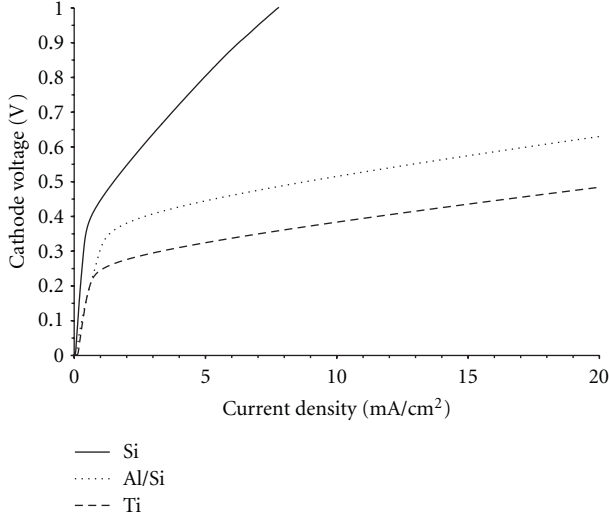$$V_f = -\frac{1}{2} T_e \ln\left(\frac{M T_e}{m T_i}\right), \tag{3}$$

FIGURE 6: Electrical characterization of RuO$_2$ NRs grown on Si, Al/Si, and Ti when used as cathode electrode in an electrolysis cell with an aqueous KOH electrolyte.
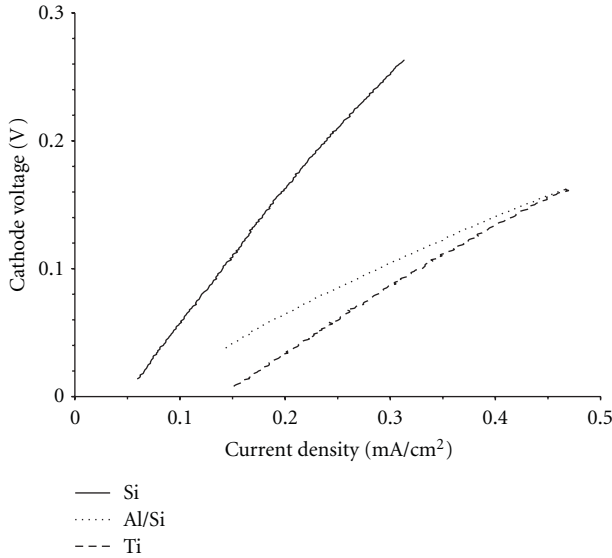


FIGURE 7: Electrical characterization of electrodes fabricated of RuO$_2$ NRs grown on Si, Al/Si, and Ti substrates. This is the low-voltage end of the curve shown in Figure 5 where the voltage is below the threshold for electrolysis.

where $V_f$ = floating potential (volts), $T_e$ = electron temperature (eV), $T_i$ = ion temperature (eV), $M$ = ion mass (kg), and $m$ = electron mass (kg).

The $V_f$ for the current system and operating conditions can be estimated to be equal to 7 to $8T_e$, or approximately 14 V [23, 24].

This result suggests that the RuO$_2$ NR nucleation site will be maintained at this floating potential, in the neighborhood of 14 V relative to ground, and this body will then electrically attract ions from the discharge to this site. In theory, the flux of ions will be equivalent to the flux of electrons to this
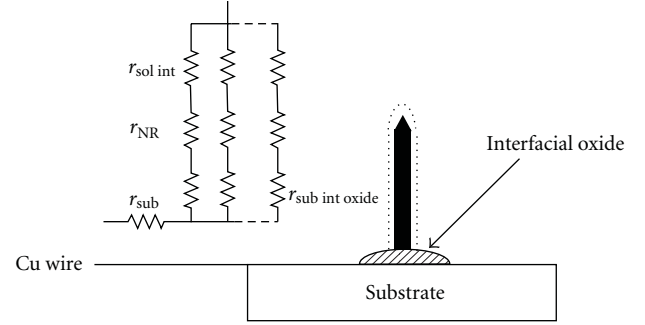


FIGURE 8: Sketch of the proposed circuit model for a single RuO$_2$ NR on the substrate surface in the electrolyte solution.
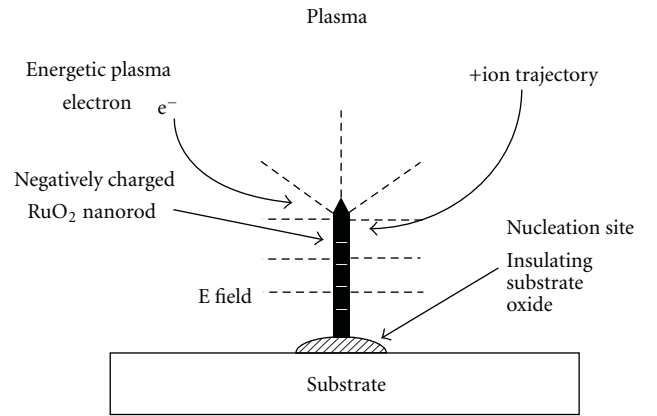


FIGURE 9: Proposed growth mechanism of conductive nanoparticles on insulating substrates.

nucleation site, also known as ambipolar diffusion, see the following [24]:

$$\Gamma_e = \Gamma_i = -\frac{D_i\mu_e + D_e\mu_i}{\mu_e + \mu_i}, \qquad (4)$$

where $\Gamma_e$, $\Gamma_i$ = electron and ion flux, respectively (particles/cm$^2 \cdot$ s), $D_e$, $D_i$ = electron and ion diffusion coefficient, respectively (cm$^2$/s), and $\mu_e$, $\mu_i$ = electron and ion mobilities, respectively (cm$^2$/V$\cdot$s).

These ionic species will represent the nutrient flux, which will feed the growth of the nanorods. It is the crystallographic orientation of the developing RuO$_2$ NR which will determine its shape and direction of growth. The electric field and/or electrical potential in the vicinity of the RuO$_2$ NR acts as an electrostatic trap for ions in the ECR plasma stream. This physical process has been represented in the sketch in Figure 9. The diameter of the RuO$_2$ NR during its initial stages of growth is very narrow and acts as an effective electrostatic trap. This can account for the observation that the RuO$_2$ NRs appear to nucleate instantaneously. Continued growth is a much slower process that involves surface migration across the substrate surface and up the NR surface.

## 4. Conclusions

The nucleation and growth of $RuO_2$ nanorods by the plasma-enhanced sputtering process require the existence of an electrically insulated substrate surface. The growth of the $RuO_2$ NRs on insulating surfaces was attributed to the collection of ionic Ru-containing species produced in the sputter process. The developing $RuO_2$ NR becomes negatively charged as a result of the escaping higher-mobility electrons from the gaseous discharge. The negatively charged $RuO_2$ NR then collects positively charged ionic Ru-containing species from the sputter discharge. This process has been observed to occur in less than a minute.

## Acknowledgments

## References

[1] C. M. Lieber, "One-dimensional nanostructures: chemistry, physics & applications," *Solid State Communications*, vol. 107, no. 11, pp. 607–616, 1998.

[2] Y. Xia, P. Yang, Y. Sun et al., "One-dimensional nanostructures: synthesis, characterization, and applications," *Advanced Materials*, vol. 15, no. 5, pp. 353–389, 2003.

[3] Z. R. Dai, Z. W. Pan, and Z. L. Wang, "Novel nanostructures of functional oxides synthesized by thermal evaporation," *Advanced Functional Materials*, vol. 13, no. 1, pp. 9–24, 2003.

[4] C. N. R. Rao and A. Govindaraj, *Nanotubes and Nanowires*, Royal Society of Chemistry, London, UK, 2005.

[5] Y. T. Lin, C. Y. Chen, C. P. Hsiung, K. W. Cheng, and J. Y. Gan, "Growth of $RuO_2$ nanorods in reactive sputtering," *Applied Physics Letters*, vol. 89, no. 6, Article ID 063123, 2006.

[6] C. S. Hsieh, G. Wang, D. S. Tsai, R. S. Chen, and Y. S. Huang, "Field emission characteristics of ruthenium dioxide nanorods," *Nanotechnology*, vol. 16, no. 9, pp. 1885–1891, 2005.

[7] S. Kim, N. Koratkar, T. Karabacak, and T. M. Lu, "Water electrolysis activated by Ru nanorod array electrodes," *Applied Physics Letters*, vol. 88, no. 26, Article ID 263106, 2006.

[8] M. Knapp, A. P. Seitsonen, Y. D. Kim, and H. Over, "Catalytic activity of the $RuO_2(100)$ surface in the oxidation of CO," *The Journal of Physical Chemistry B*, vol. 108, no. 38, pp. 14392–14397, 2004.

[9] C. S. Hsieh, D. S. Tsai, R. S. Chen, and Y. S. Huang, "Preparation of ruthenium dioxide nanorods and their field emission characteristics," *Applied Physics Letters*, vol. 85, no. 17, pp. 3860–3862, 2004.

[10] A. Korotcov, H. P. Hsu, Y. S. Huang, D. S. Tsai, and K. K. Tiong, "Growth and characterization of well-aligned $RuO_2$ nanocrystals on oxide substrates via reactive sputtering," *Crystal Growth and Design*, vol. 6, no. 11, pp. 2501–2506, 2006.

[11] M. W. Cross, W. J. Varhue, D. L. Hitt, and E. Adams, "Control of ruthenium oxide nanorod length in reactive sputtering," *Nanotechnology*, vol. 19, no. 4, Article ID 045611, 2008.

[12] Y. T. Lin, C. Y. Chen, C. P. Hsiung, K. W. Cheng, and J. Y. Gan, "Growth of $RuO_2$ nanorods in reactive sputtering," *Applied Physics Letters*, vol. 89, no. 6, Article ID 063123, 2006.

[13] K. W. Cheng, Y. T. Lin, C. Y. Chen et al., "In situ epitaxial growth of $TiO_2$ on $RuO_2$ nanorods with reactive sputtering," *Applied Physics Letters*, vol. 88, no. 4, Article ID 043115, pp. 1–3, 2006.

[14] J. Gatineau, K. Yanagita, and C. Dussarrat, "A new $RuO_4$ solvent solution for pure ruthenium film depositions," *Microelectronic Engineering*, vol. 83, no. 11-12, pp. 2248–2252, 2006.

[15] P. Bunt, W. J. Varhue, E. Adams, and S. Mongeon, "Initial stages of growth of heteroepitaxial yttria-stabilized zirconia films on silicon substrates," *Journal of the Electrochemical Society*, vol. 147, no. 12, pp. 4541–4545, 2000.

[16] M. W. Cross and W. J. Varhue, "Radiative melting of crystalline ruthenium oxide nanorods," *Nanotechnology*, vol. 19, no. 43, Article ID 435705, 2008.

[17] M. Cross, M. Stewart, K. Pelletier, and W. Varhue, "$RuO_2$ nanorod coated cathode for the electrolysis of water," *International Journal of Hydrogen Energy*, vol. 37, pp. 2166–2172, 2012.

[18] G. Wang, C. S. Hsieh, D. S. Tsai, R. S. Chen, and Y. S. Huang, "Area-selective growth of ruthenium dioxide nanorods on $LiNbO_3$ (100) and Zn/Si substrates," *Journal of Materials Chemistry*, vol. 14, no. 24, pp. 3503–3508, 2004.

[19] K. Pelletier, *$RuO_2$ nanorod growth dependence on substrate material and process conditions [M.S. thesis]*, University of Vermont, Burlington, VT, USA, 2009.

[20] E. McCafferty and J. P. Wightman, "An X-ray photoelectron spectroscopy sputter profile study of the native air-formed oxide film on titanium," *Applied Surface Science*, vol. 143, no. 1, pp. 92–100, 1999.

[21] M. Morita, T. Ohmi, E. Hasegawa, M. Kawakami, and M. Ohwada, "Growth of native oxide on a silicon surface," *Journal of Applied Physics*, vol. 68, no. 3, pp. 1272–1281, 1990.

[22] K. Gloos, P. J. Koppinen, and J. P. Pekola, "Properties of native ultrathin aluminium oxide tunnel barriers," *Journal of Physics Condensed Matter*, vol. 15, no. 10, pp. 1733–1746, 2003.

[23] J. S. Lille, P. E. McGaughnea, and W. J. Varhue, "Parameter space map of an electron cyclotron resonance plasma in a compact chamber," *IEEE Transactions on Plasma Science*, vol. 29, no. 3, pp. 417–423, 2001.

[24] J. R. Roth, *Industrial Plasma Engineering: Volume 1—Principles*, Institute of Physics Publishing, Philadelphia, Pa, USA, 1995.

*Research Article*

# Fabrication of Highly Rough Ag Nanobud Substrates and Surface-Enhanced Raman Scattering of $\lambda$-DNA Molecules

**Chuyun Deng, Wanyun Ma, and Jia-Lin Sun**

*State Key Lab of Low-Dimensional Quantum Physics, Department of Physics, Tsinghua University, Beijing 100084, China*

Correspondence should be addressed to Jia-Lin Sun, jlsun@tsinghua.edu.cn

Raman scattering signals can be enhanced by several orders of magnitude on surface-enhanced Raman scattering (SERS) substrates made from noble metal nanostructures. Some SERS substrates are even able to detect single-molecule Raman signals. A novel silver nanobud (AgNB) substrate with superior SERS activity was fabricated with a solid-state ionics method. The AgNB substrate was formed by tightly collocated unidirectional 100 nm size silver buds, presenting a highly rough surface topography. Distinct SERS signals of single $\lambda$-DNA molecules in water were detected on AgNB substrates. AgNB substrates were compared with disordered silver nanowire (AgNW) substrates manufactured by the same method through the SERS detection of $\lambda$-DNA solutions. This original AgNB substrate provides a reliable approach towards trace analysis of biomacromolecules and promotes the utilization of the SERS technique in biomedical research.

## 1. Introduction

Raman scattering is a characterization technique that provides fingerprint recognition by molecular vibrational and rotational energy levels indicated by the Raman peaks. Raman spectroscopy is especially suitable for biomedical studies because of its advantages in nondestructive detection, rich configuration information, easy sample preparation, and freedom from interference by water. Many applications of Raman spectroscopy in DNA, RNA, and protein research have been reported [1–5]. In recent decades, noble metal nanostructures have been discovered to have good Raman scattering enhancement ability. According to electromagnetic theories, external light can polarize free electrons on noble metal nanostructured surfaces and thereby cause vibration of the entire free surface electrons. When the frequency of external light matches that of the surface electron vibration, local charge distribution will be affected and the local field will be strongly enhanced due to surface plasmon resonance (SPR) phenomenon. For molecules adsorbed on such noble metal nanostructures, their Raman signals will be markedly intensified by SPR effects [6]. It was reported that silver nanostructure surfaces exhibited surface-enhanced Raman spectra of adsorbed molecules by several orders of magnitude and, in some cases, single-molecule Raman signals could be detected. Hence, surface-enhanced Raman scattering (SERS) substrates based on silver nanostructures have been widely employed in chemical and biomedical detection [7–14]. A large amount of outstanding metal nanostructures have been fabricated by our solid-state ionics method [15–17]. Among them a highly rough unidirectional silver nanobud (AgNB) structure has excellent SERS activity. In this work, the SERS activity of AgNBs is established by detecting the Raman signal of $\lambda$-DNA on AgNB substrate at the single-molecule level.

## 2. Materials and Methods

*2.1. Fabrication of AgNB Structures.* Our solid-state ionics method is based on the ion-conducting ability of superionic conductor thin films that are comparable to molten salts or electrolyte solutions. The superionic conductor thin film was designed as the medium to transport metal ions between metal electrodes and generate a directional ionic current. Metal atoms at the anode were ionized by the external direct current (DC) electric field and transported to the cathode through the superionic conductor thin film to grow into various nanostructured materials [15–17].

The preparation process for highly rough silver nanostructures is shown in **Figure 1**. Thin silver films of $1\,\mu m$ thickness were deposited onto two sides of a clean quartz substrate to serve as the electrodes. The interelectrode distance was 8 cm. A piece of $RbAg_4I_5$ superionic conductor thin film, about 400 nm thick with a $0.12\,\Omega^{-1}\,cm^{-1}$ ionic conductivity at room temperature, was deposited onto the whole surface of the quartz substrate as the ion-conducting medium [17]. All deposition processes were conducted at room temperature and $10^{-4}$ Pa vacuum. The external DC electric field with a constant electric current was provided by a SourceMeter (Keithley 2400, USA). Silver atoms at the anode were ionized and transported to the cathode to grow into AgNB structures through the $RbAg_4I_5$ thin film, while electrons were transported to the cathode through external conducting wires. After 3 days, silver nanostructures of square centimeter size were obtained in the cathode area. Such silver nanostructures were composed of tightly collocated 100 nm sized units as revealed by scanning electron microscopy (SEM) (**Figure 2(a)**). The 100 nm sized units were arranged like nanoscale buds growing in the same direction, leading to a highly rough surface topography, and these silver nanostructures were termed silver nanobuds (AgNBs).

The external constant electric current or, rather, the ionic current density in the $RbAg_4I_5$ thin film is the crucial parameter in the fabrication of silver nanostructures. The growth of silver nanostructures is maintained by continuous and stable ionic current as a result of the external constant electric field. Different nanostructures will be obtained as the intensity of external electric current changes. The external electric current was $12\,\mu A$ in the growth of AgNBs with unidirectional and dense configuration (**Figure 2(a)**). However, when the external electric current was decreased to $3\,\mu A$, disordered and loose silver nanowires (AgNWs) were obtained (**Figure 2(b)**). The AgNBs were made of silver according to energy dispersive spectroscopy (EDS) analysis (**Figure 2(c)**).

*2.2. Experimental Setup for SERS Analysis.* The detection of $\lambda$-DNA on AgNB substrates was carried out on a confocal Raman spectrometer (Renishaw RM2000, UK). The excitation light was a focused $Ar^+$ laser (excitation wavelength 514 nm, focal area $\sim 5\,\mu m \times 5\,\mu m$ with a $20\times$ objective). The exposure time was 20 s and the detection range was $400\text{–}2000\,cm^{-1}$. **Figure 3** illustrates the sample preparation. As-grown AgNBs were fixed on a clean slide as the SERS substrate, and a $10\,\mu L$ drop of $\lambda$-DNA (Beijing Huamei Scientific Co., China) water solution was added onto the AgNBs, followed by placement of a clean 24 mm $\times$ 24 mm coverslip of 0.17 mm thickness on the slide to seal the $\lambda$-DNA solution. Generally there would be a little spillage of the solution. The incident laser was directed vertically down and laser power on the sample was 4.7 mW during the analysis.

Six $\lambda$-DNA concentrations (50, 20, 10, 1, 0.1, and $0.01\,ng/\mu L$) were examined. The average amount of $\lambda$-DNA in the detection area for each solution was estimated from the $\lambda$-DNA concentrations, the solution volume (slightly
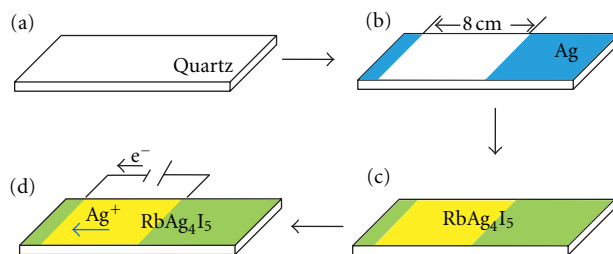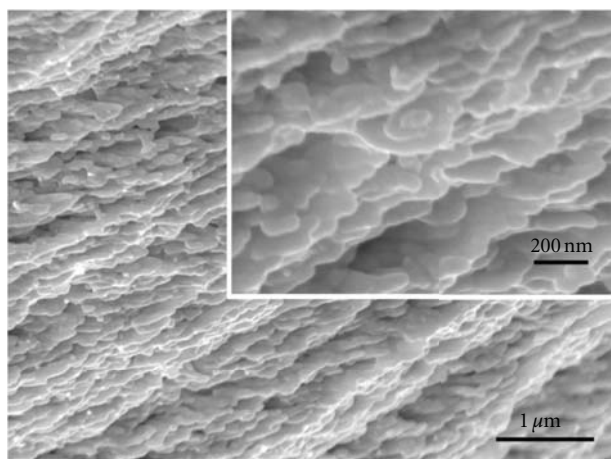


FIGURE 1: Fabrication of AgNB structures by superionic conductor thin film. (a) Clean quartz substrate was placed in the deposition chamber at room temperature and $10^{-4}$ Pa vacuum. (b) $1\,\mu m$ thick thin silver films were deposited on the quartz substrate as the electrodes. The distance between two electrodes was 8 cm. (c) 400 nm thick $RbAg_4I_5$ superionic conductor thin film was deposited on the whole substrate as the ion-conducting medium. (d) A constant electric current was provided as the external electric field to form a directional ionic current. Silver atoms at the anode were ionized and transported to the cathode to grow into AgNB structures through the $RbAg_4I_5$ thin film, while electrons were transported to the cathode through external conducting wires.

smaller than $10\,\mu L$ due to the spillage), the surface area of the coverslip (24 mm $\times$ 24 mm) and the focal area of the laser ($\sim 5\,\mu m \times 5\,\mu m$). For the $0.1\,ng/\mu L$ solution, the average number of $\lambda$-DNA molecules in the detection area was less than 0.8. This result indicated that the 0.1, $0.01\,ng/\mu L$ solutions were capable of revealing whether the AgNB substrate had single-molecule level SERS activity. The spectra of the AgNB substrate itself and a $20\,ng/\mu L$ $\lambda$-DNA solution on clean glass substrate without AgNB were also analyzed as controls.

## 3. Results and Discussion

SERS spectra of the six samples and two control groups are shown in **Figure 4**. No evident peak was seen in the red curve of $\lambda$-DNA-only control, whereas several distinct peaks were exhibited by the $20\,ng/\mu L$ sample, for example, at 979, 1380, and $1594\,cm^{-1}$. Such a difference provided evidence of a remarkable enhancement from the AgNB substrate. The 0.1 and $0.01\,ng/\mu L$ solutions shared common features, including the quantity and intensities of characteristic peaks, distinguishing them from other four samples. According to the estimation result, these two groups both represented single-molecule signals, and hence the single-molecule level SERS activity of AgNB substrates has been demonstrated.

Information on secondary structures, backbone conformations and phosphate group interactions are indicated in the Raman spectra of DNA molecules. Strong and distinct characteristic peaks were all labeled in **Figure 4** and their tentative assignments were presented in **Table 1**. Common peaks of the six solutions are approximately at 890, 1045, 1161, 1380, 1456, 1596, and $1694\,cm^{-1}$. The 890, 1161, and $1456\,cm^{-1}$ peaks reflect vibrational and deformation modes of deoxyribose. The $1045\,cm^{-1}$ peak represents the phosphate group interaction, and those at 1380, 1596 and $1694\,cm^{-1}$ correspond to thymine, adenine and guanine (T, A, G) [18–23]. In addition, there are two more common

(a)
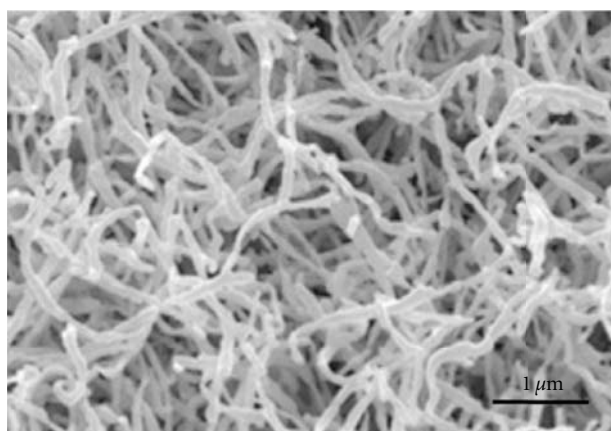


(b)
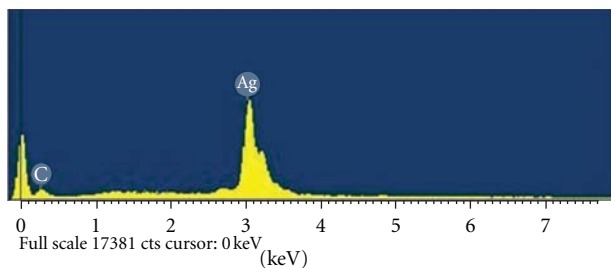


(c)

FIGURE 2: SEM and EDS analyses of AgNB structures. (a) SEM image of AgNB structures (the external electric current is $12\,\mu$A in the fabrication process). AgNB structures were highly rough, dense, and unidirectional, composed of tightly collocated 100 nm sized units like nanoscale buds growing in the same direction. (b) SEM image of AgNW structures with disordered and loose configuration obtained by decreasing the external electric current to $3\,\mu$A in the fabrication process. (c) EDS analysis of AgNB structures.

peaks at 1000 and 1260 cm$^{-1}$ for the 10, 1, 0.1, and 0.01 ng/$\mu$L samples. Moreover, the single-molecule samples (0.1 and 0.01 ng/$\mu$L) share another two peaks at 1285 cm$^{-1}$ and 1486 cm$^{-1}$. The 20 and 50 ng/$\mu$L, samples of higher concentration have fewer common features with the four solutions of lower concentration. We conclude that the differences between these samples are mainly attributed
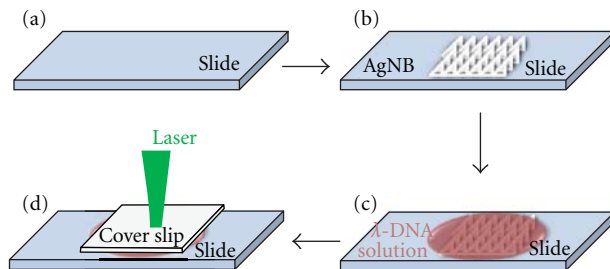


FIGURE 3: Preparation of $\lambda$-DNA samples on AgNB substrates. As-grown AgNBs were fixed on a clean slide as the SERS substrate, and then a $10\,\mu$L drop of $\lambda$-DNA water solution was added onto the AgNBs, thereafter a clean 24 mm $\times$ 24 mm coverslip of 0.17 mm thickness was placed on the slide to seal the $\lambda$-DNA solution. The incident laser was directed vertically down for the analysis.
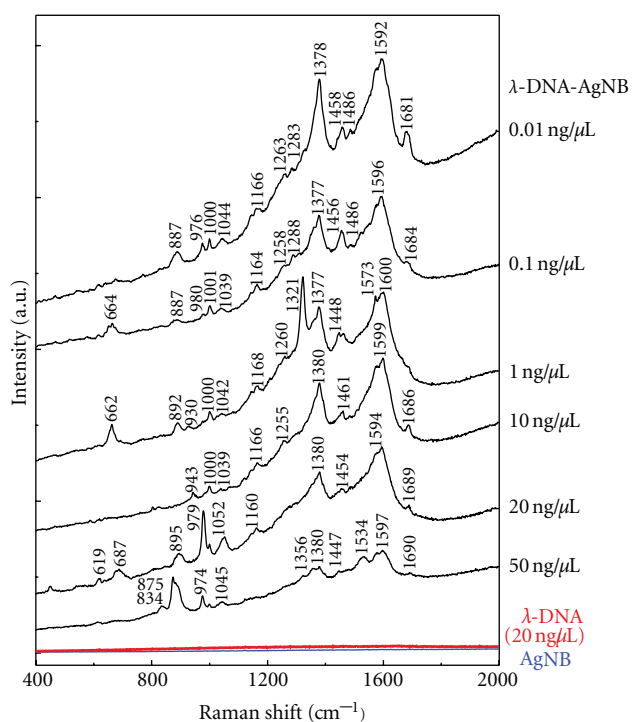


FIGURE 4: SERS spectra of six $\lambda$-DNA-AgNB samples (black) and two control samples (red and blue). The red spectrum was for 20 ng/$\mu$L $\lambda$-DNA solution on a clean glass substrate without AgNB. The blue spectrum was for the AgNB substrate itself. The laser power on the sample was 4.7 mW and the exposure time was 20 s.

to changing spatial configurations of long strand DNA molecules in water. At low concentration, the interactions between $\lambda$-DNAs are weaker, allowing $\lambda$-DNA molecules to freely extend and therefore the more similar are the Raman spectra. At higher concentration, the interactions between $\lambda$-DNAs are stronger, $\lambda$-DNA molecules are more likely to condense, markedly affecting the Raman spectra. The low concentration samples are able to display detection of a freely extended single $\lambda$-DNA molecule.

The disordered AgNW structures in Figure 2(b) are not comparable to the AgNB structures in respect of SERS

TABLE 1: Tentative assignments for SERS spectra of λDNAs on AgNB substrate.

| λDNA concentration | | | | | | Tentative assignment[a,b] |
|---|---|---|---|---|---|---|
| 50 ng/μL | 20 ng/μL | 10 ng/μL | 1 ng/μL | 0.1 ng/μL | 0.01 ng/μL | |
| | 687 | | 662 | 664 | | G |
| 834 | | | | | | $PO_2^-$ |
| 875 | 895 | 943 | 892, 930 | 887 | 887 | Deoxyribose |
| 974 | 979 | 1000 | 1000 | 980, 1001 | 976, 1000 | Deoxyribose |
| 1045 | 1052 | 1039 | 1042 | 1039 | 1044 | $PO_2^-$ |
| | 1161 | 1166 | 1168 | 1164 | 1166 | Deoxyribose |
| | | 1255 | 1260 | 1258 | 1263 | T, C, A |
| | | | 1288 | 1283 | | C, A |
| 1356 | | | 1321 | | | A, G |
| 1380 | 1380 | 1380 | 1377 | 1377 | 1378 | T, A, G |
| 1447 | 1454 | 1461 | 1448 | 1456,1486 | 1458,1486 | Deoxyribose, $CH_2$ |
| 1534 | | | | | | A |
| 1597 | 1594 | 1599 | 1573,1600 | 1596 | 1592 | A, G |
| 1690 | 1689 | 1686 | | 1684 | 1681 | T |

[a] Based on [18–23]. [b] A: adenine; G: guanine; C: cytosine; T: thymine.
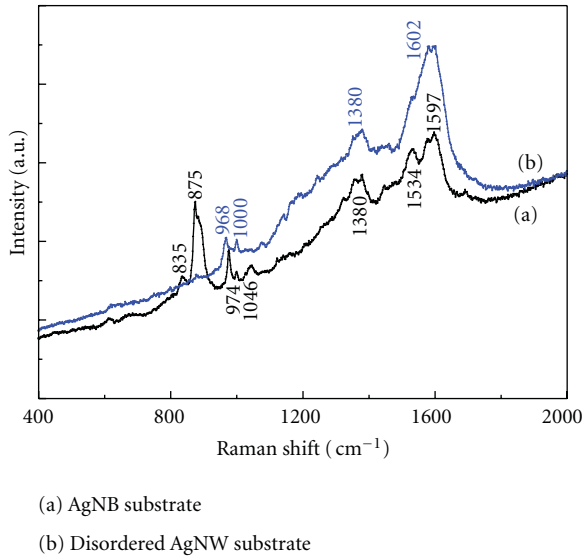


(a) AgNB substrate

(b) Disordered AgNW substrate

FIGURE 5: SERS spectra of λ-DNA samples (50 ng/μL) on the AgNB substrate (a) and on the disordered AgNW substrate (b). Characteristic peaks of λ-DNA on the AgNB substrate were more distinguishable than those on the disordered AgNW substrate, with relatively high intensity and low fluorescence background.

activity. Spectra of λ-DNA samples (50 ng/μL) on the AgNB substrate and on the disordered AgNW substrate are displayed in Figure 5. The characteristic peaks of λ-DNA on the AgNB substrate were more distinguishable than those on the disordered AgNW substrate, with relatively high intensity and low fluorescence background. In addition, the spectrum obtained on the AgNB substrate had seven distinct peaks, while that found with the disordered AgNW substrate only had four.

SERS activity is strongly dependent on the surface topography of the substrate. It is demonstrated in hot-spot theories that the localized field enhancement is more intense with more hot-spots on the surface of noble metal materials, and so the amount of hot-spots is related to SERS activity [24–27]. The AgNB substrate has nanoscale roughness and a unidirectional dense structure, making it a perfect environment for hot-spots and the generation of significant localized field enhancements. The disordered AgNW substrate only has microscale roughness and a loose structure, precluding the generation of sufficient hot-spots to bring about comparable SERS activity. The results demonstrate that most of the excitation energy was transferred into Raman scattering of detected molecules on the AgNB substrate through SPR effects, and the signal-to-noise ratio was heightened.

## 4. Conclusions

In this letter, we have reported a highly rough and unidirectional AgNB substrate with excellent SERS activity. We have shown that AgNB substrates are capable of detecting λ-DNA at the single-molecule level, and discussed the SERS spectra of λ-DNA molecules. We have also demonstrated that such dense and unidirectional AgNB structures are better SERS substrates than similarly made loose and disordered AgNW structures. This novel AgNB substrate is associated with a much lower detection limit than former SERS substrates, providing an efficient and reliable approach for biomedical analysis.

## Acknowledgments

# References

[1] Y. W. C. Cao, R. Jin, and C. A. Mirkin, "Nanoparticles with Raman spectroscopic fingerprints for DNA and RNA detection," *Science*, vol. 297, no. 5586, pp. 1536–1540, 2002.

[2] R. Tuma, "Raman spectroscopy of proteins: from peptides to large assemblies," *Journal of Raman Spectroscopy*, vol. 36, no. 4, pp. 307–319, 2005.

[3] G. Haran, "Single-molecule raman spectroscopy: a probe of surface dynamics and plasmonic fields," *Accounts of Chemical Research*, vol. 43, no. 8, pp. 1135–1143, 2010.

[4] J. H. Kim, M. Kataoka, D. Shimamoto et al., "Raman and fluorescence spectroscopic studies of a DNA-dispersed double-walled carbon nanotube solution," *ACS Nano*, vol. 4, no. 2, pp. 1060–1066, 2010.

[5] C. Mallidis, J. Wistuba, B. Bleisteiner et al., "In situ visualization of damaged DNA in human sperm by Raman microspectroscopy," *Human Reproduction*, vol. 26, no. 7, pp. 1641–1649, 2011.

[6] J. Gersten and A. Nitzan, "Electromagnetic theory of enhanced Raman scattering by molecules adsorbed on rough surfaces," *The Journal of Chemical Physics*, vol. 73, no. 7, pp. 3023–3027, 1980.

[7] K. Kneipp, Y. Wang, H. Kneipp et al., "Single molecule detection using surface-enhanced Raman scattering (SERS)," *Physical Review Letters*, vol. 78, no. 9, pp. 1667–1670, 1997.

[8] S. Nie and S. R. Emory, "Probing single molecules and single nanoparticles by surface-enhanced Raman scattering," *Science*, vol. 275, no. 5303, pp. 1102–1106, 1997.

[9] H. Xu, E. J. Bjerneld, M. Käll, and L. Börjesson, "Spectroscopy of single hemoglobin molecules by surface enhanced Raman scattering," *Physical Review Letters*, vol. 83, no. 21, pp. 4357–4360, 1999.

[10] M. Kahl and E. Voges, "Analysis of plasmon resonance and surface-enhanced Raman scattering on periodic silver structures," *Physical Review B*, vol. 61, no. 20, pp. 14078–14088, 2000.

[11] K. Kneipp, H. Kneipp, and J. Kneipp, "Surface-enhanced raman scattering in local optical fields of silver and gold nanoaggregates-from single-molecule raman spectroscopy to ultrasensitive probing in live cells," *Accounts of Chemical Research*, vol. 39, no. 7, pp. 443–450, 2006.

[12] E. J. Blackie, E. C. Le Ru, and P. G. Etchegoin, "Single-molecule surface-enhanced raman spectroscopy of nonresonant molecules," *Journal of the American Chemical Society*, vol. 131, no. 40, pp. 14466–14472, 2009.

[13] J. A. Dieringer, K. L. Wustholz, D. J. Masiello et al., "Surface-enhanced Raman excitation spectroscopy of a single rhodamine 6G molecule," *Journal of the American Chemical Society*, vol. 131, no. 2, pp. 849–854, 2009.

[14] S. Rao, S. Raj, S. Balint et al., "Single DNA molecule detection in an optical trap using surface-enhanced Raman scattering," *Applied Physics Letters*, vol. 96, no. 21, Article ID 213701, 2010.

[15] Y. Cao, H. S. Sun, J. L. Sun, G. Y. Tian, Z. Xing, and J. H. Guo, "Preparation and structural characterization of superionic conductor RbAg4I5 crystalline grain film," *Chinese Physics Letters*, vol. 20, no. 5, pp. 756–758, 2003.

[16] S. Shi, J. Sun, G. Zhang, J. Guo, and Z. Wang, "The growth of thin silver nanowires bundle using RbAg4I 5 crystal grain thin film and the ionic conductivity of the thin film," *Physica B*, vol. 362, no. 1–4, pp. 266–270, 2005.

[17] J. L. Sun, J. H. Zhang, W. Liu et al., "Shape-controlled synthesis of silver nanostructures," *Nanotechnology*, vol. 16, no. 10, pp. 2412–2414, 2005.

[18] W. L. Peticolas, "Raman spectroscopy of DNA and proteins," *Methods in Enzymology*, vol. 246, pp. 389–416, 1995.

[19] H. Deng, V. A. Bloomfield, J. M. Benevides, and G. Thomas, "Dependence of the Raman signature of genomic B-DNA on nucleotide base sequence," *Biopolymers*, vol. 50, no. 6, pp. 656–666, 1999.

[20] H. Wei and H. Xu, "Surface-enhanced Raman scattering of $\lambda$-DNA," *Applied Physics A*, vol. 89, no. 2, pp. 273–275, 2007.

[21] J. De Gelder, K. De Gussem, P. Vandenabeele, and L. Moens, "Reference database of Raman spectra of biological molecules," *Journal of Raman Spectroscopy*, vol. 38, no. 9, pp. 1133–1147, 2007.

[22] L. L. Sun, Y. J. Sun, F. G. Xu et al., "Atomic force microscopy and surface-enhanced raman scattering detection of DNA based on DNA-nanoparticle complexes," *Nanotechnology*, vol. 20, no. 12, Article ID 125502, 2009.

[23] C. M. Muntean, N. Leopold, A. Halmagyi, and S. Valimareanu, "Surface-enhanced Raman spectroscopy of DNA from leaves of in vitro grown apple plants," *Journal of Raman Spectroscopy*, vol. 42, no. 4, pp. 844–850, 2011.

[24] A. M. Michaels, J. Jiang, and L. Brus, "Ag Nanocrystal Junctions as the Site for Surface-Enhanced Raman Scattering of Single Rhodamine 6G Molecules," *Journal of Physical Chemistry B*, vol. 104, no. 50, pp. 11965–11971, 2000.

[25] J. Margueritat, H. Gehan, J. Grand et al., "Influence of the number of nanoparticles on the enhancement properties of surface-enhanced raman scattering active area: sensitivity versus repeatability," *ACS Nano*, vol. 5, no. 3, pp. 1630–1638, 2011.

[26] A. Lee, G. F. S. Andrade, A. Ahmed et al., "Probing dynamic generation of hot-spots in self-assembled chains of gold nanorods by surface-enhanced raman scattering," *Journal of the American Chemical Society*, vol. 133, no. 19, pp. 7563–7570, 2011.

[27] N. J. Borys and J. M. Lupton, "Surface-enhanced light emission from single hot spots in tollens reaction silver nanoparticle films: linear versus nonlinear optical excitation," *Journal of Physical Chemistry C*, vol. 115, no. 28, pp. 13645–13659, 2011.

*Research Article*

# Diffusion-Controlled Solid-State Formation of CoSb Phase from Co/Sb-Multilayered Nanowires

## Seong Gi Jeon,[1] Ho Sun Shin,[2] Jin Yu,[1] and Jae Yong Song[2, 3]

[1] *Department of Materials Science and Engineering, Korea Advanced Institute of Science and Technology, Daejeon 305-701, Republic of Korea*
[2] *Center for Nanocharacterization, Korea Research Institute of Standards and Science, Daejeon 305-340, Republic of Korea*
[3] *Department of Nano Science, University of Science and Technology, Daejeon 305-350, Republic of Korea*

Correspondence should be addressed to Jae Yong Song, jysong@kriss.re.kr

The physical properties of materials on a nanometer scale are known to be different from those of bulk form due to dimensional confinement effects and high specific surface-to-volume ratio. In this study, the size effects on the diffusion and reaction at the interface of dissimilar nanowires (NWs) were investigated. Co/Sb-multilayered NWs of $15 \pm 1$ and $19 \pm 2$ nm in radius have been grown within anodic aluminum oxide templates using a pulsed potentiodynamic electrodeposition method. XRD and TEM results demonstrated that the multilayered NWs were transformed to a CoSb phase through a solid-state reaction at the temperature in the range of 653 to 693 K. The kinetics of the solid-state reaction was analyzed and found to be diffusion controlled at the interface between Co and Sb phases. The reaction was controlled by the dominant diffusion of Sb atoms. The activation energies for the solid-state reaction were estimated to be 0.9 and 0.7 eV/atom for the multilayered NWs with radii of 15 and 19 nm, respectively.

## 1. Introduction

Synthesis of one-dimensional nanomaterials is a rapidly growing research area with applications in energy generating, energy storage, and environmental sensing [1]. It is well-known that materials on a nanometer scale have exceptional physical/chemical properties in comparison with the bulk form. To date, a number of studies have examined the size effects on surface energies [2], elastic moduli [3, 4], melting temperatures [5], superconductivity [6], and lattice deformation [7, 8] for nanowires (NWs). The size-dependent properties are due to the dimensional confinement, high surface-to-volume ratio, and surface relaxation related to imperfection of coordination number on the surface [9].

In a similar vein, the metallurgical phenomena of phase transformation, solid-state diffusion, and melting behavior can be affected by the size effects because the high surface-to-volume ratio can enhance the atomic mobility at the surface with certain imperfect coordination number [10, 11]. Recently, it has been reported that phase transformation

and solid-state diffusion on a nanometer scale are greatly influenced by confined-nanoscale geometry [12–14].

Template-based electrochemical synthesis of NWs is generally used because this process has several merits of controlling the diameter of NWs, low cost, and large-area deposition. Recently, pulsed electrochemical deposition has been used to control the composition of alloy deposits within templates [15–18].

We selected Co and Sb in order to investigate the solid-state reaction in the form of NWs because the reaction between Co and Sb can result in the formation of several stoichiometric compounds such as CoSb, $CoSb_2$, and $CoSb_3$; these compounds have attracted much attention in the fields of secondary Li-ion batteries and thermoelectric devices [19, 20], because a vertical configuration of one-dimensional nanostructure offers distinct benefits over a lateral configuration in its utilization of a high specific surface area. As an anode of secondary Li-ion batteries, the small radius of NWs allows for better accommodation of large-volume changes without the initiation of fracture. And the high

(a)                                          (b)                                          (c)
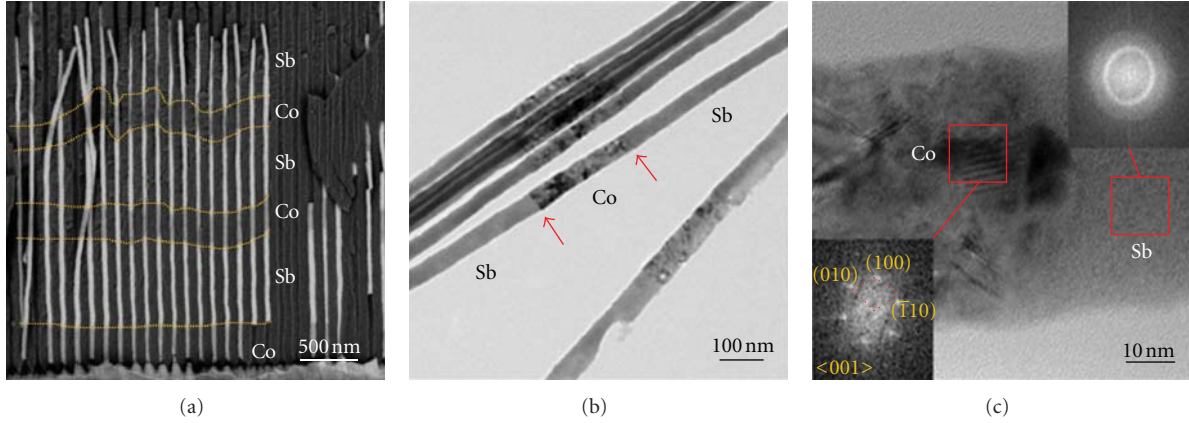
FIGURE 1: (a) SEM image, (b) bright field TEM image, and (c) HR-TEM image at the interface between Co and Sb segments of Co/Sb-multilayered nanowires ($r_{NW}$ = 15 nm). The insets denote the FFT images of the marked areas.

specific surface area of NWs can contribute to the lowering of the lattice thermal conductivity and the enhancement of thermoelectric figure of merit [19].

In this study, we investigated an alternative growth method of a Co and Sb NW array using pulsed potentio-dynamic electrodeposition based on the different reduction potentials of Co and Sb cations. The diffusion-controlled solid-state reaction, confined in a cross-sectional area of several tens of nanometers, was analyzed.

## 2. Experimental Procedure

Anodic aluminum oxide (AAO) templates were synthesized on Al foil (99.99%) by a two-step anodization process in 0.3 M oxalic acid (40 V) at 274 K. Then, the remaining Al foil was removed in an etching solution composed of 0.1 M $CuCl_2$ and 20 wt% HCl. The barrier layer of the AAO template was removed in 0.5 M $H_3PO_4$ solution at 303 K for the following electrodeposition process. A 150 nm thick Au layer was deposited on one side of the AAO template using an RF sputtering system; this layer served as a working electrode in the electrochemical deposition process. Using a pore-widening process [5], we fabricated two AAO templates with a pore radius of 15 ± 1 and 19 ± 2 nm. The detailed procedures of preparing the AAO templates can be found in previous reports [5, 8].

Electrodeposition was carried out using a potentio/galvanostat (Solartron 1280z) as a power source with a three-electrode setup; a saturated Ag/AgCl electrode as a reference; a Pt wire as a counter electrode; an AAO as a working electrode. The electrolyte (pH 1.5) for the electrodeposition of Co/Sb-multilayered NWs was composed of 0.1 M $CoSO_4 \cdot 7H_2O$, 0.01 M $SbCl_3$, and 0.14 M tartaric acid. We consecutively conducted alternative electrodepositions of Co and Sb for the multilayered Co/Sb NWs in the pulsed potentiodynamic mode. We used reduction potentials ($V_R$) of −1.3 and −0.8 V (versus saturated Ag/AgCl) for the growth of Co and Sb segments, respectively. When changing the $V_R$ to −1.3 and −0.8 V, Co and Sb phases, respectively, were deposited onto the AAO templates. From

SEM observation, the respective growth rates of Co and Sb NWs were experimentally determined to be 10 and 2 nm·s⁻¹.

The NWs in the AAO templates were heat treated in a vacuum of $4 \times 10^{-6}$ Torr in a temperature range of 653 to 693 K. A field-emission scanning electron microscope (SEM, Hitachi S4800), X-ray diffractometer (XRD, Rigaku, D/MAX-RC, 12 kW), and transmission electron microscope (TEM, Tecnai G2 F30, 300 kV) were used to analyze the crystal structures and morphologies of the multilayered NWs before and after the heat treatment. For the purpose of TEM characterization, the AAO structure was dissolved in a 1 M NaOH solution. The remaining NWs were rinsed in distilled water and were dispersed in ethanol. We prepared the TEM specimen by dropping the NW dispersed ethanol solution on a TEM grid.

## 3. Results and Discussion

Figure 1(a) shows a typical cross-sectional SEM image of the Co/Sb-multilayered NWs with a radius of $r_{NW}$ = 15 nm within the AAO template. At first, the Co segment (dark region) was deposited at the bottom of the template, and then the Sb segment (bright region) was consecutively deposited at the top of the Co segment along the pore channels of the template. After three cycles of $V_R$ modulation from −1.3 V to −0.8 V, three bilayers of Co/Sb were repeatedly synthesized, as shown in Figure 1(a). The interface boundaries are indicated by the dotted yellow lines shown in Figure 1(a). The lengths of the Co and Sb segments were 300 ± 40 and 600 ± 50 nm, respectively. In Figure 1(b), a bright-field TEM image shows that each segment of Co and Sb was densely interconnected at the interfaces. Figure 1(c) shows a high-resolution (HR) TEM image of the interface between Co and Sb segments. The insets indicate the fast Fourier transformation (FFT) images corresponding to the marked areas in the Co and Sb segments, respectively. The FFT image from the Sb segment shows a diffuse ring pattern indicating that the Sb segment is in an amorphous state. The FFT image from the Co segment shows that the Co segment
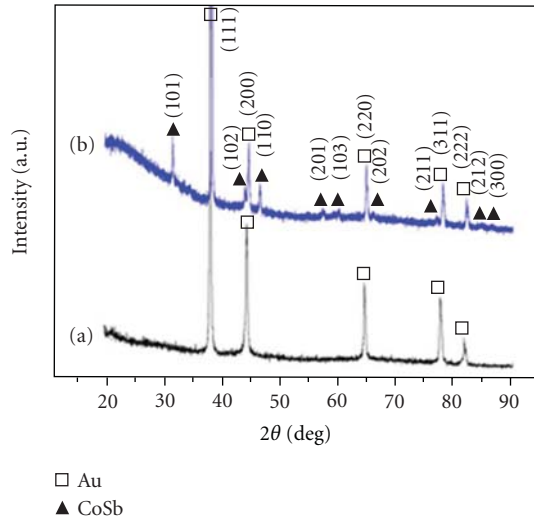
FIGURE 2: XRD patterns of Co/Sb-multilayered nanowires ($r_{NW}$ = 15 nm) (a) in the as-prepared state and (b) after heat treatment at 673 K for 10 min.



FIGURE 3: (a) Bright field TEM image and (b) HR-TEM image of Co/Sb-multilayered nanowires ($r_{NW}$ = 15 nm) after heat treatment at 673 K for 10 min. The inset denotes the FFT image of the marked area of the CoSb segment.



FIGURE 4: SEM images of the multilayered nanowires ($r_{NW}$ = 15 nm) with isothermal heat treatment time of up to 30 min at 673 K.

has a hexagonal closed packed crystal structure with a [001]-zone axis. Although the marked area of the Co segment was analyzed and found to be of crystalline phase, it should be mentioned that most of the other parts of the Co segment have an amorphous structure. From the HR TEM analysis shown in Figure 1(c), it can be supposed that the Co segment has a mixed phase of Co nanocrystals (grain size less than 10 nm), in a very limited region, and Co in an amorphous phase. The TEM results were in a good agreement with the XRD results shown in Figure 2(a). Figure 2(a) shows the XRD pattern of the Co/Sb-multilayered NWs ($r_{NW}$ = 15 nm) in the as-prepared state. In Figure 2(a), there are no reflection peaks from elemental Co and Sb, or Co-Sb compound phases, indicating that Co and Sb segments in the as-prepared state were in an amorphous state. Figure 2(b) shows the XRD pattern of the Co/Sb-multilayered NWs of $r_{NW}$ = 15 nm after the heat treatment at 673 K for 10 min. The XRD pattern of the Co/Sb-multilayered NWs of $r_{NW}$ = 19 nm after heat treatment is not shown here because it was almost the same as that of the NWs of $r_{NW}$ = 15 nm. During the heat treatment, the transformation of the Co/Sb-multilayered structure into CoSb phase occurred at the interface between Co and Sb, regardless of the wire radius, as shown in Figure 2(b).

Figure 3 displays the bright-field and HR TEM images of Co/Sb-multilayered NWs ($r_{NW}$ = 15 nm) after heat treatment at 673 K. It was observed that the Co segment was shortened from the initial length (300 nm) to 130 nm, and that the CoSb segment (about 230 nm in length) formed after the heat treatment, as can be seen in Figure 3(a). The HR TEM image and the corresponding FFT result shown in the inset of Figure 3(b) show a crystalline segment indexed as a hexagonal CoSb phase resulting from the solid-state reaction between Co and Sb segments. The CoSb segment was disconnected from the Sb segment, as shown in Figures 4 and 5, while the interface between Co and CoSb segments was
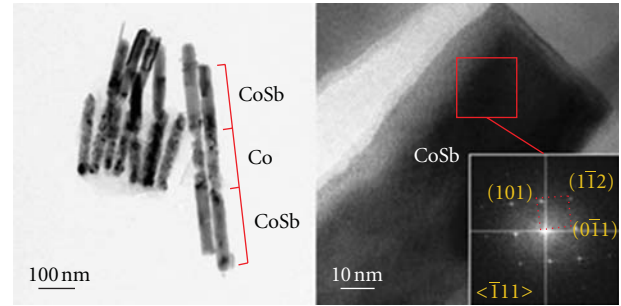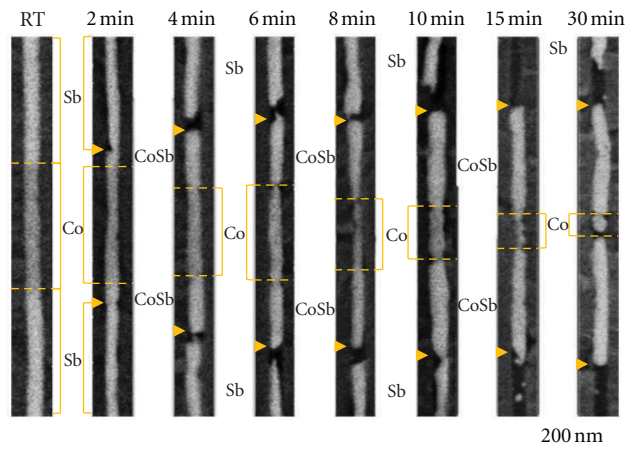
connected despite the formation of the small notches that are shown in Figures 3 to 5. This suggests that the diffusion of Sb atoms toward the Co segment was dominant during the solid-state reaction. Although the dominant diffusion of Sb atoms causes a molar volume expansion, it is presumed that the volume expansion occurs along the longitudinal direction of the pores due to the confinement within the nanotemplates. In Figures 4 and 5, it should be noted that the interface between Sb and CoSb segments started to disconnect after heat treatment for 4 min. Despite this disconnection, the CoSb segments grew with heat treatment time up to 30 min. The Sb atoms needed for the formation of the CoSb segment are presumed to be supplied by the sublimation of the Sb segment as well as by surface diffusion along the wall surface of the AAO template. Previously, it was reported that Sb can be sublimated in vacuum at 650 K [21] and that Sb NWs sublimated at 769 K in ambient atmosphere [22]. Accordingly, the heat treatment was conducted in the range of 653 to 693 K for proper measurement of the solid-state reaction rate.

The transformation kinetics from Co/Sb-multilayer to CoSb phase was investigated by the isothermal heat treatment of the Co/Sb-multilayered NWs. As can be seen in
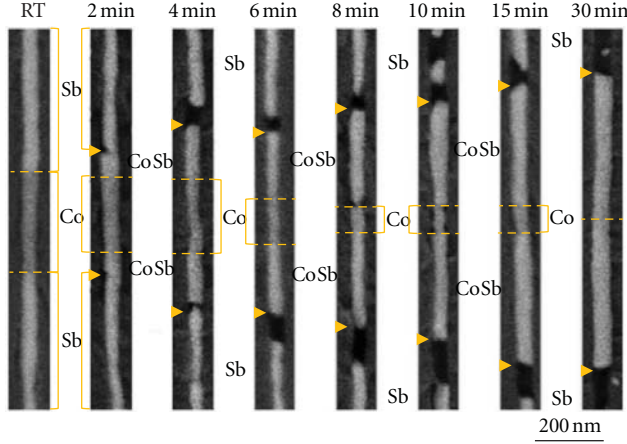
FIGURE 5: SEM images of the multilayered nanowires ($r_{NW}$ = 19 nm) with isothermal heat treatment time of up to 30 min at 673 K.

Figure 4, the Co segment was transformed to a CoSb segment by the dominant diffusion of Sb atoms in the Co/Sb-multilayered NWs with $r_{NW}$ of 15 nm. The length of the Co segment (dark region between the dotted lines) decreased with the time, while that of the CoSb segment (between the dotted lines and to the triangle) increased with the heat treatment time out of the Co segment ends. After heat treatment for 30 min, a 40 nm length Co segment remained, while a 270 nm length CoSb segment formed, as shown in Figure 4. In the case of Co/Sb-multilayered NWs of $r_{NW}$ = 19 nm, very similar reactions were observed, as can be seen in Figure 5. Interestingly, the Co segment was almost consumed in forming the CoSb segment after 30 min, as can be seen in Figure 5. After heat treatment, the lengths of the CoSb NWs were observed to be about 350 nm.

As can be seen in Figures 4 and 5, the lengths ($\lambda$) of the CoSb segments were measured with the variation of the heat treatment time. The length of the CoSb segment was determined as the average value out of ten measurements of the length of each NW. Figure 6 shows the variations of CoSb length with the heat treatment time. The variations of CoSb lengths with the time showed similar behavior for the two NWs with radii of $r_{NW}$ = 15 and 19 nm. The variations of CoSb lengths with the time were fitted by the following relation:

$$\lambda = (Dt)^n. \tag{1}$$

Here, $D$ and $t$ denote a diffusion coefficient and diffusion time; $n$ is a diffusion exponent. When $n = 0.5$, the variation of the CoSb lengths was in good agreement with the fitting line. It is wellknown that $n = 1$ implies a reaction-controlled process, while $n = 0.5$ indicates a diffusion-controlled process [23]. Therefore, the data and fitting shown in Figure 6 suggest that the solid-state reaction of the CoSb formation occurred in a diffusion-controlled mode. The overall reaction rate was controlled by Sb diffusion through the CoSb phase, which was evidenced by the formation of
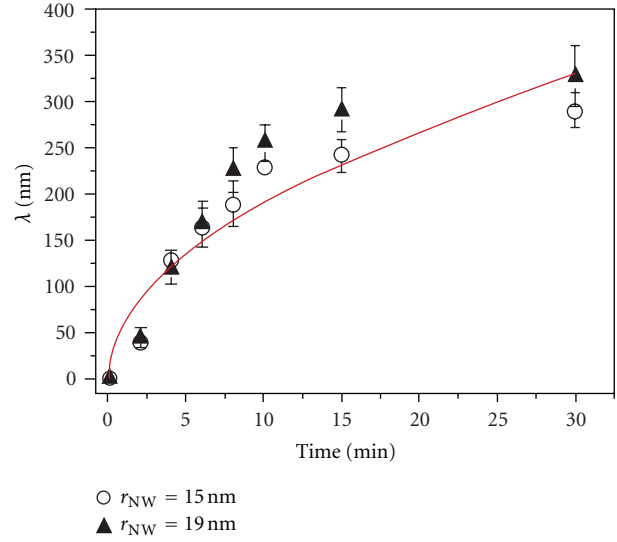


FIGURE 6: Variations of CoSb length ($\lambda$) with isothermal heat treatment time at 673 K. The curve (red line) was fitted according to (1) and $n = 0.5$.
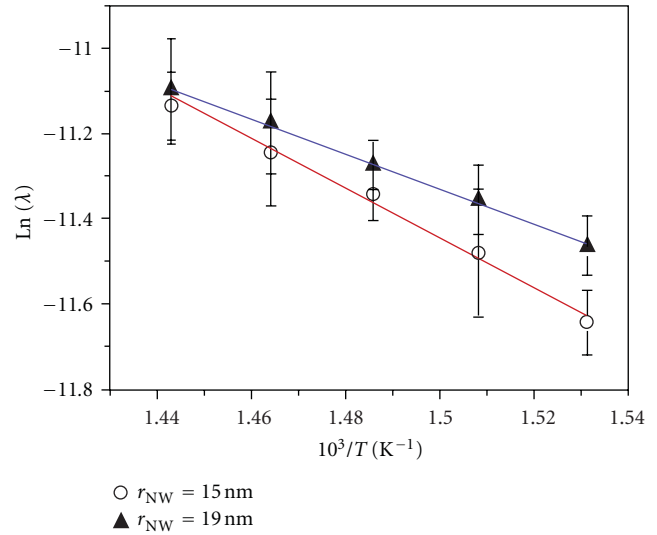


FIGURE 7: Variations of CoSb length on log scale (in unit of cm) with inverse heat treatment temperature in the range of 653 to 693 K.

the notches beside the Co segment and the disconnection between the CoSb and Sb phases.

Using the Arrhenius relation of $D = D_0 \exp(-Q/kT)$, (1) is reduced to the following relation:

$$\ln \lambda = A - \frac{Q}{(2kT)}. \tag{2}$$

Here, $A$, $k$, $T$, and $Q$ denote a constant, the Boltzmann constant, temperature, and the activation enthalpy for solid-state diffusion, respectively. The lengths of the CoSb segment were measured by varying the heat treatment temperature in the range of 653 to 693 K. The variations of $\ln \lambda$ with the inverse temperature, $1/T$, were linearly fitted in Figure 7.

According to (2), the slopes of the linear fits in the plot of $\ln \lambda$ with $1/T$ are equal to the values of $Q/(2k)$. Thus, the activation enthalpies were estimated to be 0.9 and 0.7 eV/atom for the Co/Sb-multilayered NWs of $r_{NW} = 15$ and 19 nm, respectively. The estimated activation enthalpies indicate the barrier energy needed for the diffusion through the CoSb phase because the reaction was controlled by the diffusion of Sb atoms, as discussed above. Considering the overlapped standard deviations of data shown in Figure 7, it is supposed that the activation enthalpies of the solid-state reactions for the two NW radii were not very different from each other. They are lower than the activation enthalpies (2.7 and 1.3 eV/atom) needed for the diffusion of Co in bulk Fe and Sb in bulk Sn, respectively [24, 25]. This suggests that the activation energy for atomic diffusion on a nanometer scale can be slightly lower than that in bulk form, which is in agreement with previous reports [10, 11].

## 4. Conclusion

We have produced a Co/Sb-multilayered NW array within an AAO template using pulsed potentiodynamic electrode-position. After heat treatment, the amorphous Co/Sb-multilayered NWs transformed into CoSb crystalline phase through a solid-state reaction. We analyzed the solid-state reaction, which was confined in the nanotemplate, in order to understand the phase transformation kinetics on a nanometer scale. From the heat treatment experiment, it was confirmed that the solid-state reaction between Co and Sb segments is diffusion controlled and that the Sb diffusion through the CoSb phase is the dominant process. The activation enthalpies for the solid-state reaction were estimated to be 0.9 eV/atom for $r_{NW} = 15$ nm and 0.7 eV/atom for $r_{NW} = 19$ nm. It is supposed that the activation enthalpies for solid-state diffusion in the NWs are lower than those for the bulk form. Further experimental studies on the effects of wire radius on the solid-state diffusion kinetics are needed to quantitatively analyze the size effects.

## Acknowledgment

## References

[1] Y. Xia, P. Yang, Y. Sun et al., "One-dimensional nanostructures: synthesis, characterization, and applications," *Advanced Materials*, vol. 15, no. 5, pp. 353–389, 2003.

[2] G. Ouyang, X. Tan, and G. Yang, "Thermodynamic model of the surface energy of nanocrystals," *Physical Review B*, vol. 74, no. 19, Article ID 195408, 2006.

[3] C. Q. Chen, Y. Shi, Y. S. Zhang, J. Zhu, and Y. J. Yan, "Size dependence of Young's modulus in ZnO nanowires," *Physical Review Letters*, vol. 96, no. 7, Article ID 075505, 4 pages, 2006.

[4] E. C. C. M. Silva, L. Tong, S. Yip, and K. J. Van Vliet, "Size effects on the stiffness of silica nanowires," *Small*, vol. 2, no. 2, pp. 239–243, 2006.

[5] H. S. Shin, J. Yu, and J. Y. Song, "Size-dependent thermal instability and melting behavior of Sn nanowires," *Applied Physics Letters*, vol. 91, no. 17, Article ID 173106, 2007.

[6] M. Tian, J. Wang, J. S. Kurtz et al., "Dissipation in quasi-one-dimensional superconducting single-crystal Sn nanowires," *Physical Review B*, vol. 71, no. 10, Article ID 104521, 7 pages, 2005.

[7] J. Eymery, V. Favre-Nicolin, L. Fröberg, and L. Samuelson, "X-ray measurements of the strain and shape of dielectric/metallic wrap-gated InAs nanowires," *Applied Physics Letters*, vol. 94, no. 13, Article ID 131911, 2009.

[8] H. S. Shin, J. Yu, J. Y. Song, H. M. Park, and Y. S. Kim, "Origins of size-dependent lattice dilatation in tetragonal Sn nanowires: surface stress and growth stress," *Applied Physics Letters*, vol. 97, no. 13, Article ID 131903, 2010.

[9] C. Q. Sun, "Size dependence of nanostructures: impact of bond order deficiency," *Progress in Solid State Chemistry*, vol. 35, no. 1, pp. 1–159, 2007.

[10] A. I. Persson, M. W. Larsson, S. Stenström, B. J. Ohlsson, L. Samuelson, and L. R. Wallenberg, "Solid-phase diffusion mechanism for GaAs nanowire growth," *Nature Materials*, vol. 3, no. 10, pp. 677–681, 2004.

[11] Y. C. Chou, W. W. Wu, L. J. Chen, and K. N. Tu, "Homogeneous nucleation of epitaxial CoSi$_2$ and NiSi in Si nanowires," *Nano Letters*, vol. 9, no. 6, pp. 2337–2342, 2009.

[12] Y. C. Chou, W. W. Wu, S. L. Cheng et al., "In-situ TEM Observation of repeating events of nucleation in epitaxial growth of nano CoSi$_2$ in nanowires of Si," *Nano Letters*, vol. 8, no. 8, pp. 2194–2199, 2008.

[13] V. C. Holmberg, M. G. Panthani, and B. A. Korgel, "Phase transitions, melting dynamics, and solid-state diffusion in a nano test tube," *Science*, vol. 326, no. 5951, pp. 405–407, 2009.

[14] A. M. Gusak and K. N. Tu, "Interaction between the Kirkendall effect and the inverse Kirkendall effect in nanoscale particles," *Acta Materialia*, vol. 57, no. 11, pp. 3367–3373, 2009.

[15] X. Dou, Y. Zhu, X. Huang, A. Li, and G. Li, "Effective deposition potential induced size-dependent orientation growth of Bi-Sb alloy nanowire arrays," *Journal of Physical Chemistry B*, vol. 110, no. 43, pp. 21572–21575, 2006.

[16] W. J. Li, W. L. Yu, and C. Y. Yen, "Pulsed electrodeposition of Bi$_2$Te$_3$ and Bi$_2$Te$_3$/Te nanowire arrays from a DMSO solution," *Electrochimica Acta*, vol. 58, no. 1, pp. 510–515, 2011.

[17] L. Chen, H. Hu, Y. Li, G. Chen, S. Yu, and G. Wu, "Ordered CoSb$_3$ nanowire arrays synthesized by electrodeposition," *Chemistry Letters*, vol. 35, no. 2, pp. 170–171, 2006.

[18] H. Cheng, H. H. Hng, J. Ma, and X. J. Xu, "Effects of various deposition parameters on the co-deposition behavior of cobalt antimony in citric-based solution," *Journal of Materials Research*, vol. 23, no. 11, pp. 3013–3020, 2008.

[19] M. S. Dresselhaus, G. Chen, M. Y. Tang et al., "New directions for low-dimensional thermoelectric materials," *Advanced Materials*, vol. 19, no. 8, pp. 1043–1053, 2007.

[20] C. K. Chan, H. Peng, G. Liu et al., "High-performance lithium battery anodes using silicon nanowires," *Nature Nanotechnology*, vol. 3, no. 1, pp. 31–35, 2008.

[21] B. V. L'vov and A. V. Novichikhin, "Quantitative interpretation of the evaporation coefficients for the decomposition or sublimation of some substances in vacuo," *Thermochimica Acta*, vol. 290, no. 2, pp. 239–251, 1997.

[22] X. Zhang, Y. Ding, Y. Zhang, Y. Hao, G. Meng, and L. Zhang, "Thermal behavior of antimony nanowire arrays embedded in anodic aluminum oxide template," *Journal of Thermal Analysis and Calorimetry*, vol. 89, no. 2, pp. 493–497, 2007.

[23] J. W. Christian, *The Theory of Transformation in Metals and Alloys*, Pergamon, Oxford, UK, 1975.

[24] F. H. Huang and H. B. Huntington, "Diffusion of Sb[124], Cd[109], Sn[113], and Zn[65] in tin," *Physical Review B*, vol. 9, no. 4, pp. 1479–1488, 1974.

[25] D. W. James and G. M. Leak, "Self-diffusion and diffusion of cobalt in alpha and delta-iron," *Philosophical Magazine*, vol. 14, no. 130, pp. 701–713, 1966.

*Research Article*

# Facile Hydrothermal Synthesis and Optical Properties of Monoclinic CePO$_4$ Nanowires with High Aspect Ratio

**Nuengruethai Ekthammathat,[1] Titipun Thongtem,[1, 2] Anukorn Phuruangrat,[3] and Somchai Thongtem[2, 4]**

[1] *Department of Chemistry, Faculty of Science, Chiang Mai University, Chiang Mai 50200, Thailand*

[2] *Materials Science Research Center, Faculty of Science, Chiang Mai University, Chiang Mai 50200, Thailand*

[3] *Department of Materials Science and Technology, Faculty of Science, Prince of Songkla University, Hat Yai, Songkhla 90112, Thailand*

[4] *Department of Physics and Materials Science, Faculty of Science, Chiang Mai University, Chiang Mai 50200, Thailand*

Correspondence should be addressed to Titipun Thongtem, ttpthongtem@yahoo.com
and Anukorn Phuruangrat, phuruangrat@hotmail.com

Received 14 April 2012; Accepted 10 July 2012

Academic Editor: Yanqiu Zhu

One-dimensional cerium phosphate (CePO$_4$) nanowires (NWs) were successfully synthesized by a facile and simple hydrothermal method at 200°C for 12 h, using Ce(NO$_3$)$_3$·6H$_2$O and Na$_3$PO$_4$·12H$_2$O as starting materials, and followed by pH adjusting to be 1–3 using HNO$_3$ (conc.). Phase, morphologies, and vibration modes of the as-synthesized CePO$_4$ products, characterized by XRD, SEM, TEM, and FTIR, were proved to be perfect and uniform monoclinic CePO$_4$ nanowires with aspect ratio of more than 250 for the product synthesized in the solution with the pH of 1. The UV-visible and photoluminescence (PL) spectrometers were used to investigate optical properties of the as-synthesized monoclinic CePO$_4$ nanowires.

## 1. Introduction

Since the discovery of carbon nanotubes by Iijima in 1990, a number of one-dimensional (1D) nanotubes, nanorods, and nanowires, have widely attracted interest for worldwide scientists, due to their novel physical and chemical properties caused by their low-dimensional and quantum-sized effects for different applications. In addition, these 1D nanomaterials can play an important role in functional nanodevices for light emitting diodes (LEDs), solar cells, single-electron transistors, lasers, and fluorescence for biological labels. Controling the synthesis of anisotropic nanostructured materials may therefore bring towards some unique properties and further enhance performances for a variety of applications [1–3].

Rare earth phosphate materials with unique 4f-5d and 4f-4f electronic transition have been widely used as high-performance luminescent devices, magnetic materials, catalysts, time-resolved fluorescence labels, and other functional materials. They are well known for the production of phosphor, sensor, and heat-resistant materials. Among them,

CePO$_4$ as well as its solid solutions is able to be used as highly efficient emitters for green light of luminescent devices. The monoclinic CePO$_4$ monazite, one of the most stable materials although at a temperature as high as 1200 K, is appropriate for heat-resistant ceramic applications. It exists for billions of years by forming solid solutions with tetravalent actinide ions, such as U$^{4+}$ and Th$^{4+}$. Thus it is a promising material for nuclear waste storage. But for hexagonal CePO$_4$, it is able to apply for tribological applications due to its natural layered structure [2–6].

In this paper, synthesis and formation mechanism of monoclinic CePO$_4$ nanowires (NWs) with high aspect ratio by a hydrothermal method without the use of surfactant and template as morphological controlling agents were reported. This method is simple, inexpensive, highly effective, and appropriate for synthesizing of other 1D nanomaterials.

## 2. Experiment

All reagents, Ce(NO$_3$)$_3$·6H$_2$O, Na$_3$PO$_4$·12H$_2$O, and HNO$_3$, bought from Sigma-Aldrich Co. LLC., were analytical grade

and used without further purification. For a typical synthesis of monoclinic $CePO_4$ NWs, 0.003 mol $Ce(NO_3)_3 \cdot 6H_2O$ was dissolved in 10 mL distilled water with the subsequent adding of 10 mL 0.003 M $Na_3PO_4 \cdot 12H_2O$ solution. The solution pH was adjusted to 1, 1.5, 2, and 3 using $HNO_3$ (conc.). Then, each of these solutions was transferred into Teflon containers, which were put in home-made stainless steel autoclaves. The autoclaves were tightly closed, heated at 200°C for 12 h in an electric oven, and left naturally cool down to room temperature. Then the as-synthesized precipitates were separated by filtration, washed with deionized water several times and ethanol, and dried at 70°C for 12 h. The final products appeared as light green solid powder.

The crystalline phases and crystalline degree of the as-synthesized nanostructured products were analyzed by X-ray diffractometer (XRD, Philips X'Pert MPD) operating at 45 kV 35 mA and using Cu K$_\alpha$ line in $2\theta = 10° - -60°$. The morphology investigation was carried out by field emission scanning electron microscope (FE-SEM, JEOL JSM-6335F) operating at 15 kV, transmission electron microscope (TEM, JEOL JEM-2010), and high resolution transmission electron microscope (HRTEM) using LaB$_6$ electron gun operated at 200 kV. The samples for EM analysis were prepared by sonicating of dry products in absolute ethanol for 15 min. For SEM analysis, the solutions were dropped on aluminum stubs, dried in ambient atmosphere, and coated by Au sputtering to increase electrical conductivity. But for TEM analysis, 3–5 drops of the suspensions were put on carbon-coated copper grids which were dried in ambient atmosphere. Fourier transform infrared (FTIR, *PerkinElmer* RX 1) spectrophotometer was carried out in the range of 4000 to 400 cm$^{-1}$ with 4 cm$^{-1}$ resolution. Their optical properties were studied by a UV-visible (UV-vis) spectrometer (Lambda 25 PerkinElmer) using a UV lamp with the resolution of 1 nm and a fluorescence spectrophotometer (LS50BPerkinElmer) using 450 W Xe lamp with 0.2 nm resolution.

## 3. Results and Discussion

Phase of the product was characterized by X-ray powder diffraction (XRD) as shown in Figure 1. The XRD pattern was readily specified as monoclinic $CePO_4$ structure of the JCPDS database number 32-0199 [7]. There were no detection of any peaks of impurities of $CeO_2$ and hexagonal $CePO_4$ in this paper. Its lattice parameters ($a$, $b$, and $c$) and volume ($V$) of unit cell were calculated from the equations for monoclinic structure below

$$\frac{1}{d^2} = \frac{1}{\sin^2\beta}\left[\frac{h^2}{a^2} + \frac{k^2\sin^2\beta}{b^2} + \frac{l^2}{c^2} - \frac{2hl\cos\beta}{ac}\right],$$

$$V = abc\sin\beta,$$

$$(1)$$

where $h$, $k$, and $l$ are the Miller indices, $d$ is the plane spacing, and $\beta$ is the angle between the $a$ and $c$ axes (103.46°) [8]. The calculated lattice parameters of monoclinic $CePO_4$ structure were $a = 6.7852$ Å, $b = 7.0802$ Å, and $c = 6.4523$ Å—in good accordance with those of the JCPDS database ($a = 6.8004$ Å, $b = 7.0231$ Å, and $c = 6.4717$ Å). The calculated cell volume of the as-synthesized $CePO_4$ NWs was 301.45 Å$^3$, higher than
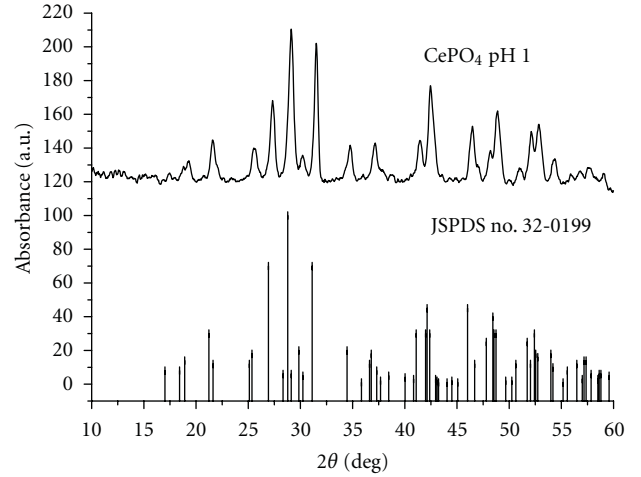


Figure 1: XRD pattern of $CePO_4$ NWs synthesized by the 200°C and 12 h hydrothermal reaction of the solution with the pH of 1, compared with the JCPDS database.

Table 1: The 1D $CePO_4$ products synthesized by the 200°C and 12 h hydrothermal reaction of the solutions with different pH values.

| Solution pH | Length ($\mu$m) | Diameter (nm) | Aspect ratio |
|---|---|---|---|
| 1 | 5.00–7.00 | 20 | 250–350 |
| 1.5 | 2.00–5.00 | 20 | 100–250 |
| 2 | 1.00–1.50 | 15 | 67–100 |
| 3 | 0.20–0.30 | 10 | 20–30 |

that of its bulk of 300.60 Å$^3$. The increase in the cell volume indicated that lattice of the NWs was more distorted than that of their bulk [9, 10].

Figure 2 shows FTIR spectra of $CePO_4$ NWs synthesized by the hydrothermal reaction at the pH of 1 adjusted by $HNO_3$ solution. The vibrations of $CePO_4$ NWs were due to the $PO_4^{3-}$ tetrahedrons, belonging to the $A_1(R) + E(R) + 2F_2(IR + R)$. The $\nu_1(A_1)$ (symmetric stretching mode) and $\nu_2(E)$ (symmetric bending mode) are Raman (R) active, and the $\nu_3(F_2)$ (asymmetric stretching mode) and $\nu_4(F_2)$ (asymmetric bending mode) are R and IR doubly active modes. The symmetry of $PO_4^{3-}$ ions in the $CePO_4$ crystals decreases from $T_d$ to $C_1$, and thus the non-IR modes become IR active [10]. The broad band at 3460 cm$^{-1}$ was assigned as the O–H stretching vibration of water molecules, adsorbed on surface of the product. The bands at 1200–400 cm$^{-1}$ wavenumbers were assigned as the vibrations of $PO_4^{3-}$ groups. Those centered at 1052 cm$^{-1}$ were specified as the asymmetric stretching vibrations of the $PO_4^{3-}$ groups and those at 609 cm$^{-1}$ and 536 cm$^{-1}$ were as the O–P–O bending vibrations. Four medium-intensity peaks between 700 and 400 cm$^{-1}$ were caused by bending of P–O links in $PO_4^{3-}$ distorted tetrahedrons. The P–O stretching peak was split bands due to the removal of degeneracy of tetrahedral vibrations, corresponding to the characteristic peaks of phosphate groups of monoclinic cerium phosphate. In the monazite monoclinic phase, the tetrahedral phosphate groups are distorted in the nine fold coordination of lanthanide atoms
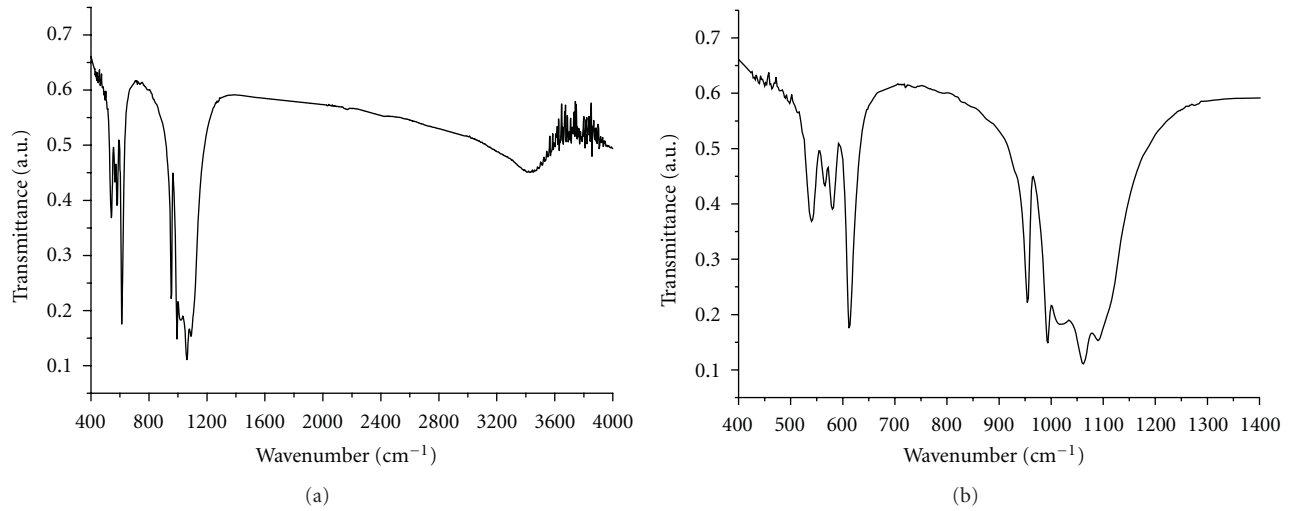
FIGURE 2: FTIR spectra of CePO$_4$ NWs synthesized by the 200°C and 12 h hydrothermal reaction of the solution with the pH of 1. (a) 4000–400 cm$^{-1}$ and (b) 1400–400 cm$^{-1}$.



FIGURE 3: SEM images of CePO$_4$ synthesized by the 200°C and 12 h hydrothermal reaction of the solution with the pH of (a–d) 3, 2, 1.5, and 1, respectively.

TABLE 2: Individual component of PL spectrum of CePO$_4$ NWs. Emission intensities were calculated from areas under the corresponding curves.

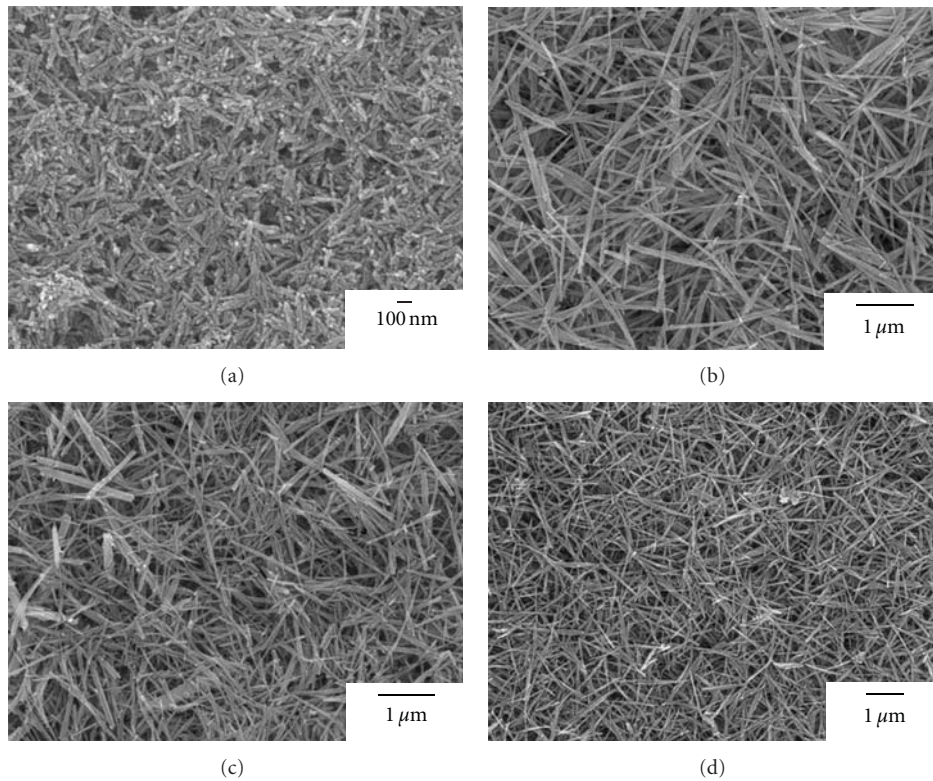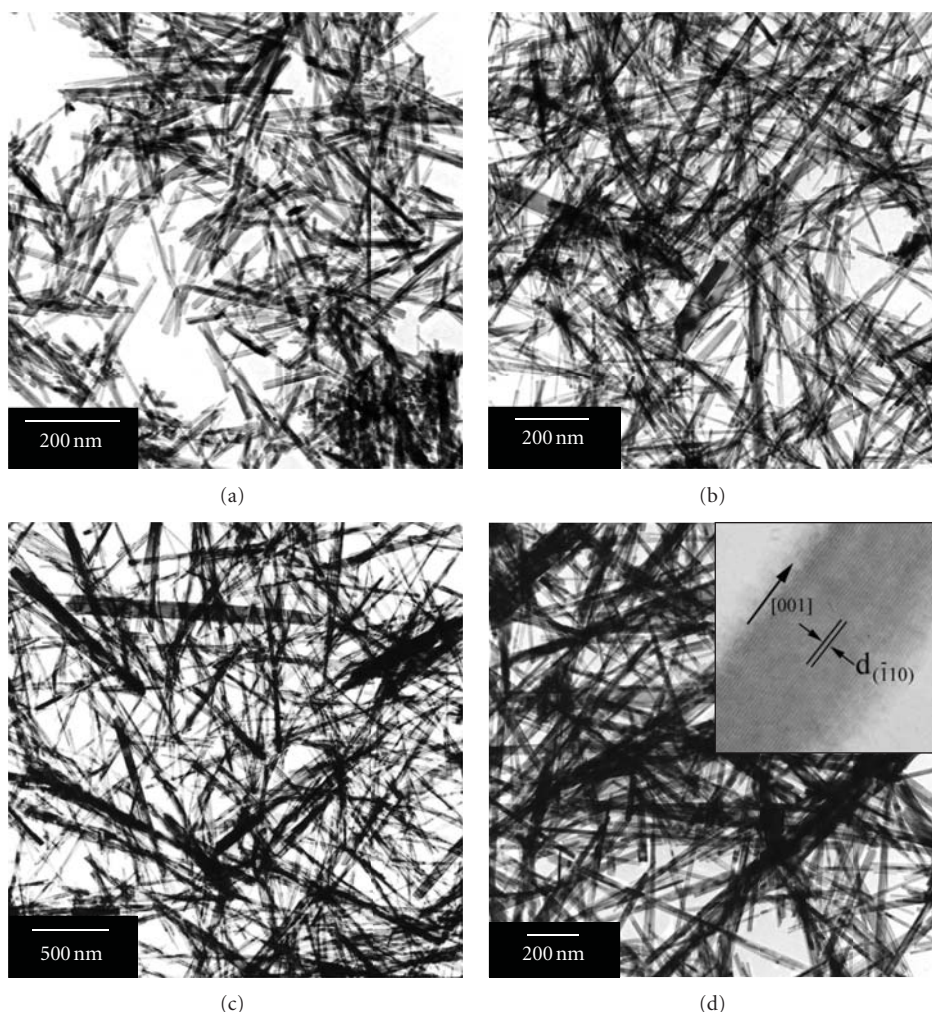| Individual component | Emission wavelength (nm) | Area under curve | Intensity (%) |
|---|---|---|---|
| P1 | 361.36 (ultraviolet) | 381.56 | 6.00 |
| P2 | 388.24 (ultraviolet) | 1505.29 | 23.65 |
| P3 | 438.46 (violet) | 2449.46 | 38.49 |
| P4 | 482.52 (blue) | 160.49 | 2.52 |
| P5 | 505.94 (green) | 1867.22 | 29.34 |

(a)

(b)

(c)

(d)

FIGURE 4: TEM images of CePO$_4$ synthesized by the 200°C and 12 h hydrothermal reaction of the solution with the pH of (a–d) 3, 2, 1.5, and 1, respectively. Inserted HRTEM image of (d) shows the growth direction and crystallographic plane of the NW.

and the phosphate absorptions are split accordingly. The stretching modes appeared as a cluster of very strong peaks at 954, 993, 1052, and 1092 cm$^{-1}$. The adsorption of NO$_3{}^{-}$ anions (1380 and 878 cm$^{-1}$) from the precursor was not detected, indicating that the product was very pure phase [10–13].

The product morphology (Figure 3) was characterized by a scanning electron microscope (SEM), and was able to specify the evolution in the length of one-dimensional CePO$_4$ product-influenced by pH of the solutions. Only the monoclinic CePO$_4$ nanorods with 200 to 300 nm long and 10 nm in diameter were synthesized by the 200°C and 12 h hydrothermal reaction of the precursor solution with the pH of 3. Upon adjusting the pH values to 2 and 1.5, some CePO$_4$ nanorods were transformed into CePO$_4$ nanowires (NWs) with 1 to 5 μm in length and 15 to 20 nm in diameter. At the precursor solution pH of 1, the whole CePO$_4$ NWs with aspect ratio > 250 were synthesized. The aspect ratios for different solution pH were summarized in Table 1, which showed the influence of pH values on the lengths and diameters of 1D CePO$_4$. In this paper, uniform CePO$_4$ NWs

with high aspect ratio were successfully synthesized by the 200°C and 12 h hydrothermal reaction of the solution with the pH of 1.

To further show the real morphologies of the as-synthesized monoclinic CePO$_4$ at the pH of 1–3, the products were characterized by a transmission electron microscope (TEM) (Figure 4). At the pH of 3, the product was structurally uniform nanorods. Their average diameter was 10 nm and length was up to 300 nm. Mixed nanowires and nanorods were detected at the pH of 2 and 1.5. The whole CePO$_4$ NWs with longer than 5 μm and diameter of 20 nm were synthesized at the pH of 1. The growth direction of monoclinic CePO$_4$ NWs was investigated by high resolution transmission electron microscope (HRTEM) as shown in the inset of Figure 4(d). It shows that the lattice spacing was about 4.81 Å, corresponding to the (−110) plane, with the growth direction of single monoclinic CePO$_4$ crystal along the [001] direction-parallel to the (−110) plane.

In general, the anisotropic growth of one-dimensional materials was driven by several factors such as surface energy, structure, electrostatic force, and surfactant. In this paper,
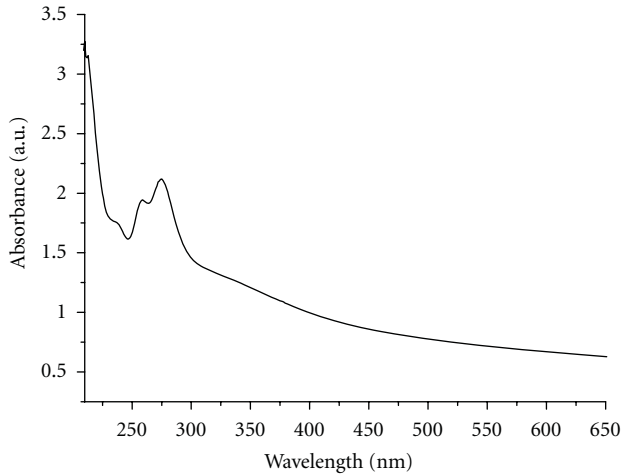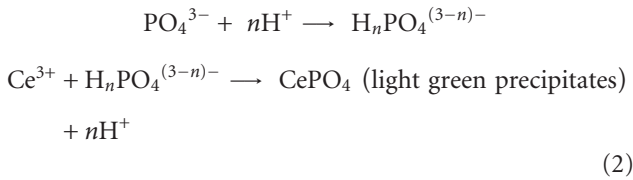
FIGURE 5: UV-visible spectrum of CePO$_4$ NWs synthesized by the 200°C and 12 h hydrothermal reaction of the solution with the pH of 1.
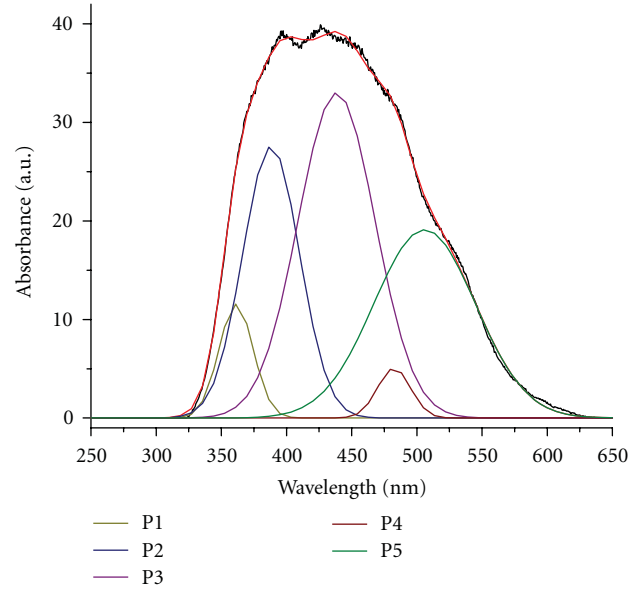


FIGURE 6: PL spectrum of CePO$_4$ NWs synthesized by the 200°C and 12 h hydrothermal reaction of the solution with the pH of 1. Centers of the five deconvoluted peaks from left to right are in sequence as P1, P2, P3, P4, and P5.

the anisotropic CePO$_4$ NWs was controlled by the chemical potential. The faster ionic migration usually promoted the reversible pathway between fluid and solid phases, leaving ions to reside in the right positions of crystal lattice [14]. The formation mechanism of CePO$_4$ NWs is able to explain as follows:

$$PO_4^{3-} + nH^+ \longrightarrow H_nPO_4^{(3-n)-}$$

$$Ce^{3+} + H_nPO_4^{(3-n)-} \longrightarrow CePO_4 \text{ (light green precipitates)}$$

$$+ nH^+$$

(2)

Ce(NO$_3$)$_3$·6H$_2$O and Na$_3$PO$_4$·12H$_2$O were mixed in distilled water, with the following of pH adjusting using HNO$_3$ (conc.). During the hydrothermal treatment of the solution with the pH of 1, the clear colorless solution was heated up under high pressure. Concurrently, the Ce$^{3+}$ and H$_n$PO$_4^{(3-n)-}$ chemical potentials were raised up, including the faster ionic migration in the solution. During cooling, these ions combined to form light green precipitates of monoclinic CePO$_4$ NWs—in accordance with the reports of Zhang and Guan [3].

The optical properties of CePO$_4$ NWs hydrothermally synthesized in the solution with the pH of 1 were investigated by UV-visible and photoluminescence (PL) spectroscopy. The CePO$_4$ NWs for the analyses were ultrasonically dispersed in absolute ethanol for 10 min. Their UV-visible absorption spectrum (Figure 5) is in the range of 220 to 650 nm. The absorption was detected as a strong band in the ultraviolet range, caused by the f–d electron transition of Ce$^{3+}$ atoms in the lattice. It shows the major absorption peak at 274 nm coupled with a small shoulder at 257 nm. These bands were overlapping as the excited states were strongly split by the crystal field. Moreover, these results are in consistent with the data for transition from the Ce$^{3+}$ $^2$F$_{5/2}$(4f$^1$) ground state to the five crystal field split levels of the Ce$^{3+}$ $^2$D (5d$^1$) excited states, namely, the $^2$D$_{5/2}$ and $^2$D$_{3/2}$ [9, 15].

Figure 6 shows the PL spectrum at room temperature of CePO$_4$ NWs using the excitation wavelength of 325 nm. It displays a broad emission peak of the CePO$_4$ NWs over the 325 to 625 nm range. To estimate the contribution of each, it was necessary to deconvolute the PL spectrum. By using the Gaussian analysis, the deconvoluted results shows that the PL profile was at the best for five deconvoluted peaks. The first, second, and third were in the ultraviolet spectrum, the fourth in the blue range, and the fifth in the green wavelength. Each component represents different types of electronic transition, linked with the atomic arrangement and surface defects. The PL spectrum exhibits strong emission peaks centered at 388.24 nm (ultraviolet) and 438.46 nm (violet) [13, 16, 17]. Emission wavelength, color, and intensity of each component of CePO$_4$ NWs are shown in Table 2. The strongest intensity of the PL spectrum for CePO$_4$ NWs corresponded to the 438.46 nm violet wavelength with 38.49% of the whole emission.

## 4. Conclusions

In summary, uniform CePO$_4$ NWs with aspect ratio of more than 250 were synthesized by the facile hydrothermal method. Their formation mechanism was also discussed in this paper. Different lengths and sizes of CePO$_4$ products were influenced by the pH values. The uniform monoclinic CePO$_4$ NWs were synthesized in the solution with the pH of 1. These NWs show the strong absorption in the ultraviolet range due to the f–d electron transition of Ce$^{3+}$ atoms in crystal lattice. Their PL emission shows a broad band df 325 to 625 nm range with the strongest emission at 438.46 nm in the violet region.

## Acknowledgments

## References

[1] L. Qian, W. Du, Q. Gong, and X. Qian, "Controlled synthesis of light rare earth phosphate nanowires via a simple solution route," *Materials Chemistry and Physics*, vol. 114, no. 1, pp. 479–484, 2009.

[2] W. Fan, W. Zhao, L. You et al., "A simple method to synthesize single-crystalline lanthanide orthovanadate nanorods," *Journal of Solid State Chemistry*, vol. 177, no. 12, pp. 4399–4403, 2004.

[3] Y. Zhang and H. Guan, "Hydrothermal synthesis and characterization of hexagonal and monoclinic $CePO_4$ single-crystal nanowires," *Journal of Crystal Growth*, vol. 256, no. 1-2, pp. 156–161, 2003.

[4] J. Bao, R. Yu, J. Zhang et al., "Low-temperature hydrothermal synthesis and structure control of nano-sized $CePO_4$," *CrystEngComm*, vol. 11, no. 8, pp. 1630–1634, 2009.

[5] Y. B. Yin, X. Shao, L. M. Zhao, and W. Z. Li, "Synthesis and characterization of $CePO_4$ nanowires *via* microemulsion method at room temperature," *Chinese Chemical Letters*, vol. 20, no. 7, pp. 857–860, 2009.

[6] M. Cao, C. Hu, Q. Wu, C. Guo, Y. Qi, and E. Wang, "Controlled synthesis of $LaPO_4$ and $CePO_4$ nanorods/nanowires," *Nanotechnology*, vol. 16, no. 2, pp. 282–286, 2005.

[7] "Powder Diffract. File," JCPDS-ICDD, 12 Campus Boulevard, Newtown Square, PA 19073-3273, U.S.A., 2001.

[8] C. Suryanarayana and M. G. Norton, *X-Ray Diffraction: A Practical Approach*, Plenum Press, New York, NY, USA, 1998.

[9] Y. P. Fang, A. W. Xu, R. Q. Song et al., "Systematic synthesis and characterization of single-crystal lanthanide orthophosphate nanowires," *Journal of the American Chemical Society*, vol. 125, no. 51, pp. 16025–16034, 2003.

[10] K. Wang, J. Zhang, J. Wang et al., "Growth defects and infrared spectra analysis of $CePO_4$ single crystals," *Journal of Applied Crystallography*, vol. 38, no. 4, pp. 675–677, 2005.

[11] N. Sumaletha, K. Rajesh, P. Mukundan, and K. G. K. Warrier, "Environmentally benign sol-gel derived nanocrystalline rod shaped calcium doped cerium phosphate yellow-green pigment," *Journal of Sol-Gel Science and Technology*, vol. 52, no. 2, pp. 242–250, 2009.

[12] L. Ma, W. X. Chen, Y. F. Zheng, and Z. D. Xu, "Hydrothermal growth and morphology evolution of $CePO_4$ aggregates by a complexing method," *Materials Research Bulletin*, vol. 43, no. 11, pp. 2840–2849, 2008.

[13] M. Yang, H. You, Y. Zheng et al., "Hydrothermal synthesis and luminescent properties of novel ordered sphere $CePO_4$ hierarchical architectures," *Inorganic Chemistry*, vol. 48, no. 24, pp. 11559–11565, 2009.

[14] G. Fasol, "Nanowires: small is beautiful," *Science*, vol. 280, no. 5363, pp. 545–546, 1998.

[15] F. Zhang and S. S. Wong, "Ambient large-scale template-mediated synthesis of high-aspect ratio single-crystalline, chemically doped rare-earth phosphate nanowires for bioimaging," *ACS Nano*, vol. 4, no. 1, pp. 99–112, 2010.

[16] M. Guan, J. Sun, T. Shang, Q. Zhou, J. Han, and A. Ji, "A facile synthesis of cerium phosphate nanofiber by solution-solid method," *Journal of Materials Science & Technology*, vol. 26, no. 1, pp. 45–48, 2010.

[17] G. Li, K. Chao, H. Peng, K. Chen, and Z. Zhang, "Facile synthesis of $CePO_4$ nanowires attached to $CeO_2$ octahedral micrometer crystals and their enhanced photoluminescence properties," *The Journal of Physical Chemistry C*, vol. 112, no. 42, pp. 16452–16456, 2008.

*Research Article*

# Effect of Cr Content on the Properties of Magnetic Field Processed Cr-Doped ZnO-Diluted Magnetic Semiconductors

## Shiwei Wang, Weiqiang Bo, Min Zhong, Cong Liu, Ying Li, Mingyuan Zhu, Yemin Hu, and Hongmin Jin

*Laboratory for Microstructures, School of Materials Science and Engineering, Shanghai University, 149 Yanchang Road, Shanghai 200072, China*

Correspondence should be addressed to Shiwei Wang, wenruru@sina.com

Cr-doped ZnO-diluted magnetic semiconductor (DMS) nanocrystals with various Cr contents were synthesized by hydrothermal method under high magnetic field. The result indicated that both the amount of Cr contents and high magnetic field significantly influenced crystal structure, morphology, and magnetic property of Cr-doped ZnO DMSs. When the Cr contents increased from 1 at% to 5 at%, the morphology of grains sequentially changed from flower-like to rod-like and then to the flake-like form. All the samples remained hexagonal wurtzite structure after Cr ions were doped into the ZnO crystal lattice. The Cr doping led to the increasing amount of defects and even enhanced the magnetic property of the matrix materials. All the Cr-doped ZnO DMSs obtained under high magnetic field exhibited obvious ferromagnetic behavior at room temperature. The results have also shown the successful substitution of the $Cr^{3+}$ ions for the $Zn^{2+}$ ions in the crystal lattice.

## 1. Introduction

Recently the interest in diluted magnetic semiconductors (DMSs) has significantly increased because of their unique magnetic property and potential applications in many fields [1–6]. Ferromagnetic DMSs with Curie temperatures (Tc) above room temperature are usually obtained by doping magnetic ions into the host semiconductors. Zinc oxide is one of representative semiconductor [7, 8], due to its wide bandgap of 3.37 eV and large exciton energy (60 meV). As a transition metal ion, $Cr^{3+}$ is often used as a dopant for ZnO because of the close ionic radius with $Zn^{2+}$ and the ferromagnetic stability of Cr-doped ZnO DMSs [9, 10].

Currently, many methods have been reported to fabricate ZnO DMSs, such as vapor-phase growth [11], thermal decomposition [12], seed-mediated [13], and reverse micelle [14]. Recently, our group has successfully developed a novel hydrothermal method under high magnetic field to prepare a series of transition metal ions ($Cr^{3+}$, $Mn^{2+}$, $Co^{2+}$) doped ZnO DMSs. According to our previous work, it

revealed that high magnetic field played an important role in introducing ions into ZnO crystal lattice and improving the magnetic properties [15–17]. In the present work, the effect of Cr content on the structure, morphology, and magnetic property of Cr-doped ZnO DMSs prepared by HPMF method was investigated in detail.

## 2. Experimental

A hydrothermal method with pulsed magnetic field of 4 Tesla (T) was used to synthesize the Cr-doped ZnO DMS materials with different Cr nominal contents (1 at%, 2 at%, 3 at%, 5 at%). The typical synthesis process was as follows. A 12 mL 1.33 M solution of potassium hydroxide was slowly dropped into a solution of 4 mL of 1.00 M zinc acetate. The mixture was stirred at 273 K for 0.5 hours. Then, a desired amount of 0.02 M chromium nitrate solution, which was calculated according to the nominal Cr content, was slowly dropped into the former mixture at 273 K in the ice bath, and followed by stirring for 1 h. The entire mixtures with
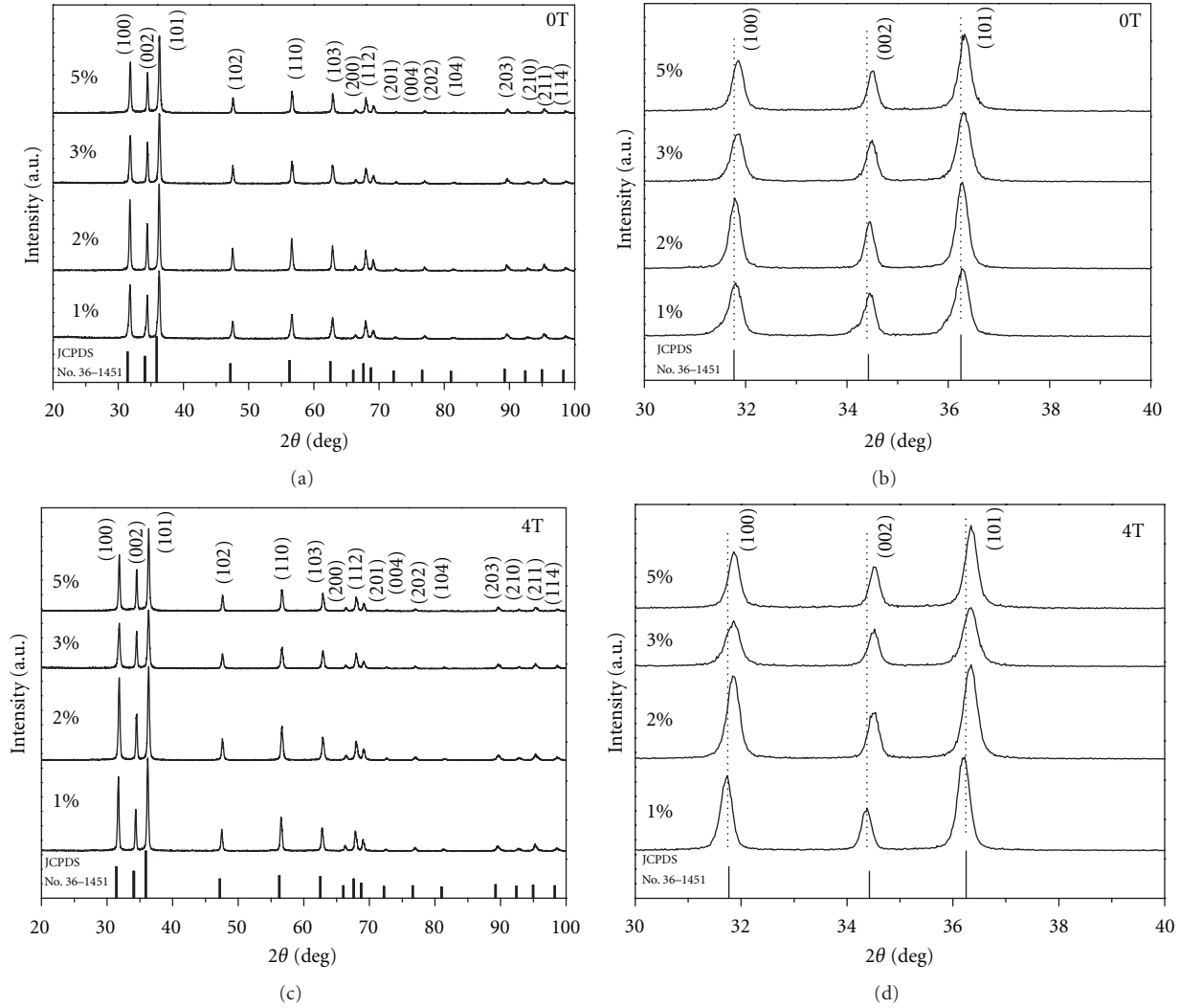
Figure 1: XRD patterns of 1%, 2%, 3%, and 5% Cr-doped ZnO synthesized under 0 T ((a), (b)) and 4 T ((c), (d)) magnetic fields.

a certain concentration of chromium nitrate in zinc acetate solution were then transferred into autoclave (25 mL) and maintained at 453 K for 4 h with 4 T pulsed magnetic field (the obtained sample named as 4T-$N$%) or without pulsed magnetic field (named as 0T-$N$%), respectively, in which $N$ presents the Cr nominal content. Finally, the precipitated products were washed with distilled water three times and dried at 373 K for 10 h.

The crystal structures of the samples were determined by X-ray diffraction (XRD) equipped with CuK$_\alpha$ radiation ($\lambda = 1.5406$ Å). Field emission scanning electron microscope (FE-SEM, JEOL JSM-6700) was used to observe the morphologies. The Raman scattering spectra of the samples were recorded by a Renishaw InVia Confocal micro-Raman system using the 785 nm line as excitation source. Magnetic property of the samples was measured by vibrating sample magnetometer (VSM, Lakeshore 7407). The valence state of the Cr element was analyzed by X-ray photoelectron spectroscopy (XPS) (Thermo ESCALAB 250).

## 3. Results and Discussion

Figure 1 shows the XRD patterns of the Cr-doped ZnO DMSs with various Cr contents synthesized with and without 4 T magnetic fields. All the diffraction peaks (Figures 1(a) and 1(c)) are sharp and match well with those of hexagonal wurtzite structure of ZnO (space group: P63mc (186), JCPDS no. 36-145). No Cr, Cr oxides, or any other impurity-phase peaks are observed which reveals that Cr-doped ZnO DMSs maintain a highly pure crystalline wurtzite structure. Comparing the diffraction peaks (100), (002), and (101) of Cr-doped ZnO DMSs (Figures 1(b) and 1(d)), the peaks shift to larger angles with the increase of Cr contents and the highest shift is for sample with 5% Cr nominal content. The reason is due to the smaller ion radius of Cr$^{3+}$ (0.63 Å) comparing to that of Zn$^{2+}$ (0.74 Å). The lattice constants of ZnO decrease slightly after Cr ions doped into the crystal lattice which cause the main peaks moving to the higher angles. The higher the content of Cr ions in the ZnO lattice, the farther the peaks move. Furthermore, the diffraction
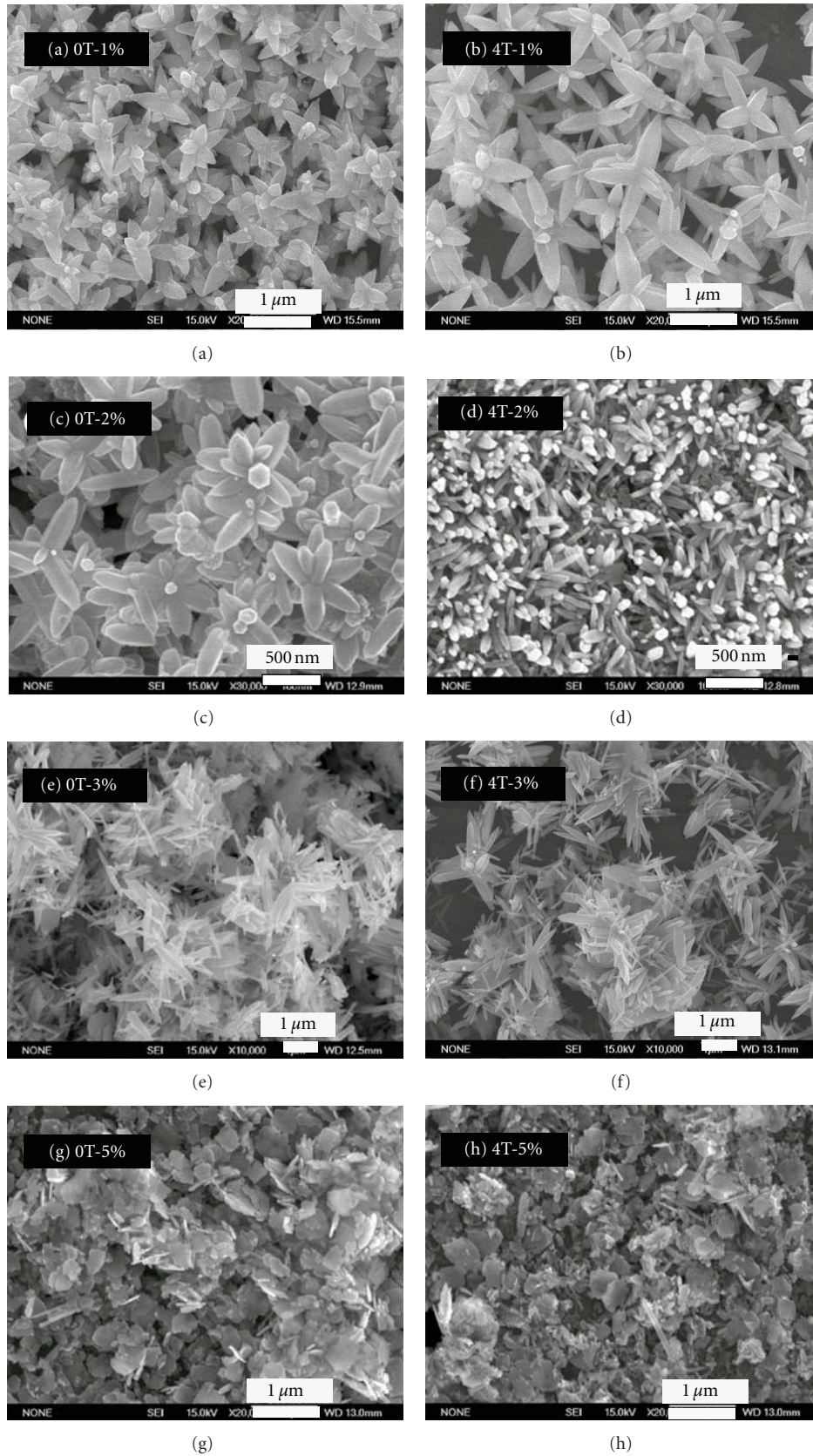
Figure 2: SEM images of Cr-doped ZnO with different Cr nominal content synthesized under 0 T ((a), (c), (e), (g)) and 4 T magnetic fields ((b), (d), (f), (h)).
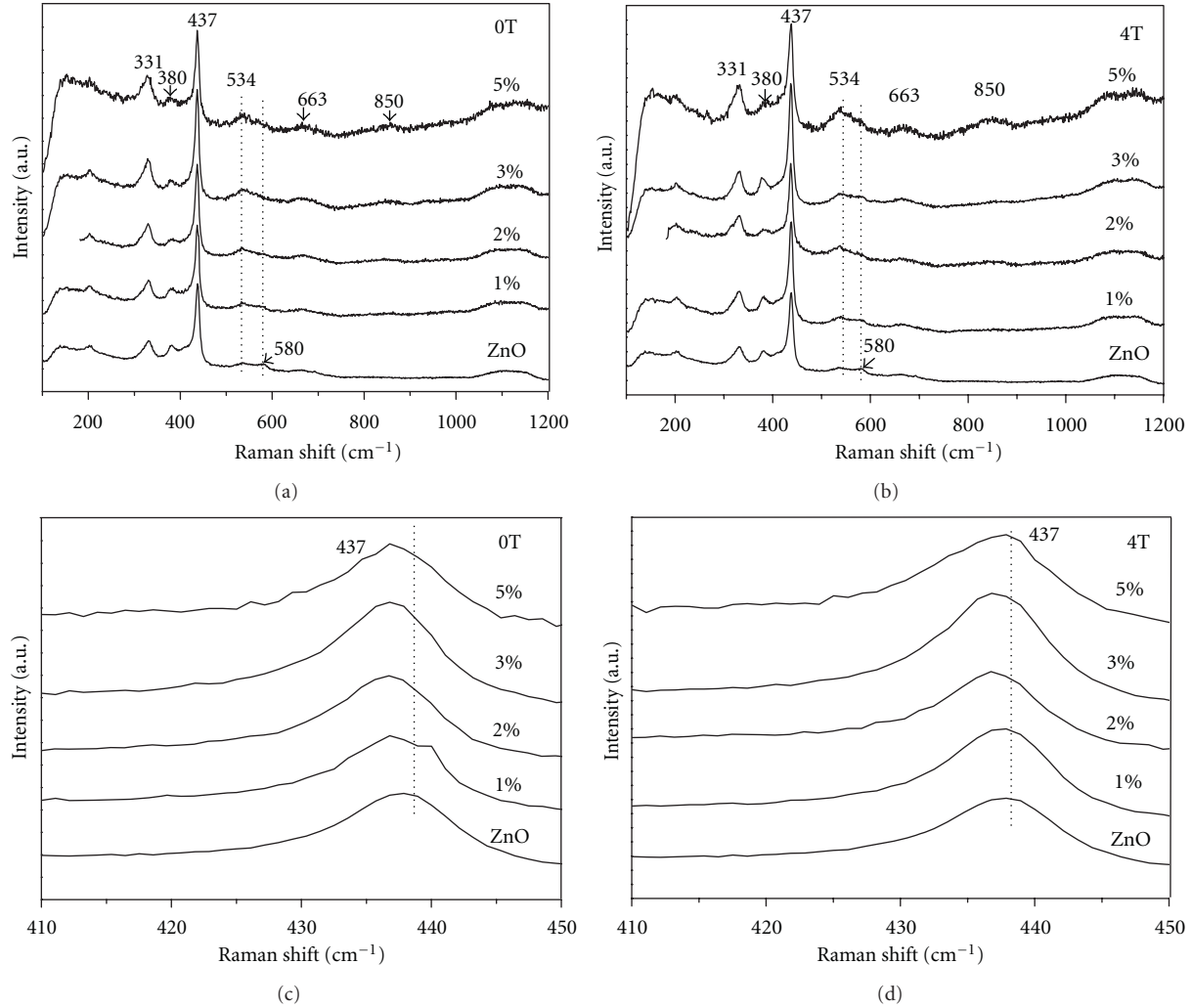
(a)



(b)



(c)



(d)

FIGURE 3: Raman spectra of Cr-doped ZnO DMSs with different Cr nominal contents obtained under 0 T ((a), (c)) and 4 T ((b), (d)) magnetic fields, respectively.

peaks (100), (002), and (101) of samples synthesized under 4 T magnetic field move to larger angles comparing with those of the same Cr content samples synthesized without magnetic field, which indicates that, under high magnetic field, larger amount of Cr ions were doped into the ZnO lattice.

Figure 2 shows the SEM images of Cr-doped ZnO with various Cr nominal contents synthesized under 0 T and 4 T magnetic fields. It is observed that with the Cr contents' increase from 1% to 5%, the morphologies of particles change from flower shape to rod shape and eventually to flake shape. For samples with Cr nominal content of 1% (Figures 2(a) and 2(b)), the grains are both flower shape, but the sizes are different, as sizes of the 4T-1% are much smaller than that of 0T-1%. However, for the 2% Cr content samples (Figures 2(c) and 2(d)), both crystalline shapes and sizes are different, the 4T-2% sample appears as fine dense rod shape with rod diameter of 50–100 nm, whereas the 0T-2% sample appears as flower shape with rod diameter of 100–250 nm. Both of

the samples with Cr nominal content of 3% (Figures 2(e) and 2(f)) appear with irregular rod shape with a little difference in particles size. When the Cr nominal content reaches 5% (Figures 2(g) and 2(h)), both samples appear with irregular flake shapes, while the 4T-5% sample shows more small grains than the 0T-5% sample. Clearly, the morphologies of zinc oxides grains are influenced dramatically as the Cr content increased. Concurrently high magnetic field also plays a significant role in the morphologies of Cr-doped ZnO DMSs. Tanaka et al. [18] reported that c-axis-oriented ZnO could be fabricated in a rotating sample container under static magnetic field during the hydrothermal doping process. The high pulsed magnetic field essentially provided an external energy and promoted the nucleation and growth of the grains, which finally caused the differentiation of crystal morphology.

All the EDS data (Table 1) verify that the actual incorporated Cr contents are lower than the corresponding Cr nominal contents in the doping process, and increase
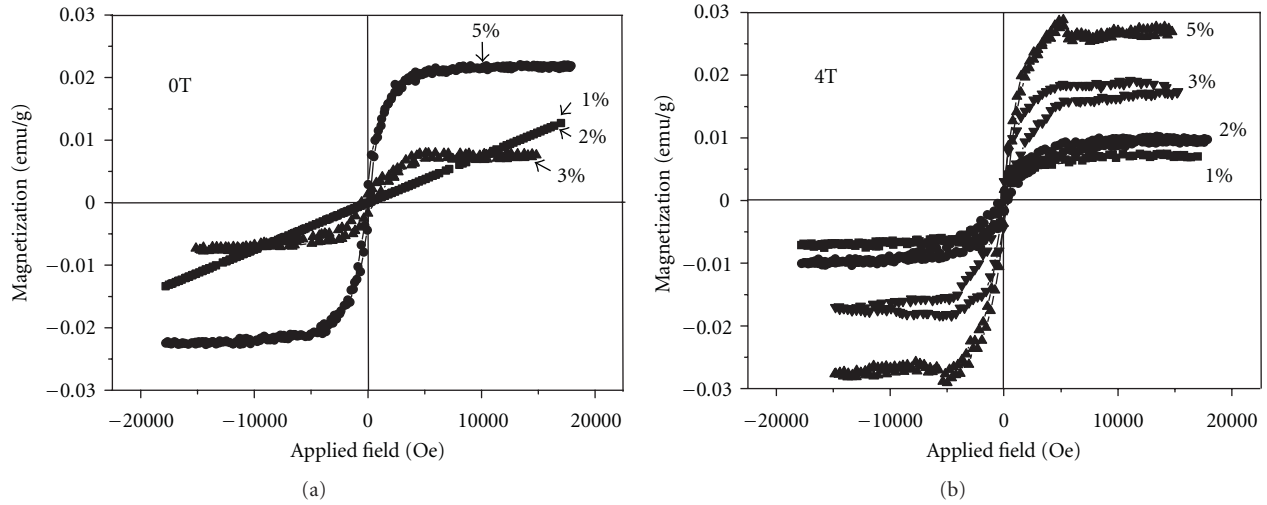
FIGURE 4: Hysteresis loops of Cr-doped ZnO DMSs with different Cr nominal contents synthesized under 0 T (a) and 4 T (b) magnetic fields, respectively.

nominal Cr contents does increase the actual incorporation of Cr. Furthermore, the incorporation of Cr into the ZnO crystal lattice is greater with applying magnetic field than without, which agrees with the results of XRD.

Raman scattering is a versatile technique to characterize the incorporation of Cr ions and the defects in the host lattice. The peak at about $437\,cm^{-1}$ assigned to the $E_2$ (high) mode of ZnO, which is the characteristic mode of the wurtzite structure and sensitive to internal stress [19]. The peak at $580\,cm^{-1}$ assigned to $A_1$ (LO) mode, which is sensitive to changes in the free carrier concentration [20]. From Figures 3(a) and 3(b), there is no obvious observed shift at $437\,cm^{-1}$ for all samples. But compared to the pure ZnO, there is a blue shift with the increase of the Cr doping as shown in the magnified Raman shift region as shown in Figures 3(c) and 3(d). These indicate that with the increase of Cr doping, a little structure disorder was occurred and the little blue shift of the peak also illustrates that the lower amount of Cr doping would not change the crystal structure significantly although defects was introduced by Cr doping. Additionally, when Cr ions were doped, the Raman peaks were slightly changed for the 1%, 2%, 3% samples, and comparing to the characteristic peaks of pure ZnO the peak at $580\,cm^{-1}$ gradually disappeared. The gradually disappearance of the $580\,cm^{-1}$ peak is created by the increase of carrier concentration. When Cr ions increased to 5%, the peak at $534\,cm^{-1}$ increased disproportionally and a new peak appeared at $850\,cm^{-1}$. This new phenomenon is rather unique for the 4T-5% sample only. All these spectroscopic changes probably indicated that the increase of Cr ions incorporation also increases the defect and structures of the ZnO nanocrystals.

Figure 4 shows the magnetic hysteresis (M-H) loops of the Cr-doped ZnO with various Cr nominal contents synthesized under 0 T and 4 T magnetic fields, respectively. It can be seen from Figure 4(a) that 0T-1% and 0T-2% samples show paramagnetic behavior, while 0T-3% and 0T-5%

TABLE 1: EDS parameters and saturation magnetization of Cr-doped ZnO DMSs synthesized with or without high magnetic fields.

| Cr nominal content (at%) | Actual Cr content (at%) | | Ms (emu/g) | |
|---|---|---|---|---|
| | 0 T | 4 T | 0 T | 4 T |
| 1 | 0.22 | 0.35 | — | 0.0075 |
| 2 | 1.1 | 1.4 | — | 0.01 |
| 3 | 2.3 | 2.4 | 0.01 | 0.02 |
| 5 | 3.1 | 3.7 | 0.02 | 0.03 |

samples show ferromagnetic behavior at room temperature. It had been discussed in our previous work [15] that the weak hybridization effect between Cr ions and defects is the reason which results in paramagnetic behavior of sample 0T-2% at 298 K. From Figure 4(b), all the samples obtained under 4 T magnetic fields manifest room temperature ferromagnetic behavior. The saturation magnetizations (Ms, Table 1) of 1%, 2%, 3%, and 5% sample under pulsed high magnetic field was enhanced compared with 0 T samples, respectively. It is believed that the occurrence of strong electronic coupling between bound polarons and Cr ions forms bound magnetic polarons (BMPs) [3], which is proposed to play an important role in the ferromagnetic origin of Cr-doped ZnO DMSs [21, 22]. Kittilstved et al. [23] suggested defect-bound carriers such that point defects hybridization with magnetic dopants would induce ferromagnetism in transition metal ions doped ZnO. In this study, we have found that, by applying high magnetic field, it can increase the incorporation of Cr ions into the ZnO crystal lattice, and this is shown by the XRD, SEM, and Raman analysis. Since more defects are introduced into the crystal lattice under high magnetic field, the hybridization between defects and Cr dopants should be more efficient, which is probably the cause of room temperature ferromagnetism and the enhancement of saturation magnetization of the Cr-doped ZnO DMSs.
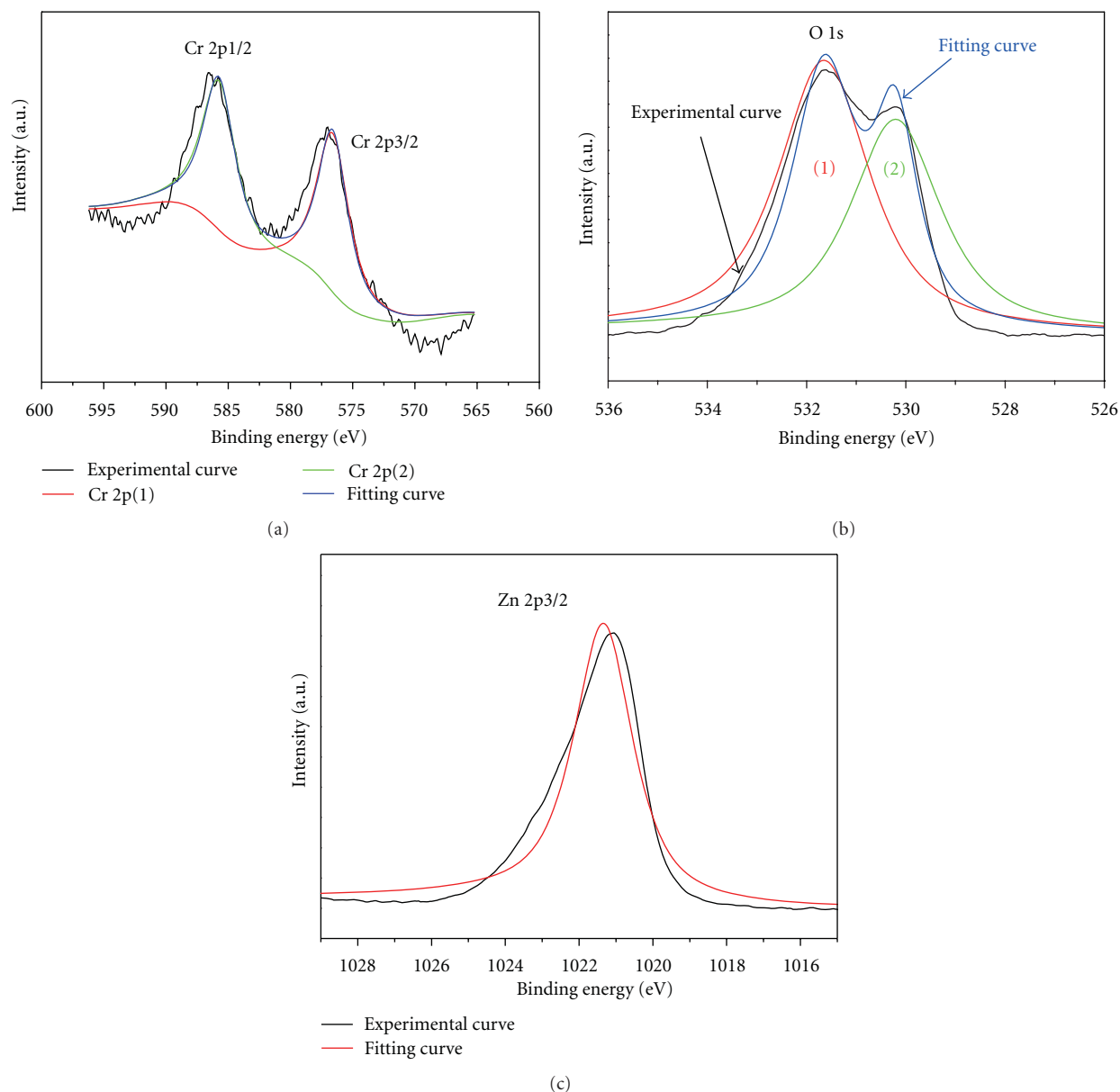
(a)

(b)



(c)

FIGURE 5: XPS spectrum of Cr-doped ZnO nanoparticles.

In order to investigate the chemical state of the host and dopant elements, the XPS studies were undertaken. XPS analysis shows the presence of Zn, Cr, and O elements in Cr-doped ZnO. The overlapped bands were resolved into separated peaks by using XPS PEAK41 software. The Cr 2p3/2, Cr 2p1/2, O 1s, and Zn 2p3/2 XPS spectral regions of the Cr-doped ZnO nanoparticle are shown in Figure 5 for 1% Cr-4T sample. Based on the Gauss fitting, the Cr 2p3/2 peak position is at 576.6 eV in the Cr-doped ZnO nanoparticle. It is clearly different from 574.2 eV of Cr metal and 576.0 eV of $Cr^{2+}$, but it is quite close to the peak position of Cr 2p3/2 (576.7 eV) in $Cr_2O_3$ [24]. It suggests that the Cr dopants in the ZnO lattice are actually the $Cr^{3+}$ ions.

## 4. Conclusions

The 1%, 2%, 3%, and 5% Cr-doped ZnO DMSs nanocrystals were synthesized by hydrothermal method under high magnetic field. Both the Cr content and high magnetic field significantly impacted the microstructure and magnetic property of Cr-doped ZnO DMSs. With the increase of Cr contents from 1% to 5%, the morphologies of particles changed from flower shape to rod shape and eventually to flake shape. After the incorporation of Cr, the ZnO DMSs nanocrystals still retained wurtzite crystal structure. The Cr doping caused the increased amount of defects and the enhancement of magnetic property of the materials. All the Cr-doped ZnO DMSs obtained under high magnetic field exhibited ferromagnetic behavior at room temperature. The

Cr ions that incorporated in the ZnO lattice were shown to be the $Cr^{3+}$ cations.

## References

[1] H. Ohno, "Making nonmagnetic semiconductors ferromagnetic," *Science*, vol. 281, no. 5379, pp. 951–956, 1998.

[2] K. R. Kittilstved, W. K. Liu, and D. R. Gamelin, "Electronic structure origins of polarity-dependent high-Tc ferromagnetism in oxide-diluted magnetic semiconductors," *Nature Materials*, vol. 5, no. 4, pp. 291–297, 2006.

[3] J. M. D. Coey, M. Venkatesan, and C. B. Fitzgerald, "Donor impurity band exchange in dilute ferromagnetic oxides," *Nature Materials*, vol. 4, no. 2, pp. 173–179, 2005.

[4] A. Samariya, R. K. Singhal, S. Kumar et al., "Defect-induced reversible ferromagnetism in Fe-doped ZnO semiconductor: an electronic structure and magnetization study," *Materials Chemistry and Physics*, vol. 123, no. 2-3, pp. 678–684, 2010.

[5] R. K. Singhal, A. Samariya, Y. T. Xing et al., "Electronic and magnetic properties of Co-doped ZnO diluted magnetic semiconductor," *Journal of Alloys and Compounds*, vol. 496, no. 1-2, pp. 324–330, 2010.

[6] R. K. Singhal, A. Samariya, S. Kumar et al., "Switch "on" and "off" ferromagnetic ordering through the induction and removal of oxygen vacancies and carriers in doped ZnO: a magnetization and electronic structure study," *Physica Status Solidi (A) Applications and Materials*, vol. 207, no. 10, pp. 2373–2386, 2010.

[7] J. H. Lim, C. K. Kong, K. K. Kim, I. K. Park, D. K. Hwang, and S. J. Park, "UV electroluminescence emission from ZnO light-emitting diodes grown by high-temperature radiofrequency sputtering," *Advanced Materials*, vol. 18, no. 20, pp. 2720–2724, 2006.

[8] J. K. Furdyna, "Diluted magnetic semiconductors," *Journal of Applied Physics*, vol. 64, no. 4, pp. R29–R64, 1988.

[9] T. Dietl, T. Dietl, H. Ohno, F. Matsukura, J. Cibert, and D. Ferrand, "Zener model description of ferromagnetism in zinc-blende magnetic semiconductors," *Science*, vol. 287, no. 5455, pp. 1019–1022, 2000.

[10] K. Sato and H. Katayama-Yoshida, "Material design for transparent ferromagnets with ZnO-based magnetic semiconductors," *Japanese Journal of Applied Physics, Part 2*, vol. 39, no. 6, pp. L555–L558, 2000.

[11] D. C. Kundaliya, S. B. Ogale, S. E. Lofland et al., "On the origin of high-temperature ferromagnetism in the low-temperature-processed Mn-Zn-O system," *Nature Materials*, vol. 3, no. 10, pp. 709–714, 2004.

[12] A. Quesada, M. A. García, P. Crespo, and A. Hernando, "Materials for spintronic: room temperature ferromagnetism in Zn-Mn-O interfaces," *Journal of Magnetism and Magnetic Materials*, vol. 304, no. 1, pp. 75–78, 2006.

[13] H. B. Wang, H. Wang, C. Zhang et al., "Effect of annealing on the magnetic properties of solution synthesized Zn1-xMnxO nanorods," *Materials Chemistry and Physics*, vol. 113, no. 2-3, pp. 884–888, 2009.

[14] D. Milivojević, J. Blanuša, V. Spasojević, V. Kusigerski, and B. Babić-Stojić, "Room temperature ferromagnetism in Zn-Mn-O," *Solid State Communications*, vol. 141, no. 12, pp. 641–644, 2007.

[15] Y. Li, Y. Li, M. Zhu et al., "Structure and magnetic properties of Cr-doped ZnO nanoparticles prepared under high magnetic field," *Solid State Communications*, vol. 150, no. 15-16, pp. 751–754, 2010.

[16] T. Yang, Y. Li, M. Y. Zhu et al., "Room-temperature ferromagnetic Mn-doped ZnO nanocrystal synthesized by hydrothermal method under high magnetic field," *Materials Science and Engineering B*, vol. 170, no. 1–3, pp. 129–132, 2010.

[17] J. Huang, M. Zhu, Y. Li et al., "Fabricating Co doped ZnO nanocrystallines by hydrothermal method with high pulsed magnetic field," *Journal of Nanoscience and Nanotechnology*, vol. 10, no. 11, pp. 7303–7306, 2010.

[18] S. Tanaka, A. Makiya, Z. Kato, and K. Uematsu, "*c*-axis oriented ZnO formed in a rotating magnetic field with various rotation speeds," *Journal of the European Ceramic Society*, vol. 29, no. 5, pp. 955–959, 2009.

[19] L. B. Duan, G. H. Rao, Y. C. Wang, J. Yu, and T. Wang, "Magnetization and Raman scattering studies of (Co,Mn) codoped ZnO nanoparticles," *Journal of Applied Physics*, vol. 104, no. 1, Article ID 013909, 5 pages, 2008.

[20] Y. Huang, M. Liu, Z. Li, Y. Zeng, and S. Liu, "Raman spectroscopy study of ZnO-based ceramic films fabricated by novel sol-gel process," *Materials Science and Engineering B*, vol. 97, no. 2, pp. 111–116, 2003.

[21] N. H. Hong, J. Sakai, N. T. Huong, N. Poirot, and A. Ruyter, "Role of defects in tuning ferromagnetism in diluted magnetic oxide thin films," *Physical Review B*, vol. 72, no. 4, Article ID 045336, 5 pages, 2005.

[22] M. Venkatesan, C. B. Fitzgerald, J. G. Lunney, and J. M. D. Coey, "Anisotropic ferromagnetism in substituted zinc oxide," *Physical Review Letters*, vol. 93, no. 17, Article ID 177206, 4 pages, 2004.

[23] K. R. Kittilstved, D. A. Schwartz, A. C. Tuan, S. M. Heald, S. A. Chambers, and D. R. Gamelin, "Direct kinetic correlation of carriers and ferromagnetism in $Co^{2+}$:ZnO," *Physical Review Letters*, vol. 97, no. 3, Article ID 037203, 4 pages, 2006.

[24] Z. Jin, T. Fukumura, M. Kawasaki et al., "High throughput fabrication of transition-metal-doped epitaxial ZnO thin films: a series of oxide-diluted magnetic semiconductors and their properties," *Applied Physics Letters*, vol. 78, no. 24, pp. 3824–3826, 2001.

*Research Article*

# Growth of Vertically Aligned ZnO Nanowire Arrays Using Bilayered Metal Catalysts

**Hua Qi, Evan R. Glaser, Josh D. Caldwell, and S. M. Prokes**

*Electronics Science and Technology Division, Naval Research Laboratory, Washington, DC 20375, USA*

Correspondence should be addressed to Hua Qi, qhqihua@yahoo.com

Vertically aligned, high-density ZnO nanowires (NWs) were grown for the first time on c-plane sapphire using binary alloys of Ni/Au or Cu/Au as the catalyst. The growth was performed under argon gas flow and involved the vapor-liquid-solid (VLS) growth process. We have investigated various ratios of catalyst components for the NWs growth and results indicate that very thin adhesion layers of Ni or Cu deposited prior to the Au layer are not deleterious to the ZnO NW array growth. Significant improvement of the Au adhesion on the substrate was noted, opening the potential for direct catalyst patterning of Au and subsequent NW array growth. Additionally, we found that an increase of in thickness of the Cu adhesion layer results in the simultaneous growth of NWs and nanoplates (NPs), indicating that in this case the growth involves both the VLS and vapor-solid (VS) growth mechanisms. Energy dispersive X-ray spectroscopy (EDX) and surface-enhanced Raman scattering (SERS) studies were also performed to characterize the resulting ZnO NW arrays, indicating that the NWs grown using a thin adhesion layer of Ni or Cu under the Au show comparable SERS enhancement to those of the pure Au-catalyzed NWs.

## 1. Introduction

One-dimensional zinc oxide (ZnO) nanowires (NWs) have been attracting much attention because they can be used to design novel nanoscale devices due to their wide band gap, high mechanical stability, and high isoelectric point [1–13]. Recently, several growth techniques to produce vertically aligned ZnO NW arrays have been studied, including the solution-based method [14] and vapor transport growth [15]. One of the well-established methods to grow nanowires is the vapor-liquid-solid (VLS) growth process, in which Au is used as the catalyst [16, 17]. In the VLS process of ZnO growth, the Au islands on the substrate serve as the nucleation sites for the condensation of Zn vapor from a nearby ZnO source, and then the ZnO NWs grow from the supersaturated liquid eutectic Zn-Au mixture.

Although vertical ZnO nanowire (NWs) arrays have been grown using pure Au catalyst [7], the use of these ZnO NW arrays in the design and fabrication of new plasmonic structures is limited due to the poor adhesion of Au on the required sapphire or GaN substrates, which is well known. Since there is very little information available on the metal catalyst adhesion issues for the growth of vertically aligned ZnO NWs or the affects of using the bilayered metal catalysts for such growth, we have initiated such a study. Thus, we have investigated the use of adhesion layers of different metals, including Cu, Ni, Cr, Ti and their bi-layers with Au, in order to grow vertically aligned ZnO NWs on c-sapphire, which would be amenable to nanopatterning and further device fabrication. In the standard single metal species catalyst VLS process, a simple binary eutectic is employed, but it becomes much more challenging in the case of bilayered metal catalysts, in which a ternary eutectic may be formed. In our study, the vertical ZnO NWs were successfully grown via bilayered metal catalysts and further characterized by high-resolution SEM/TEM with energy dispersive X-ray spectroscopy (EDX) capability. Additional characterization techniques also showed that the NWs grown using certain thin adhesion layers did not change their optical or structural properties, a necessary condition for future plasmonic device designs and fabrication.

## 2. Experimental Details

The growth of the vertical ZnO NW arrays was carried out in a horizontal quartz tube. A mixture of ZnO : C
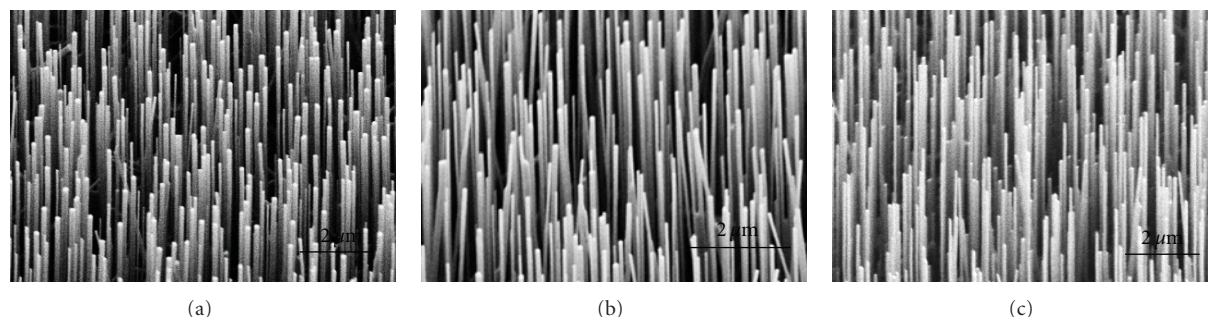
(a)

(b)

(c)

FIGURE 1: SEM images of vertical ZnO NWs grown using 1 nm Ni/5 nm Au (a), 1 nm Cu/5 nm Au (b), and 5 nm pure gold catalyst (c). Sample stage is tilted 45° while imaging.
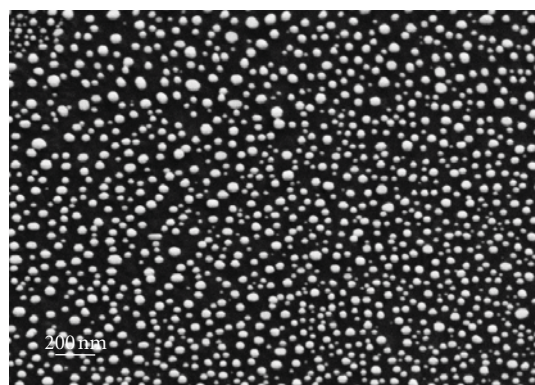


FIGURE 2: A representative SEM image of the particle sizes after the bi-layer metal thin films were deposited and annealed in a furnace, prior to the nanowires growth.



FIGURE 3: A typical SEM image of the nanowires growth with some extremely long nanowires.

(1 : 1 by weight) source powder was placed in one end of an alumina boat, and the c-sapphire substrate with the metal catalyst thin films was placed above, facing the source. The furnace was heated to 900°C while argon flowed through the tube. Pure Au, Cu, Ni, and alloys of Cu-Au, Ni-Au, Cr-Au, and Ti-Au were, respectively, deposited on separate c-sapphire substrates by an FC-2000 Temescal E-beam metals evaporation system, at an evaporation rate of 1 Å/s, and used

as the catalyst during the ZnO growth processes. The double-layer alloys were deposited by a two-step process. Firstly the sapphire was covered with a layer of Cu or Ni, which plays the important role of adhesion to the substrate. Secondly, the gold layer was deposited onto the Cu or Ni layer.

A LEO SUPRA 55 scanning electron microscope (SEM) with energy dispersive X-ray spectroscopy (EDX) capability was used to investigate the topographies and the chemical compositions of the NWs and the alloy tip formed during the growth process. The resulting NW samples that were used for the SERS analysis were as-grown samples, without any electron beam exposure in the SEM or EDX. For the lithography test process, a wraith 150 e-beam writer system and a standard procedure were employed to perform the e-beam lithography, and PMMA was used as the pattern writing resist.

For the surface-enhanced Raman spectroscopy (SERS) measurements, 8 nm of silver was deposited on the vertically aligned ZnO NWs using an FC-2000 Temescal E-beam metals evaporation system, at an evaporation rate of 0.5 Å/s. The samples were then immersed in a solution of benzenthiol ($10^{-3}$ M) for 6 h and dried for SERS analysis. The SERS of the vertical NWs array samples was performed utilizing a Delta Nu system which consists of an Olympus Microscope and a Raman spectrometer equipped with a thermoelectrically cooled CCD. The 785 nm line of a Ti: Sapphire laser was used as the excitation source to detect the SERS. The microscope utilized a 50X 0.75 NA objective for focusing the laser light. The spectra were collected with a laser power of 6 mW at the sample, and the laser spot size was about 2 $\mu$m.

## 3. Results and Discussion

The representative scanning electron microscope (SEM) images of bi-layers of 1 nm Ni/5 nm Au, 1 nm Cu/5 nm Au, and pure Au-catalyzed ZnO NWs grown on c-sapphire are shown in Figures 1(a), 1(b), and 1(c), respectively. As can be seen, the successful growth of vertical ZnO using Cu/Au and Ni/Au bi-layers is clear, and these arrays exhibited the same morphology as the NWs grown by a pure gold catalyst (Figure 1(c)). The NWs display a highly vertical alignment on the c-sapphire substrate and an average diameter between 50–150 nm, depending on the thickness of the catalyst [18].

(a)

(c)

| Element | keV | K ratio | Wt% | At% |
|---|---|---|---|---|
| Au | 2.121 | 0.8884 | 93.83 | 83.11 |
| Ni | 7.477 | 0.0185 | 1.38 | 4.1 |
| Zn | 8.637 | 0.0658 | 4.79 | 12.79 |
| Total | | | 100 | 100 |

(e)

(b)

(d)

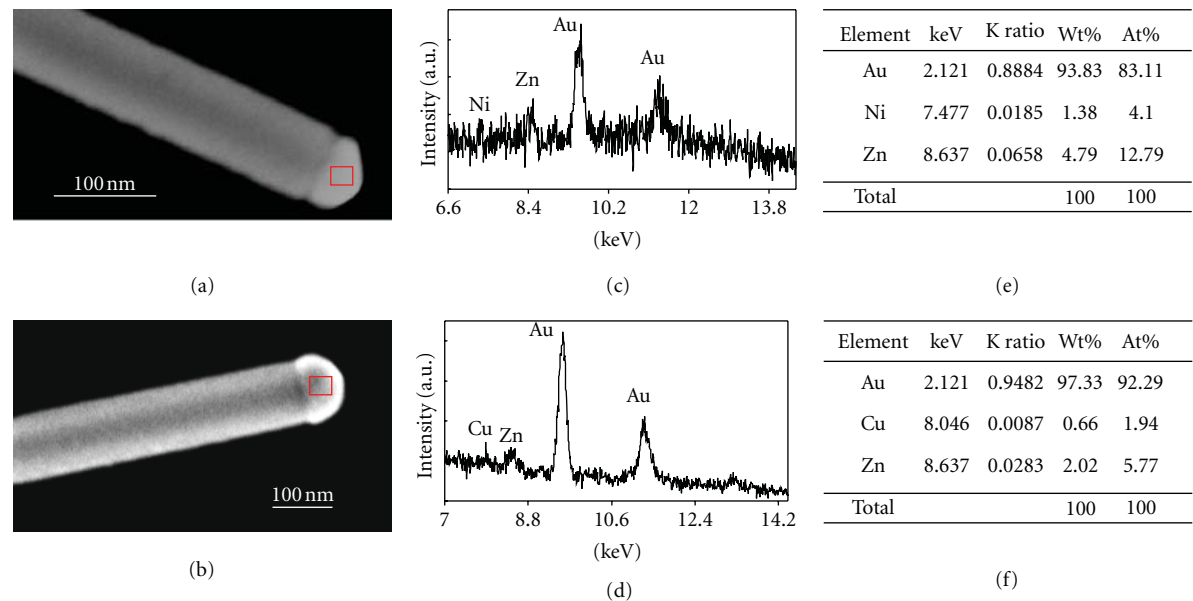| Element | keV | K ratio | Wt% | At% |
|---|---|---|---|---|
| Au | 2.121 | 0.9482 | 97.33 | 92.29 |
| Cu | 8.046 | 0.0087 | 0.66 | 1.94 |
| Zn | 8.637 | 0.0283 | 2.02 | 5.77 |
| Total | | | 100 | 100 |

(f)

FIGURE 4: High-resolution SEM images of Ni/Au-catalyzed (a) and Cu/Au-catalyzed (b) ZnO single NW. EDX analysis patterns (c and d) of the alloy tip as shown in the red rectangle areas of (a) and (b). Composites analysis reports of tip alloy (e and f).



(a)

(b)

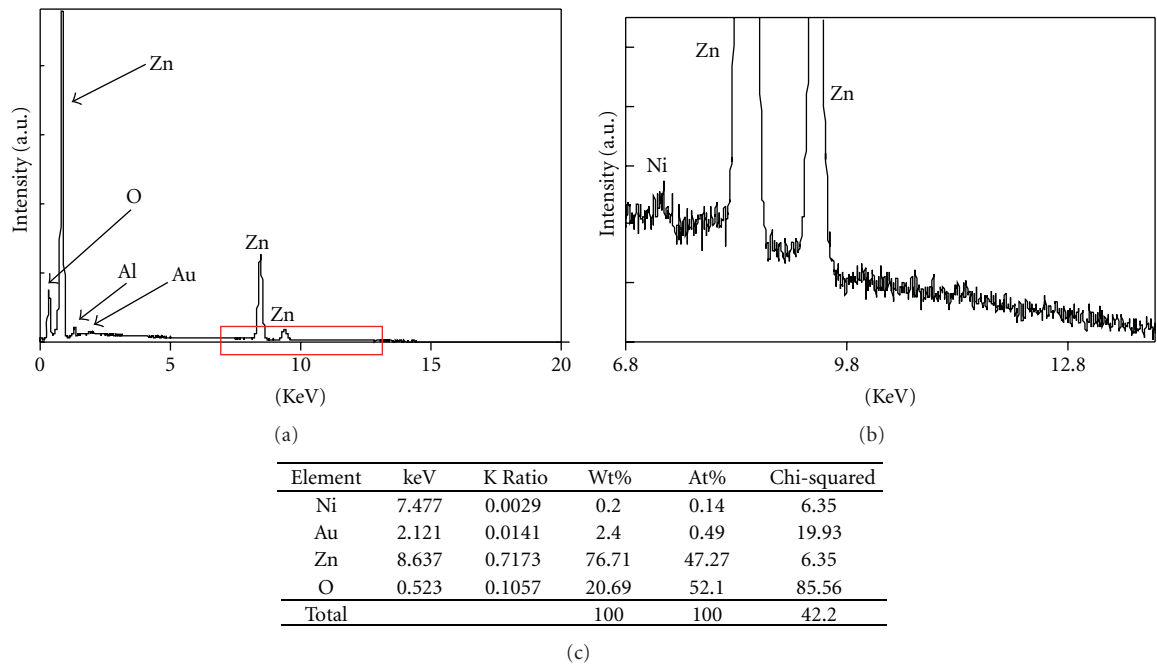| Element | keV | K Ratio | Wt% | At% | Chi-squared |
|---|---|---|---|---|---|
| Ni | 7.477 | 0.0029 | 0.2 | 0.14 | 6.35 |
| Au | 2.121 | 0.0141 | 2.4 | 0.49 | 19.93 |
| Zn | 8.637 | 0.7173 | 76.71 | 47.27 | 6.35 |
| O | 0.523 | 0.1057 | 20.69 | 52.1 | 85.56 |
| Total | | | 100 | 100 | 42.2 |

(c)

FIGURE 5: Representative energy dispersive X-ray (EDX) spectroscopy of ZnO NWs grown on sapphire with catalysts of 1 nm Ni/5 nm Au alloy (a), a close-up plot (b) of the red rectangle region, and (c) a corresponding composition analysis of the large area of ZnO NWs.

Actually the catalyst particles are not fairly similar in size in the case where we deposited thin film bi-layers, which resulted in the random nanowires growth. We studied the particle sizes after the bi-layer metal thin films were deposited and annealed in a furnace, prior to the nanowires growth. A representative SEM image is shown in Figure 2, clearly demonstrating the inhomogeneity of the particles size, which leads to a huge size distribution in diameter. The particle sizes were much more uniform though if the bi-layer thin films were first patterned using e-beam lithography. However, our study was mostly concerned with adhesion as the first step before e-beam lithography, so most of our samples were grown using unpatterned bi-layer thin films as the catalysts. The lengths of these NWs can be varied from several hundreds of nanometers to longer than ten micrometers by adjusting the growth and gas flow time. In fact, there is
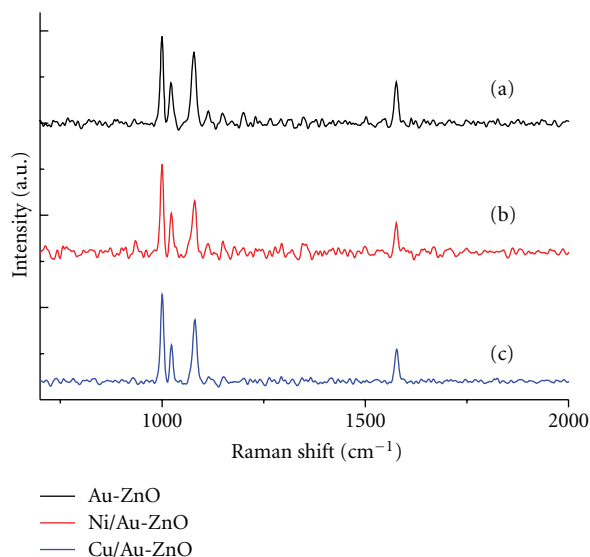
FIGURE 6: Surface-enhanced Raman spectroscopy (SERS) of vertical ZnO NWs grown using (a) pure gold, (b) Ni/Au alloy, and (c) Cu/Au alloy.

some relation between alignments with the length of the nanowire. If the nanowires grow extremely long (longer than 20 micrometers), the top of the nanowires begins to bend and cannot keep the vertical alignment, as shown in Figure 3. We have also found that the growth condition for the aligned ZnO NW arrays has to be optimized by balancing the amount of all vapor phases in the system. In addition, the oxygen content in the system also plays an important role during the growth process [19]. Since, in our case, the base vacuum of the system was around 50 mTorr, which provided sufficient oxygen partial pressure, only argon gas was introduced to the system at a rate of 45 mL/min during the whole growth process.

The NWs as grown on sapphire were further analyzed by energy dispersive X-ray spectroscopy (EDX) to confirm the successful growth and stoichiometry of the ZnO NWs. The EDX signal intensities are comparable to the Zn signal strength obtained from the NWs grown via pure Au, demonstrating the high density of NWs in these cases. To investigate the detailed information of the grown NWs with Ni/Au or Cu/Au bilayered catalysts, we performed high-resolution SEM and EDX investigations on a single NW and its alloy tip. As shown in Figures 4(a) and 4(b), the metal alloy tip was clearly observed at the end of NW, indicating that the ZnO NW growth involves the vapor-liquid-solid (VLS) mechanism. Further EDX analyses of these metal tips (the red rectangle area shown in Figures 4(a) and 4(b)) at high magnification demonstrate that the tips are indeed ternary composites of Cu/Au/Zn or Ni/Au/Zn and are not simpley an Au-Zn binary. As shown in Figures 4(c), 4(d), 4(e), and 4(f), the EDX pattern and the data analysis clearly indicate the presence of the ternary alloy during the ZnO NWs VLS growth process. In addition, the surface of the NW is smooth and no segregation was observed, which is in good agreement with our expectation based on Cu/Au or Ni/Au

phase diagrams. Specifically in the case of the Cu/Au or Ni/Au system, the phase diagrams indicate a continuous solid solution exists at the temperatures of interest in our work, so no segregation was expected. Although the phase diagram of Cu/Au also indicates a series of solid state transformations at much lower temperatures, the data indicate that they are only stable at a very narrow temperature window significantly below our growth temperature.

It is noted that less amount of Ni is observed in the tip than those initial catalyst composites as deposited. We attributed this observation to the loss of Ni by diffusion into the growing ZnO NW, since kinetics also plays an important role and it is well established that Ni is a fast diffuser in many systems. This supposition is further confirmed by using SEM/EDX to scan a large area of NWs. Figures 5(a) and 5(b) show the representative EDX curves obtained on a large area of ZnO NWs grown by 1 nm Ni/5 nm Au catalysts and a close-up plot of Ni element region. A Ni signal can be recognized clearly, and NWs composites analysis was shown in Figure 5(c), demonstrating that the ratio of Ni to Au is 0.14 to 0.49. This value is very close to the original layer composites produced by e-beam deposition, clearly indicating the diffusion of Ni during the ZnO NW growth process.

Figure 6 shows representative surface-enhanced Raman spectroscopy (SERS) spectra of benzenthiol measured on the NWs grown using Au, Cu/Au, and Ni/Au bi-layer catalysts, respectively. The major Raman peaks at 1000, 1023, 1081, and 1576 cm$^{-1}$ can be assigned to symmetric ring breathing, in-plane C–H bending, wagging of the $CH_2$ groups, and in-plane C–C stretching modes, respectively, of the phenyl ring from benzenthiol [20–23]. As can be seen, the Cu/Au or Ni/Au bi-layer catalyzed NWs result in a comparable SERS enhancement factor as that of the pure Au-catalyzed NWs, indicating that the plasmon properties of the bilayered metal-catalyzed ZnO NW arrays are not affected. In order to produce arrays with 50 nm diameters and with wire-to-wire spacing on the order of 10–50 nm for plasmonic applications, e-beam lithography is necessary, in which the use of an adhesion layer is critical. In addition, this study also provides a useful way for any other nanodevice fabrications based on the patterned ZnO NWs arrays. More characterization indicated that the optical proeperties as revealed by room-temperature photoluminescence (PL) property of these Ni/Au or Cu/Au bi-layer catalyzed NWs are comparable to those of the Au-catalyzed NWs, further demonstrating the feasibility of growing high-quality NWs via these bilayered film catalysts.

Additionally, the NWs can still grow with increasing Cu or Ni ratio in the Cu-Au and Ni-Au layers as shown in Figure 7, including the growths using catalysts (a) 3 nm Cu/3 nm Au, (b) 5 nm Cu/1 nm Au, (c) pure 5 nm Cu, (d) 3 nm Ni/3 nm Au, (e) 1 nm Ti/5 nm Au, and (f) 1 nm Cr/5 nm Au. However, the growths exhibit a mixed morphology of NWs and nanoplates (NPs), most likely a result of varying the metal content of the nucleated catalyst islands. Figure 7(b) is a typical image with clear NWs and NPs obtained on the growth using 5 nm Cu/1 nm Au catalysts. Although the NWs grow by the vapor-liquid-solid (VLS)
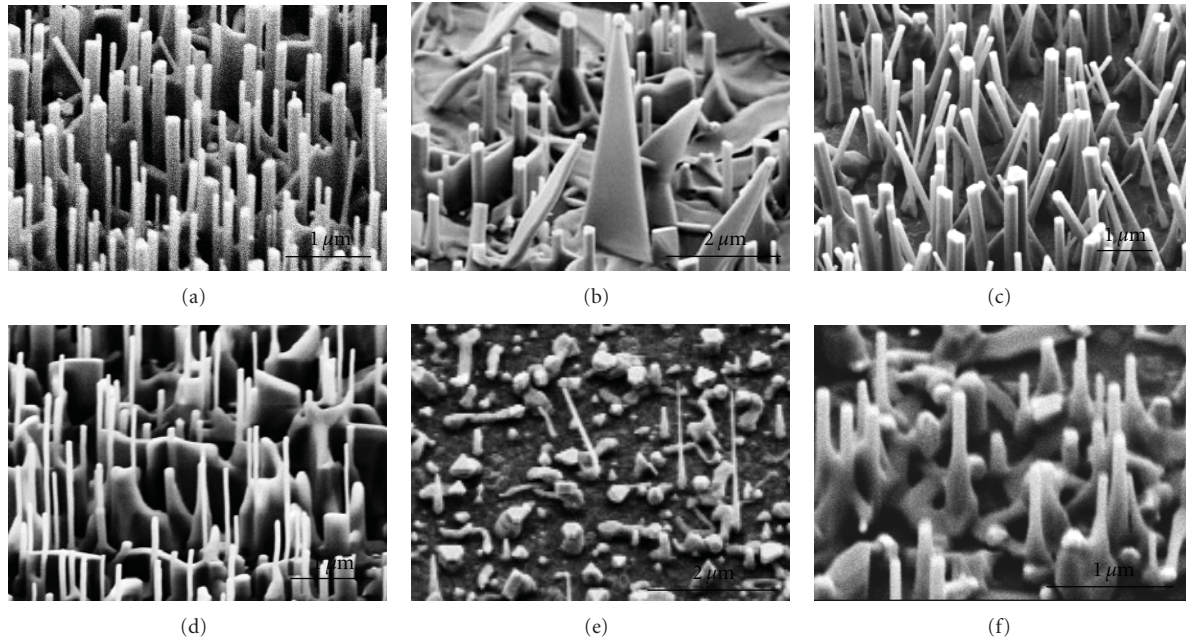
FIGURE 7: SEM images of ZnO nanostructures growth with different alloy or pure metal catalysts on sapphire. (a) Cu/Au = 3 nm/3 nm; (b) Cu/Au = 5 nm/1 nm; (c) pure Cu = 5 nm; (d) Ni/Au = 3 nm/3 nm; (e) Ti/Au = 1 nm/5 nm; (f) Cr/Au = 1 nm/5 nm.

mechanism, the NPs most likely grow by a combination of VLS-VS (vapor-solid) mechanism, which has been reported by Dong et al. and Dai et al. [24, 25], in the CdSe and CdS system. In our case, during the early stage of the growth, ZnO NWs grew from the liquid supersaturated eutectic Zn/Au/Cu mixture by the VLS mechanism. In the process of the ZnO growth, the metal alloy remains at the tip of the NW, which is clearly shown in the SEM images. At the same time, excess Zn vapor is deposited on the sidewalls of some of the already-grown NWs, resulting in the NPs growth, involving both VLS and VS growth modes. Moreover, pure Ni, Cu, Ti/Au, and Cr/Au layers were also investigated. Sparse vertical ZnO NWs were obtained using Cr 1 nm/Au 5 nm as the bi-layer catalyst, whereas very few NWs grew using Ti 1 nm/Au 5 nm. Table 1 presents the detailed information of pure metal or metal layers component catalysts, the morphology of the growth, the length, and the diameters of the resulting ZnO nanostructures as grown.

It should be pointed out that, in the case of the bilayered metal catalysts, we are dealing with a three-component system, which is a much more complicated thermodynamic case than the standard two-component system. In the case of the two-component system, it is fairly easy to obtain a phase diagram for the two constituents and from that determine the potential for the formation of a eutectic, as well as the expected eutectic temperature. In our case, however, we are dealing with a metal (Cu, Ni, Ti, or Cr)-Au-Zn that will form ternary phases. Unfortunately, these ternary phase diagrams for temperatures of interest are not available in the literature. Thus, it is impossible to obtain the eutectic point or temperature information from a phase diagram, and thus it is necessary to provide experimental data for the viability of the growth process of these NWs.

It is well known that the Scotch tape is commonly used to investigate the adhesion of metal film on a substrate [26–28]. In our study, the very thin layer of 1 nm Cu or 1 nm Ni deposited prior to the Au layer passed this Scotch tape test successfully, without causing any metal detachment, while a pure gold layer partially peeled off, confirming the need for the use of a bilayered metal.

The improvement of adhesive capability of gold on sapphire was further confirmed by e-beam lithography experiments, which are shown in Figure 8. It is clear that part of the metal layer delaminated when pure gold was used as a lift-off metal in acetone after e-beam pattern writing. In fact, the e-beam pattern lithography results in the loss of the designed pattern completely as shown in Figure 8(a). However we successfully obtained a designed pattern when a thin layer of 1 nm Ni was introduced under gold (Figure 8(b)), which clearly demonstrates the enhancement of the metal adhesion. It is well known that the formation of a Ni–O bond is much easier than that of an Au–O bond, which can enhance the adhesion of Ni on a substrate [29]. Indeed Au is an inert metal in the air, and this property obviously decreases its stickiness to the substrate. Furthermore, it has been well established by the semiconductor device community that the adhesion of Au can be significantly improved by the addition of a Ni or Cr layer.

## 4. Conclusion

High-quality vertically aligned ZnO NW arrays were grown for the first time using bilayered metal catalysts of Ni/Au and Cu/Au, respectively. We show that their structural and

TABLE 1: Experimental growth conditions and results of ZnO NW samples.

| Samples | Thickness of metal (nm) | Morphology | NW length | NW diameter (nm) |
|---|---|---|---|---|
| A | Cu : Au = 1 nm : 5 nm | Vertically aligned NW | >5 $\mu$m | 20–200 |
| B | Cu : Au = 3 nm : 3 nm | Vertical NW | >2 $\mu$m | 20–200 |
| C | Cu : Au = 5 nm : 1 nm | Mixture growth of vertical NW and nano-wall | <2 $\mu$m | 50–400 |
| D | Ni : Au = 1 nm : 5 nm | Vertically aligned NW | >5 $\mu$m | 20–200 |
| E | Ni : Au = 3 nm : 3 nm | Vertically NW and nano-wall | 500 nm–2 $\mu$m | 50–300 |
| F | Cu = 5 nm | Mostly vertical NW | >2 $\mu$m | 50–300 |
| G | Ni = 5 nm | Few sparse and short NW | <200 nm | 30–60 |
| H | Ti : Au = 1 nm : 5 nm | Few vertical NW | <3 $\mu$m | 60–150 |
| I | Cr : Au = 1 nm : 5 nm | Sparse and vertical NW | 400 nm–2 $\mu$m | 60–200 |
| J | Au = 5 nm | Vertically aligned NW | >5 $\mu$m | 20–200 |



(a)　　　　　　　　　　(b)
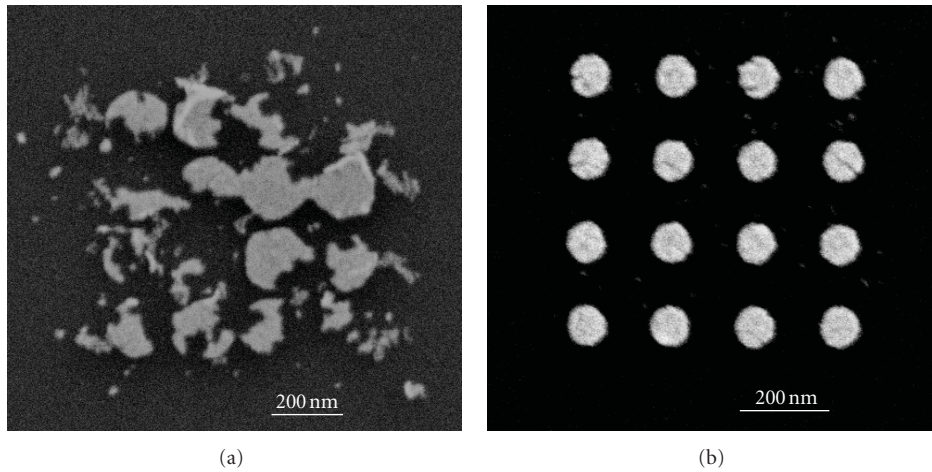
FIGURE 8: E-beam lithography and following lift-off results with (a) pure gold and (b) Ni/Au = 1 nm/5 nm alloy.

optical properties are comparable to those of pure Au-catalyzed NWs. An advantage in this case is that Ni/Au or Cu/Au bi-layers display better adhesion properties than a pure gold catalyst, enabling potential patterning of these ZnO nanowire arrays prior to growth, which is critical for potential plasmonic applications. Due to the VLS growth process, we can also demonstrate high selectivity of the vertical ZnO NW array growth, which occurs only in the patterned catalyst region. This work can have a significant impact on the ability to form very tightly spaced ordered nanowire arrays for plasmonic applications, which are not possible currently due to the adhesion problems of the Au dots formed by e-beam lithography, providing a direct route for the growth of vertically aligned ZnO NWs in any desired pattern for novel nanoscale plasmonic structures.

## Acknowledgments

## References

[1] X. D. Wang, J. Liu, Z. L. Wang, and J. Song, "Direct-current nanogenerator driven by ultrasonic waves," *Science*, vol. 316, no. 5821, pp. 102–105, 2007.

[2] Z. L. Wang and J. Song, "Piezoelectric nanogenerators based on zinc oxide nanowire arrays," *Science*, vol. 312, no. 5771, pp. 242–246, 2006.

[3] C. H. Chen, S. J. Chang, S. P. Chang et al., "Novel fabrication of UV photodetector based on ZnO nanowire/p-GaN hetero-junction," *Chemical Physics Letters*, vol. 476, no. 1–3, pp. 69–72, 2009.

[4] C. C. Lin, W. H. Lin, and Y. Y. Li, "Synthesis of ZnO nanowires and their applications as an ultraviolet photodetector," *Journal of Nanoscience and Nanotechnology*, vol. 9, no. 5, pp. 2813–2819, 2009.

[5] B. Weintraub, S. Chang, S. Singamaneni et al., "Density-controlled, solution-based growth of ZnO nanorod arrays via layer-by-layer polymer thin films for enhanced field emission," *Nanotechnology*, vol. 19, no. 43, Article ID 435302, 2008.

[6] C. Y. Lee, T. Y. Tseng, S. Y. Li, and P. Lin, "Electrical characterizations of a controllable field emission triode based on low temperature synthesized ZnO nanowires," *Nanotechnology*, vol. 17, no. 1, pp. 83–88, 2006.

[7] M. H. Huang, S. Mao, H. Feick et al., "Room-temperature ultraviolet nanowire nanolasers," *Science*, vol. 292, no. 5523, pp. 1897–1899, 2001.

[8] K. Black, A. C. Jones, I. Alexandrou, P. N. Heys, and P. R. Chalker, "The optical properties of vertically aligned ZnO nanowires deposited using a dimethylzinc adduct," *Nanotechnology*, vol. 21, no. 4, Article ID 045701, 2010.

[9] K. S. Leschkies, R. Divakar, J. Basu et al., "Photosensitization of ZnO nanowires with CdSe quantum dots for photovoltaic devices," *Nano Letters*, vol. 7, no. 6, pp. 1793–1798, 2007.

[10] Y. Tak, S. J. Hong, J. S. Lee, and K. Yong, "Fabrication of ZnO/CdS core/shell nanowire arrays for efficient solar energy conversion," *Journal of Materials Chemistry*, vol. 19, no. 33, pp. 5945–5951, 2009.

[11] V. Pachauri, A. Vlandas, K. Kern, and K. Balasubramanian, "Site-specific self-assembled liquid-gated ZnO nanowire transistors for sensing applications," *Small*, vol. 6, no. 4, pp. 589–594, 2010.

[12] J. P. Liu, C. X. Guo, C. M. Li et al., "Carbon-decorated ZnO nanowire array: a novel platform for direct electrochemistry of enzymes and biosensing applications," *Electrochemistry Communications*, vol. 11, no. 1, pp. 202–205, 2009.

[13] X Zhang, A. Hu, T. Zhang, X. Xue, J. Wen, and W. W. Duley, "Subwavelength plasmonic waveguides based on ZnO nanowires and nanotubes: a theoretical study of thermo-optical properties," *Applied Physics Letters*, vol. 96, no. 4, Article ID 043109, 2010.

[14] L. E. Greene, B. D. Yuhas, M. Law, D. Zitoun, and P. D. Yang, "Solution-grown zinc oxide nanowires," *Inorganic Chemistry*, vol. 45, no. 19, pp. 7535–7543, 2006.

[15] S. M. Prokes, O. J. Glembocki, R. W. Rendell, and M. G. Ancona, "Enhanced plasmon coupling in crossed dielectric/metal nanowire composite geometries and applications to surface-enhanced Raman spectroscopy," *Applied Physics Letters*, vol. 90, no. 9, Article ID 093105, 2007.

[16] S. Shafiei, A. Nourbakhsh, B. Ganjipour, M. Zahedifar, and G. Vakili-Nezhaad, "Diameter optimization of VLS-synthesized ZnO nanowires, using statistical design of experiment," *Nanotechnology*, vol. 18, no. 35, Article ID 355708, 2007.

[17] H. Qi, O. J. Glembocki, and S. M. Prokes, "Plasmonic properties of vertically aligned nanowire arrays," *Journal of Nanomaterials*, vol. 2012, Article ID 843402, 7 pages, 2012.

[18] Q. X. Zhao, P. Klason, and M. Willander, "Growth of ZnO nanostructures by vapor-liquid-solid method," *Applied Physics A*, vol. 88, no. 1, pp. 27–30, 2007.

[19] K. Subannajui, N. Ramgir, R. Grimm et al., "ZnO nanowire growth: a deeper understanding based on simulations and controlled oxygen experiments," *Crystal Growth & Design*, vol. 10, no. 4, pp. 1585–1589, 2010.

[20] H. Qi, D. Alexson, O. Glembocki, and S. M. Prokes, "Plasmonic coupling on dielectric nanowire core-metal sheath composites," *Nanotechnology*, vol. 21, no. 8, Article ID 085705, 2010.

[21] R. Aroca and A. Thedchanamoorthy, "Vibrational studies of molecular organization in evaporated phthalocyanine thin solid films," *Chemistry of Materials*, vol. 7, no. 1, pp. 69–74, 1995.

[22] M. Lütt, M. R. Fitzsimmons, and D. Q. Li, "X-ray reflectivity study of self-assembled thin films of macrocycles and macromolecules," *The Journal of Physical Chemistry B*, vol. 102, no. 2, pp. 400–405, 1998.

[23] H. Qi, D. Alexson, O. Glembocki, and S. M. Prokes, "The effect of size and size distribution on the oxidation kinetics and plasmonics of nanoscale Ag particles," *Nanotechnology*, vol. 21, no. 21, Article ID 215706, 2010.

[24] L. F. Dong, J. Jiao, M. Coulter, and L. Love, "Catalytic growth of CdS nanobelts and nanowires on tungsten substrates," *Chemical Physics Letters*, vol. 376, no. 5-6, pp. 653–658, 2003.

[25] G. Z. Dai, Q. L. Zhang, Z. W. Peng et al., "One-step synthesis of low-dimensional CdSe nanostructures and optical waveguide of CdSe nanowires," *Journal of Physics D*, vol. 41, no. 13, Article ID 135301, 2008.

[26] L. A. Baker, F. P. Zamborini, L. Sun, and R. M. Crooks, "Dendrimer-mediated adhesion between vapor-deposited Au and glass or Si wafers," *Analytical Chemistry*, vol. 71, no. 19, pp. 4403–4406, 1999.

[27] M. Charbonnier, Y. Goepfert, M. Romand, and D. Leonard, "Electroless plating of glass and silicon substrates through surface pretreatments involving plasma-polymerization and grafting processes," *The Journal of Adhesion*, vol. 80, no. 12, pp. 1103–1130, 2004.

[28] M. Charbonnier, M. Romand, Y. Goepfert, D. Léonard, and M. Bouadi, "Copper metallization of polymers by a palladium-free electroless process," *Surface and Coatings Technology*, vol. 200, no. 18-19, pp. 5478–5486, 2006.

[29] S. E. Kulkova, S. V. Eremeev, S. Hocker, and S. Schmauder, "Electronic structure and adhesion on metal-aluminum-oxide interfaces," *Physics of the Solid State*, vol. 52, no. 12, pp. 2589–2595, 2010.